Studies of Charged Particle Beam Dynamics on the Paul Trap Simulator Experiment Pure Ion Plasma

Moses Chung

A DISSERTATION

PRESENTED TO THE FACULTY

OF PRINCETON UNIVERSITY

IN CANDIDACY FOR THE DEGREE

OF DOCTOR OF PHILOSOPHY

RECOMMENDED FOR ACCEPTANCE

BY THE DEPARTMENT OF

ASTROPHYSICAL SCIENCES

SEPTEMBER, 2008

Abstract

Based on the compelling physics analogy between intense beam propagating through a periodic focusing quadrupole magnetic field and nonneutral pure ion plasma confined in a linear Paul trap configuration, experimental studies of intense beam propagation under the influence of self-field effects have been performed using the Paul Trap Simulator Experiment (PTSX) device. A new charge collector diagnostic has been implemented, which permits detailed measurement of the radial ion density profile that can be compared with theoretical predictions. To further investigate the trapped plasma properties, a laser-induced fluorescence (LIF) diagnostic system with accompanying barium ion source has also been developed and tested.

To achieve a well-characterized initial beam state for subsequent beam physics experiments, ion injection into the trap has been carefully optimized by characterizing various beam dynamics issues that may invalidate the physics analogy between intense coasting beam and trapped pure ion plasma in the quadrupole focusing fields. An optimized plasma is held in the quasi-equilibrium state for more than 50 ms, which is equivalent to more than 3000 full alternating-gradient (AG) focusing periods, and has a defocusing space-charge force that is about 10% of the applied transverse focusing force. The PTSX device is used to investigate basic physics of transverse beam compression. From a comparison of the analytical estimates based on a Kapchinskij-Vladimirskij (KV) beam model, experimental results on changes in

both the lattice amplitude and frequency, and particle-in-cell (PIC) simulations, it is found that a key physics issue in transverse beam compression is how to suppress the excitation of mismatch oscillations, which is often accompanied by emittance growth and halo formation. When the phase advance is low enough, adiabatic changes in the smooth-focusing frequency turn out to provide an effective control of transverse beam compression. Machine imperfection effects which are unavoidable in the operation of high-intensity accelerators are also investigated. In particular, the effects of faulty magnet sets and random noise in the AG focusing channel are considered. The excitation of mismatch oscillations is observed as a result of focusing field errors, and their characteristics are effectively explained in terms of the KV-equivalent beam model. A continuous increase in emittance that depends on the noise duration and amplitude is observed, together with the synergistic effects between collective modes and colored noise.

Dedicated to

Rev. Sung Kuh Chung,

Mrs. Ok Suk Choi,

Sinai Chung,

and Christian Choi,

for their love, support, and prayer.

Acknowledgments

"Give thanks to the LORD, for he is good! His faithful love endures forever."

Psalms 107:1

I am deeply indebted to many people who have made this thesis work possible. First and foremost, I would like to thank my advisors, Prof. Ronald Davidson and Dr. Philip Efthimion, who provided me the opportunity to work on such a unique experiment, invaluable instructions, and continuous encouragement. I owe many thanks to Dr. Erik Gilson, who patiently taught me almost everything about the PTSX device. He showed me how enjoyable physics could be. I have greatly benefitted from Andy Carpe's excellent technical support. All the laboratory tricks, tips, hands-on skills, and wisdom, if I have, are from him. Their friendship and humor made the L113 a great place to work. I must also express my gratitude to my thesis readers, Drs. Robert Kaita and Hong Qin. In addition to their constructive comments and suggestions, Dr. Kaita has been a spiritual mentor for many years and Dr. Qin gave a lot of physics insight through his coauthored book with Prof. Davidson. I am thankful to Dr. Richard Majeski not only for serving as a committee member but also for sharing his extensive experimental knowledge on every Monday meeting.

I am grateful to Mikhail Dorf who provided tremendous insight and understanding on the key experimental results through his gifted simulation skill. For the laser and optical system, I gratefully acknowledge the help and support from Dr. Jill Foley

encouragement. Thanks to Jong-Kyu Park for perturbing equilibrium state of my office with corny gossips every night. Thanks to Woochang Lee for providing me lots of (illegal) entertainment stuff on weekends. Thanks to Jongsoo You for sacrificing one of his fingernails in helping my moving. Thanks to Eisung Yoon for giving me a chance to learn patience by not showing up for an important ride appointment.

Strong recommendation and guidance from Prof. Sang-Hee Hong and Prof. Yong-Seok Hwang at Seoul National University, and Prof. Suwon Cho at Kyonggi University ultimately lead me here. In particular, I'd like to thank Prof. Hong for his warm-hearted understanding and encouragement that made this long journey possible. I also wish to thank Dr. Vladimir Shiltsev and Dr. Andreas Jansson at Fermilab for offering me a prestigious opportunity to work at Accelerator Physics Center. To share dreams with friends, to encourage each other, and to see the dreams come true are wonderful things. As we shared 25 years ago, I think I became a sort of scientist, not great yet though. I'm very proud of and thankful to my 25-year-old friends, Prof. Sang-Ha Kim at Yonsei University Wonju College of Medicine, You-Sik Kim, a lead guitarist at fusion jazz group "Acid Rain", and Jae-Woo Chung at MIT Media Lab. Thanks to Yong-Ho Kim, Jae-Choon Seol, Tae-Kyun Chung, Dano Kim, Sin-Kyu Kim, Won-Jong Jin, and a new friend Hua Wang for their continuing friendship regardless of where we are.

Special thanks to Mom, Dad, Sinai, and Christian for their inexhaustible love, financial and spiritual support, and prayer. Special thanks to Teriyaki Boys, It's a Grind, and Starbucks Coffee.

Contents

List of Figures

List of Tables

Chapter 1

Introduction

For the optimal design and stable operation of high-intensity accelerators and beam transport systems, it is essential to develop a basic understanding of the beam dynamics with significant space-charge effects [DAVIDSON and QIN, 2001]. In this thesis, based on the physics analogy between intense beam propagating through a periodic focusing quadrupole magnetic field and nonneutral pure ion plasma confined in a compact Paul trap configuration [DAVIDSON *et al.*, 2000], experimental studies of intense beam propagation have been performed using the Paul Trap Simulator Experiment (PTSX) device [GILSON *et al.*, 2004]. The PTSX device is a linear Paul trap [PAUL and STEINWEDEL, 1953] which consists of three cylindrical electrodes of radius $r_w = 10$ cm that are sliced into four 90° azimuthal sectors. The trap confines nonneutral ion plasmas radially by applying an oscillatory voltage $\pm V_0(t)$ to the central electrodes. A DC bias voltage, $+\hat{V}$, applied to the end electrodes, confines the nonneutral ion plasma axially.

1.1 Background

1.1.1 Nonneutral Plasmas and Intense Beams

A nonneutral plasma is defined as a many-body collection of charged particles in which there is not overall charge neutrality [DAVIDSON, 1990]. In principle, nonneutral plasmas are more easily confined than neutral plasmas, and consequently, can be more easily controlled and studied in relatively simple experimental setup like Malmberg-Penning traps [MALMBERG and DEGRASSIE, 1975; PENNING, 1936] and Paul traps [PAUL and STEINWEDEL, 1953]. Similar to the electrically neutral plasmas [CHEN, 1984; GOLDSTON and RUTHERFORD, 1995], nonneutral plasmas exhibit shielding of perturbed electric fields on a scale of the Debye length (Debye shielding) and support various organized (collective) motions such as plasma oscillations, waves, and instabilities. However, there are fundamental differences between nonneutral plasmas and neutral plasmas. Nonneutral plasmas have intense self-electric fields since they have a net charge, and can produce self-magnetic fields in high-current configurations [DAVIDSON, 1990]. These self fields have a large influence on detailed plasma behavior and stability properties. A few examples of nonneutral plasmas are pure electron plasmas in Malmberg-Penning traps for the investigations of basic plasma properties, laser-cooled pure ion plasmas in Paul traps for atomic clock applications, and antimatter plasmas such as positrons and antiprotons for basic atomic and molecular physics [NRC, 1995]. On the more practical side, nonneutral plasmas are widely applied to the the development of many high-power microwave devices used for radar, satellite communications, RF heating of fusion plasmas, and high-intensity accelerators for basic research in high energy and nuclear physics.

A charged particle beam is defined as a collection of charged particles all traveling in nearly the same direction with the nearly the same speed [ROSENZWEIG, 2003]. Particle beams are usually generated from a particle source and injected into the main accelerator where charged particles are focused and bent by use of magnets, and accelerated by use of electromagnetic fields in cavities or waveguides. Recent applications of charged particle beams [DAVIDSON and QIN, 2001; REISER, 1994; WANGLER, 1998] such as heavy ion fusion, spallation neutron sources, and high-gain X-ray free electron lasers, however, require much higher beam currents and charge densities than conventional accelerator systems. For such intense beams, understanding the effects of self fields produced by the beam space charge and current on the detailed dynamics and stability behavior of the beam is increasingly important [DAVIDSON and QIN, 2001]. While tenuous beams are readily described by single particle and linear beam dynamics [WIEDEMANN, 1999; LEE, 2004], intense beam requires extensive consideration of self-field forces through linear and nonlinear analysis [DAVIDSON and QIN, 2001; QIAN, 1995; STRASBURG, 2001], or advanced numerical simulations [FRIEDMAN *et al.*, 1992; QIAN *et al.*, 1997; QIN *et al.*, 2000].

There is a compelling similarity between the physics of nonneutral plasmas and the physics of intense charged particle beams. An intense beam can be considered as a nonneutral plasma in the frame of reference of the beam. Hence, similar to laboratory-confined pure electron plasmas or pure ion plasmas, an intense beam is expected to exhibit many collective properties during propagation through a focusing channel. Many theoretical models and techniques developed for the description of nonneutral plasmas can provide a systematic treatment of the equilibrium, stability, and transport properties of intense charged particle beams. Most interestingly, the

collective processes and nonlinear transverse dynamics of an intense beam propagating through a periodic focusing quadrupole magnetic field (see Sec. 1.1.2) is fully equivalent to the transverse dynamics of a nonneutral plasma trapped in an oscillating quadrupole electric field [DAVIDSON *et al.*, 2000], such as a pure ion plasma confined in a linear Paul trap (see Sec. 1.1.3).

1.1.2 Periodic Focusing Quadrupole Magnetic Field

As mentioned earlier, charged particle beams are transversely focused by use of external magnets arranged along the desired beam path. In most accelerators and beam transport systems, the arrangement of magnets is periodic with a repetitive sequence of identical modules (*periodic focusing*). The simplest and most common periodic focusing module is a combination of two quadrupole magnet sets with alternating polarity of field gradients, which is often termed an alternating-gradient (AG) focusing lattice. Development of AG focusing in the 1950's [COURANT *et al.*, 1952; COURANT and SNYDER, 1958] was a major breakthrough in the history of accelerator development. AG focusing is also called strong focusing in contrast to the weak focusing of the betatron, in which the focusing is achieved only in one transverse dimension [WIEDEMANN, 1999; ROSENZWEIG, 2003]. In the AG focusing system, due to the simultaneous focusing in the two transverse dimensions, the transverse beam size is significantly reduced. Hence, we usually have a thin beam with $a, b \ll S$, where a and b are the characteristic x- and y-dimensions of the beam, and S is the axial periodicity length of the AG focusing lattice. For small values of x and y ($|x|, |y| \ll S$), the AG quadruple magnetic field $\mathbf{B}_q(\mathbf{x}) = B_x^q \hat{\mathbf{e}}_x + B_y^q \hat{\mathbf{e}}_y$ near the beam axis in Fig. 1.1 can be approximated to leading order by [DAVIDSON, 1990]

$$\mathbf{B}_q(\mathbf{x}) = B_q'(z)(y\hat{\mathbf{e}}_x + x\hat{\mathbf{e}}_y). \tag{1.1}$$
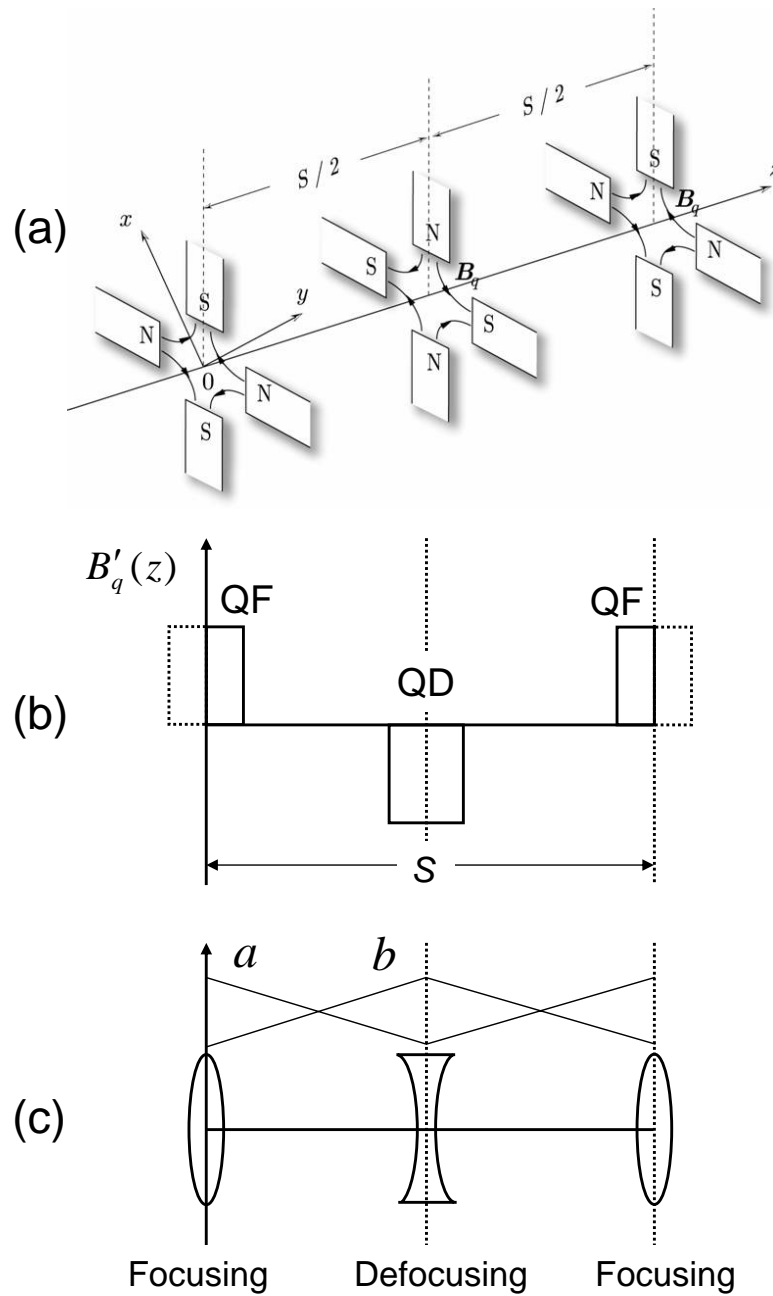
Figure 1.1: (a) Schematic of magnet sets producing an alternating-gradient quadrupole field with axial periodicity length S. Note that the quadrupole magnet sets are rotated by 90° every half-lattice period ($S/2$). (b) Schematic of the FODO (Focusing-Off-Defocusing-Off) lattice with piece-wise constant $B'_q(z)$ (QF:focusing quadrupole, QD:defocusing quadrupole). (c) Thin lens approximation of the FODO lattice with characteristic $x(y)$-dimension of the beam, $a(b)$.

Here, the field gradient coefficient $B'_q(z)$ is defined by $B'_q(z) \equiv (\partial B^q_x/\partial y)_{(0,0)} = \left(\partial B^q_y/\partial x\right)_{(0,0)}$, and $B'_q(z) = B'_q(z + S)$ has axial periodicity length S. For $B'_q(z) > 0$, the quadrupole field focuses (defocuses) the beam in the $x(y)$-direction, while for $B'_q(z) < 0$, the quadrupole field defocuses (focuses) the beam in the $x(y)$-direction. Note from Eq. (1.1) that $\nabla \cdot \mathbf{B}_q$ vanishes exactly, and $|\nabla \times \mathbf{B}_q|$ is of order a/S (or b/S) times $|B'_q|$. This suggests that for a thin beam, Eq. (1.1) is a valid approximation to the vacuum quadrupole magnetic field generated from the quasi-steady-state ($\partial/\partial t = 0$) external current sources [DAVIDSON and QIN, 2001].

For the case of hard-edged quadrupole magnets with small end-field effects [WIEDE-MANN, 1999], an AG focusing lattice can be approximated to have piece-wise constant values of the field gradient, and be composed of a focusing (F) and defocusing (D) quadrupoles with field-free drift spaces (O) in between [Fig. 1.1(b)]. This FODO lattice is the most widely used lattice in accelerator systems because of its simplicity, flexibility, and beam dynamical stability [WIEDEMANN, 1999]. Moreover, when the length of the quadrupole magnet is small compared to the axial periodicity length S, the transverse motion of a beam particle in a FODO lattice can be described by a beam ray trajectory in converging (focusing) or diverging (defocusing) lenses with finite focal length $|f| \geq S/2$ (*thin lens approximation*) [WIEDEMANN, 1999; LEE, 2004]. Hence, it is expected that characteristic beam dimensions evolve out of phase with the direction of the focusing force, i.e., beam width is maximum (minimum) at the focusing (defocusing) element [Fig. 1.1(c)].

For an intense beam, the repulsive self-field force associated with the net space charge becomes comparable with the externally applied AG focusing force. The self-field force is generally nonlinear, and can directly and immediately affect the dynamics of intense beam propagation. Therefore, for the optimal design and stable operation

of high-intensity accelerators and beam transport systems, most of which are based on AG focusing, it is of practical importance to understand the basic equilibrium, stability, and transport properties of an intense beam propagating through an AG focusing lattice.

1.1.3 The Paul Trap

The Paul trap (also known as a quadrupole ion trap, RF trap, or ion trap) is a device that permits the trapping of ions by applying radio frequency (RF) AC voltages in combination with DC voltages [WIKIPEDIA, 2008]. The invention of the Paul trap is attributed to Wolfgang Paul who received the Nobel Prize in Physics in 1989 for this work [PAUL and STEINWEDEL, 1953]. The Paul trap has two configurations: one is the three-dimensional form which consists of two hyperbolic end caps facing each other and a hyperbolic ring electrode between the two end caps (Fig. 1.2), and the other is the linear form which is made of four parallel electrodes (rod or segmented cylinder) and two DC end caps (see Fig. 2.1 of **Chapter 2**). Both Paul trap configurations are designed to create a saddle-shaped electrostatic potential distribution near the device center. Interestingly, the intuitive explanation and lowest-order approximation of how a Paul trap confines ions is the same as AG focusing in accelerator systems. Since the applied field affects the acceleration of the ion motion, the position lags behind (to lowest order by one half-cycle). So the ions are at defocused positions when the field is focusing and visa versa. In addition, the ions move further in the half-cycle when they are moving from a strong-field region to a weak-field region than vise versa, so there is a net inward drift. Such a net inward force is often termed ponderomotive force [CHEN, 1984]. Note that when there is no gradient in the focusing field strength, the average ion motion will drift linearly in time with
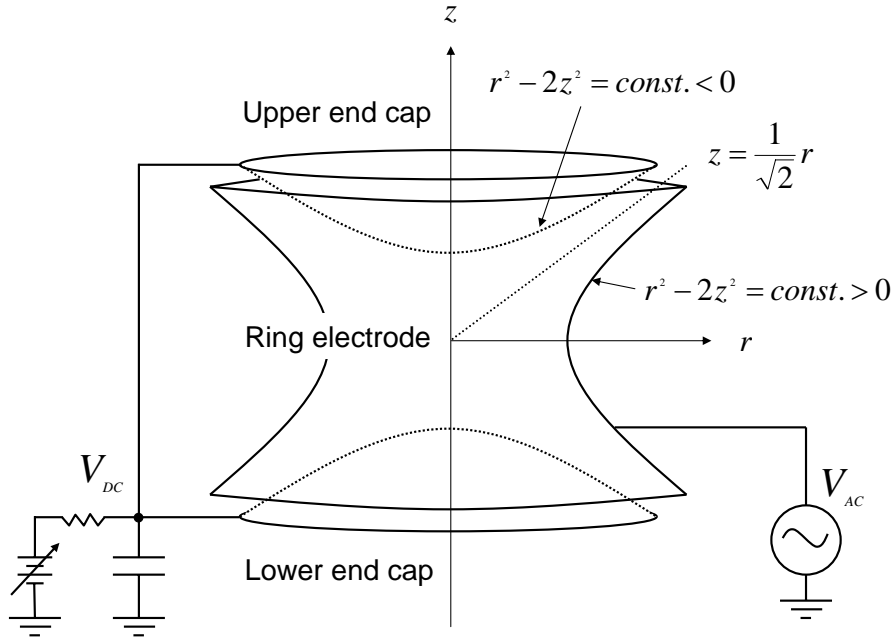
Figure 1.2: Schematic of three-dimensional form of Paul trap.

its initial velocity. This analogy between the effects of a quadrupole magnetic and electric fields on charged particles has lead to the idea of using a single-species trap to study the dynamics of intense beams in accelerators. In recent papers, Davidson *et al.* [DAVIDSON *et al.*, 2000] proposed a linear Paul trap, while Okamoto and Tanaka [OKAMOTO and TANAKA, 1999] proposed a solenoidal magnetic trap, to simulate periodically focused intense beam propagation. Further, Kjærgaard and Drewsen [KJÆRGAARD and DREWSEN, 2001] proposed a pulse-excited linear Paul trap to study crystalline beam properties in storage rings. In addition, there are many other applications of the Paul trap. Theses include: mass spectroscopy, quantum computing, atomic clocks, environmental monitoring, antimatter traps, and Coulomb crystal formation [MAJOR *et al.*, 2005], to mention a few examples.

1.2   Motivation

Periodic focusing accelerators and transport systems [Davidson, 1990; Davidson and Qin, 2001; Reiser, 1994; Wangler, 1998; Edwards and Syphers, 1993; Wilson, 2004] have a wide range of applications ranging from basic scientific research in high energy and nuclear physics to applications such as heavy ion fusion, ion-beam-driven high energy density physics, tritium production, nuclear waste transmutation, and spallation neutron sources and high-gain X-ray free electron lasers for material and biological research. Recent trends for those advanced applications are using very intense beams that are accelerated or stored through extremely long AG focusing channels on the order of kilometers to achieve the required beam properties [Rosenzweig, 2003]. For example, the currently envisioned International Linear Collider (ILC) [Brau *et al.*, 2007] will use two 11 km-long linear accelerators (linacs) to accelerate electron and positron beams with unprecedented precision in beam control (tens of nanometers at the collision spot). This leads to the need for a detailed understanding of the equilibrium, stability, and transport properties of long-distance beam propagation subject not only to the applied focusing field but also to the self fields produced by the beam space charge and current. Through analytical investigations based on the nonlinear Vlasov-Maxwell equations [Davidson, 1990; Davidson and Qin, 2001], numerical simulations using particle-in-cell (PIC) models and nonlinear perturbative simulation techniques [Friedman *et al.*, 1992; Qian *et al.*, 1997; Qin *et al.*, 2000], and advanced beam instrumentations and diagnostics [Minty and Zimmermann, 2003; Strehl, 2006], considerable progress has been made in developing an improved understanding of the collective processes and nonlinear beam dynamics characteristic of intense beam propagation. Nonetheless, due to the lack of dedicated experimental devices for fundamental studies, it is very difficult to verify the results

from the theories and numerical simulations, and to apply them to the design of new accelerator facilities with confidence. Experimental studies on existing accelerators, which are typically very expensive to operate, are limited in beam time and beam parameters. For example, for the case of the Superconducting Super Collider (SSC) which was aborted in 1993 due to significant cost overruns, the lack of confidence in predicting the dynamic aperture (the largest beam oscillation amplitude which is still stable in the presence of nonlinear fields [WIEDEMANN, 1999]) led to the design of a beam pipe size much larger than necessary [RYNE *et al.*, 1999]. This resulted in significant cost overruns in manufacturing thousands of superconducting magnets.

Recently, as an alternative approach to provide testbed for advanced theoretical models and numerical simulations, several small-scale and cost-effective intense beam experiments have been proposed. These include the beam halo experiments on the Low-Energy Demonstration Accelerator (LEDA) at Los Alamos National Laboratory [ALLEN *et al.*, 2002], the University of Maryland Electron Ring (UMER) [WALTER *et al.*, 2006], and the Paul Trap Simulator Experiment (PTSX) at the Princeton Plasma Physics Laboratory [GILSON *et al.*, 2004]. These facilities provide research opportunities for fundamental studies of collective processes on long time scales such as beam mismatch, emittance growth, and beam halo formation. While LEDA and UMER are laboratory-frame experiments which scale down an actual linear transport channel and a circular accelerator respectively, PTSX is a beam-frame experiment which builds on the physics equivalence between an intense coasting beam and a trapped nonneutral pure ion plasma. Highlights of each experiment are described in the following section.
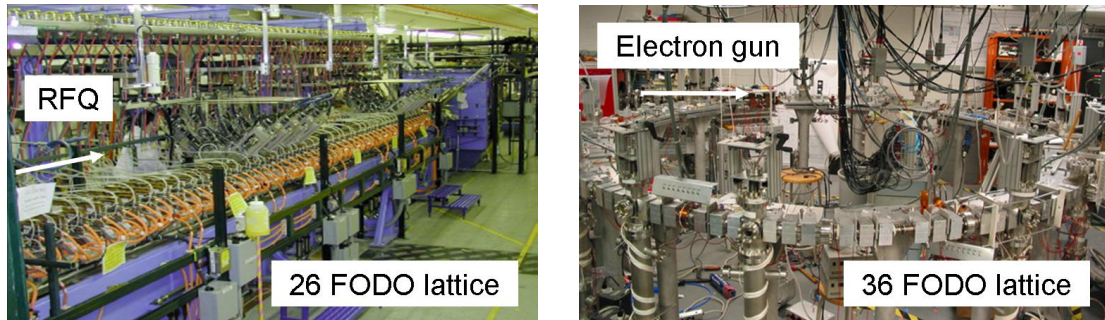
(a) An intense proton beam is injected from radio frequency quadrupole (RFQ) linac into the 26-FODO lattice transport channel.

(b) An intense electron beam is injected from thermionic electron gun into the 36-FODO lattice circulation ring.

Figure 1.3: Photographs of (a) Low-Energy Demonstration Accelerator (LEDA) and (b) University of Maryland Electron Ring (UMER).

1.3 Overview of Intense Beam Experiments

1.3.1 Low-Energy Demonstration Accelerator (LEDA)

The Low-Energy Demonstration Accelerator (LEDA) is a high-current continuous-wave (CW) proton accelerator at Los Alamos National Laboratory (LANL), which was initiated by the Accelerator for the Production of Tritium (APT) program to demonstrate the technically challenging front end of a 1000-MeV, 100-mA proton accelerator [ALLEN *et al.*, 2002]. Its operation from 1999 to 2001 demonstrated the feasibility of creating extremely high beam current. As an application of the high-intensity feature of LEDA, beam halo experiments have been performed in a 52-quadrupole periodic focusing transport channel (26 FODO lattice) installed at the end of LEDA [see Fig. 1.3(a)]. Beam halo is an extended low-density region outside the beam core, which often causes further beam loss and radioactivation of the accelerator structure. Understanding the basic physics mechanism for halo formation is one of the critical issues in the design and operation of high-intensity accelerators.

In the LEDA halo experiment, a 6.7-MeV proton beam from a 350-MHz Radio Frequency Quadrupole (RFQ) linac section is injected into the transport channel with several settings of beam current. The focusing gradients of the first four quadrupole magnets are independently adjusted to match or mismatch the injected beam to the transport channel. For an initially mismatched beam, there is a slow transverse envelope oscillation superimposed on the fast oscillation due to the periodic focusing. These envelope oscillations drive some particles to very large transverse amplitude through a resonant mechanism. The channel length of 11 m corresponds to the development of about ten mismatch oscillations, enough to observe at least the initial stages of emittance growth and halo formation caused by beam mismatch. The major diagnostic elements in LEDA are the transverse beam-profile scanners, each of which consists of 33-μm-diameter carbon wire to measure dense beam core and a pair of 1.5-mm-thick graphite scraper plates for outer beam halo. A significant shoulder in the transverse density distribution has been measured at the exit of the channel as a result of beam mismatch and halo formation [ALLEN *et al.*, 2002]. The experimental results support the simple particle-core model of halo formation in mismatched beams [WANGLER *et al.*, 1998]. However, due to the finite length of the transport channel, the observation of longer-time-scale phenomena such as saturation of the mismatch oscillation is limited.

1.3.2 University of Maryland Electron Ring (UMER)

The University of Maryland Electron Ring (UMER) uses a nonrelativistic ($\sim$10 keV) electron beam created within a Pierce-type thermionic gun to study intense beam physics by circulating the beam in compact fast-cycling synchrotron over many lattice periods [WALTER *et al.*, 2006]. UMER is a versatile experimental platform with

a beam current of up to 100 mA and a pulse length as long as 100 ns. Intercepting and nonintercepting diagnostic apparatus are positioned every 20° around the ring, which allows time-resolved measurements of the beam position, beam current density, and emittance. The main circulation ring of UMER is composed of 36 FODO lattice periods, each of which consists of two printed-circuit (PC) quadrupoles for focusing and a PC dipole for 10° bending, with a period length of 32 cm [see Fig. 1.3(b)]. In addition, Helmholtz coils are mounted on each ring chamber to cancel the horizontal component of the earth's magnetic field. As a convenient measure of the influence of space charge on the beam, the normalized intensity χ (or equivalently $\hat{s}$ defined in the next section), which is the ratio of the space-charge force to the external focusing force, has been introduced [REISER, 1994]. In UMER, χ can vary from 0.2 to 0.9, which covers the range from the emittance-dominated regime to the space-charge-dominated regime. Research topics currently being investigated on UMER include both transverse dynamics (beam matching, halo formation, strongly asymmetric beams, transverse space-charge waves, etc.) and longitudinal dynamics (bunch capture/shaping, evolution of energy spread, longitudinal space-charge waves, etc.). Recently, multi-turn transport of an electron beam up to 125 turns of the ring (4500 full lattice periods) has been demonstrated for $\chi = 0.21$ with some degradation of beam quality [KISHEK, 2007]. Hence, it is expected that multi-turn operation at higher beam intensity requires refinement of the steering and matching control in the injection line, and the use of induction modules to compensate the longitudinal spread of the beam.

1.3.3   Paul Trap Simulator Experiment (PTSX)

The Paul Trap Simulator Experiment (PTSX) at Princeton Plasma Physics Laboratory (PPPL) is a compact linear Paul trap that simulates the collective processes and nonlinear transverse dynamics of an intense beam propagating through a periodic focusing quadrupole magnetic field. The idea of studying beam dynamics using a linear Paul trap confining a one-component plasma was proposed by Davidson *et al.* [DAVIDSON *et al.*, 2000]. The equivalence of the Paul trap configuration to intense beam propagation through a periodic focusing quadrupole field is discussed in **Chapter 2** of this thesis. After a two-year construction period, the PTSX device was commissioned by Dr. Erik Gilson *et al.* in 2003 [GILSON *et al.*, 2003a,b], successfully demonstrating quiescent beam propagation over equivalent distances of tens of kilometers, and accessing a wide operating range with stable confinement of the charge bunch [GILSON *et al.*, 2004]. A Faraday-cup diagnostic was used to measure the radial density profiles of the plasmas, and the experimental data were in good agreement with a simple force balance model [DAVIDSON and QIN, 2001] for a range of system parameters where the mismatch between the plasma and the focusing channel is not too large. Values of the normalized intensity parameters $\hat{s} = \omega_p^2(0)/2\omega_q^2$ up to 0.8 were achieved, where $\omega_p(r)$ is the local plasma frequency and ω_q is the average transverse focusing frequency [DAVIDSON and QIN, 2001]. The normalized intensity parameter describes whether the beam is emittance dominated ($\hat{s} \ll 1$) or space-charge dominated ($\hat{s} \to 1$), and is equivalent to the normalized intensity parameter χ used for UMER but more convenient for use in the beam frame. The PTSX device consists of three co-linear cylinders with radius $r_w = 0.1$ m, each divided into four 90° azimuthal sectors (see Figs. 3.1 and 3.5 in **Chapter 3**). The plasma is confined radially in the central 2 m-long cylinder by oscillating voltages. The two end cylinders are each 0.4

m long, and static voltages on the end cylinders confine the ions axially. Details of the PTSX device and diagnostics are described in **Chapter 3** of this thesis.

1.4   Thesis Overview

In this thesis research, detailed experimental studies have been performed on the PTSX device to increase our basic understanding of the transverse dynamics of intense beam propagation through a periodic focusing quadrupole magnetic field.

As indicated in the previous sections, the PTSX device has several unique features compared with other scaled intense beam experiments. First, the PTSX device is a beam-frame experiment based on the equivalence of the transverse dynamics of an intense coasting beam and a trapped pure ion plasma. Hence, it is critical to have a well-characterized trapped plasma without effects that may invalidate the physics similarity. Second, due to the very good confinement of nonneutral plasmas in a Paul trap and the capability of applying arbitrary lattice waveforms, the PTSX device has a great advantage in observing the long-time-scale emittance growth induced by transverse beam compression or machine imperfections. Third, because of the very different plasma parameters (low density and energy, pure ion plasma) and unique confinement configuration (particle trapping by means of time-varying electric fields), use of conventional plasma diagnostic methods such as a Langmuir probe, phosphor screen, or interferometry are typically not applicable to the PTSX device. In particular, the lack of non-destructive diagnostics makes it difficult to determine the detailed plasma behavior during the middle of a trapping cycle. Indeed, it is generally challenging to develop non-destructive diagnostics for the PTSX device.

To address these issues, several important and new research activities have been performed on the PTSX device. First, the ion injection process has been optimized to achieve a well-characterized initial beam state by considering various factors such as injection beam mismatch, production of fast ions, two-stream interactions, and virtual cathode formation. Second, experiments on transverse beam compression have been performed. Changes in both the lattice amplitude and the lattice period are considered. Emittance growth during the compression is measured and compared with analytical theory and numerical simulations. Third, machine imperfection effects have been investigated. In particular, the effects of faulty magnet sets and random noise are considered. The excitation of envelope oscillations are identified as a result of focusing field errors, and a continuous increase in emittance that depends on the noise duration and amplitude are observed. Finally, as a non-destructive diagnostic, a laser-induced fluorescence (LIF) diagnostic system and a compact barium ion source have been developed and tested. This thesis is organized in the following manner.

Chapter 2 provides derivations and discussions of various theoretical frameworks of intense beam dynamics relevant to subsequent chapters. The equivalence between the Paul trap configuration and intense beam propagation through a periodic focusing quadrupole magnetic field is presented, including a discussion of limitations of the analogy. In support of the analysis of the experimental data obtained in the PTSX device, several beam dynamics models are presented. Single-particle orbits are first introduced, including a discussion of the smooth-focusing approximation. To describe an ensemble of particles, the envelope equations are derived using the Kapchinskij-Vladimirskij (KV) distribution function. The beam equilibrium is presented in the smooth-focusing approximation, and the corresponding global force balance equation is derived.

Chapter 3 describes the PTSX apparatus. A general overview of the basic equipment, including vacuum system and electrode control system, is presented. The operation of the PTSX device is described, together with the characteristic plasma parameters. The cesium ion source which has been used for the initial phase of PTSX experiments is described. The design, fabrication, and data acquisition of the radially scanning charge collector system for the measurement of the low levels of charge are also presented. It is demonstrated that the radial ion charge profiles can be measured accurately to as low as the 1 fC range, which is adequate to detect the formation of halo particles. As an effort to develop a non-destructive diagnostic in the PTSX device, the design and installation of the barium ion source and laser-induced fluorescence (LIF) diagnostic system are described, together with initial test results.

Chapter 4 addresses the ion injection optimization processes to achieve a well-characterized initial plasma. Various factors that may invalidate the physics similarity, such as injection beam mismatch, production of fast ions, two-stream interactions, and virtual cathode formation, are characterized with the goal of finding optimum ion injection conditions. When the external focusing field is too weak or the self-field force is too strong, it is observed that the initial beam experiences mismatch oscillations, which leads to a shoulder in radial density profile measured in the downstream region. The population of the fast ions, which results from the particle trapping using a DC bias voltage, is minimized by the optimal timing of the inject-trap-dump-rest cycle. Two-stream interactions and virtual cathode formation set the upper and lower limits of the axial beam velocity. Finally, a well-matched initial plasma has been obtained with a normalized beam intensity $\hat{s} \sim 0.2$ and a nearly Gaussian radial profile. This initial plasma is stable for more than 50 ms (3000 FODO equivalent lattice periods), and serves as a baseline case for the subsequent experiments.

Chapter 5 presents key results and analysis of the experiments on transverse beam compression. Both changes in the lattice amplitude and changes in the lattice period are considered. From a comparison of the analytical estimates, experimental results, and particle-in-cell (PIC) simulations, it is found that the key physics issue in transverse beam compression is how to suppress the excitation of mismatch oscillations, which are usually accompanied by emittance growth and halo formation. When the phase advance is low enough, adiabatic changes in the smooth-focusing frequency turned out to be an effective control of transverse beam compression, minimizing the emittance growth. During the frequency modulation experiments, frequency overshoot (or undershoot) of the instantaneous frequency has been observed, which provides useful insights into single-particle orbit instabilities and collective mode excitations.

Chapter 6 of this thesis contains experimental investigations of the transverse beam dynamics in response to various machine imperfection effects present in high-intensity accelerators. Faulty magnet effects are simulated by spoiling the voltage waveform for a few or several lattice periods. A non-trivial oscillatory behavior in the on-axis signal has been observed, which is effectively explained in terms of collective mode excitations and beam mismatch in a KV-equivalent beam. Random noise effects are studied by adding a small random ripple on top of the applied voltage waveform. Noise-enhanced emittance growth is demonstrated, which may affect intense beam transport over long propagation distances in linacs, or the length of the beam lifetime in storage rings. In particular, the synergistic effects of collective modes and colored noise are observed, which is consistent with theoretical predictions and numerical simulations.

Finally, **Chapter 7** summarizes the conclusions drawn from the earlier chapters and identifies possible areas of future research.

Chapter 2

Theoretical Background

2.1 Principles of the Paul Trap Simulator Experiment (PTSX)

In this section, we present a brief theoretical description that illustrates the equivalence between the Paul trap configuration and intense beam propagation through a periodic focusing quadrupole magnetic field.

2.1.1 Intense Beam Propagation

We consider an intense charged particle beam with average axial momentum $p_b = \gamma_b m_b \beta_b c$ propagating in the z-direction through a periodic focusing quadrupole magnetic field with axial periodicity length $S = const$. Here, $(\gamma_b - 1)m_b c^2$ is the directed axial kinetic energy of the beam particles, $\gamma_b = (1 - \beta_b^2)^{-1/2}$ is the relativistic mass factor, $V_b = \beta_b c$ is the average axial velocity, m_b is the rest mass of a beam particle,

and c is the speed of light *in vacuo*. We assume a thin beam with

$$a, \ b \ll S, \tag{2.1}$$

where a and b are the characteristic x- and y- dimensions of the beam. Furthermore, the beam is assumed to be continuous in the z-direction. The *thin-beam approximation* in Eq. (2.1) permits a Taylor expansion of the applied focusing fields about the beam axis at $(x, y) = (0, 0)$. Consistent with Eq. (2.1), we can also make use of the *paraxial approximation* [DAVIDSON, 1990; DAVIDSON and QIN, 2001]

$$v_x^2, \ v_y^2, \ (v_z - V_b)^2 \ll V_b^2, \tag{2.2}$$

and the particle motion in the beam frame is nonrelativistic. In addition, we introduce the scaled time variable $s = \beta_b ct$, and the dimensionless transverse velocities $x' = dx/ds$ and $y' = dy/ds$. From now on, as is customary in accelerator physics, we denote by s the configuration space coordinate measured along the principal direction of beam propagation, i.e., $s = z$ [WIEDEMANN, 1999; LEE, 2004]. Then, within the framework of the assumptions summarized above, the nonlinear beam dynamics in the transverse, laboratory-frame phase space (x, y, x', y') is described by the evolution of the distribution function $f_b(x, y, x', y', s)$.

With regard to the self-generated electric and magnetic fields, we make use of the *electrostatic* and *magnetostatic approximations* [DAVIDSON and QIN, 2001]. That is, the self-generated electric and magnetic fields, $\mathbf{E}^s(\mathbf{x}, t)$ and $\mathbf{B}^s(\mathbf{x}, t)$, are approximated by

$$\begin{aligned} \mathbf{E}^s &= -\nabla \phi^s, \\ \mathbf{B}^s &= \nabla \times A_z^s \hat{\mathbf{e}}_z, \end{aligned} \tag{2.3}$$

where the self-field potentials, $\phi^s(\mathbf{x}, t)$ and $A_z^s(\mathbf{x}, t)$, are determined self-consistently from Maxwell's equations

$$\nabla_\perp^2 \phi^s = -\frac{q_b n_b}{\epsilon_0} = -\frac{q_b}{\epsilon_0} \int dx' dy' f_b,$$
$$\nabla_\perp^2 A_z^s = -\mu_0 q_b n_b V_b = -\mu_0 q_b V_b \int dx' dy' f_b, \qquad (2.4)$$

where q_b is the beam particle charge, ϵ_0 is permittivity of free space, μ_0 is permeability of free space, and $n_b(x, y, s) = \int dx' dy' f_b$ is the number density of beam particles. Here, we assume the axial velocity spread is small in comparison with the directed axial velocity $V_b = \beta_b c$, and approximate $\nabla^2 \simeq \nabla_\perp^2 = \partial^2/\partial x^2 + \partial^2/\partial y^2$ in consistent with the thin-beam approximation. In addition, we can approximate $A_z^s = V_b \phi^s/c^2$ from Eq. (2.4). The transverse Lorenz force due to the self fields can be expressed as

$$\begin{aligned} \mathbf{F}_\perp^s &= q_b \left(\mathbf{E}^s + V_b \hat{\mathbf{e}}_z \times \mathbf{B}^s\right)_\perp \\ &= -q_b \nabla_\perp \left(\phi^s - V_b A_z^s\right) \\ &= -q_b \left(1 - \beta_b^2\right) \nabla_\perp \phi^s, \end{aligned} \qquad (2.5)$$

and the normalized self-field potential can be defined by

$$\psi(x, y, s) = \left(\frac{1}{\gamma_b^2}\right) \frac{q_b \phi^s}{\gamma_b m_b \beta_b^2 c^2}. \qquad (2.6)$$

The factor $1/\gamma_b^2$ is associated with the fact that the focusing self-magnetic force produced by the axial beam current reduces the net self-field (self-electric plus self-magnetic) force on a beam particle [DAVIDSON and QIN, 2001]. In particular, for the case of relativistic electron beam, self-magnetic force nearly cancels the effective self-electric force [WANGLER, 1998]. Hence, self-field effect is more significant for proton or heavy ion beams at the lower velocities.

For a thin beam, the transverse focusing force on a beam particle produced by the periodic focusing quadrupole magnetic field given by $\mathbf{B}_q(\mathbf{x}) = B_x^q \hat{\mathbf{e}}_x + B_y^q \hat{\mathbf{e}}_y$ (see

Chapter 1) can be approximated over the cross-section of the beam as

$$
\begin{aligned}
\mathbf{F}_{foc} &= q_b V_b \hat{\mathbf{e}}_z \times \left(B_x^q \hat{\mathbf{e}}_x + B_y^q \hat{\mathbf{e}}_y \right) \\
&= -q_b V_b B_q'(s) \left[x \hat{\mathbf{e}}_x - y \hat{\mathbf{e}}_y \right],
\end{aligned}
\tag{2.7}
$$

where (x, y) is the transverse displacement of a particle from the beam axis, and the field gradient coefficient $B_q'(s)$ is defined by

$$
B_q'(s) \equiv \left(\frac{\partial B_x^q}{\partial y} \right)_{(x,y)=(0,0)} = \left(\frac{\partial B_y^q}{\partial x} \right)_{(x,y)=(0,0)},
\tag{2.8}
$$

and $B_q'(s) = B_q'(s + S)$ has axial periodicity length S. If we define the s-dependent focusing coefficient $\kappa_q(s + S) = \kappa_q(s)$ by

$$
\kappa_q(s) = \frac{q_b V_b B_q'(s)}{\gamma_b m_b \beta_b^2 c^2},
\tag{2.9}
$$

then the laboratory-frame Hamiltonian $\hat{H}_\perp(x, y, x', y', s)$ for the transverse single-particle motion is given (in dimensionless variables) by

$$
\hat{H}_\perp = \frac{1}{2}(x'^2 + y'^2) + \frac{1}{2}\kappa_q(s)(x^2 - y^2) + \psi(x, y, s).
\tag{2.10}
$$

Finally, the nonlinear beam dynamics and collective process in the laboratory-frame transverse phase space is described self-consistently by the Vlasov-Maxwell equations

$$
\left\{ \frac{\partial}{\partial s} + x' \frac{\partial}{\partial x} + y' \frac{\partial}{\partial y} + \left(-\kappa_q(s)x - \frac{\partial \psi}{\partial x} \right) \frac{\partial}{\partial x'} + \left(+\kappa_q(s)y - \frac{\partial \psi}{\partial y} \right) \frac{\partial}{\partial y'} \right\} f_b = 0,
\tag{2.11}
$$

and

$$
\begin{aligned}
\left(\frac{\partial^2}{\partial x^2} + \frac{\partial^2}{\partial y^2} \right) \psi &= -\frac{1}{\epsilon_0} \frac{q_b^2 / \gamma_b^2}{\gamma_b m_b \beta_b^2 c^2} \int dx' dy' f_b \\
&= -\frac{2\pi K_b}{N_b} \int dx' dy' f_b.
\end{aligned}
\tag{2.12}
$$

Here, $N_b = \int dx dy n_b$ is the number of beam particles per unit axial length, and K_b is the dimensionless self-field perveance defined by [LAWSON, 1958]

$$K_b = \left(\frac{1}{4\pi\epsilon_0}\right) \frac{2N_b q_b^2/\gamma_b^2}{\gamma_b m_b \beta_b^2 c^2}, \tag{2.13}$$

which is the ratio of self-field energy to axial kinetic energy. Proportional to the beam current $I_b = q_b N_b \beta_b c$ but independent of the radial beam dimensions, the self-field perveance K_b is a convenient dimensionless measure of the beam intensity during axial beam propagation. The Vlasov-Maxwell equations (2.11) and (2.12) are strongly nonlinear because the self-field potential ψ is coupled with f_b through Maxwell's equations, and are widely used to describe the stability and transport properties of an intense beam propagating through a periodic focusing quadrupole magnetic field.

2.1.2 Paul Trap Configuration

From the previous section, we note that the particle motion in the beam frame is nonrelativistic, and that the periodic quadrupole focusing terms in Eqs. (2.10) and (2.11) can be simulated in the laboratory frame by applying oscillatory quadrupole electric fields. Therefore, it is possible to study the nonlinear transverse beam dynamics described by Eqs. (2.10), (2.11), and (2.12) in a compact Paul trap configuration [DAVIDSON *et al.*, 2000; OKAMOTO and TANAKA, 1999; KJÆRGAARD and DREWSEN, 2001].

To simulate an axially continuous intense charged particle beam, we consider a long nonneutral plasma column with length $\sim 2L$ and characteristic radius $r_p \ll 2L$, confined axially by applied DC voltages $+\hat{V} = const.$ on end cylinders at $z = \pm L$. The particles constituting the nonrelativistic pure ion plasma have charge q and mass m. With respect to transverse confinement of the particles in the $x - y$ plane, there
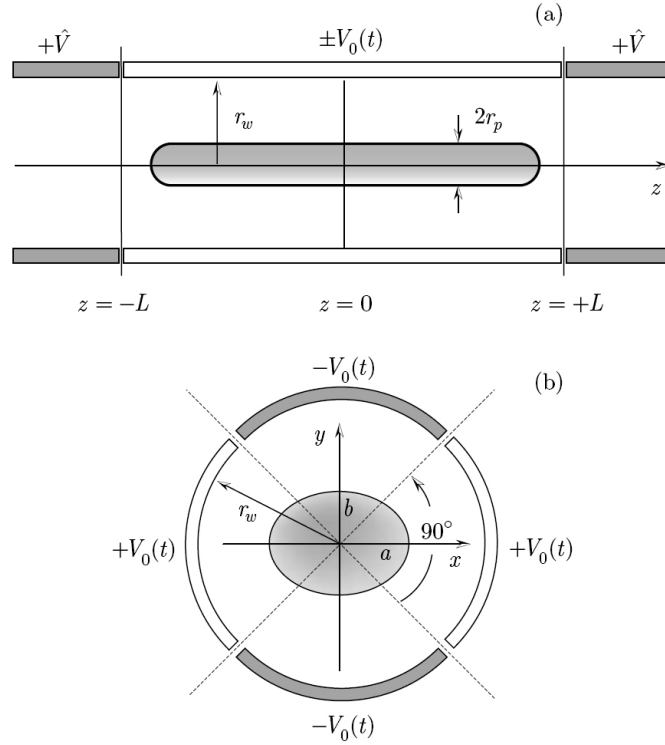
Figure 2.1: (a) Side view and (b) end view of the Paul trap configuration [Davidson and Qin, 2001].

is no applied axial magnetic field ($\mathbf{B}_0 = B_0 \hat{\mathbf{e}}_z = 0$). Rather, segmented cylindrical electrodes at radius r_w have applied oscillatory voltage $\pm V_0(t)$ with alternating polarity on adjacent segments. Here, the applied voltage $V_0(t)$ is oscillatory with $V_0(t + T) = V_0(t)$ and $\int_0^T dt V_0(t) = 0$, where $T = const.$ is the period, and $f_0 = 1/T$ is the oscillation frequency. For the typical operating conditions in the Paul trap ($r_w f_0 \ll c$), inductive electromagnetic effects are negligible. Neglecting end effects ($\partial/\partial z = 0$), and representing the applied electric field by $\mathbf{E}_a = -\nabla_\perp \phi_q(x, y, t)$, where $\nabla_\perp \cdot \mathbf{E}_a = 0$ and $\nabla_\perp \times \mathbf{E}_a \simeq 0$, it is readily shown that the solution to $\nabla_\perp^2 \phi_q(x, y, t) = 0$ that satisfies the appropriate boundary conditions at $r = r_w$ is given by [Davidson

et al., 2000]

$$\phi_q(x, y, t) = \frac{4V_0(t)}{\pi} \sum_{l=1}^{\infty} \frac{\sin(l\pi/2)}{l} \left(\frac{r}{r_w}\right)^{2l} \cos(2l\theta) \qquad (2.14)$$

for $0 \le r \le r_w$ and $0 \le \theta \le 2\pi$. Near the cylinder axis ($r \ll r_w$), Eq. (2.14) readily gives to lowest order

$$\phi_q(x, y, t) = \frac{1}{2} \frac{m}{q} \kappa_q(t) \left(x^2 - y^2\right), \qquad (2.15)$$

where the time-dependent oscillatory quadrupole focusing coefficient $\kappa_q(t+T) = \kappa_q(t)$ is defined by

$$\kappa_q(t) \equiv \frac{8qV_0(t)}{m\pi r_w^2}, \qquad (2.16)$$

which has dimensions of $[\text{s}^{-2}]$ (note that the s-dependent focusing coefficient $\kappa_q(s)$ defined in the previous section has dimensions of $[\text{m}^{-2}]$). Most importantly, from Eq. (2.14), the leading-order correction to Eq. (2.15) is of order $(1/3)(r/r_w)^4$. Hence, for sufficiently small r_p/r_w, the quadrupole potential in Eq. (2.15) is a very accurate representation of the applied focusing potential.

We now construct the Hamiltonian for the transverse particle motion in the quadrupole potential, neglecting axial variations ($\partial/\partial z = 0$). Denoting the (dimensional) transverse particle velocities by $\dot{x} = dx/dt$ and $\dot{y} = dy/dt$, and the self-field electrostatic potential due to the plasma space charge by $\phi^s(x, y, t)$, it readily follows that the (dimensional) Hamiltonian $H_\perp(x, y, \dot{x}, \dot{y}, t)$ describing the transverse particle motion is given by

$$H_\perp(x, y, \dot{x}, \dot{y}, t) = \frac{1}{2}m(\dot{x}^2 + \dot{y}^2) + \frac{1}{2}m\kappa_q(t)(x^2 - y^2) + q\phi^s(x, y, t). \qquad (2.17)$$

Since the axial beam current is quite small in the trap, the self-magnetic force is negligible. We recognize that the transverse Hamiltonian in Eq. (2.17) is identical in functional form to the transverse Hamiltonian defined in Eq. (2.10) provided we make the replacements summarized in Table 2.1.

Finally, the nonlinear Vlasov-Poisson equations describing the self-consistent evolution of the distribution function $f(x, y, \dot{x}, \dot{y}, t)$ and the self-field electrostatic potential $\phi^s(x, y, t)$ in the transverse phase space $(x, y, \dot{x}, \dot{y})$ can be expressed as

$$\left\{\frac{\partial}{\partial t} + \dot{x}\frac{\partial}{\partial x} + \dot{y}\frac{\partial}{\partial y} + \left(-\kappa_q(t)x - \frac{q}{m}\frac{\partial \phi^s}{\partial x}\right)\frac{\partial}{\partial \dot{x}} + \left(+\kappa_q(t)y - \frac{q}{m}\frac{\partial \phi^s}{\partial y}\right)\frac{\partial}{\partial \dot{y}}\right\} f = 0,$$

(2.18)

and

$$\begin{aligned}
\left(\frac{\partial^2}{\partial x^2} + \frac{\partial^2}{\partial y^2}\right)\left(\frac{q}{m}\phi^s\right) &= -\frac{q^2}{\epsilon_0 m}n(x, y, t) \\
&= -\frac{2\pi K}{N}\int d\dot{x}d\dot{y}f,
\end{aligned}$$

(2.19)

where $n(x, y, t) = \int d\dot{x}d\dot{y}f$ is the particle number density in the Paul trap, $N = \int dxdy n(x, y, t)$ is the number of particles per unit axial length (particle line density), and K is the dimensional self-field perveance defined by

$$K = \frac{1}{4\pi\epsilon_0}\frac{2Nq^2}{m}.$$

(2.20)

Therefore, the collective process and nonlinear transverse dynamics described by the nonlinear Vlasov-Poisson equations (2.18) and (2.19) for the one-component nonneutral plasma configuration in Fig. 2.1 are identical to those described by Eqs. (2.11) and (2.12) for an intense beam propagating through a periodic focusing quadrupole magnetic field, provided we make the replacement in Table 2.1.

2.1.3 Limitations of Paul Trap Analogy

As noted earlier, the Paul trap analogy described above is intended to simulate the transverse dynamics of a *continuous* and *thin* beam propagating in a periodic focusing quadrupole magnetic field. Furthermore, the Hamiltonian in Eq. (2.17) and the

	Intense relativistic beam	Nonneutral trapped plasma
Time variable	$s = V_b t = \beta_b c t$ [m]	t [s]
Velocity	$x' = \frac{dx}{ds}, y' = \frac{dy}{ds}$ [1]	$\dot{x} = \frac{dx}{dt}, \dot{y} = \frac{dy}{dt}$ [m/s]
Focusing field	$\mathbf{B}_q = B_q'(s)(y\hat{\mathbf{e}}_x + x\hat{\mathbf{e}}_y)$ [T]	$\mathbf{E}_q = -\frac{8V_0(t)}{\pi r_w^2}(x\hat{\mathbf{e}}_x - y\hat{\mathbf{e}}_y)$ [V/m]
Focusing coefficient	$\kappa_q(s) = \frac{q_b}{\gamma_b m_b}\frac{1}{\beta_b^2 c^2} V_b B_q'(s)$ [m^{-2}]	$\kappa_q(t) = \frac{q}{m}\frac{8V_0(t)}{\pi r_w^2}$ [s^{-2}]
Smooth focusing coefficient in sinusoidal lattice with amplitude $\hat{\kappa}_q$	$\kappa_{sf} = \frac{1}{2}\frac{\hat{\kappa}_q^2 S^2}{(2\pi)^2}$ [m^{-2}]	$\kappa_{sf} = \frac{1}{2}\frac{\hat{\kappa}_q^2}{(2\pi)^2}f_0^2$ [s^{-2}]
Characteristic focusing frequency	$\omega_{\beta\perp} = \beta_b c\sqrt{\kappa_{sf}}$ [s^{-1}]	$\omega_q = \sqrt{\kappa_{sf}}$ [s^{-1}]
Self-field potential	$\psi(x,y,s) = \frac{q_b}{\gamma_b m_b}\frac{1}{\beta_b^2 c^2}\frac{\phi^s(x,y,s)}{\gamma_b^2}$ [1]	$\frac{q}{m}\phi^s(x,y,t)$ [m^2/s^2]
Plasma frequency	$\hat{\omega}_{pb} = \left(\frac{\hat{n}_b q_b^2}{\gamma_b m_b \epsilon_0}\right)^{1/2}$ [s^{-1}]	$\hat{\omega}_p = \left(\frac{\hat{n}q^2}{m\epsilon_0}\right)^{1/2}$ [s^{-1}]
Smooth-focusing vacuum phase advance	$\sigma_v^{sf} = \sqrt{\kappa_{sf}}S$ [1]	$\sigma_v^{sf} = \sqrt{\kappa_{sf}}/f_0$ [1]
Intensity parameter	$s_b = \frac{\hat{\omega}_{pb}^2/\gamma_b^2}{2\omega_{\beta\perp}^2}$ [1]	$\hat{s} = \frac{\hat{\omega}_p^2}{2\omega_q^2}$ [1]
Self-field perveance	$K_b = \frac{1}{4\pi\epsilon_0}\frac{2N_b q_b^2/\gamma_b^2}{\gamma_b m_b \beta_b^2 c^2}$ [1]	$K = \frac{1}{4\pi\epsilon_0}\frac{2Nq^2}{m}$ [m^2/s^2]
Transverse Hamiltonian	$\hat{H}_\perp(x,y,x',y',s) = \frac{1}{2}(x'^2 + y'^2)$ $+ \frac{1}{2}\kappa_q(s)(x^2 - y^2) + \psi^s(x,y,s)$ [1]	$\frac{1}{m}H_\perp(x,y,\dot{x},\dot{y},t) = \frac{1}{2}(\dot{x}^2 + \dot{y}^2)$ $+ \frac{1}{2}\kappa_q(t)(x^2 - y^2) + \frac{q}{m}\phi^s(x,y,t)$ [m^2/s^2]

Table 2.1: Equations for the transverse dynamics of an intense relativistic beam propagating through a periodic focusing quadrupole magnetic field, and for a nonneutral plasma trapped in the oscillating quadrupole electric field of a Paul trap.

nonlinear Vlasov-Poisson equations (2.18) and (2.19) describe only the transverse dynamics of the long nonneutral plasma column ($2L \gg r_p$) in Fig. 2.1, and z-variation and axial particle motions are not included in the description. While such a model is expected to provide a good description of the transverse dynamics of the nonneutral plasma column for $2L \gg r_p$, there are important limitations on the range of applicability of the Paul trap analogy for simulating the propagation of a continuous beam through a periodic focusing lattice.

Most importantly, the nonneutral plasma column illustrated in Fig. 2.1 is confined axially, and the particles execute axial bounce motion between the ends of the plasma column (nearly at $z = \pm L$). If we denote the characteristic axial velocity of a particle with axial kinetic energy E_b by $v_b = (2E_b/m)^{1/2}$, then the characteristic bounce time is $\tau_b \sim 4L/v_b$. At low-to-moderate density, the characteristic period τ_q for transverse motion and characteristic plasma radius r_p are approximately related by $\tau_q \sim 2r_p/v_t$, where $v_t = (T_i/m)^{1/2}$ is the thermal speed of ions with temperature T_i. Therefore, in an approximate sense, the transverse and axial oscillation periods stand in the ratio $\tau_q/\tau_b \sim (r_p/2L)(v_b/v_t)$. On a time scale $\tau_q \sim \tau_b$, the finite-length effects of the axial bounce motion of a particle become important, and limit the validity of the Paul trap analogy with the propagation of a continuous beam through a periodic focusing lattice. For sufficiently large $2L \gg r_p$ and moderate v_b, however, the axial bounce period τ_b can be very long. As illustrative parameters, consider the case where $r_p = 1$ cm, $2L = 200$ cm, and the frequency $f_0 = 1/T$ of the applied oscillatory voltage $V_0(t)$ is set to $f_0\tau_q \gtrsim 4$ for stability. Further, we assume that particles are injected with axial kinetic energy $E_b = 5$ eV and ion temperature $T_i = 0.1$ eV. In this case, $\tau_b \sim 20\tau_q \sim 80T$. Hence, a typical particle in Fig. 2.1 experiences the effects of 80

oscillation periods of the quadrupole focusing potential (80 equivalent lattice periods) before it executes one axial bounce in the trap.

Another limiting factor of the Paul trap analogy is the effect of collisions. Collisional effects in high-energy beams in actual accelerators and transport lines are often negligible. Therefore, if collisional effects become significant for the nonneutral plasma in the trap, then the Paul trap analogy is no longer valid. The characteristic collision time for scattering of ions by background neutral atom is [HUBA, 2004]

$$\tau_{in} \approx \frac{1}{n_n \sigma_s^{in} v_t}, \tag{2.21}$$

where n_n is the average neutral density, and σ_s^{in} is the ion-neutral collision cross section, typically $\sim 5 \times 10^{-15}$ cm^2 and weakly dependent on temperature. If we use the ideal gas law $n_n = P/T_r$, it is estimated that $\tau_{in} > 2$ sec when the base pressure P is kept below 10^{-7} Torr at room temperature $T_r = 300$ K. The characteristic collision time for ions colliding with other ions is given [GOLDSTON and RUTHERFORD, 1995]

$$\tau_{ii} \approx \frac{12\pi^{3/2} \epsilon_0^2 m^2 v_t^3}{n_i q^4 \ln \Lambda}, \tag{2.22}$$

where n_i is the average ion density and $\ln \Lambda$ is Coulomb logarithm, to good approximation ~ 14 for the PTSX parameters. For the typical operating conditions for the PTSX, it is estimated that $\tau_{ii} > 0.5$ sec when $n_i < 10^6$ cm^{-3}. Hence, by limiting the trapping time of ions below several hundred milliseconds, we can avoid collisional effects.

2.1.4 System Parameters

The detailed transverse motion of individual particles in the PTSX is approximately composed of both a rapid oscillation with frequency f_0 and a slow oscillation with

characteristic frequency ω_q. In the *smooth-focusing approximation* [DAVIDSON, 1990; REISER, 1994; DAVIDSON and QIN, 2001], where there is averaging over the rapid motion with frequency f_0, orbit equations with a constant focusing coefficient are often used to describe the average effects of the periodic focusing quadrupole field. The expression for the average focusing frequency ω_q in the smooth-focusing approximation is given by [DAVIDSON and QIN, 2001]

$$\omega_q = \sqrt{\left\langle \left(\int_{t_0}^{\tilde{t}} dt \kappa_q(t) \right)^2 \right\rangle_T - \left\langle \left(\int_{t_0}^{\tilde{t}} dt \kappa_q(t) \right) \right\rangle_T^2}, \tag{2.23}$$

where $\langle \cdots \rangle_T$ denotes the temporal average over one oscillation period.

$$\langle \cdots \rangle_T (t) = \frac{1}{T} \int_{t-T/2}^{t+T/2} d\tilde{t} \cdots. \tag{2.24}$$

Two illustrative examples of oscillatory waveforms for the quadrupole focusing coefficient $\kappa_q(t) = (8q/m\pi r_w^2)V_0(t)$ are shown in Fig. 2.2. Here, Fig. 2.2(a) corresponds to a sinusoidal waveform with $\kappa_q(t) = \hat{\kappa}_q \sin(2\pi t/T)$, where $\hat{\kappa}_q = (8q/m\pi r_w^2)\hat{V}_0$ and $\hat{V}_0 = |V_0(t)|_{\text{max}}$. This sinusoidal waveform is least taxing on the bandwidth limit of the electronic system of the PTSX device [GILSON *et al.*, 2004] and is an approximation to a quadrupole lattice with short magnets with significant fringe fields. The smooth-focusing frequency for the case of the sinusoidal waveform is given approximately by

$$\omega_q = \frac{8q}{m\pi r_w^2} \left(\frac{\hat{V}_0}{f_0} \right) \frac{1}{2\pi\sqrt{2}}. \tag{2.25}$$

Figure 2.2(b) corresponds to a periodic step-function lattice with maximum amplitude $\hat{\kappa}_q$ and filling factor η. This FODO lattice (Focusing-Off-Defocusing-Off) has hard-edged quadrupole magnets and is an idealization of a magnetic alternating-gradient
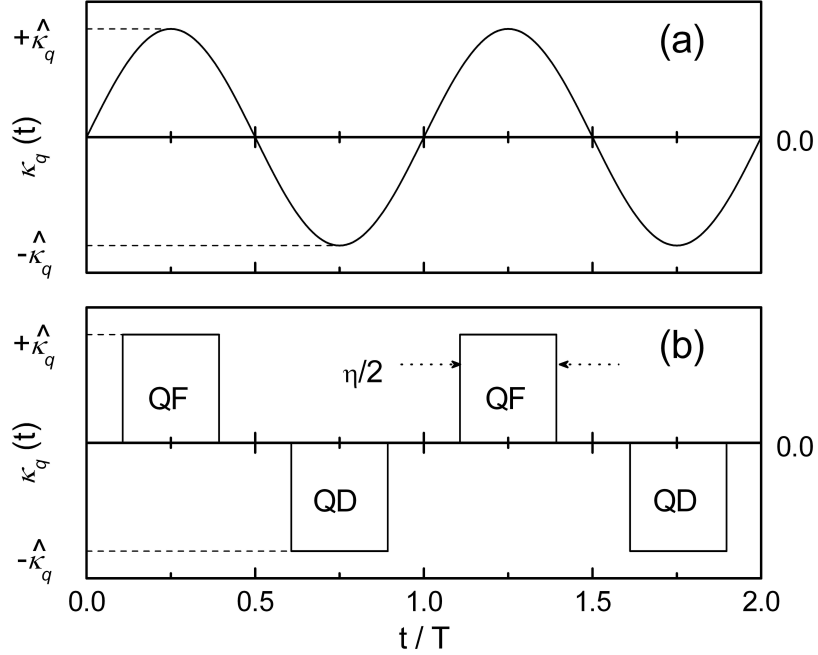
Figure 2.2: Illustrative oscillatory waveforms for the quadrupole focusing coefficient $\kappa_q(t)$ corresponding to (a) the sinusoidal waveform $\kappa_q(t) = \hat{\kappa}_q \sin(2\pi t/T)$, and (b) a periodic step-function waveform with maximum amplitude $\hat{\kappa}_q$ and filling factor η.

transport system. The smooth-focusing frequency for the case of a periodic step-function lattice is given approximately by

$$\omega_q = \frac{8q}{m\pi r_w^2} \left(\frac{\hat{V}_0}{f_0}\right) \frac{\eta}{4} \sqrt{\left(1 - \frac{2}{3}\eta\right)}. \tag{2.26}$$

It is interesting to note that when $\eta = 0.572$, both the sinusoidal waveform and the periodic step-function lattice give the same value of the smooth-focusing frequency. Experiments performed to date using PTSX have employed a sinusoidal waveform [GILSON *et al.*, 2004].

The actual slow transverse oscillation frequency (depressed betatron frequency) is determined by including the net radial force. The self-electric field of the nonneutral

plasma is repulsive and serves to depress the transverse oscillation frequency. For uniform density plasma, the depressed betatron frequency ν_b for slow transverse particle oscillations is approximately given by

$$\nu_b^2 = \omega_q^2 - \frac{\hat{\omega}_p^2}{2}. \tag{2.27}$$

Here, we denote the uniform plasma density by $\hat{n}$ and the corresponding plasma frequency by $\hat{\omega}_p = (\hat{n}q^2/\epsilon_0 m)^{1/2}$. An important dimensionless parameter $\hat{s}$ that measures the normalized beam intensity and self-field force on a particle is defined by

$$\hat{s} \equiv \frac{\hat{\omega}_p^2/2}{\omega_q^2}. \tag{2.28}$$

The factor $1/2$ associated with $\hat{\omega}_p^2$ in Eqs. (2.27) and (2.28) is a geometric factor which results when a rigorous calculation of the collective oscillation frequency is carried out [DAVIDSON and QIN, 2001]. For the transverse confinement of a beam particle by applied focusing field, we require that $\hat{s} < 1$, or equivalently $\nu_b^2 > 0$.

Particles in general travel for several oscillation periods of $V_0(t)$ before completing one slow transverse oscillation, and the advance in phase of the slow transverse oscillation that the particle undergoes per oscillation period T is called the *phase advance* σ. Due to the self-electric field, the phase advance σ is smaller than the *vacuum phase advance* σ_v that is computed in the absence of space-charge effects. The quantity σ/σ_v is a measure of the relative strength of space-charge effects as compared to the strength of the applied focusing field. In the smooth-focusing approximation which is valid for vacuum phase advance $\sigma_v \lesssim 2\pi/5 = 72°$, σ_v is estimated to be

$$\sigma_v^{sf} = \frac{\omega_q}{f_0}. \tag{2.29}$$

Further, for a uniform density profile, the depressed vacuum phase advance is related to $\hat{s}$ by the relation $\sigma^{sf} = \sigma_v^{sf}(1 - \hat{s})^{1/2}$ in the smooth-focusing approximation.

In storage rings and circular accelerators, it is customary to introduce the tune ν (often, especially in the European literature, it is denoted by Q), which is defined as the number of slow transverse oscillations that a particle makes as it circulates once around the ring with circumference C. In the absence of the beam, the *undepressed tune* is approximately $\nu_0 = C\omega_q/2\pi V_b$, where V_b is the axial beam velocity. In the presence of the unform density beam, however, the *depressed tune* ν is given by $\nu = \nu_0(1 - \hat{s})^{1/2}$. The corresponding *tune shift* that results from the beam space charge is given by $\Delta\nu = \nu - \nu_0 = \nu_0 \left[(1 - \hat{s})^{1/2} - 1\right]$, and *tune depression* is given by

$$\frac{\nu}{\nu_0} = (1 - \hat{s})^{1/2}. \tag{2.30}$$

The dimensionless parameter ν/ν_0 is complementary to the normalized intensity parameter $\hat{s}$ in the way in which it characterizes the relative strength of the space-charge effects. We also note that $\nu/\nu_0 = \sigma^{sf}/\sigma_v^{sf}$.

2.1.5   Operating Range

As mentioned earlier, transverse confinement of the nonneutral plasma column by the focusing field requires $\hat{s} < 1$ or $\hat{\omega}_p/\sqrt{2} < \omega_q$. On the other hand, to avoid so-called the single-particle orbit instability associated with an overly strong focusing field, the vacuum phase advance σ_v should be less than $180°$. In the smooth-focusing approximation for a sinusoidal waveform of $V_0(t)$, this condition can be expressed as $\sigma_v^{sf} = \omega_q/f_0 < 0.9080\pi/\sqrt{2} \ (= 115.6°)$. Combining these inequalities gives

$$\frac{1}{\sqrt{2}} \left(\frac{\hat{n}q^2}{\epsilon_0 m}\right)^{1/2} < \frac{8q\hat{V}_0}{m\pi r_w^2 f_0} \frac{1}{2\sqrt{2\pi}} < 0.9080\frac{\pi}{\sqrt{2}} \times f_0. \tag{2.31}$$

The inequalities in Eq. (2.31) are expected to assure robust transverse confinement of the plasma particles in the PTSX. The PTSX device is capable of reaching and exceeding the right-most inequality in Eq. (2.31). Note that this limit can be expressed
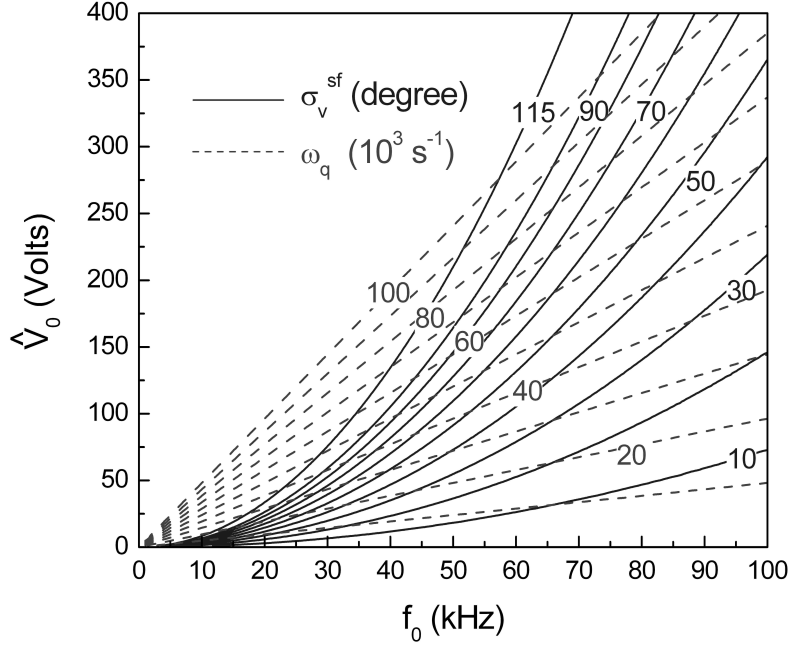
Figure 2.3: In the $(f_0, \hat{V}_0)$ parameter space, curves of constant vacuum phase advance σ_v^{sf} are parabolae, while the curves of constant average focusing frequency ω_q are straight lines [GILSON *et al.*, 2003b].

as a quadratic relationship between $\hat{V}_0$ and f_0 which are the parameters directly controlled in the laboratory. Due to electronics limitations, we normally operate the system in the parameter space $(f_0 < 100 \text{ kHz}, \hat{V}_0 < 400 \text{ Volts})$. Combining these conditions and Eq. (2.31) for a singly ionized cesium ion yields $\omega_q \lesssim 100 \times 10^3 \text{ s}^{-1}$, and $\hat{n} \lesssim 1.5 \times 10^6 \text{ cm}^{-3}$. The density limit is consistent with the collisionless plasma condition discussed in Sec. 2.1.3.

2.2 Beam Dynamics in the Paul Trap Simulator Experiment (PTSX)

In this section, we present several beam dynamics models that are relevant to the analysis of the experimental results of the PTSX in the subsequent chapters. For the quadruple focusing field, a sinusoidal waveform

$$\kappa_q(t) = \hat{\kappa}_q \sin(2\pi f_0 t + \Phi) \tag{2.32}$$

is adopted. Here, an arbitrary constant phase Φ has been introduced in Eq. (2.32). When the initial beam is in the focusing (F) and defocusing (D) phases, then $\Phi = \pm\pi/2$, and when in the drift (O) phase, then $\Phi = 0$.

2.2.1 Single-Particle Orbits

For the quadrupole focusing field given in Eq. (2.32), the single-particle motion in the absence of space-charge effects and end effects is governed by the Mathieu equation,

$$\frac{d^2}{dt^2}x(t) + \hat{\kappa}_q \sin(2\pi f_0 t + \Phi)x(t) = 0, \tag{2.33}$$

with a similar equation for $y(t)$, provided we make the replacements $x(t) \rightarrow y(t)$ and $\hat{\kappa}_q \rightarrow -\hat{\kappa}_q$ in Eq. (2.33).

Detailed properties of the solutions for $x(t)$ to Mathieu's equation (2.33) have been extensively tabulated by Abramowitz and Stegun [ABRAMOWITZ and STEGUN, 1972]. The first-order solution $\tilde{x}(t)$ can be approximated as follows:

$$\tilde{x}(t) = x_{sf}(t)\left[1 + \frac{\sigma_v^{sf}}{\pi\sqrt{2}}\sin(2\pi f_0 t + \Phi)\right], \tag{2.34}$$

with the smooth-focusing motion term $x_{sf}(t)$ given by (for $\cos\phi_0 \neq 0$)

$$x_{sf}(t) = \frac{x_0}{\cos\phi_0\left[1 + (\sigma_v^{sf}/\pi\sqrt{2})\sin\Phi\right]}\cos(\omega_q t + \phi_0). \tag{2.35}$$
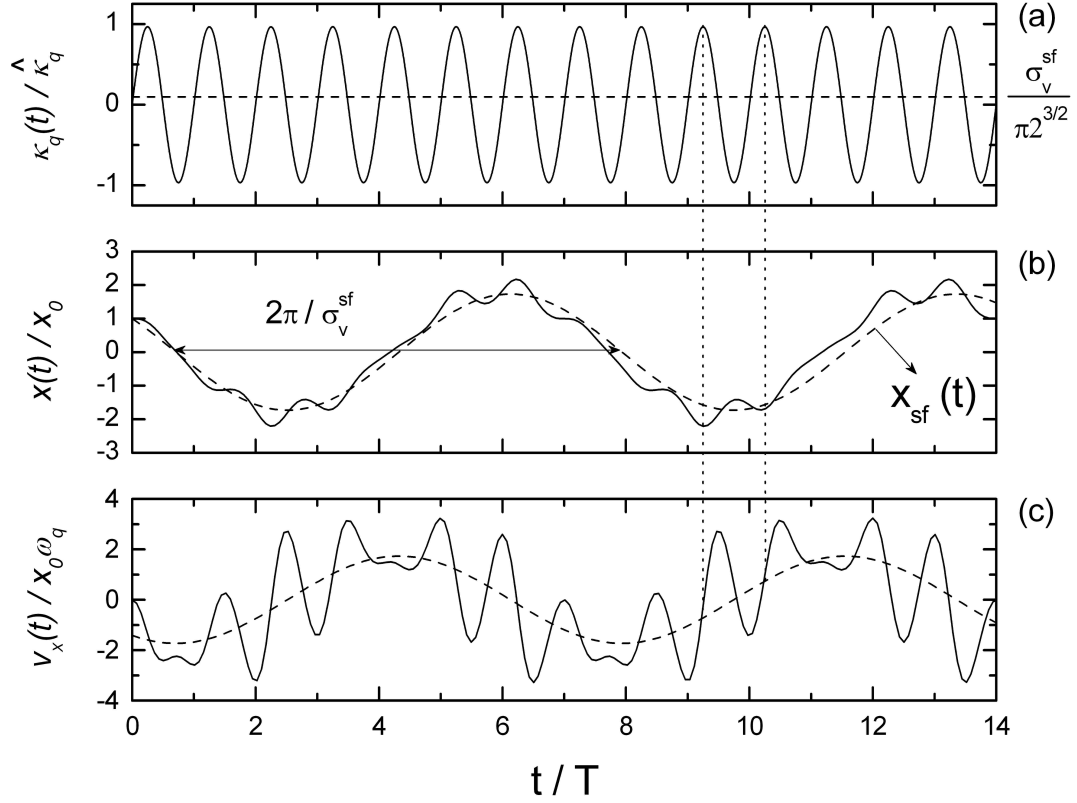
Figure 2.4: Illustrative examples of (a) focusing coefficient $\kappa_q(t)$, and time history of (b) position and (c) velocity of single-particle motion in the PTSX. Here, $\sigma_v^{sf} = 49.8°$, $\Phi = 0$, $x(t = 0) = x_0$, and $\dot{x}(t = 0) = 0$. The dashed lines correspond to the contributions from the smooth-focusing motion term in Eq. (2.34) with $\phi_0 = \tan^{-1}\sqrt{2}$. When σ_v^{sf} is too high, the single-particle motion is overfocused and becomes unstable (i.e., $\sigma_v^{sf} \to 115.6°$). When σ_v^{sf} is too low, the transverse focusing is too weak and single-particle motion becomes vulnerable to the defocusing space-charge force (i.e., $\hat{s} \to 1$).

Here, ω_q is the smooth-focusing frequency in Eq. (2.25), $\sigma_v^{sf} = \omega_q/f_0$ is the smooth-focusing vacuum phase advance, and x_0 and ϕ_0 are constants determined from the initial conditions $x(t = 0) = \tilde{x}(t = 0) = x_0$ and $\dot{x}(t = 0) = \dot{\tilde{x}}(t = 0)$. The smooth-focusing motion term represents a simple harmonic oscillation with spring constant $m\omega_q^2$, where the restoring force is the ponderomotive force associated with rapidly oscillating inhomogeneous electric fields [CHEN, 1984]. The approximate solution Eq. (2.34) is valid only for sufficiently small σ_v^{sf}, and when $\sigma_v^{sf} > 115.6°$, the solutions for $x(t)$ to Eq. (2.33) are unstable (i.e., grow without bound). If one is near the stability limit, then the actual value of vacuum phase advance σ_v has to be obtained by integrating Eq. (2.33) numerically over several focusing periods. Making use of Floquet's theorem [WIEDEMANN, 1999] allows us to determine the exact phase advance through the relation

$$\sigma_v = \cos^{-1}\left\{\frac{x(t) + x(t + 2T)}{2x(t + T)}\right\}, \tag{2.36}$$

which is indeed independent of t, and the single-particle orbit remains stable for $\sigma_v < 180°$. As shown in Fig. 2.5, the smooth-focusing vacuum phase advance σ_v^{sf} is in good agreement with the exact (numerically-calculated) vacuum phase advance σ_v for $\sigma_v \lesssim 2\pi/5 = 72°$, suggesting that the smooth-focusing approximation is valid provided the σ_v is sufficiently small. Possible end effects on the single-particle orbits due to axial bouncing motions in the PTSX are discussed in **Appendix A**.

2.2.2 Envelope Equations

To describe an ensemble of particles in a periodic focusing quadrupole field with self-field force, we consider an axially-uniform long charge bunch with uniform number density $n(x, y, t) = \hat{n}(t)$ (independent of x and y, but dependent on t) within
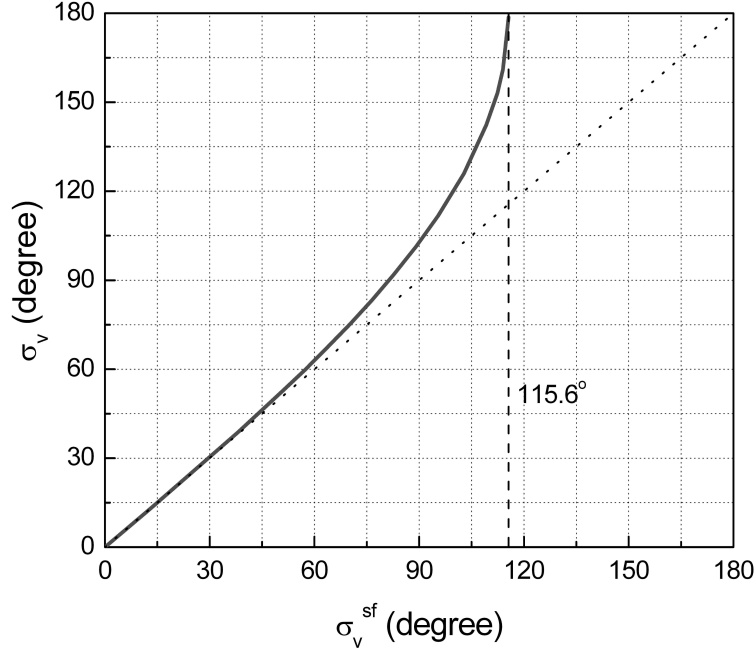
Figure 2.5: Plot of the (exact) vacuum phase advance σ_v calculated numerically from Eq. (2.36) versus the vacuum phase advance σ_v^{sf} determined using ω_q as calculated in the smooth-focusing approximation for the sinusoidal lattice function. The agreement is very good for $\sigma_v \lesssim 2\pi/5 = 72°$.

the elliptical cross-section $0 \leq x^2/a^2(t) + y^2/b^2(t) \leq 1$, and zero density outside. Here, $a(t)$ and $b(t)$ are the x- and y-direction envelopes (or half-width) of the beam. Such a periodically-focused uniform-density beam is obtained self-consistently for the choice of the Kapchinskij-Vladimirskij (KV) distribution function [KAPCHINSKIJ and VLADIMIRSKIJ, 1959; DAVIDSON and QIN, 2001], which is the only known exact, periodically-focused equilibrium solution to the nonlinear Vlasov-Poisson equations (2.18) and (2.19), including intense self-field effects. In this KV beam, the line density $N = \int dxdy n(x, y, t) = \hat{n}\pi ab = const.$, and the self-field potential is given by

[DAVIDSON, 1990; DAVIDSON and QIN, 2001]

$$\frac{q}{m}\phi^s(x, y, t) = -\frac{2K}{a+b}\left[\frac{1}{a}x^2 + \frac{1}{b}y^2\right],\tag{2.37}$$

in the beam interior. Here, we have taken $\phi^s = 0$ at $(x, y) = (0, 0)$ without loss of generality, and assumed $a, b \ll r_w$, which means that image-charge effects [ALLEN and REISER, 1996; QIAN *et al.*, 2003] from the conducting wall at radius r_w are neglected.

Even though the KV beam is singular and unphysical (i.e., has a highly-inverted distribution in phase space), it can describe the root-mean-squared (rms) behavior of a beam with a more realistic transverse phase-space distribution, when the two beams have the same line density and rms beam quality (such as rms emittance defined later). This concept of *equivalent beams* was first introduced by Lapostolle [LAPOSTOLLE, 1971] and Sacherer [SACHERER, 1971] in 1971 and has been a useful approximation for beam dynamics analysis. Important parameters in the concept of equivalent beams include the rms x and y dimensions of the beam, $\langle x^2 \rangle^{1/2}$ and $\langle y^2 \rangle^{1/2}$, and the x and y direction rms beam velocities, $\langle \dot{x}^2 \rangle^{1/2}$ and $\langle \dot{y}^2 \rangle^{1/2}$. Here, the statistical average of a phase function $\xi(x, y, \dot{x}, \dot{y}, t)$ over the four-dimensional phase space is denoted by $\langle \xi \rangle (t)$ and is defined by

$$\langle \xi \rangle = \frac{\int dx dy d\dot{x} d\dot{y}\, \xi f}{\int dx dy d\dot{x} d\dot{y}\, f},\tag{2.38}$$

where $f(x, y, \dot{x}, \dot{y}, t)$ is the distribution function. Note that for a KV beam, $\langle x^2 \rangle^{1/2} = a(t)/2$ and $\langle y^2 \rangle^{1/2} = b(t)/2$.

To quantitatively describe the beam quality, the concept of rms emittance [LA-POSTOLLE, 1971; SACHERER, 1971] is introduced. The rms emittance is not only related to the phase-space volume occupied by the beam particles (which should be

conserved by Liouville's theorem), but also dependent on the distortion (filamentation) produced by nonlinear forces [REISER, 1994; WANGLER, 1998]. If the motions in the x and y directions are decoupled, as often happens in beam transport systems [STREHL, 2006], we can define two transverse phase planes $(x, \dot{x})$ and $(y, \dot{y})$, and corresponding x- and y-transverse emittances, $\epsilon_x(t)$ and $\epsilon_y(t)$, which are given by [REISER, 1994; QIAN, 1995]

$$\epsilon_x(t) = 4 \left[\left\langle x^2 \right\rangle \left\langle \dot{x}^2 \right\rangle - \left\{ \frac{1}{2} \frac{d}{dt} \left\langle x^2 \right\rangle \right\}^2 \right]^{1/2}, \tag{2.39}$$

$$\epsilon_y(t) = 4 \left[\left\langle y^2 \right\rangle \left\langle \dot{y}^2 \right\rangle - \left\{ \frac{1}{2} \frac{d}{dt} \left\langle y^2 \right\rangle \right\}^2 \right]^{1/2}. \tag{2.40}$$

Because these emittances are defined in the beam frame (i.e., laboratory frame of the PTSX) and are not affected by the axial motion, they can be said to be *normalized.* If both transverse focusing and space-charge forces are linearly proportional to transverse displacement (such as for the KV beam), the emittances defined by Eqs. (2.39) and (2.40) can be shown to be conserved by Liouville's theorem [DAVIDSON and QIN, 2001]. For the KV beam, the transverse rms emittance is directly proportional to the phase-space area *uniformly* occupied by the beam particles by factor $1/\pi$, and its value is invariant in the smooth-focusing approximation [DAVIDSON and QIN, 2001].

Making use of Eq. (2.37) to express self-field forces and following the procedures in Davidson and Qin [DAVIDSON and QIN, 2001; COURANT and SNYDER, 1958] readily gives

$$\frac{d^2}{dt^2} a(t) + \kappa_q(t) a(t) - \frac{2K}{a(t) + b(t)} = \frac{\epsilon_x^2}{a^3(t)}, \tag{2.41}$$

$$\frac{d^2}{dt^2} b(t) - \kappa_q(t) b(t) - \frac{2K}{a(t) + b(t)} = \frac{\epsilon_y^2}{b^3(t)}, \tag{2.42}$$

which describe the evolutions of x- and y-direction envelopes of the KV beam, $a(t)$ and $b(t)$, in periodic focusing quadruple field $\kappa_q(t)$. The envelope equations (2.41)

and (2.42) represent a system of two nonlinear, second-order coupled differential equations which, in general, must be solved numerically for given initial conditions $\{a(0), \dot{a}(0), b(0), \dot{b}(0)\}$. If two beams have the same perveance (or equivalently, line density or current), rms emittances, and initial conditions as the KV beam, then the transverse rms dimensions of the two beams evolve identically according to Eqs. (2.41) and (2.42). However, there is an implicit assumption in this concept that the rms emittance of the two beams being compared remains the same or that the emittance change in time is known a priori [REISER, 1994]. This assumption is in general not correct, especially when there is a free energy source for emittance growth such as charge nonuniformity [QIAN, 1995] and rms mismatch [REISER, 1991].

When the rms dimensions of a beam have the same oscillation frequency as the focusing field, the beam is said to be *rms-matched* and emittance growth is minimized. For a KV beam, the rms matching condition can be expressed as $a(t + T) = a(t)$ and $b(t + T) = b(t)$, resulting in $f(x, y, \dot{x}, \dot{y}, t + T) = f(x, y, \dot{x}, \dot{y}, t)$ and $\langle a(t)b(t)\rangle_T = \bar{r}_b^2 = const$. On the other hand, if the beam is rms-mismatched, nonlinear forces can give rise to a filamentation in phase space causing the rms emittance to increase [LAPOSTOLLE, 1971; WANGLER, 1998]. This process cannot be described solely by the envelope equations for the equivalent KV beam. When the beam is mismatched in a quadrupole focusing channel, the two transverse degrees of freedom in Eqs. (2.41) and (2.42) yield two fundamental oscillation modes, which are the breathing mode and the quadrupole mode. For the breathing mode, the evolution of $\langle a(t)\rangle_T$ and $\langle b(t)\rangle_T$ are in-phase body-wave perturbations, and the frequency is approximately given by [REISER, 1994; DAVIDSON and QIN, 2001]

$$\omega_B \approx 2\omega_q \left[1 - \frac{1}{2}\left(\frac{K}{\bar{r}_b^2 \omega_q^2}\right)\right]^{1/2}.$$

(2.43)

On the other hand, for the evolution of $\langle a(t) \rangle_T$ and $\langle b(t) \rangle_T$ for the out-of-phase surface-wave perturbations of the quadrupole mode, the frequency is approximately given by [REISER, 1994; DAVIDSON and QIN, 2001]

$$\omega_Q \approx 2\omega_q \left[1 - \frac{3}{4}\left(\frac{K}{\bar{r}_b^2 \omega_q^2} \right) \right]^{1/2}. \tag{2.44}$$

Note that $\omega_q \leq \omega_Q \leq \omega_B \leq 2\omega_q$ and $\omega_Q = \omega_B = 2\omega_q$ for $K \to 0$. Generally, beam mismatch produces a mixed mode composed of both breathing and quadrupole modes. In the mixed mode, there often appears a slow amplitude modulation in the oscillations of the mean radius $\sqrt{a(t)b(t)}$ [see Fig. 2.6(b)].

2.2.3 Envelope Oscillation and Halo Formation

In the smooth-focusing approximation for a KV beam with $\epsilon_x = \epsilon_y = \epsilon = const.$, the envelope equations (2.41) and (2.42) can be further simplified as [DAVIDSON and QIN, 2001]

$$\frac{d^2}{dt^2} r_b(t) + \omega_q^2 r_b(t) - \frac{K}{r_b(t)} = \frac{\epsilon^2}{r_b^3(t)}, \tag{2.45}$$

which determines the (slow) evolution of the average beam envelope of the KV beam $r_b(t) = \sqrt{2}\left\langle x_{sf}^2 + y_{sf}^2 \right\rangle^{1/2} = \sqrt{2}R_b(t)$ with average transverse emittance ϵ given as

$$\epsilon = 2R_b \left[\left\langle \dot{x}_{sf}^2 + \dot{y}_{sf}^2 \right\rangle - \left(\frac{dR_b}{dt} \right)^2 \right]^{1/2}. \tag{2.46}$$

Here, $(x_{sf}, y_{sf}, \dot{x}_{sf}, \dot{y}_{sf})$ are slow variables in the smooth-focusing approximation.

The rms matching condition is then $r_b(t) = const.$ and $\partial f / \partial t = 0$. For a matched beam, $d^2 r_b / dt^2 = 0$ in Eq. (2.45) and the matched-beam radius $\bar{r}_b$ is given by

$$\bar{r}_b^2 = \frac{K + \sqrt{K^2 + 4\epsilon^2 \omega_q^2}}{2\omega_q^2}. \tag{2.47}$$
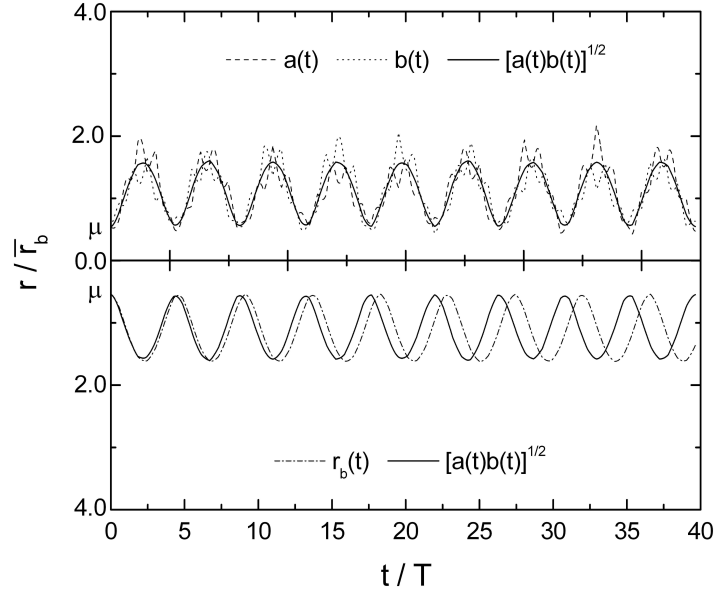
(a) $\Phi = \pi/2$. A pure breathing mode is excited.
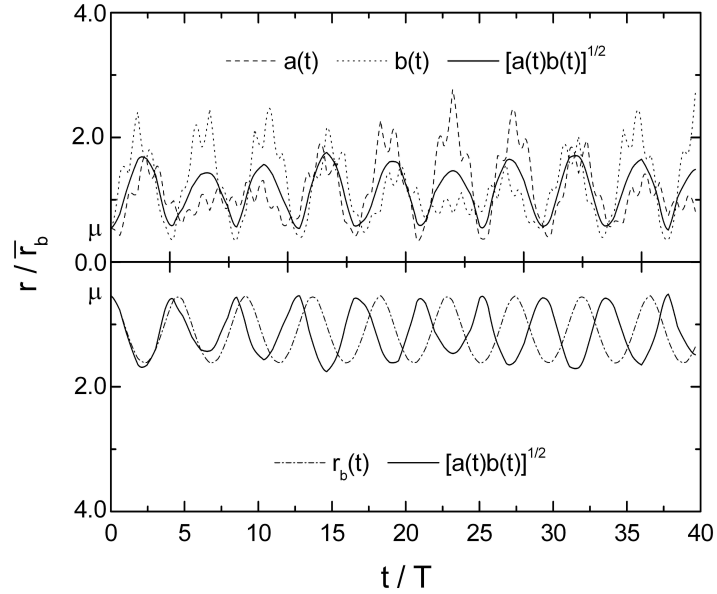
(b) $\Phi = 0$. A mixed mode is excited.

Figure 2.6: Time evolutions of the x- and y-beam envelopes, $a(t)$ and $b(t)$, mean radius $[a(t)b(t)]^{1/2}$, and beam radius $r_b(t)$ in the smooth-focusing approximation. Here, we consider a KV beam with strong injection mismatch for $\mu = 0.54$, $\bar{s} = 0.85$, $\sigma^{sf} \approx 49.8°(1 - \bar{s})^{1/2}$, and $\sigma \approx 51.4°(1 - \bar{s})^{1/2}$. Initially, $\{a(0), \dot{a}(0), b(0), \dot{b}(0)\} = \{\mu\bar{r}_b, 0, \mu\bar{r}_b, 0\}$ and $\epsilon_x = \epsilon_y = \epsilon = \bar{r}_b^2\omega_q(1 - \bar{s})^{1/2}$.

If the initial beam radius r_{bi} is unequal to the $\bar{r}_b$, the imbalance between focusing and defocusing forces excites a symmetric breathing mode, resulting in oscillations of the beam envelope $r_b(t)$ and on-axis density $\hat{n}(t)$. The frequency of this breathing mode ω_B can be approximated as

$$\omega_B = 2\omega_q \left(1 - \frac{\bar{s}}{2}\right)^{1/2}, \tag{2.48}$$

where $\bar{s} = K / \left(\bar{r}_b^2 \omega_q^2\right)$ is the normalized intensity for the matched beam. Note that the value of $\hat{s}$ is oscillating according to the envelope oscillations while $\bar{s} = const$. After introducing the scaled variables $R = r_b / \bar{r}_b$ and $\tau = \omega_q t$, the dimensionless equation of motion for the envelope oscillations becomes

$$\frac{d^2 R}{d\tau^2} + R - \frac{(1 - \bar{s})}{R^3} - \frac{\bar{s}}{R} = 0. \tag{2.49}$$

To describe the degree of initial mismatch, we also introduce the mismatch parameter defined by $\mu = r_{bi} / \bar{r}_b$. Hence, Eq. (2.49) depends only on the two dimensionless parameters $\bar{s}$ and μ, when the initial beam is assumed to be stationary $(dr_{bi}/dt = 0)$.

Numerical simulations [WANGLER *et al.*, 1998; RYNE *et al.*, 1999] and experiments [KEHNE *et al.*, 1991; ALLEN *et al.*, 2002] show that beam mismatch is one of the main sources for the formation of a tail in the density distribution. This tail is the so-called *beam halo*. Such a halo leads to beam loss and radioactivation when high energy particles intercept the accelerator structures. To make a simple quantitative prediction of halo formation in the PTSX, we consider the motion of a test particle that interacts with the external focusing force and time-dependent space-charge force of the mismatched beam core, which can be expressed as

$$\frac{d^2 X}{d\tau^2} + X = \bar{s} \times \begin{cases} X/R^2, & |X| < R, \\ 1/X, & |X| \geq R, \end{cases} \tag{2.50}$$

(a) $\mu = 0.54$ and $\bar{s} = 0.85$.

(b) $\mu = 0.54$ and $\bar{s} = 0.2$.

(c) $\mu = 0.95$ and $\bar{s} = 0.85$.

(d) $\mu = 0.95$ and $\bar{s} = 0.2$.
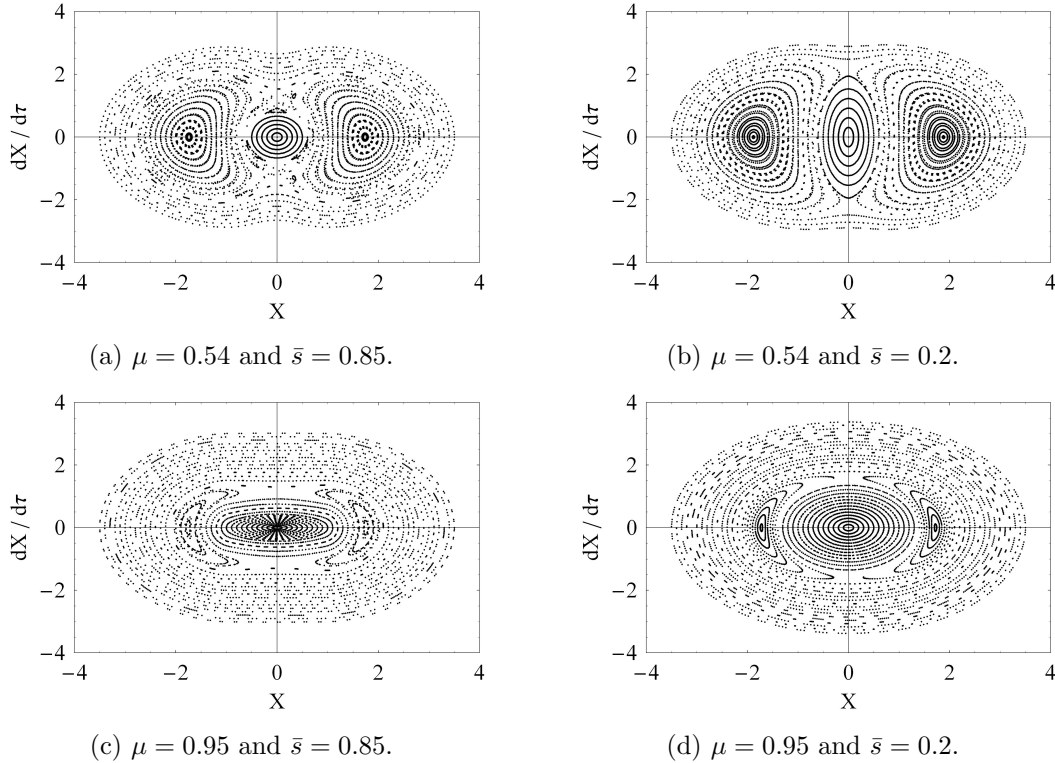
Figure 2.7: Stroboscopic plots of test particles in the mismatched beam. The particles are plotted in $(X, dX/d\tau)$ space every time the core oscillation reaches its minimum, which corresponds to the occurrence of the maximum displacement of the resonant orbit. The nonlinear force outside the beam core makes the oscillation period of the single particle depend on oscillation amplitude. On the other hand, the maximum single particle displacement within the beam core occurs when the core is at its maximum radius. Evolution of mismatched beam core for case (a) is illustrated in Fig. 2.6. Initially, test particles are distributed uniformly in the region $(0.1 \leq X \leq 3.5, dX/d\tau = 0)$.

where, $X = x/\bar{r}_b$. For the present analysis, we assume axisymmetry and the case of zero canonical angular momentum, corresponding to one-dimensional particle motion in the x-direction, say, with $y = 0$ and $dy/dt = 0$ [STRASBURG, 2001]. Note that the particles experience a nonlinear force proportional to $\bar{s}/X$ when they are spatially outside the core, and from Gauss's law this force is independent of the instantaneous size of the beam core R. This *particle-core model* [WANGLER *et al.*, 1998; GERIGK, 2004] predicts that the halo is formed from the parametric resonance between test particles near the beam edge and envelope oscillations induced by the initial mismatch. If the single particle's oscillation frequency has a 1:2 parametric ratio with the oscillation frequency of the core, the particle picks up energy from the core and increases its oscillation amplitude until the resonant condition becomes out of phase [GLUCKSTERN, 1994; GERIGK, 2004]. The general tendency is that the maximum amplitude of the halo particles depends on the mismatch parameter μ, while the growth rate of halo formation increases with normalized intensity $\bar{s}$ [WANGLER *et al.*, 1998]. For example, in the case of a strong initial mismatch ($\mu = 0.54$), as illustrated in Figs. 2.7(a) and 2.7(b), particles initially within the core can have a maximum amplitude of $\sim 3\bar{r}_b$, which is about 50% larger than the maximum envelope of the mismatched core (see Fig. 2.6).

Here, it should be also noted that particles inside the beam core cannot pick up all of the applied focusing force due to the repulsive space-charge force. The spring constant for transverse particle motion is depressed to be $\nu_b^2 \approx \omega_q^2(1 - \bar{s})$. Hence, phase-space particle trajectories inside the core shrink considerably in the $dX/d\tau$ direction for the case of higher $\bar{s}$ [see Figs. 2.7(a) and 2.7(c)]. The parameters used in Figs. 2.6 and 2.7 have been chosen for the analysis of the experimental results presented in Sec. 4.1.

2.2.4 Beam Equilibrium

A nonneutral collection of ions confined by an external periodic focusing potential will relax to a quasi-equilibrium state. In equilibrium, local radial force balance on a fluid element of ions with charge q and mass m in the smooth-focusing approximation is given by [DAVIDSON and QIN, 2001]

$$\frac{\partial}{\partial r}P_\perp(r) = -qn(r)\frac{\partial}{\partial r}\phi^s(r) - m\omega_q^2 n(r)r, \tag{2.51}$$

where $n(r)$ is the equilibrium radial density profile, ω_q is the applied smooth-focusing frequency, and r is the radial distance from the beam axis. Here, the space-charge potential $\phi^s(r)$ is determined self-consistently from Poisson's equation $r^{-1}\partial_r\left(r\partial_r\phi^s\right) = -qn(r)/\epsilon_0$, and $P_\perp(r) = n(r)T_\perp(r)$ is the perpendicular pressure profile which is proportional to transverse temperature profile $T_\perp(r)$. A necessary condition for transverse confinement of the ions is that the applied focusing force in Eq. (2.51) should be sufficiently strong to exceed the defocusing self-field force, i.e., $m\omega_q^2 n(r)r > qn(r)E_r^s$, where $E_r^s = -\partial\phi^s/\partial r = (q/\epsilon_0 r)\int_0^r dr r n(r)$ is the radial space-charge field that solves Poisson's equation. For present purposes, we assume that $n(r)$ is a monotonically decreasing function of r from the on-axis value $n(r = 0) = \hat{n}$. Then for small r, we obtain $E_r^s = (q/2\epsilon_0)\hat{n}r$, and have the requirement

$$\hat{s} \equiv \frac{\hat{\omega}_p^2/2}{\omega_q^2} < 1. \tag{2.52}$$

Here, $\hat{\omega}_p^2 = \hat{n}q^2/\epsilon_0 m$ is the on-axis ($r = 0$) plasma frequency-squared.

We now consider an anisotropic equilibrium distribution function f^0 in the smooth-focusing approximation of the form

$$f^0 = F(H_\perp)G(p_z), \tag{2.53}$$

where the perpendicular Hamiltonian $H_\perp$ can be expressed as

$$H_\perp = \frac{p_x^2 + p_y^2}{2m} + V(r), \tag{2.54}$$

with effective potential for the transverse particle motion $V(r)$ being defined by

$$V(r) = \frac{1}{2}m\omega_q^2 r^2 + q\phi^s(r). \tag{2.55}$$

Here, equilibrium properties ($\partial/\partial t = 0$) are assumed to be azimuthally symmetric ($\partial/\partial\theta = 0$) and independent of axial coordinate ($\partial/\partial z = 0$). Assuming the axial momentum distribution $G(p_z)$ to be normalized according to $\int_{-\infty}^{\infty} dp_z G(p_z) = 1$, it follows that

$$n(r) = \int dp_x dp_y dp_z f^0 = \int_0^\infty \pi dp_\perp^2 F\left(\frac{p_\perp^2}{2m} + V(r)\right), \tag{2.56}$$

and

$$
\begin{aligned}
P_\perp(r) &= n(r)T_\perp(r) \\
&= \frac{1}{2}\int dp_x dp_y dp_z (p_x \dot{x}_{sf} + p_y \dot{y}_{sf})f^0 \\
&= \int_0^\infty \pi dp_\perp^2 \left(\frac{p_\perp^2}{2m}\right) F\left(\frac{p_\perp^2}{2m} + V(r)\right).
\end{aligned}
\tag{2.57}
$$

Here, $(p_x, p_y) = m(\dot{x}_{sf}, \dot{y}_{sf})$, $p_\perp^2 = p_x^2 + p_y^2$, and use has been made of $\int_{-\infty}^{\infty} dp_x \int_{-\infty}^{\infty} dp_y \cdots = \int_0^\infty \pi dp_\perp^2 \cdots$. We now operate on Eq. (2.51) with $2\pi \int_0^{r_w} dr r^2 \cdots$, and carry out an integration by parts assuming $P_\perp(r = r_w) = 0$. This gives the exact global force balance equation [DAVIDSON and QIN, 2001]

$$m\omega_q^2 R_b^2 = 2\bar{T}_\perp + \frac{Nq^2}{4\pi\epsilon_0}, \tag{2.58}$$

which is valid for the entire class of anisotropic equilibrium functions $f^0 = F(H_\perp)G(p_z)$ expressed in Eq. (2.53). Here, $N = 2\pi \int_0^{r_w} dr r n(r)$ is the line density, $R_b^2 =$

$(2\pi/N)\int_0^{r_w} drr r^2 n(r)$ is the mean-square radius of the beam, and $\bar{T}_\perp$ is the effective transverse temperature defined by

$$\bar{T}_\perp = \frac{2\pi}{N}\int_0^{r_w} drr \left\langle \frac{p_\perp^2}{2m} \right\rangle_{p_x,p_y} n(r). \tag{2.59}$$

The notation $\langle\cdots\rangle_{p_x,p_y}$ denotes the statistical average over the equilibrium distribution function in the transverse momentum subspace. Note that the effective transverse temperature $\bar{T}_\perp$ measures the kinetic energy per particle averaged over the transverse phase space (i.e., $\bar{T}_\perp = m \left\langle \dot{x}_{sf}^2 + \dot{y}_{sf}^2 \right\rangle_0 /2$) in the smooth-focusing equilibrium, where fast micromotion associated with quadrupole focusing frequency f_0 has been averaged out, and there is no drift motion in the fluid element ($dR_b/dt = 0$).

Thermodynamically, a possible beam equilibrium state can be best described by a thermal equilibrium distribution with a constant temperature [DAVIDSON, 1990; REISER and BROWN, 1993; BROWN and REISER, 1995; DAVIDSON and QIN, 1999]. Practically, only beams in storage rings and circular accelerators can have enough lifetime to relax to a thermal equilibrium state via Coulomb collisions [REISER, 1994]. In fast transient systems, such as high-gain free-electron lasers and high-intensity linear accelerators, relaxation mechanisms are too slow to be relevant, and if beam equilibria are found, they are usually a property of the particle source used [ROSEN-ZWEIG, 2003]. For these cases, however, nonlinear stochastic space-charge forces may significantly speed up the relaxation process by the thermalization of free energy or equipartitioning, resulting in emittance growth and beam degradation [REISER, 1991]. A beam that is injected from the source in a state close to the thermal equilibrium distribution can minimize emittance growth resulting from the relaxation toward equilibrium. Hence, an understanding of thermal equilibrium properties, such as the equilibrium density profile and relations between global equilibrium parameters, is of great practical importance.

We consider the case where $F(H_\perp)$ is specified by thermal equilibrium distribution

$$F = \frac{\hat{n}}{(2\pi m \hat{T}_\perp)} \exp\left(-\frac{H_\perp}{\hat{T}_\perp}\right), \tag{2.60}$$

where $\hat{T}_\perp$ is a positive constant which will be identified with uniform beam temperature. Substituting Eq. (2.60) into Eqs. (2.56) and (2.57) readily gives

$$n(r) = \hat{n} \exp\left\{-\frac{\frac{1}{2} m \omega_q^2 r^2 + q\phi^s(r)}{\hat{T}_\perp}\right\}, \tag{2.61}$$

and $P_\perp(r) = n(r)\hat{T}_\perp$. Here, we again take $\phi^s(r = 0) = 0$ without loss of generality, so that $\hat{n}$ can be identified with the on-axis number density. As expected, the transverse temperature profile is isothermal (independent of position), with $T_\perp(r) = \hat{T}_\perp = const.$ Further, $\bar{T}_\perp = \hat{T}_\perp$ is the measure of particle's random or thermal energy. Finally, Poisson's equation becomes

$$\frac{1}{r}\frac{\partial}{\partial r} r \frac{\partial}{\partial r} \phi^s(r) = -\frac{q}{\epsilon_0}\hat{n}\exp\left\{-\frac{\frac{1}{2}m\omega_q^2 r^2 + q\phi^s(r)}{\hat{T}_\perp}\right\}, \tag{2.62}$$

which is a nonlinear differential equation for the space-charge potential $\phi^s(r)$.

After introducing dimensionless variables $\rho = r/r_\beta$ and $\chi = q\phi^s/\hat{T}_\perp$, Eq. (2.62) can be expressed in the equivalent form

$$\frac{1}{\rho}\frac{\partial}{\partial \rho}\rho\frac{\partial}{\partial \rho}\chi = -4\hat{s}\exp\left[-\rho^2 - \chi\right], \tag{2.63}$$

where $r_\beta^2 = 2\hat{T}_\perp/m\omega_q^2$ is the zero-beam-intensity mean-square radius. Numerical integration of Eq. (2.63) gives a numerically tabulated function, $\chi(\rho, \hat{s})$, which can be used to calculate a new dimensionless parameter [DAVIDSON and QIN, 1999]

$$\delta_b(\hat{s}) = \frac{1}{4\pi\epsilon_0}\frac{Nq^2}{2\hat{T}_\perp} = \hat{s}\int_0^\infty d\rho\rho\exp\left[-\rho^2 - \chi(\rho, \hat{s})\right], \tag{2.64}$$

that measures the relative space-charge force compared to the thermal pressure force. Here, for further simplicity, the integration limit has been set to infinity without
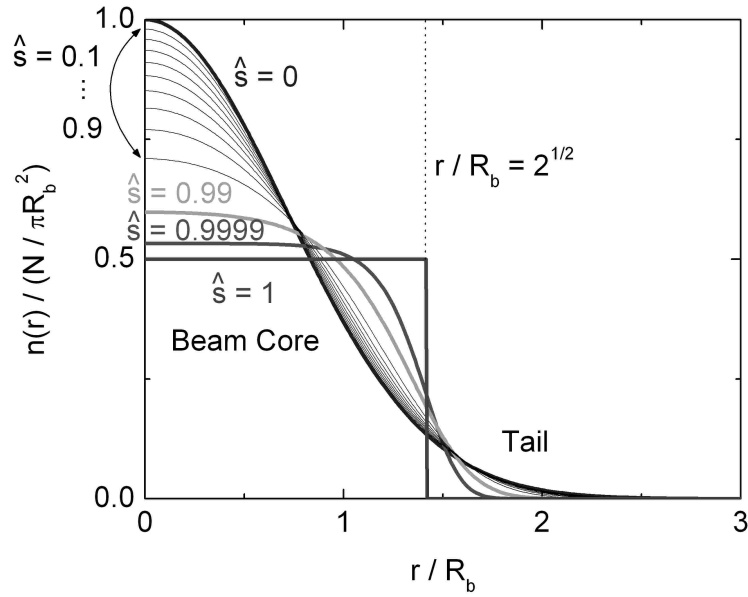
(a) Linear versus r/R_b scale.
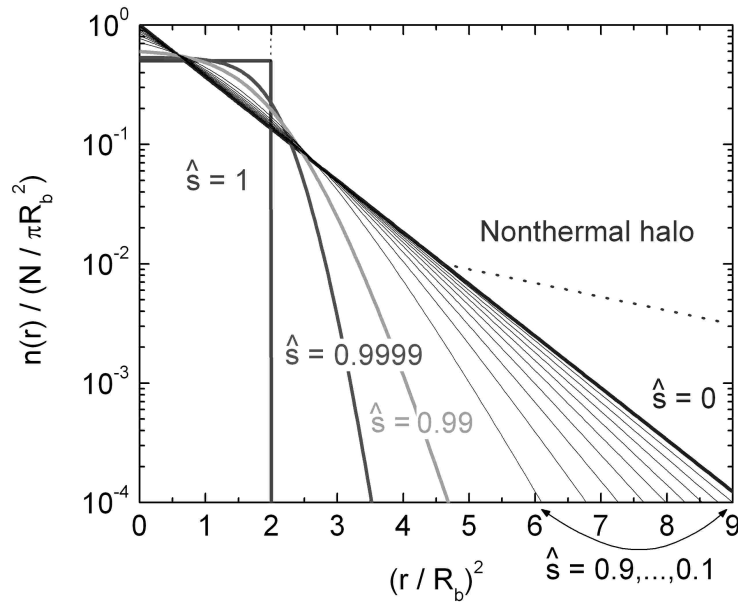
(b) Log versus $(r/R_b)^2$ scale

Figure 2.8: Plots of normalized thermal equilibrium density profiles $n(r)/(N/\pi R_b^2)$ (a) in the linear versus r/R_b scale and (b) in the log versus $(r/R_b)^2$ scale for different values of normalized beam intensity $\hat{s}$. The density distribution of nonthermal halo particles (dotted line) is much more extended and more densely populated than the natural Debye tail of a thermal equilibrium beam.

loss of significant accuracy, provided that $r_\beta \ll r_w$. A beam is emittance-dominated for $\delta_b \ll 1 (\hat{s} \to 0)$, while it is space-charge dominated for $\delta_b \gg 1 (\hat{s} \to 1)$. The mean-square radius R_b^2 can be expressed in terms of δ_b as

$$R_b^2 = r_\beta^2 (1 + \delta_b), \tag{2.65}$$

which is equivalent to the global force balance equation (2.58). To describe shape changes of equilibrium density profiles according to the beam intensity, we define a dimensionless form factor which is defined by [GILSON *et al.*, 2007a]

$$\zeta(\hat{s}) = \frac{N}{\hat{n}\pi R_b^2} = \frac{2\delta_b(\hat{s})}{\hat{s}\,[1 + \delta_b(\hat{s})]}. \tag{2.66}$$

The equilibrium density profile is Gaussian when $\hat{s} \to 0$ and $\zeta = 1$, whereas the profile is uniform when $\hat{s} \to 1$ and $\zeta = 2$. The population of the tail portion of the beam can be quantified by the profile parameter h defined by [ALLEN and WANGLER, 1998]

$$h = \frac{3}{2} \frac{\left\{\int_0^\infty d\rho \rho^5 \exp\left[-\rho^2 - \chi\right]\right\} \left\{\int_0^\infty d\rho \rho \exp\left[-\rho^2 - \chi\right]\right\}}{\left\{\int_0^\infty d\rho \rho^3 \exp\left[-\rho^2 - \chi\right]\right\}^2} - 2. \tag{2.67}$$

The profile parameter h is used to compare the peakedness of a distribution to that of a Gaussian distribution ($h = 1$ for a Gaussian). The presence of significant nonthermal halo particles usually corresponds to $h > 1$ [see Fig. 2.8(b)]. Another important parameter that measures the scale length over which a local charge perturbation from the thermal equilibrium state can be effective is the thermal Debye length [DAVIDSON and QIN, 2001]. The on-axis thermal Debye length $\lambda_D = \left(\epsilon_0 \hat{T}_\perp / \hat{n} q^2\right)^{1/2}$ can be expressed as

$$\frac{\lambda_D}{r_b} = \frac{1}{2\sqrt{2}\hat{s}\,[1 + \delta_b(\hat{s})]}, \tag{2.68}$$

in units of the outer radius of equivalent uniform density beam $r_b = \sqrt{2} R_b$.

(a) Thermal beam intensity parameter.

(b) Form factor.

(c) Profile parameter.

(d) Thermal Debye length.
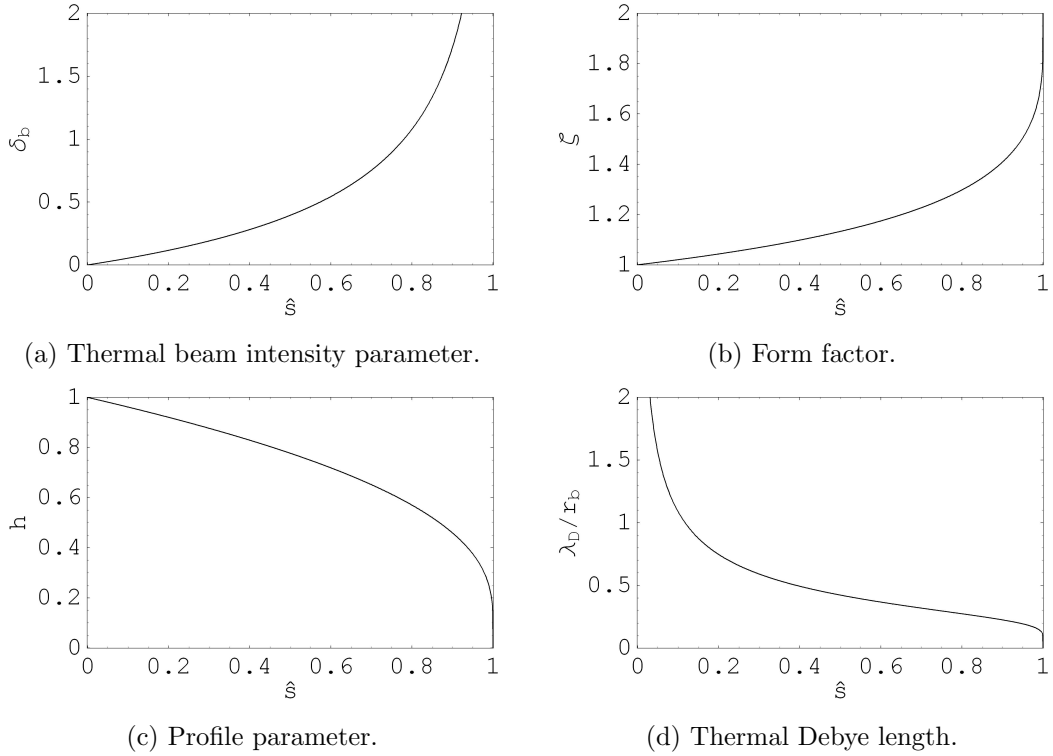
Figure 2.9: Plots of dimensionless parameters describing the characteristics of thermal equilibrium density profiles as a function of normalized beam intensity $\hat{s}$.

2.2.5 Longitudinal Dynamics

For analytical simplicity in dealing with the axial momentum distribution $G(p_z)$, we introduce here the drifting Lorentzian distribution for the counter-streaming ions in the PTSX as

$$G(p_z) = \frac{\Delta_\parallel/2}{\pi\left[(p_z - mv_b)^2 + \Delta_\parallel^2\right]} + \frac{\Delta_\parallel/2}{\pi\left[(p_z + mv_b)^2 + \Delta_\parallel^2\right]}, \qquad (2.69)$$

where v_b is the average axial speed of streaming ions and $\Delta_\parallel = const. > 0$ is a measure of the axial momentum spread which is related to the effective axial thermal speed $v_{T\parallel} = (2T_\parallel/m)^{1/2}$, by $\Delta_\parallel = mv_{T\parallel}$. Here, $T_\parallel$ is the effective longitudinal temperature. Note from Eq. (2.69) that $1 = \int_{-\infty}^{\infty} dp_z G(p_z)$ and $0 = \int_{-\infty}^{\infty} dp_z v_z G(p_z)$. In actual accelerators, the temperature anisotropy $(T_\perp > T_\parallel)$ is well known to develop naturally

[STARTSEV *et al.*, 2003]. This is mostly due to longitudinal cooling by acceleration [REISER, 1994]. For example, for a beam of charged particles with charge q that is accelerated through a voltage ΔV, a simple estimate shows that the final and initial longitudinal temperatures are related in the nonrelativistic case by $T_{\|f} = T_{\|i}^2/(2q\Delta V)$. However, in the PTSX, ΔV is usually less than 9 V, and the longitudinal cooling effect turns out be to very weak. Particle-in-cell (PIC) simulations using the 3D WARP code [FRIEDMAN *et al.*, 1992; DORF, 2006] show that the space-charge forces from the virtual cathode near the source couple the longitudinal and transverse thermal motions, resulting in $T_{\|} \approx T_{\perp}$. Possible two-stream interactions in the PTSX are discussed in **Appendix B**, based on the drifting Lorentzian distribution introduced in Eq. (2.69).

2.3 Summary and Discussion

For the optimal design and stable operation of high-intensity accelerators and beam transport systems, it is essential to develop a basic understanding of the beam dynamics with significant space-charge effects. Several simplified beam dynamics models such as test particle calculations (Secs. 2.2.1 and 2.2.3, and **Appendix A**), envelope equations based on an equivalent KV beam (Sec. 2.2.2), and a thermal equilibrium model (Sec. 2.2.4) can give some insights on intense beam propagation. For the self-consistent description of an intense beam, however, one must generally solve the nonlinear Vlasov-Maxwell equations (2.11) and (2.12) using advanced numerical methods that employ particle-in-cell (PIC) models and nonlinear perturbative simulation techniques [FRIEDMAN *et al.*, 1992; QIAN *et al.*, 1997; QIN *et al.*, 2000].

Due to the lack of dedicated experimental devices for fundamental studies, it is difficult to verify the results from the numerical simulations and to develop robust physical models. In Sec. 2.1, we have shown that there is a compelling physics analogy between intense beam propagation through an AG focusing lattice and nonneutral plasma confined in a compact Paul trap configuration. Hence, experimental studies of nonneutral plasma properties in the PTSX device can provide an alternative path for the detailed study of intense charged particle beam dynamics. The operation of PTSX has been optimized for $\hat{s} \sim 0.2$, which corresponds to the case where the space-charge force contributes to about 10% of the total applied focusing force. In this operating regime, it is expected that the self-consistent effects of the nonlinear space-charge force, such as emittance growth, can be observed experimentally and be compared with theory and PIC simulations.

Chapter 3

Experimental Apparatus

In this chapter, the Paul Trap Simulator Experiment (PTSX) apparatus is described. Section 3.1 gives a general overview of the basic equipment and operation of the PTSX device, Sec. 3.2 describes the cesium ion source which has been used for the initial phase of PTSX experiments, Sec. 3.3 describes the charge collector diagnostic for measuring the radial ion density profile, and finally Sec. 3.4 is devoted to the laser-induced fluorescence (LIF) diagnostic system with accompanying barium ion source.

3.1   The Paul Trap Simulator Experiment Device

The Paul Trap Simulator Experiment (PTSX) device is a linear Paul Trap [PAUL and STEINWEDEL, 1953] constructed from a 2.8 m-long, $r_w = 10$ cm-radius, gold-plated stainless steel cylinder as shown in Figs. 3.1 and 3.2. The cylinder is divided into two 40 cm-long end cylinders and a $2L = 2$ m-long central cylinder. All cylinders are azimuthally divided into four 90° sectors so that when an oscillating voltage $V_0(t)$ is applied with alternating polarity on adjacent segments, the resulting electric field
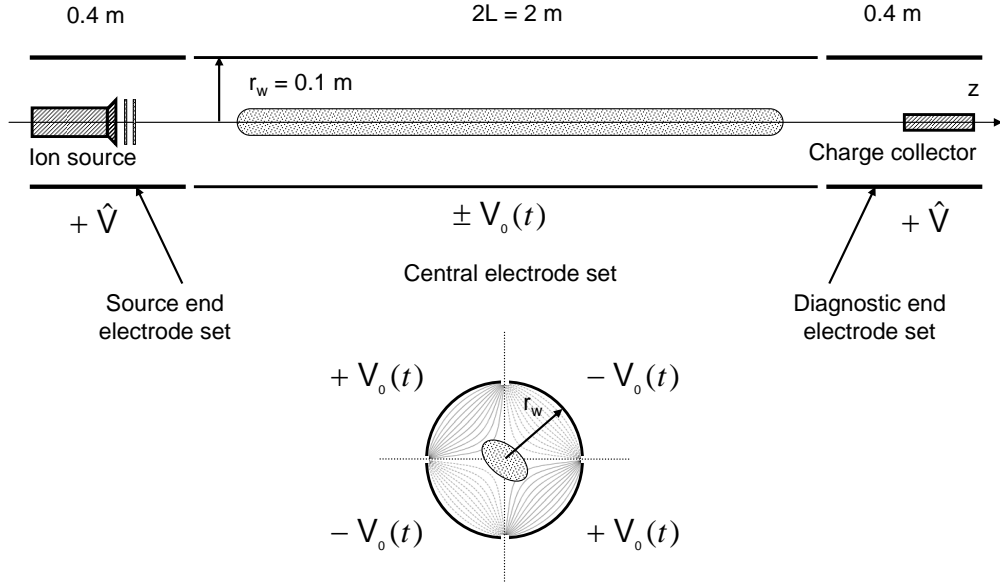
Figure 3.1: Schematic diagram of the PTSX device showing the quadrupole electrodes, cesium ion source, and charge collector.

becomes an oscillating quadruple field near the trap axis. This quadrupole electric field exerts a ponderomotive force that confines the pure ion plasma radially. To trap the plasma axially, the two end electrodes are biased to a constant positive voltage $+\hat{V}$. The gold plating of the electrodes increases the surface conductivity so that small patches of charge do not build up on the surface and influence the behavior of the trapped plasma. Note that, to place the charge collector along the null of the quadrupole potential and to facilitate the laser-induced fluorescence (LIF) diagnostic set up (Sec. 3.4), the electrodes are installed after rotating 45° azimuthally from the configuration used in the theoretical analysis (compare Figs. 2.1 and 3.1). The aluminum rings and insulating spacers support the electrodes, and in-vacuum insulated wires are attached to each electrode surface using lead-free silver solder [Fig. 3.2(b)]. Adjustments of the set screws that move the ball-bearings on the
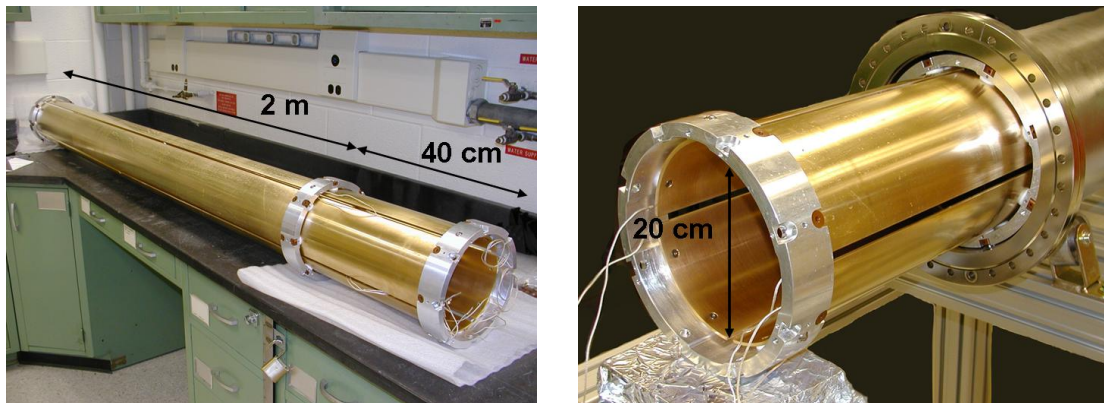
(a) Central and source end electrode sets.
(b) Diagnostic end electrode set.

Figure 3.2: The gold-plated stainless-steel electrodes are supported by the aluminum rings with teflon and vespel spacers.

aluminum rings with the use of a theodolite allow alignment of the center of the electrodes to within 1 mm.

The cesium ion source is located on the trap axis near the center of one of the short electrode sets so that ion injection is not affected by the fringe fields (Sec. 3.2). The charge collector is mounted on a linear motion feedthrough at the other end of the short electrode set, and moves in the transverse direction along a null of the applied potential in order to minimize the perturbation on the quadrupole potential configuration (Sec. 3.3). The construction of the PTSX device has been completed by Dr. Erik Gilson *et al.* in 2003 after a two-year construction period [GILSON *et al.*, 2003a,b], and initial experiments successfully demonstrated quiescent beam propagation over equivalent distances of tens of kilometers over a wide operating range [GILSON *et al.*, 2004].

3.1.1 Operation Principle

The PTSX device manipulates the plasma using an inject-trap-dump-rest cycle, and the one-component plasmas created in the trap are highly reproducible. The time duration of the injecting (t_i), trapping (t_t), dumping (t_d), and resting (t_r) phases can be varied independently, and the total cycle time is $t_{\text{cycle}} = t_i + t_t + t_d + t_r$. For the applied voltage waveform, a sinusoidal waveform $V_0(t) = \hat{V}_0 \sin(2\pi f_0 t)$ is used.

(a) During injection, the short electrodes on the source end (injection electrodes) are made to oscillate with the same voltage waveform, $\pm V_0(t)$, as the central electrodes, which allows the ions to stream into the trap [Fig. 3.3(a)]. Because ions are injected from the ion source with a circular, stationary cross section into a transverse focusing system in which the matched state has a pulsating elliptical beam envelope, the injected plasma column is always somewhat mismatched to the alternating-gradient (AG) focusing lattice (see Figs. 1.1 and 2.2). This type of mismatch is inherent and unavoidable with the ion source as presently configured. We can minimize this injection mismatch by setting $r_s \sim \sqrt{2} R_b$, where r_s is the radius of the emission surface and R_b is the rms radius of the matched beam.

(b) The short electrodes on the diagnostic end (dump electrodes) are biased to a DC voltage $+\hat{V}$ so that the ions bounce off the potential barrier. In order to minimize the number of ions present in the vicinity of the injection electrodes when the electrodes are switched to their static trapping voltage $+\hat{V}$, the time duration of injecting (t_i) is kept less than the axial bounce time (τ_b) and ion injection is stopped at a short time Δt_i before the end of the injecting stage [Fig. 3.3(b)]. Although, the ion source is operated in a steady-state manner, ion injection can be controlled by adjusting the bias voltage on the emission surface (V_s). Hence, to stop the ion emission, V_s is switched to a negative bias voltage. Possible two-stream interactions
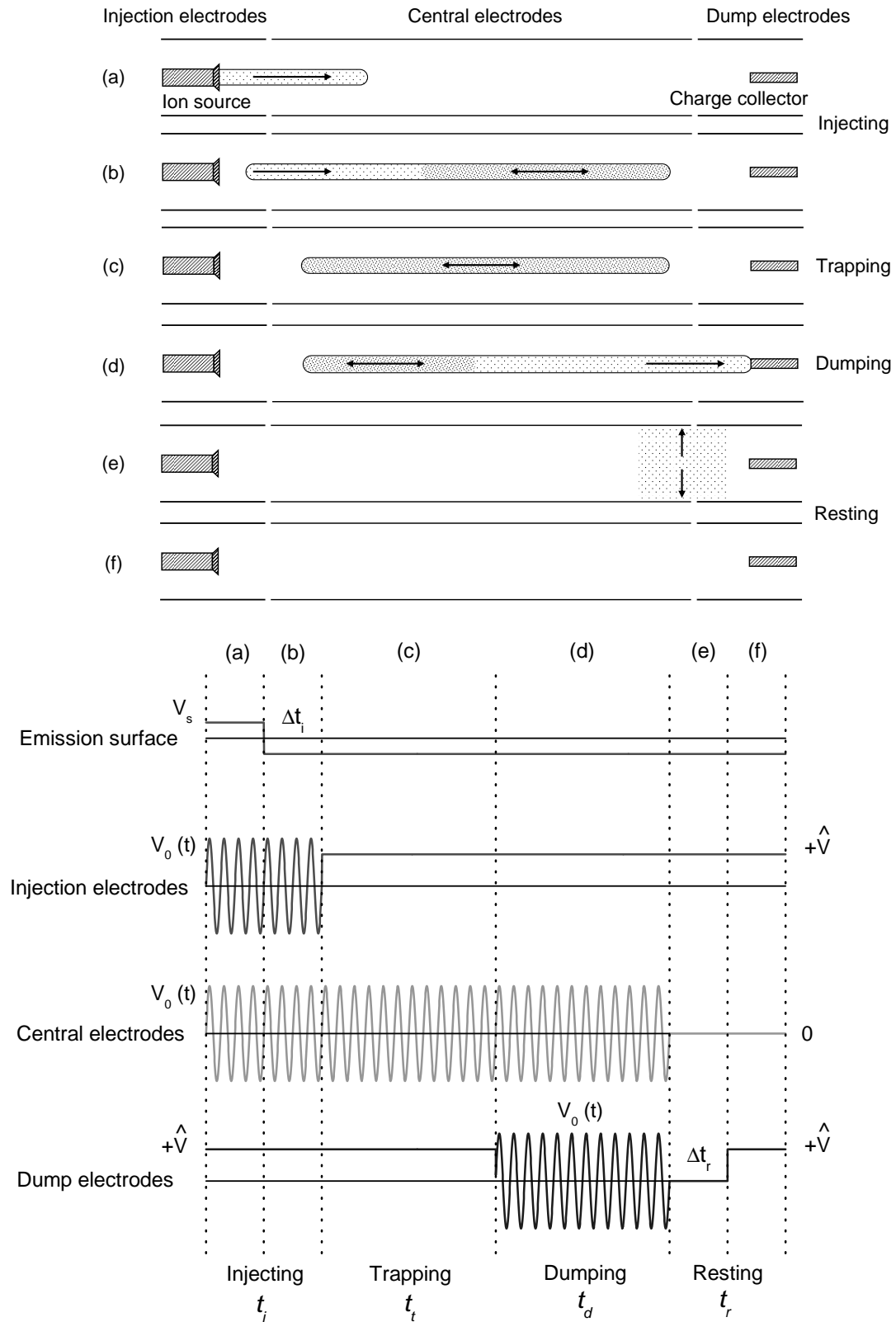
Figure 3.3: Operation sequence of the PTSX. The shaded regions in the plasma columns indicate the overlapping of two counter-streaming beams.

from the overlapping of two counter-streaming beams are estimated to be weak for the nominal injection conditions in PTSX (**Appendix B**).

(c) After injection is finished, the plasma is allowed to relax for several bounce periods so that the residual mismatch oscillation is damped away. The time duration of trapping (t_t) is $t_t \lesssim 300$ ms to prevent collisional effects from playing a significant role. Due to axial potential leak from the end electrodes to the central electrodes, the plasma length L_p is less than the trap length $2L$ [Fig. 3.3(c)]. The characteristic parameters of the typical trapped plasma in PTSX are summarized in Table 3.1.

(d) The charge collector is a destructive diagnostic that requires dumping the plasma out of the trap each cycle. During dumping, the dump electrodes are made to oscillate with the same voltage waveform as the central electrodes, which allows the ions to stream out of the trap through the axial drift motion [Fig. 3.3(d)]. Due to the finite axial beam velocity, the collected charge signal is effectively averaged over dozens of oscillation periods $T = 1/f_0$. The reproducibility of this process allows us to construct a radial charge profile out of multiple measurements at different radial positions of the collector for each shot. In addition, by trapping the plasma with different time durations, the time evolution of the trapped plasma properties can also be measured. No bias voltage is applied to the collector plate, otherwise ion motion will be affected by the position of the charge collector. The time duration of dumping (t_d) should be longer than the axial bounce time (τ_b), and is normally set to $t_d \geq 15$ ms to make sure the trap becomes empty. In the dumping stage, the inherent beam mismatch is present when the charge bunch with line density $N/2$ is separated from the initially matched beam with line density N. The degree of beam mismatch can be given by $\mu = R_{bi}/R_{bf} \approx (1 + \delta_b)/(1 + \delta_b/2)$. Here, $R_{bi(f)}$ is the initial (final) rms beam radius, and δ_b is the thermal beam intensity parameter introduced in **Chapter**

Quantity	Symbol	Characteristic value
Background gas pressure	P	5×10^{-9} Torr
Applied AC focusing voltage	$\hat{V}_0$	150.4 V
Applied DC bias voltage	$\hat{V}$	36 V
Applied magnetic field	B_0	0 G
Plasma length	L_p	170 cm
Plasma rms radius	R_b	0.85 cm
Debye length (on-axis)	λ_D	0.88 cm
Plasma density (on-axis)	$\hat{n}$	0.89×10^5 ions/cm^3
Plasma line density	N	1.6×10^5 ions/cm
Plasma parameter	N_D	2.6×10^5 ions
Applied AC focusing frequency	f_0	60 kHz
Smooth-focusing frequency	$\omega_q/2\pi$	8.4 kHz
Plasma frequency (on-axis)	$\hat{\omega}_p/2\pi$	5.4 kHz
Breathing mode frequency	$\omega_B/2\pi$	15.8 kHz
Quadrupole mode frequency	$\omega_Q/2\pi$	15.3 kHz
Ion-neutral collision time	τ_{in}	$\gtrsim 2.0$ sec
Ion-ion collision time	τ_{ii}	$\gtrsim 0.5$ sec
Axial bounce time	τ_b	1.9 msec
Axial beam energy	E_b	3 eV
Axial beam current	I_b	5.4 nA
Axial beam velocity	v_b	2.09×10^3 m/s
Ion thermal velocity	v_t	0.27×10^3 m/s
Ion temperature	T_i	0.1 eV
Space-charge potential	$\phi^s(0) - \phi^s(r_w)$	0.13 V

Table 3.1: Characteristic parameters of the PTSX pure ion plasma. The plasma parameter N_D is the number of particles in a Debye sphere [CHEN, 1984].

2. For the case of moderately low space-charge density beams ($\hat{s} = 0.2 \sim 0.3$), it is estimated that $\mu \lesssim 10\%$ and the matched beam profile is projected onto the charge collector without significant perturbation.

(e) Two resting stages are added at the end of the dumping stage to prepare a new cycle. Even though most of the ions have streamed out of the trap during the dumping process, it is observed that there remains a small number of residual ions with extremely low axial velocity. These residual ions are negligible in contributing a radial charge profile. However, to get rid of any possible accumulated effect of these ions, we switch the voltages of the central and dump electrodes to ground for the time duration Δt_r. The residual ion cloud in the trap will expand toward the grounded electrodes at the thermal speed v_t, and will be neutralized at the room-temperature electrode surfaces [Fig. 3.3(e)]. Normally, we set $\Delta t_r = 5$ ms, which is much longer than the characteristic expansion time $r_w/v_t \sim 0.4$ ms.

(f) Finally, we switch the voltage of the dump electrodes from ground to $+\hat{V}$ and make the system ready for the new cycle [Fig. 3.3(f)]. The time duration of resting (t_r) can be arbitrarily chosen for $t_r > \Delta t_r$, and is used to set the total cycle time t_{cycle} to a desired value.

Detailed analysis and further discussion of the injection process outlined here are presented in **Chapter 4** of this thesis.

3.1.2 Vacuum System

The PTSX vacuum chamber is approximately 134.5 in. in overall length, and consists mainly of a 10 in. O.D. electropolished stainless-steel chamber with Conflat (CF) metal-seal flanges (Fig. 3.4). The aluminum rings with teflon and vespel insulating spacers support the electrodes while keeping them electrically isolated from
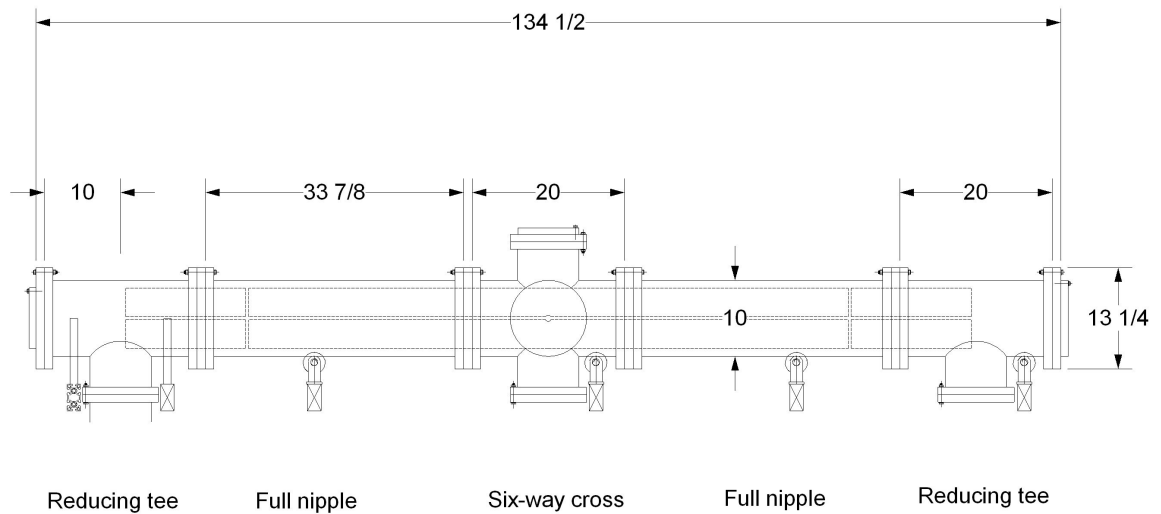
Figure 3.4: Schematic drawing of the PTSX vacuum flanges. Electrodes inside the flanges are indicated by the dashed lines. All dimensions are in inches.
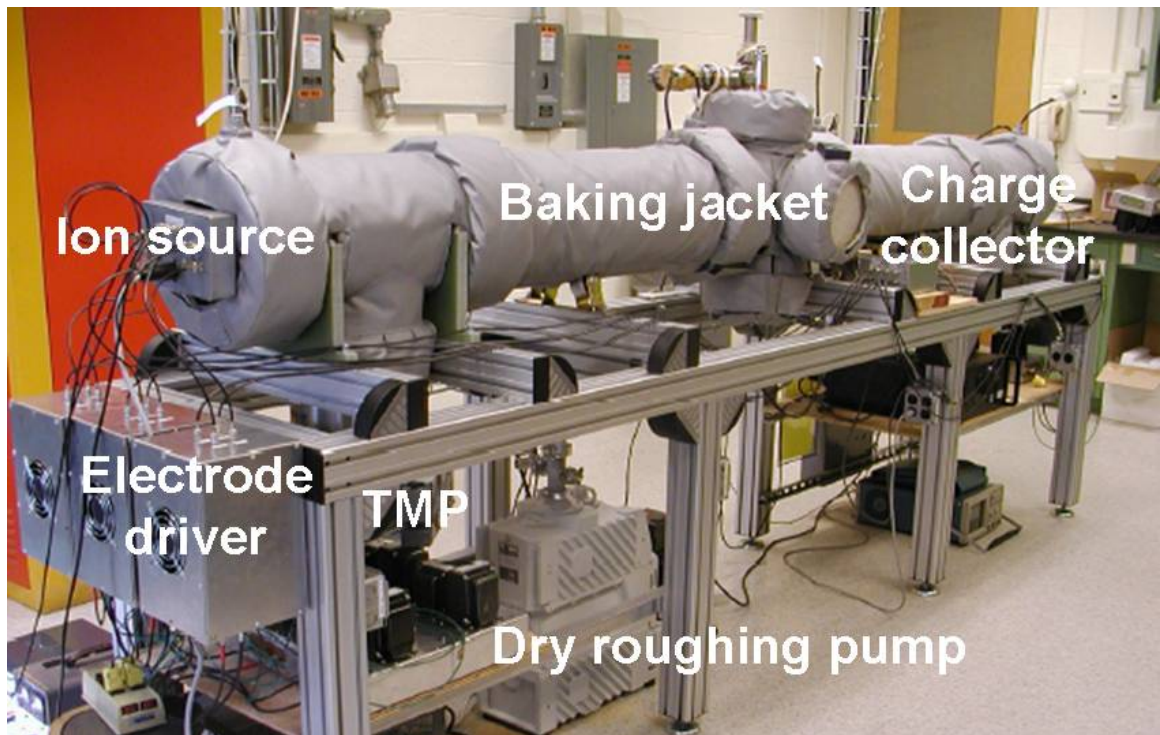
Figure 3.5: Photograph of the PTSX device.
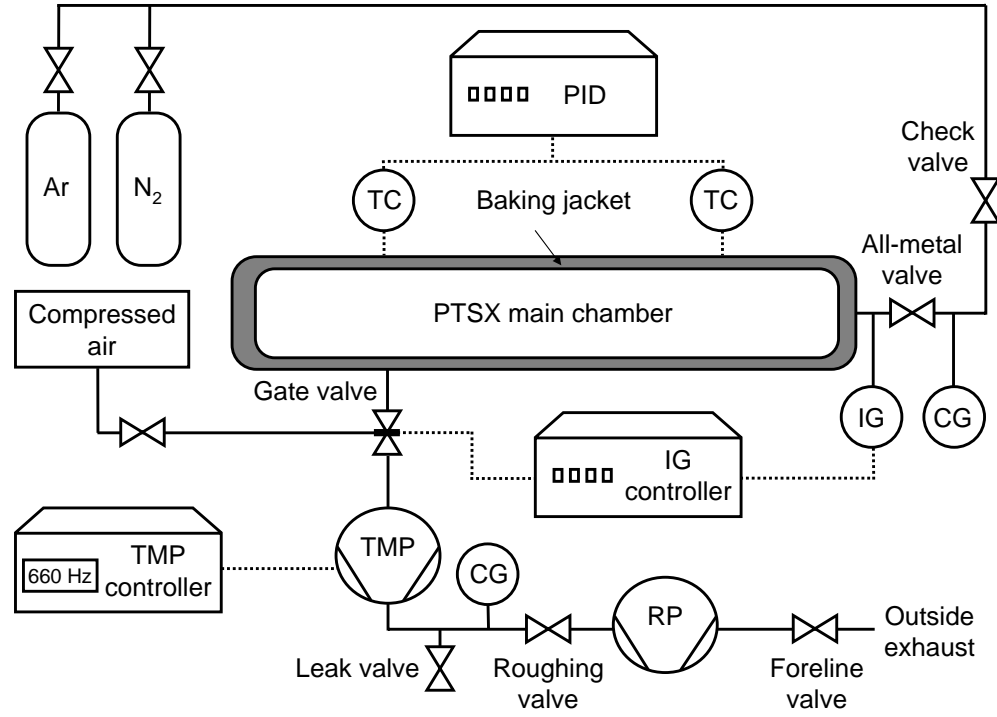
Figure 3.6: Schematic diagram of the PTSX vacuum system. Solid lines represent the flow of gas, while dotted lines represent the electrical signals.

the vacuum chamber. A centrally-located, six-way cross accommodates the laser-induced fluorescence (LIF) diagnostic described later in this chapter. The chamber is enclosed by custom-made baking jacket (Fig. 3.5) whose temperature is monitored by two thermocouples (TC) and adjusted by proportional-integral-derivative (PID) controllers. Considering the permissible temperature ranges of the lead-free solder ($\lesssim 220$ °C) and insulating spacers ($\lesssim 260$ °C) used inside the vacuum chamber, the maximum baking temperature is set to be 200 °C. The PTSX device is evacuated using a turbomolecular pump (TMP) with a pumping speed of 1000 ℓ/sec, which is backed by an oil-free (dry) scroll-type roughing pump (RP) with a pumping speed of 600 ℓ/min. The maximum forevacuum pressure of the TMP is 10 Torr, and the

ultimate pressure is 7.5×10^{-11} Torr. The pumping utilizes a "T" section near the injection electrodes in order to permit good axial access to the device. Changes in operating pressure are measured with a nude ionization gauge (IG) near the dump electrodes. As shown in Fig. 3.6, the foreline and vent pressures (mostly from Ar) are measured by convectron gauges (CG). In order to prevent neutral collisions from affecting the plasma behavior, the base pressure of PTSX is kept below 5×10^{-9} Torr after a week-long bake at 200 °C. When the ion source is on, the operating pressure rises up to $10^{-8} \sim 10^{-7}$ Torr. Even in this case, the characteristic ion-neutral collision time is $\tau_{in} \gtrsim 2$ sec, and the trapped plasma is collisionless to very good approximation.

3.1.3 Electrode Control System

To apply the oscillatory voltage $\pm V_0(t)$, a National Instruments 5411 Arbitrary Function Generator Card (NI PCI-5411) with a 20 MHz clock rate and a 2 M-sample, 16-bit waveform memory is used. This PCI card has a single analog output connector whose voltage levels are ± 5 V with 12-bit resolution for nominal 50 Ω load termination. The memory architecture of the card imposes certain restrictions on the waveform size and resolution. The minimum size of a single waveform is 256 samples and the number of samples must be divisible by 8. For a 20 MHz clock rate, the time resolution becomes $\Delta t = 1/(20 \text{ MHz}) = 50$ nsec. These requirements adjust the actual frequency of a single waveform according to

$$\frac{n_1}{f_0 + \Delta f} = \{256 + 8(n_2 - 1)\} \Delta t, \tag{3.1}$$

where f_0 is original desired frequency, $f_0 + \Delta f$ is adjusted frequency, and n_1 and n_2 are positive integers that minimize $|\Delta f|$. For example, if we set $f_0 = 60$ kHz, then
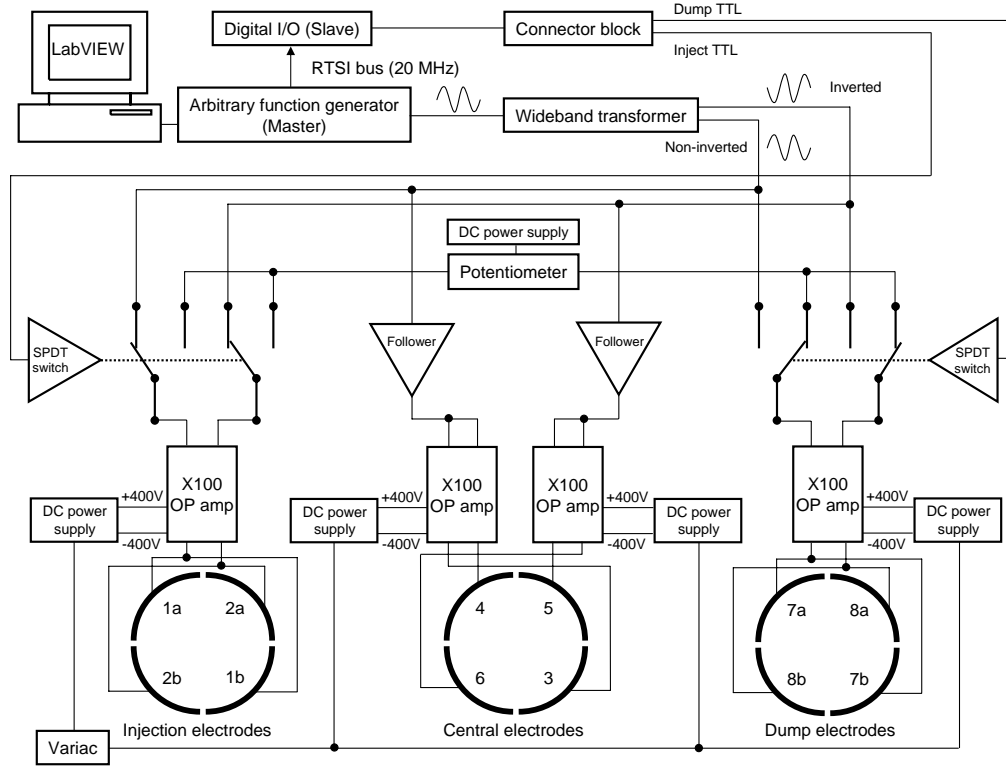
Figure 3.7: Schematic diagram of the PTSX electrode control system.

from Eq. (3.1), $n_1 = 1$, $n_2 = 11$, and the final frequency is adjusted to $f_0 + \Delta f = 59.5238$ kHz. Such a slight adjustment in frequency is not noticeable for most of the PTSX experiments, except for the aliasing pattern in the on-axis density oscillation presented in **Chapter 4** of this thesis. By looping a single waveform many times and linking different waveforms together, a long arbitrary waveform is generated to simulate a wide variety of periodic-focusing quadrupole lattice patterns.

To create the train of TTL (Transistor-Transistor Logic) pulses that controls the timing of the injecting, trapping, and dumping of the plasma, a National Instruments 6534 Digital I/O Card (NI PCI-6534) is used. We use 3 channels of the PCI card that switch on and off the bias voltages of the injection electrodes, dump electrodes, and emission surface. The output of each channel is either 5 V for "On", or 0 V for "Off".

For example, an "On" signal (5 V) switches the voltages of the short electrodes from $\pm V_0(t)$ to a DC bias $+\hat{V}$, and essentially closes the trap so that no ions can pass through. On the other hand, an "Off" signal (0 V) switches the voltages from $+\hat{V}$ to $\pm V_0(t)$, allowing ions to pass through the short electrodes.

To prevent an unwanted phase delay between the waveform from the NI PCI-5411 and the TTL pattern from the NI PCI-6534, the two cards are made to have the same clock rate (20 MHz). Moreover, to ensure synchronization, a marker pulse is added to the very beginning of the first waveform of the NI PCI-5411. This marker pulse is used to initially trigger the NI PCI-6534 via the RTSI (Real-Time System Integration) bus line to start the TTL pattern generation.

As illustrated in Fig 3.7, the waveform signal from the arbitrary function generator is split into $+V_0(t)$ and $-V_0(t)$ by a pair of unbalanced wideband transformers and these signals are sent to a set of solid-state SPDT (Single Pole Double Throw) switches. Based on the TTL pattern from the digital I/O card, the switches allow the end electrodes to receive either the DC voltage $+\hat{V}$ for trapping, or $\pm V_0(t)$ for injecting and dumping the plasma. The amplitude of the DC voltage $+\hat{V}$ is adjusted by a potentiometer from 36 to 150 V. The central electrodes always have a voltage waveform $\pm V_0(t)$, but can be biased to ground by setting $|V_0(t)|_{\max} \equiv \hat{V}_0 = 0$ V. To compensate for the phase difference between the central and end electrode signals due to the SPDT switches, two voltage followers are inserted for the central electrode waveform $\pm V_0(t)$.

The signals are then sent to high-voltage operational amplifiers (Apex Microtechnology PA94) with ± 400 V supply voltages (Fig. 3.8). The system can apply signals up to $\hat{V}_0 = 400$ V and $f_0 = 100$ kHz to the electrodes. These limits are set by the supply voltage limit, 100 mA continuous output current limit, and the frequency
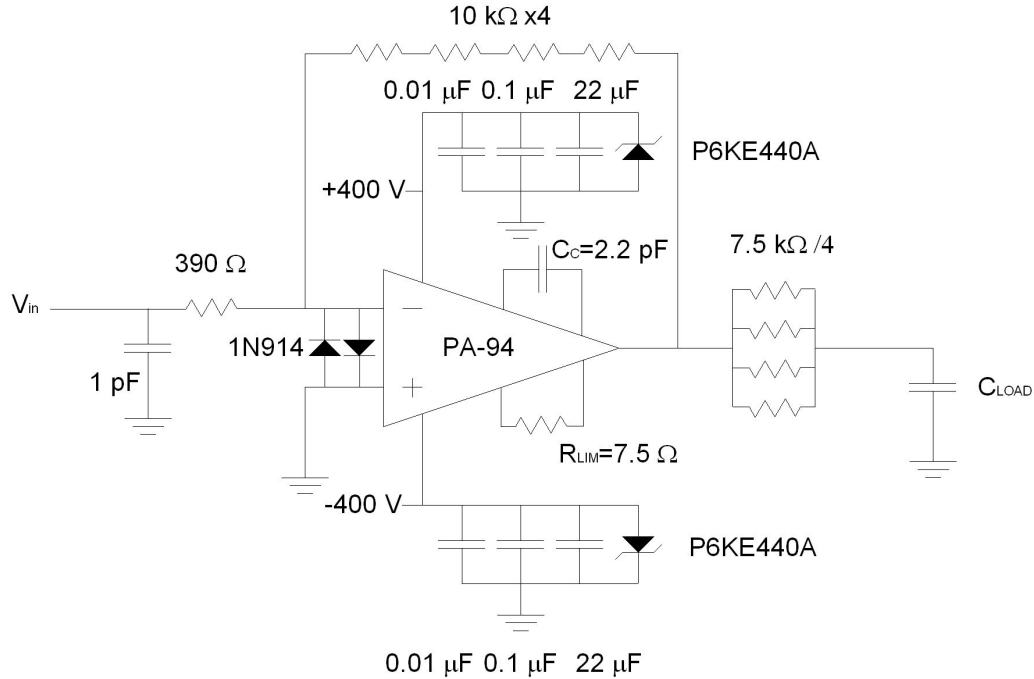
Figure 3.8: Schematic circuit diagram of the PTSX electrode driver [GILSON, 2008].

bandwidth of the operational amplifiers. To eliminate high-frequency noise on the voltage input V_{in}, an input bypass capacitor has been added, setting the 3dB point of the low-pass filter at $f_{3dB} \approx 400$ kHz. The voltage gain of this inverting amplifier is $-V_{out}/V_{in} \approx 100$. To ensure stable operation of the amplifier at such a high gain, a compensation capacitor C_C of 2.2 pF and a current limit resistor R_{LIM} of 7.5 Ω are added. For overvoltage protection, general-purpose 1N914 diodes are used on the input voltages and unidirectional zener diodes are used in the supply voltages. Each electrode of the PTSX device represents a capacitive load and draws increasing current at higher frequencies. The capacitances of the long and short electrode sectors are measured to be ~ 270 pF and ~ 90 pF, respectively [GILSON *et al.*, 2003a]. These capacitances are measured by a simple capacitive voltage divider with respect to ground. To achieve stability in driving purely capacitive loads, a load resistance of

1.875 kΩ is added on the voltage output, making the load not purely capacitive, and all the BNC cables ($\sim$ 30.5 pF/ft) which deliver voltage signals to the electrodes are made to have the same lengths. A variac transformer optimizes the performance of the electrode drivers by adjusting the AC input voltages of the DC power supplies. Even though a heatsink, a thermal washer, and a cooling fan maintain the temperature of the system properly, the extra heat produced by high-voltage and high-speed operation occasionally damages the operational amplifier (on the average once a year for 8 copies of the electrode driver).

3.2 Cesium Ion Source

Cesium ions (Cs^+) were used in the initial phase of the PTSX experiment because of cesium's large mass (133 amu) and the commercial availability of sources. The ion source consists of a 0.6 in. diameter aluminosilicate cesium emitter (Heatwave Labs TB-118) surrounded by a Pierce electrode, followed by an acceleration grid and a deceleration grid (Fig. 3.9). This triode grid system has flexibility to change the extraction field strength without changing the beam energy. Cesium is melted into the emitter surface, which is an extremely porous tungsten disc welded to the molybdenum heater body. When the emitter surface is heated, cesium is ionized through contact ionization with tungsten which has a high work function ($\sim$ 4.55 eV). The heater is a non-inductively wound coil of molybdenum wire solidly potted into the molybdenum body with high purity alumina (Al_2O_3). A DC power supply is connected to the heater, keeping the source temperature 900 $\sim$ 1200 °C with 7 $\sim$ 13 A of applied current. The thermionic electron emission from the emission surface is

negligible. In any event, electrons cannot be confined in PTSX due to their small mass.

The Pierce electrode is made of copper and has a 67.5° opening angle to compensate for possible beam divergence due to space-charge forces [PIERCE, 1940]. Because the ion beam energy is relatively low in the PTSX experiment, 85% transparent electroformed copper meshes have been used for the fabrication of the acceleration and deceleration grids. To avoid the possible formation of a virtual cathode (i.e., an axial potential structure generated by space charge), we set the distance between the emission surface and acceleration grid (d_1) to be larger than the distance between the acceleration and deceleration grids (d_2), i.e., $d_1 > d_2$ [HUMPHRIES, 1990]. While the two grids and the Pierce electrode are electrically insulated using machinable ceramic spacers, the emission surface is biased with the voltage of the Pierce electrode. The amount of charge injected can be controlled easily by adjusting the voltages on the emitter surface (V_s), acceleration grid (V_a), and deceleration grid (V_d) of the ion source. Normally, we set $V_s > V_a > V_d \geq 0$ V to minimize the effects of virtual cathode. The voltage difference between the emitter surface and the acceleration grid determines the extraction voltage $V_e = V_s - V_a$, and the voltage difference between the emitter surface and the deceleration grid adjusts the axial beam velocity $v_b = \sqrt{2q(V_s - V_d)/m}$.

In Fig. 3.10, we present the axial beam current $I_b = qNv_b$ measured by allowing the ion to stream directly from the source to the large copper plate at the diagnostic end electrodes for different values of extraction voltage V_e. For the case of space-charge-limited flow [DAVIDSON, 1990; GOLDSTON and RUTHERFORD, 1995], it is expected that $I_b \approx I_{CL}$ from current density conservation. Here, the Child-Langmuir current I_{CL} is estimated by $I_{CL} \approx (4\epsilon_0/9d_1^2)(2q/m)^{1/2}V_e^{3/2} \times \pi r_s^2 \times (0.85)^2$, where r_s

(a) Aluminosilicate cesium ion source.

(b) Pierce electrode.

(c) Acceleration (or deceleration) grid.

(d) Ion source assembly.

Figure 3.9: Photographs of the cesium ion source.
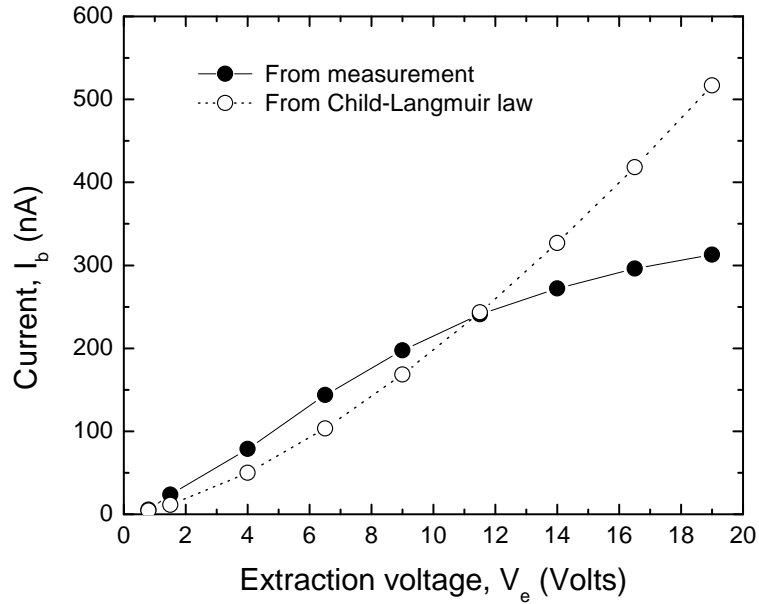
Figure 3.10: The current extracted from the source actually collected on the large copper plate at the diagnostic end electrodes (solid circles) and estimated from the Child-Langmuir law (open circles).

is the radius of the emission surface, and $(0.85)^2$ term represents transparency of the grids. Figure 3.10 shows, however, that I_b depends linearly on V_e rather than the $V_e^{3/2}$ scaling of the Child-Langmuir law for $V_e \lesssim 10$ V. On the other hand when $V_e \gtrsim 10$ V, I_b is saturated and becomes much smaller than I_{CL}. Despite the departure from the Child-Langmuir law, this control allows us to fill the trap with a wide range of ion densities.

3.3 Radially Scanning Charge Collector

3.3.1 Mechanical Description

The primary diagnostic on PTSX is a radially scanning charge collector on the dumping end of the device. The charge collector is mounted on a linear motion feedthrough

with a 6-in. stroke that allows the assembly to go from 2 in. beyond the device center
to being completely withdrawn from the trap. The original charge collector was based
on a commercially-available Faraday cup that consists of a stack of three 0.75-in. by
1.5-in. plates that support the cup and has small apertures. In order to reduce the
effect of stray charge striking the edges of these plates and confounding the measure-
ments, the assembly was enclosed in a copper box that measured 1 in. across by 3
in. tall, and was not symmetrically placed about the collection aperture. This results
in a boundary condition for the electric potential that varies as the Faraday cup is
moved, and this is evidenced in the data as an offset in the position of the peak charge
density. To assure a boundary condition that is independent of the position of the
Faraday cup, a slotted 8-in. diameter copper disk is placed in front of the Faraday
cup. Although this eliminates the dependence of the measurement on the position of
the Faraday cup, the dumped plasma now broadens significantly as it approaches the
diagnostic. The time-dependent oscillating voltage that normally confines the plasma
radially, gradually becomes a constant axial field in the vicinity of the copper disk,
and there is no longer a transverse confining field.

The original Faraday cup has been replaced by a charge collector with a simpler
design on PTSX [GILSON *et al.*, 2005]. Figure 3.11(a) shows a schematic of the final
charge collector, and Figs. 3.11(b) and (c) show photographs of the final collector in
place in PTSX. The 5 mm diameter head of a copper nail now serves as the collection
surface. A coaxial wire is connected to the body of the nail, and the wire and nail
are inserted into a thin, alumina rod that insulates the collector from the conductive
support rod. The ceramic rod, in turn, is inserted into a 3/16 in. diameter, stainless
steel support rod. The base of this rod is clamped into a block that sits atop the
arm of the linear motion feedthrough. Thus, the collection surface sits approximately
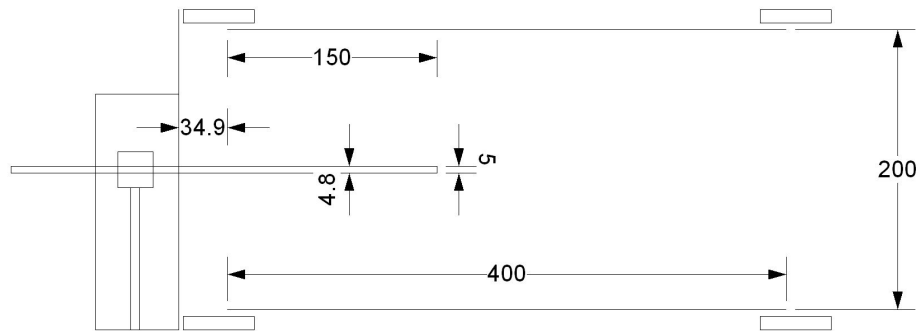
(a) The charge collector plate is placed transversely at a null of the applied quadrupole potential and axially away from the the fringe fields. All dimensions are in mm.
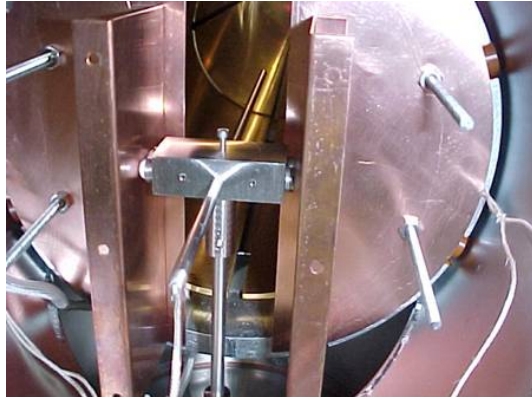
(b) The charge collector is guided in the horizontal direction by a pair of copper plates attached to a slotted copper disk at the end of the PTSX device.

(c) The 5 mm diameter head of a copper nail serves as the collection plate.

Figure 3.11: Schematic drawing and photographs of the charge collector.

halfway into the dumping electrodes, thereby avoiding fringe fields. Since this thin support rod is grounded and moves in a null of the fully time-dependent voltage, the charge collector has a minimum impact on the potential structure within the dumping electrodes. Measurements show that the radial charge profile no longer exhibits the broadening associated with the equipotential copper disk used previously, and the profile is well-centered. Moreover, because of the low axial kinetic energy of the ions, there is no need for an additional structure to suppress secondary electron emission.

3.3.2 Model 6514 Electrometer

The Model 6514 electrometer [KEITHLEY, 1998] makes charge measurements with 10 fC resolution. In the electrometer, an accurately known capacitor is placed in the feedback loop of the amplifier so that the voltage developed is proportional to the charge, which is the integral of the input current. The voltage is then scaled and displayed digitally as charge. The integration time of the A/D converter affects the amount of reading noise, as well as the ultimate reading rate of the charge measurement [KEITHLEY, 1998]. The integration time is specified in terms of the number of power line cycles (PLC), where 1 PLC for 60 Hz is 16.67 ms. If the A/D converter integrates for an amount of time equal to an integer number of 1 PLC, then the signal components from the power line noise, which tend to be periodic, can be cancelled. In the PTSX device, charge measurement is optimized for a 6 PLC reading rate which corresponds to a 100 ms integration time. In addition, to reduce the periodic noise from the AC/DC switching of the end electrodes, the cycle time t_{cycle} is set to be a divisor of the integration time. Figure 3.12 indicates that setting t_{cycle} to be a divisor of the integration time averages out coupling from the electrodes and makes background signal less noisy.
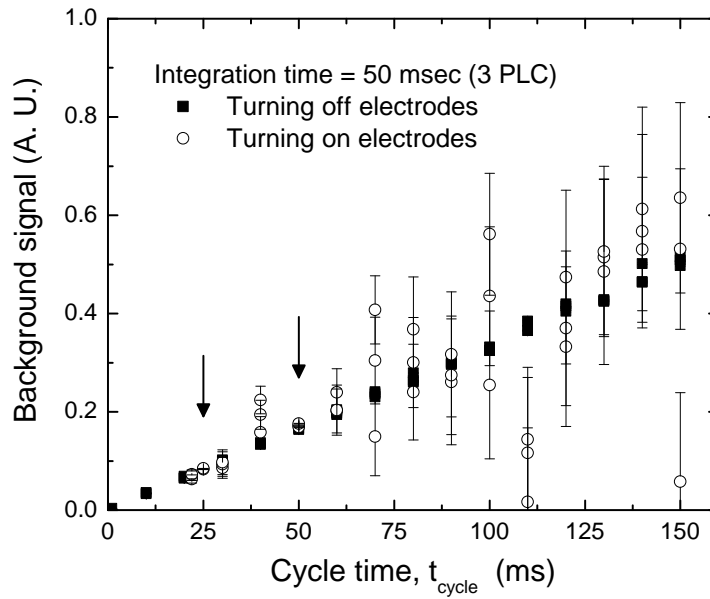
(a) Integration time = 50 msec (3 PLC).
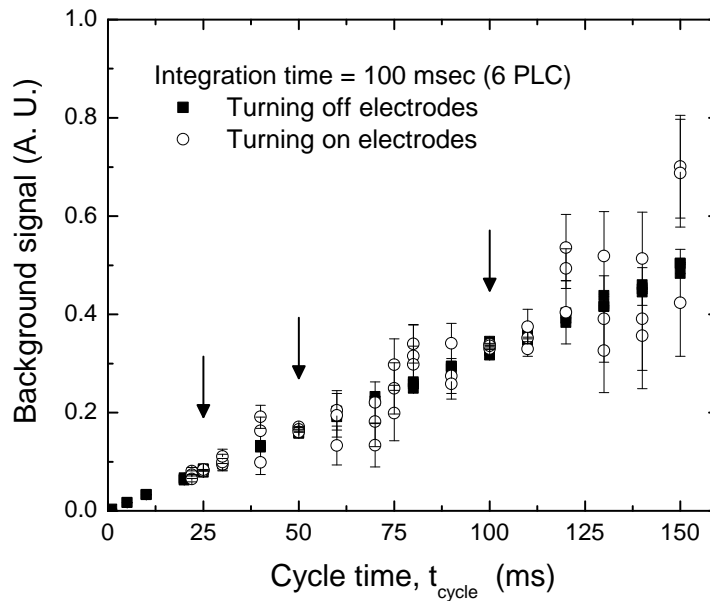
(b) Integration time = 100 msec (6 PLC).

Figure 3.12:   The background signal measured without trapped ions is linearly proportional to the cycle time of PTSX operation. When the electrodes are turned on, the background signal becomes noisy (open circles). Setting the cycle time to be a divisor of the integration time averages out coupling from the electrodes (indicated by arrows). Considering that the dumping time is $t_d \geq 15$ ms, the cycle time is usually set to be $t_{\text{cycle}} \geq 25$ ms.

In the charge measurement using the electrometer, the input offset current is usually very low. However, for low level charge measurements, as in the PTSX device, even this small offset current can generate a significant error factor after long-time integration. The typical input offset current in the Model 6514 electrometer is about 4 fA, which will cause the offset in the charge measurement Q_{offset} to be about 0.4 fC for $t_{cycle} = 100$ ms. Due to the temperature dependence of the input offset current and a number of other external current sources in the system, it is very difficult to determine the exact offset current of the entire system and subtract it from the actual reading. A general rule of thumb is to set $Q_{offset} \sim 1$ fC and cut off the charge measurement when $Q(r) < Q_{offset}$, allowing an additional uncertainty associated with subtracting the offset. Other unwanted currents can result from triboelectric effects, electrostatic interference, and magnetic fields. Triboelectric currents are generated by charges created between a conductor and an insulator due to friction [KEITHLEY, 2004]. In the PTSX device, insulated cable delivering collected charges inside the vacuum chamber creates some noise when subjected to expansion and contraction. One easy solution is to wait several seconds after moving the position of the charge collector. Electrostatic interference is recognizable when hand or body movements near the experiment cause erroneous or unstable readings. Magnetic fields from neighboring experiments can also introduce fluctuations in the readings. To minimize these two effects, the electrometer has been shielded with a grounded high permeability metal (so called μ-metal).

In calibrating the internal voltage offset of the electrometer, which drifts with time and temperature, we perform zero check and zero correction for every charge measurement. The zero check feature provides a mean for internal zero verification, and the zero correction feature corrects the internal offset so that the display reads

zero with no input signal. When turning on the zero check feature, the accumulated charges in the charge collector and the BNC cable dissipate through the 10 MΩ resistor. After turning off the zero check feature, a new measurement cycle begins. However, the residual charges remaining in the system often cause sudden changes in the charge reading (known as zero check hop). This effect gives rise to a nonlinear increase in charge in the initial phase of the measurement (see Fig. 3.13), which becomes significant particularly for low charge level. A convenient way to deal with this effect is to avoid the nonlinear regime by starting the charge measurement several seconds after the zero check. The measured charge signal is transferred to a LabVIEW program of PC in the ASCII data format through a GPIB interface. The Model 6514 electrometer can be used within one minute after it is turned on. However, it should be allowed to warm up for at least one hour to achieve optimum performance.

3.3.3 Radial Profile and Inferred Quantities

If the true density profile $n(r')$ is uniform in the z direction and axisymmetric in the smooth-focusing approximation, the total charge collected per cycle $Q(r)$ by the collector plate centered at radius r can be related to $n(r')$ as

$$Q(r) = qL_p \int_0^{r_c} \rho d\rho \int_0^{2\pi} d\theta n(r'), \tag{3.2}$$

where $r' = (r^2 + \rho^2 - 2r\rho\cos\theta)^{1/2}$ is the local radius, r_c is the size of the circular collecting plate, and L_p is the plasma length, which can be estimated either from numerical simulations or the analytical formula for the axial potential distribution (see **Appendix A**). To increase the collected charge signal out of a low beam current density, the size of the charge collector has been chosen to be $r_c = 2.5$ mm, which is much larger than the opening of the commercial Faraday cup ($r_c \lesssim 0.5$ mm). By

noting that the typical density profile in the PTSX device is close to Gaussian, we obtain

$$n(\bar{r}) \approx \frac{Q(r)/q}{\pi r_c^2 L_p},$$
(3.3)

where for $r \lesssim r_c$, $\bar{r} \approx [r^2 + r_c^2/2]^{1/2}$, and for $r > r_c$, $\bar{r} \approx r\,[1 + O(r_c^2/r^2)]$. The exact on-axis density $\hat{n} = n(r = 0)$ can be approximately determined by extrapolation from the two nearest data points to $r = 0$.

The mean-square radius of the trapped plasma column can be calculated from either $n(r)$ or $Q(r)$ according to

$$R_b^2 = \left\langle r^2 \right\rangle = \frac{1}{N} \int_0^{r_w} dr 2\pi r r^2 n(r) \approx \frac{1}{Q_b} \int_0^{r_w} dr 2\pi r r^2 Q(r),$$
(3.4)

where $N = 2\pi \int_0^{r_w} dr r n(r)$ is the line density, and $Q_b = 2\pi \int_0^{r_w} dr r Q(r)$ is the total charge in the trap for one cycle. The integrals are evaluated numerically using the Simpson rule with relative errors of order $(\delta r_i/R_b)^5$, where δr_i is the radial spacing between measurements, which is typically 2.54 mm. Since the collected charge is necessarily averaged over many focusing periods, the values of R_b calculated from Eq. (3.4) can be interpreted as the rms radius of the beam in the smooth-focusing approximation. The effective transverse temperature $\bar{T}_\perp$ of the ions is inferred from global force balance equation as [DAVIDSON and QIN, 2001]

$$\bar{T}_\perp = \frac{1}{2} \left[m\omega_q^2 R_b^2 - \frac{Nq^2}{4\pi\epsilon_0} \right].$$
(3.5)

This temperature is a measure of the average (random) kinetic energy of the beam particles in the smooth-focusing equilibrium. For a matched beam in thermal equilibrium, $\bar{T}_\perp$ is approximately equal to the thermal temperature of the ion source, i.e., $\bar{T}_\perp \approx T_s$. Furthermore, the average transverse emittance in the beam frame can be estimated as

$$\epsilon \approx 2R_b \left(\frac{2\bar{T}_\perp}{m} \right)^{1/2}.$$
(3.6)
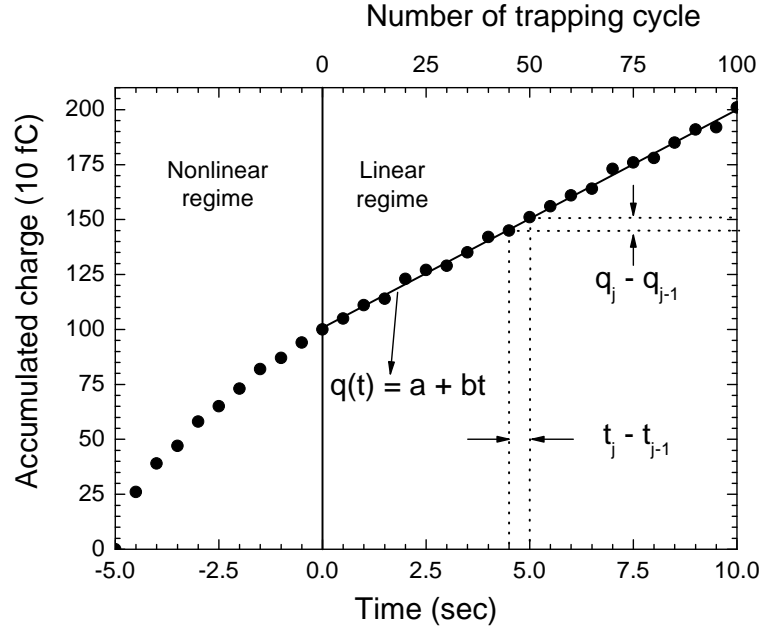
Figure 3.13:   Illustrative example of repeated charge measurement. The resolution of the accumulated charge measurement is 10 fC, which is set by the electrometer. We wait for 5 sec (or more, if necessary) and collect data only in the linear regime for 10 sec, which corresponds to 100 trapping cycles for $t_{\text{cycle}} = 100$ ms. Due to the finite speed of the GPIB communication between the electrometer and the LabVIEW interface, the total number of data readout N_t is about 20 out of 100 cycles.

3.3.4   Data Reduction and Error Analysis

Since the charge collected during one cycle time t_{cycle} is usually quite small ($\lesssim 1$ pC), we make repeated measurements to improve the resolution and reduce the uncertainty in obtaining the charge per cycle. For a given radius, we record the accumulation of charge as a discrete function of time, (t_j, q_j), for $j = 0, 1, \cdots, N_t - 1$ (see Fig. 3.13). Here, N_t is the total number of data readout, and the period of one data readout is $\Delta t_j = t_j - t_{j-1}$. If the charge is measured exactly, then its accumulation becomes a linear function of time. Therefore, we use a linear function, $q(t) = a + bt$, to apply a

least-squares fit, which allows us to calculate the charge per cycle Q as

$$
\begin{aligned}
Q &= \frac{1}{N_t - 1} \times \sum_{j=1}^{N_t-1} \{q_j - q_{j-1}\} \times \frac{t_{\text{cycle}}}{\Delta t_j} \\
&\approx \frac{1}{N_t - 1} \times \sum_{j=1}^{N_t-1} \{(a + bt_j) - (a + bt_{j-1})\} \times \frac{t_{\text{cycle}}}{\Delta t_j} \\
&= b \times t_{\text{cycle}}.
\end{aligned}
\tag{3.7}
$$

The total charge accumulation time $(t_{N_t-1} - t_0)$ is usually 10 sec in PTSX operation. The instrumental uncertainty associated with each measurement j can be estimated as

$$
\sigma^2 \simeq \frac{1}{N_t - 2} \sum_{j=0}^{N_t-1} \{q_j - (a + bt_j)\}^2,
\tag{3.8}
$$

which does not change with N_t. Moreover, from the formula for propagation of errors [BEVINGTON and ROBINSON, 1992], the uncertainty in determining the charge per cycle Q is estimated as

$$
\sigma_Q^2 \simeq \frac{1}{(N_t - 1)^2} \sum_{j=1}^{N_t-1} (\sigma^2 + \sigma^2) \times \left(\frac{t_{\text{cycle}}}{\Delta t_j}\right)^2,
\tag{3.9}
$$

which is the standard error of the true mean. Note that the uncertainty σ_Q decreases as N_t is increased.

The charge per cycle is sampled at discrete radial positions r_i with uncertainty $\sigma_Q(r = r_i) = \sigma_i$. For the purpose of estimating errors in the inferred quantities from the charge measurements, it is most straightforward to approximate the integral by a simple summation as

$$
Q_b \approx \sum_{i=1}^{i_{\text{max}}} (Q_i - Q_{\text{offset}}) 2\pi r_i \delta r_i,
\tag{3.10}
$$

$$
R_b^2 \approx \frac{1}{Q_b} \sum_{i=1}^{i_{\text{max}}} r_i^2 (Q_i - Q_{\text{offset}}) 2\pi r_i \delta r_i,
\tag{3.11}
$$

where $Q_i = Q(r = r_i)$, $\delta r_i = r_i - r_{i-1}$, and i_{max} is the maximum radial index satisfying $Q_i \geq Q_{\text{offset}}$. As mentioned earlier, the offset originates from the external noise and

the input offset current in the electrometer. Usually, this offset is very small (~ 1 fC), and the uncertainty in setting the offset can be estimated as $\sigma_{\text{offset}} \sim Q_{\text{offset}}$. Finally, applying the error propagation formula yields

$$\sigma_{Q_b}^2 \approx \sum_{i=1}^{i_{\max}} (2\pi r_i \delta r_i)^2 \left[\sigma_i^2 + \sigma_{\text{offset}}^2\right], \tag{3.12}$$

$$\sigma_{R_b}^2 \approx \frac{1}{4R_b^2 Q_b^2} \sum_{i=1}^{i_{\max}} r_i^4 (2\pi r_i \delta r_i)^2 \left[\sigma_i^2 + \sigma_{\text{offset}}^2\right]. \tag{3.13}$$
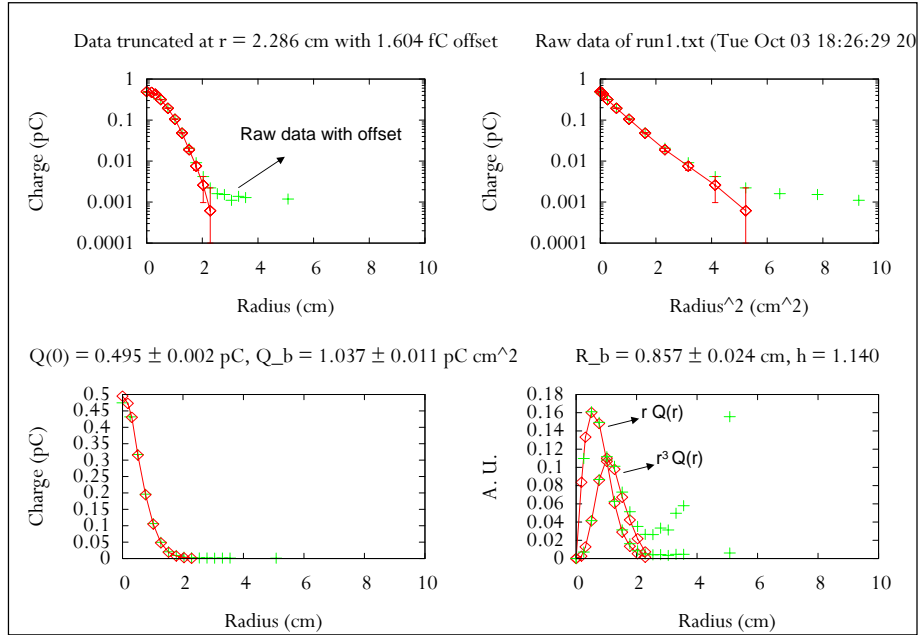
Figure 3.14: An example of the output generated by the LabVIEW interface of the Model 6514 electrometer and the post-processing Python [MARTELLI, 2003] script. The radial profile is truncated when the charge signal is saturated near 1 fC on the log scale. This prevents the small external noise and input offset current from contributing significantly to the calculation of $R_b \propto \int dr r^3 Q(r)$ at large radii. Here, errors in Q_b and R_b are calculated from Eqs. (3.12) and (3.13), respectively, and h is the profile parameter defined in **Chapter 2** ($h = 1$ for Gaussian).

3.4 Laser-Induced Fluorescence (LIF) Diagnostic System

The initial experiments in the PTSX device with a cesium ion source and a radially scanning charge collector diagnostic have been very successful in providing many important physical insights into injection mismatch (**Chapter 4**), transverse beam compression (**Chapter 5**), and machine imperfection effects (**Chapter 6**). However, for the in-situ measurements of the transverse density profile and the velocity distribution function in the PTSX device [CHUNG *et al.*, 2005b], which are essential for the detailed study of beam mismatch and halo particle production, a laser-induced fluorescence (LIF) diagnostic system has been developed in parallel with the PTSX experiments described in **Chapters 4−6**. Because the optical transition of barium ions is more relevant to LIF than cesium ions, barium ions have been chosen as the preferred ion species [CHUNG *et al.*, 2005a, 2007a]. In this section, the development of the barium ion source and the installation of the LIF system are summarized together with initial test results.

3.4.1 Compact Barium Ion Source with Platinum Ionizer

Theoretical Consideration

Barium ions are produced at the hot metal surface by contact ionization. Traditionally, rhenium and tungsten have been used for the hot metal plate to produce both ions by contact ionization, and electrons by thermionic emission. Because electrons are not used in the PTSX device, platinum is a more favorable choice for the hot
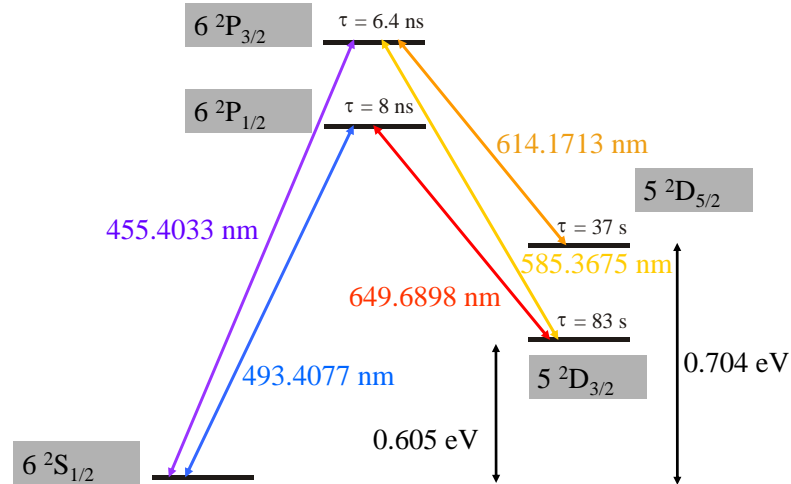
Figure 3.15: Energy level diagram for Ba^+ with transition wavelengths in air, natural lifetimes τ, and energy level differences between the ground state and metastable states [KOERBER et al., 2002].

metal plate because of its higher work function than rhenium and tungsten. Platinum's work function is 5.65 eV, and its melting point is 1768 °C.

The available optical transition lines of barium ions are presented in Fig. 3.15. Although there are several visible transition lines for the laser excitation of barium ions, the transition from the $5^2D_{3/2}$ metastable state has been considered first, mainly because a stable, operating, broadband, and high-power laser system is available for experiments in this region of the red spectrum [FOLEY, 2005]. Ions excited from the metastable state $5^2D_{3/2}$ to the excited state $6^2P_{1/2}$ decay to the ground state $6^2S_{1/2}$ almost immediately (8 ns), emitting blue-green light (493.41 nm).

The ionization probability for contact ionization (or surface ionization) can be calculated using the formula given by the Saha-Langmuir equation for thermal equilibrium conditions. For a barium ion, where two metastable states lie within about 0.7 eV from the ground state (see Fig. 3.15), the possibility of the ion being excited

into metastable states must be considered as well. Hence, it is expected that the ionization probabilities for the ground state ions (P_i) and the metastable ions (P_i^*) are equal to or less than the theoretical estimates given by

$$P_i = \frac{g_i}{g_a \exp\left(\frac{E_i - W}{T}\right) + g_i + \sum_* g_i^* \exp\left(\frac{-\Delta E^*}{T}\right)}, \tag{3.14}$$

$$P_i^* = \frac{g_i^* \exp\left(\frac{-\Delta E^*}{T}\right)}{g_a \exp\left(\frac{E_i - W}{T}\right) + g_i + \sum_* g_i^* \exp\left(\frac{-\Delta E^*}{T}\right)}. \tag{3.15}$$

Here, W and T are the work function and temperature of the hot metal plate (platinum in this case), E_i is the ionization potential of the atom, and ΔE^* is the energy difference between the ground and metastable states. The quantities g_a, g_i, and g_i^* are statistical weights of the atoms, ground state ions, and metastable ions, respectively. The statistical weight g can be calculated from the total angular momentum quantum number J using the familiar relationship, $g = 2J + 1$.

It is interesting to note that for the case of contact ionization of barium vapor on platinum, $E_i (= 5.21$ eV$) < W (= 5.65$ eV$)$ and P_i^* is inversely proportional to T. This might suggest that platinum ionizer could be operated at a very low temperature. However, Eq. (3.15) is only valid when the metal surface temperature is above the critical temperature (or threshold temperature) T_c [WILSON and BREWER, 1973; KAMINSKY, 1965]. When $T < T_c$, the evaporation rate of atoms decreases and the surface coverage of adsorbed atoms increases, which in turn causes the effective work function of the composite surface to decrease and finally results in a sharp drop in net ion current [WILSON and BREWER, 1973; KAMINSKY, 1965]. Therefore, it is essential to maintain the surface of the ionizer above the critical temperature. The critical temperature for contact ionization on platinum differs for different ion species. For most cases, $T_c \gtrsim 1000$ °C [KAMINSKY, 1965]. Hence, the ionizer temperature of the newly developed ion source is normally set to 1000 °C. If the ionizer temperature
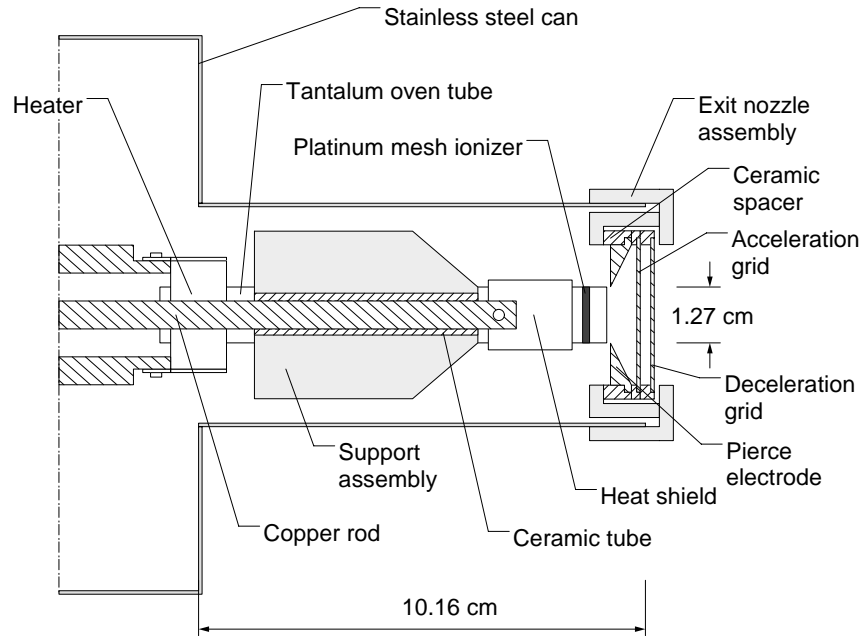
Figure 3.16: Schematic diagram of the barium ion source assembly.

is too hot, it is then possible to burn out the platinum. For an ionizer temperature of 1000 °C, it is estimated from Eqs. (3.14) and (3.15) that the fraction of barium ions produced by the hot platinum surface will be 98.7% in the ground state ($6^2S_{1/2}$), 0.8% in the $5^2D_{3/2}$ metastable state, and 0.5% in the $5^2D_{5/2}$ metastable state. Because the typical ion density in PTSX is about 10^5 cm^{-3}, the $5^2D_{3/2}$ metastable ion density will be about $10^2 \sim 10^3$ cm^{-3}, which is slightly above the detection limit for typical LIF diagnostics [MURAOKA and MAEDA, 2001]. Hence, suppression of background signals and sufficiently long integration times are essential for meaningful LIF data.

Description of Ion Source Assembly

The design concept for the barium ion source described here is based on the compact metal-ion source developed for heavy ion beam probes used for plasma diagnostics

[SAKAI *et al.*, 1983; KATSUMATA *et al.*, 1994; MURAKAMI *et al.*, 1996]. The ion source is composed of a beam material oven and a metal ionizer. The oven is a tantalum tube with a radius of 0.635 cm and a length of 10.16 cm (Fig. 3.16). The radial tube dimension is adequate to make sure that the beam is rms-matched to the externally applied focusing field for the nominal operating conditions in PTSX. The length of the tantalum tube is chosen in such a way that heat conduction and radiation processes sustain the proper temperature distribution along the tube. Normally, the tantalum tube is maintained at temperatures higher than 400 °C to decompose any barium oxide layer. The ionizer consists of a stack of platinum meshes which are woven from 0.1 mm platinum wires and have a 62.7% open area. The platinum meshes are inserted into the open end of the oven tube, and the vapor of the beam material is ionized on the hot platinum wire surfaces as it passes through the tube. Two tantalum heaters are wrapped around the tube and the ionizer, respectively. Each heater has its own heat shield to increase the thermal efficiency and is connected to a high-current power supply through thick (0.635 cm in diameter) copper rods. The temperatures of the oven and the ionizer are controlled by adjusting the currents of the power supplies and monitored by two K-type thermocouples attached to these components. The currents of the power supplies for the oven and the ionizer can be increased up to 150 A and 250 A, respectively. To minimize oxidization, barium is loaded into the oven inside an argon-filled tent. About 6 g of barium allowed $2 \sim 3$ months of operations in the initial experiments.

The ionizer is surrounded by a Pierce electrode, followed by an acceleration grid and a deceleration grid to extract the desired ion current and adjust the final ion kinetic energy (Fig. 3.17). To further increase the ion density, a positive bias voltage ($\gtrsim$ 10 V) is usually applied to the ionizer. The Pierce electrode and two grids are
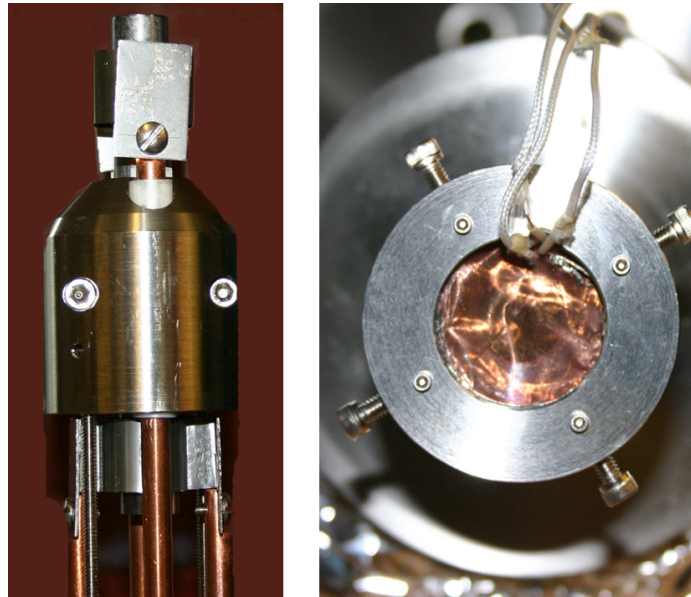
Figure 3.17: Assembly of tantalum oven tube, platinum mesh ionizer, tantalum heaters, and copper rods (left). Assembly of Pierce electrode, acceleration grid, and deceleration grid mounted on top of the stainless steel can (right).

electrically insulated using machinable ceramic spacers (Macor). Because the ion beam energy is relatively low for the PTSX device, 85%-transparent, electroformed copper meshes have been used for the acceleration and deceleration grids. However, due to the chemical reaction with the barium vapor, the lifetime of the copper mesh can be limited. Hence, nickel and tantalum meshes have been adopted for more recent experiments. The Pierce electrode is made of stainless steel and has a 67.5° opening angle to produce laminar flow of the beam ions. The entire assembly consisting of the oven, ionizer, and heater is surrounded by a large stainless steel can to prevent the neutral barium from contaminating the electrodes and reduce visible radiation from the hot glowing ion source. To further reduce the background light, which may decrease the signal-to-noise ratio of the LIF measurement, a carbon coating (Aquadag) is applied to the inside of the source end electrodes. To facilitate the
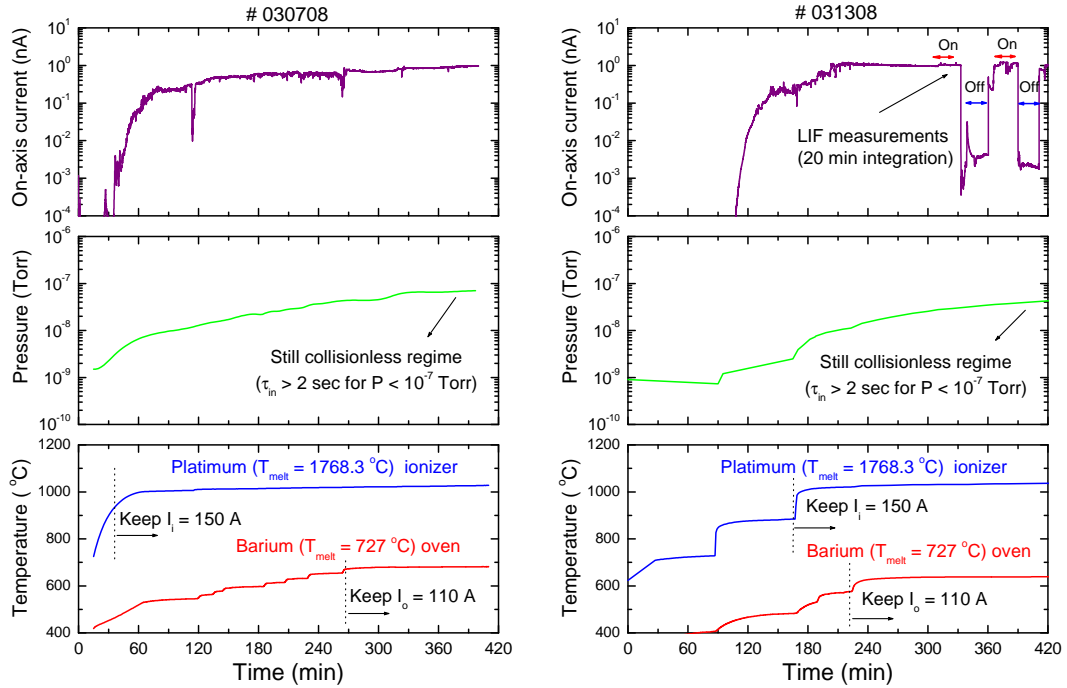
(a) Operation without LIF measurement.   (b) Operation with LIF measurement.

Figure 3.18: Characteristics of the barium ion source in streaming-mode operation of the PTSX device. Time evolution of (top) the on-axis beam current generated by the barium ion source, (middle) background pressure, and (bottom) temperatures of the oven and the ionizer.

loading of barium and the replacement of the platinum mesh, the grid assembly is mounted on top of the stainless steel can.

The typical characteristics of the barium ion source in streaming-mode operation of the PTSX device are shown in Fig. 3.18. For the LIF measurements, background subtraction is required. Hence, for a given experimental setup, we record two CCD images with the barium ion source on and off. The barium ion source can be effectively turned off by applying zero focusing fields in the PTSX electrodes.

3.4.2 Laser-Induced Fluorescence (LIF) Diagnostic

Population Dynamics

For the initial test of the LIF system, streaming-mode operation of the PTSX device is employed to make optimum use of the metastable ions. Since there is a continuous supply of metastable ions into the detection volume through drift motion, we can write down rate equations for the populations of the metastable state (n_1), excited state (n_2), and ground state (n_3) with source-sink terms according to [HILL, 1983]

$$\frac{dn_1}{dt} = -n_1 B_{12} \rho_\nu(\nu_0) + n_2 B_{21} \rho_\nu(\nu_0)$$
$$+ A_{21} n_2 + \frac{(n_1^0 - n_1)}{\tau_d}, \tag{3.16}$$

$$\frac{dn_2}{dt} = +n_1 B_{12} \rho_\nu(\nu_0) - n_2 B_{21} \rho_\nu(\nu_0)$$
$$- A_{21} n_2 - A_{23} n_2 + \frac{(n_2^0 - n_2)}{\tau_d}, \tag{3.17}$$

$$\frac{dn_3}{dt} = +A_{23} n_2 + \frac{(n_3^0 - n_3)}{\tau_d}. \tag{3.18}$$

Here, A_{ij} and B_{ij} are the Einstein coefficients [DEMTRODER, 2002], n_i^0 is the initial population of each state, τ_d is the characteristic ion transit time through the detection volume, and $\rho_\nu(\nu_0)$ is the spectral energy density of the laser around the resonance frequency ν_0. For the broadband operation of the laser, we assume that the laser power P_L is evenly distributed around ν_0 with spectral width $\Delta \nu_L$, i.e., $\rho_\nu(\nu_0) \approx P_L / cA\Delta\nu_L$. Here, A is the cross sectional area of the laser beam. The saturation intensity of the laser I_{sat}, which makes the spontaneous emission equal to the stimulated emission, is given by

$$I_{sat} = \frac{A_{21} + A_{23}}{A_{21}} \frac{8\pi h \nu_0^3}{c^2} \Delta\nu_L, \tag{3.19}$$

and is typically $I_{sat} = 141$ mW/mm^3 for the LIF scheme considered here. Note that there will be no significant increase in the LIF signal after the laser intensity is above
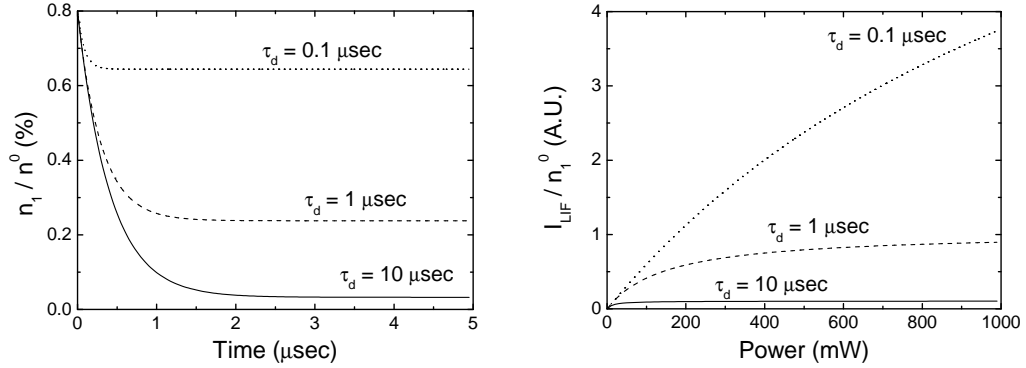
(a) Evolutions of the metastable popula-
tion.

(b) LIF intensity at steady state.

Figure 3.19: Plots of (a) time evolutions of the metastable population $n_1(t)$ with the laser power of $P_L = 360$ mW for the different values of τ_d, and (b) dependence of the steady state LIF intensity on P_L and τ_d. Here, the initial metastable population is assumed to be $n_1^0/n^0 = 0.8\%$.

I_{sat}. The number of photons emitted from the detection volume V to the collection optics with solid angle Ω per unit time is given by

$$I_{LIF} = \eta \left(\frac{\Omega}{4\pi} \right) V A_{23} n_2, \qquad (3.20)$$

where η is the overall efficiency of the collection optics .

As shown in Fig. 3.19(a), the population of the metastable state is quickly de-pleted to the final steady state value, which is strongly dependent on τ_d. Steady-state solutions of rate equations in Fig. 3.19(b) illustrate the dependence of the LIF inten-sity I_{LIF} on the ion flux into the detection volume ($\sim 1/\tau_d$), the incident laser power P_L, and the initial metastable density n_1^0. Taking $\tau_d \sim 1 - 10$ μsec in the PTSX de-vice, we note that I_{LIF} is less sensitive to the spatial and temporal variations of the laser power when $P_L \gtrsim 300$ mW. As the laser power becomes even higher, the level of the stray light will increase accordingly and there will be no further improvement in the signal-to-noise ratio.

Hardware Setup

The continuous-wave (CW) laser used in this research is a Coherent 899-21 ring dye laser that is optically pumped by an argon ion laser [FOLEY, 2005]. DCM dye is used with EPH solvent, giving output powers of up to 800 mW at around 650 nm, appropriate for matching the $5^2D_{3/2}$ to $6^2P_{1/2}$ transition. A Burleigh wavemeter is used to measure the output wavelength, and the laser power is monitored with an Ophir photodiode power meter. An optical isolator is inserted in the beam path before coupling to a multimode fiber, which carries the laser beam across the laboratory to the PTSX apparatus. The three-plate birefringent filter (BRF) allows broadband operation via rapid mode-hopping of the longitudinal modes over approximately 2 GHz ($\approx$ 10 modes), which is matched to the Doppler width range of the transition in the typical PTSX experimental condition (see **Appendix C**). During the long integration of the LIF signal, however, increased mode-hopping across the BRF modes due to the ambient temperature changes can occur. Hence, it is recommended to adjust the BRF in the course the experiment so that the laser wavelength is always matched to the transition wavelength.

At the fiber output, a commercial laser beam line generator has been installed to increase the detection volume and fully utilize the available metastable barium ions. The line generator, which uses a Powell lens, transforms the collimated laser beam into a line with a uniform output intensity. A Powell lens with 10° fan angle and 0.8 mm linewidth can result in a detection volume with a width of $\sim$ 6.8 cm near the PTSX center (see Fig. 3.22). For the safety interlock, a beam shutter and a shutter controller are employed. Before shining the dye laser, the laser path is aligned via low-power He-Ne laser, adjusting a precise rotation stage where the line generator and beam shutter assembly is mounted [Fig. 3.21(a)]. To suppress the stray light, i.e., the
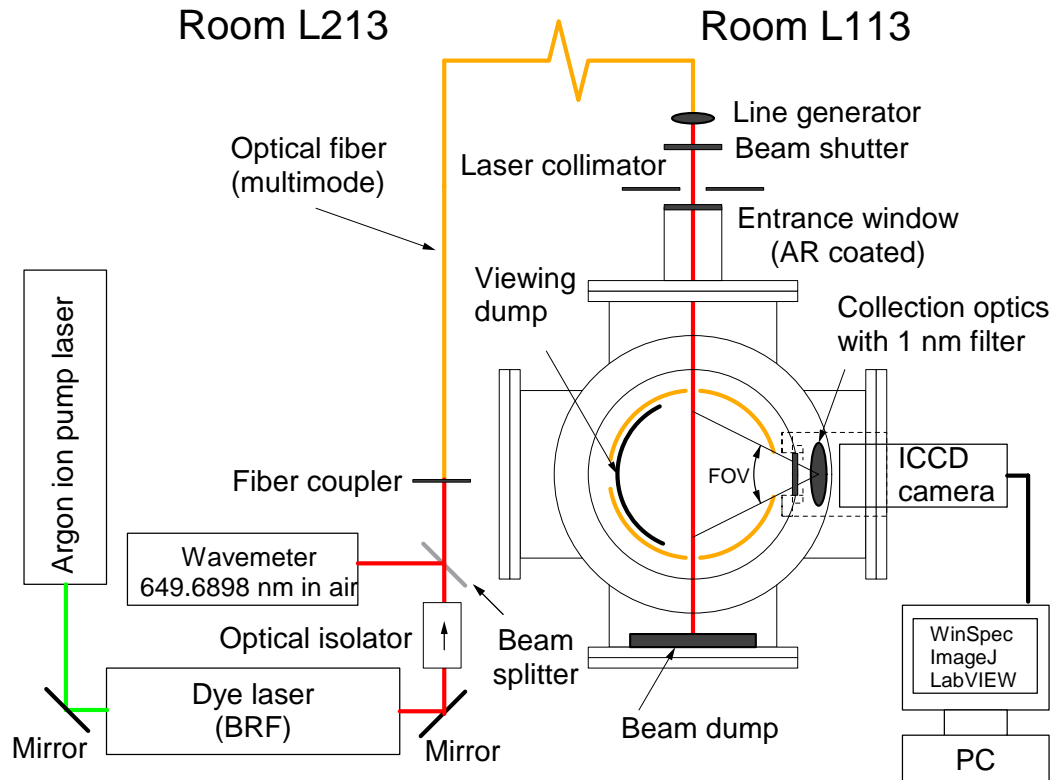
(a) Schematic diagram of the laser-induced fluorescence (LIF) diagnostic setup.
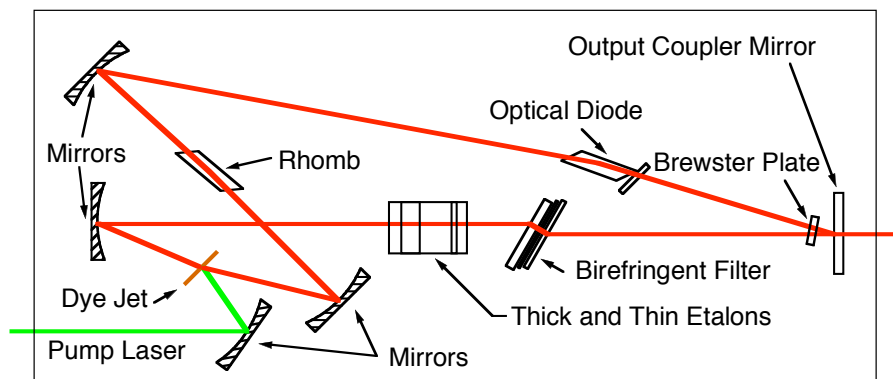
(b) Schematic diagram of the dye laser operation [FOLEY, 2005].

Figure 3.20: Schematic diagram of (a) the laser-induced fluorescence (LIF) diagnostic setup and (b) the dye laser operation. For the broadband operation considered in the PTSX, only a birefringent filter (BRF) is employed for the frequency selection.

(a) Entrance window for laser.   (b) Viewport for CCD camera.
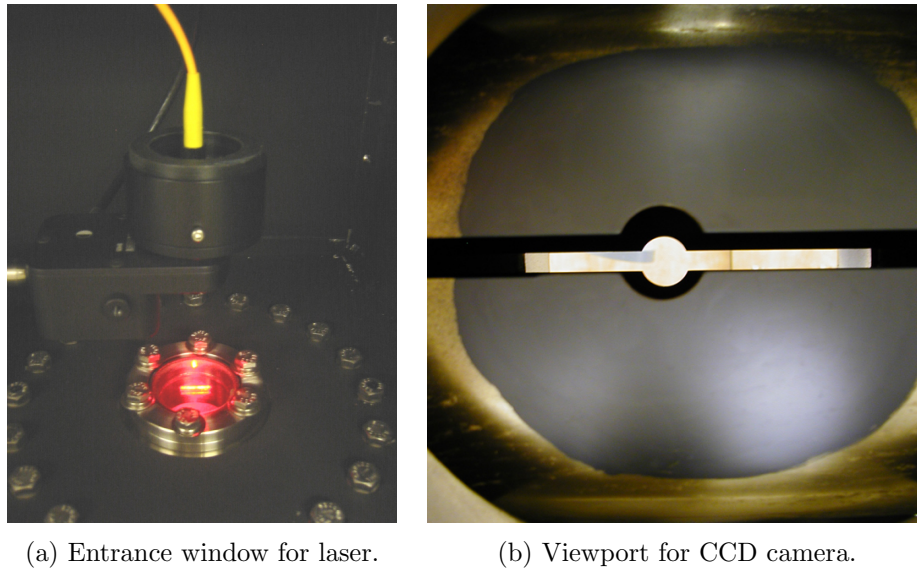
Figure 3.21: Photographs of (a) the entrance window for laser and (b) the viewport for CCD camera. In photograph (a), the laser beam sheet appears bright red line on the entrance window. In photograph (b), the central electrodes are coated with conductive carbon particles (Aquadag) to reduce possible reflections.

part of the incoming laser light reaching the detection system through reflection at windows, electrodes, and the vacuum vessel walls, an anti-reflection coating is applied to the entrance window, a laser collimator is installed, and a stack of razor blades has been employed as a beam dump. In addition, the line generator and beam shutter are enclosed by a light-tight aluminum box so that no background room light enters into the entrance window.

The fluorescence light passes through the 1-in. O.D. hole in the central electrode [Fig. 3.21(b)], a glass vacuum window, a narrow bandpass interference filter, and a C-mount lens with a diameter comparable to the 1-in. O.D. hole. The filter has a 1 nm bandwidth with a 10^{-4} out-of-band blocking. The central wavelength of the filter has been tuned to slightly over the wavelength of the $6^2P_{1/2}$ to $6^2S_{1/2}$ transition to compensate for the wavelength shift with angle of incidence. Finally, a Princeton

Instruments ICCD-MAX intensified CCD camera captures the fluorescence image digitally. The CCD camera has 16-bit A/D converter with 512×512 resolution, and uses a microchannel plate (MCP) image intensifier fiber-optically coupled to the CCD array. The thermoelectric cooler mounted on the heat removal block and the external fan keep the temperature to $-20\,°\mathrm{C}$. In order that the overall detection system has a wide field-of-view (FOV) and covers the entire transverse dimension of the plasma column, a custom-made reentrant viewport has also been installed.

The major source of background light is the glowing red-hot barium ion source, which is operated at around $1000\,°\mathrm{C}$. To reduce the scattered light from the ion source, the background of the observation path has to appear black. For this purpose, a so-called viewing dump has been installed. In order not to affect the performance of the electrodes, conductive carbon particles (Aquadag) are applied as a coating. This coating reduces the scattered light by two orders-of-magnitude. The focal length of the lens and the length of the extension tube have been adjusted so that the CCD camera is focused mostly onto the darkest region of the viewing dump.

Because of the long integration time (~ 20 min) and high gain to detect the small LIF signal, the CCD camera itself generates noise as well. This noise includes thermally-induced dark current, readout noise, intensifier noise, and hot pixels. To improve the signal-to-noise ratio (SNR), we subtract the background image without a barium ion beam from the image with a barium ion beam with keeping other conditions (laser power and ion source temperature) same. Finally, we obtain an image of the net fluorescence light in which the intensity is proportional to the local ion density. Initial test results in Fig. 3.22 show, however, that the background light is so dominant that the SNR is rather inadequate to reconstruct the radial density profile from the LIF measurements. The fundamental difficulty of this LIF scheme
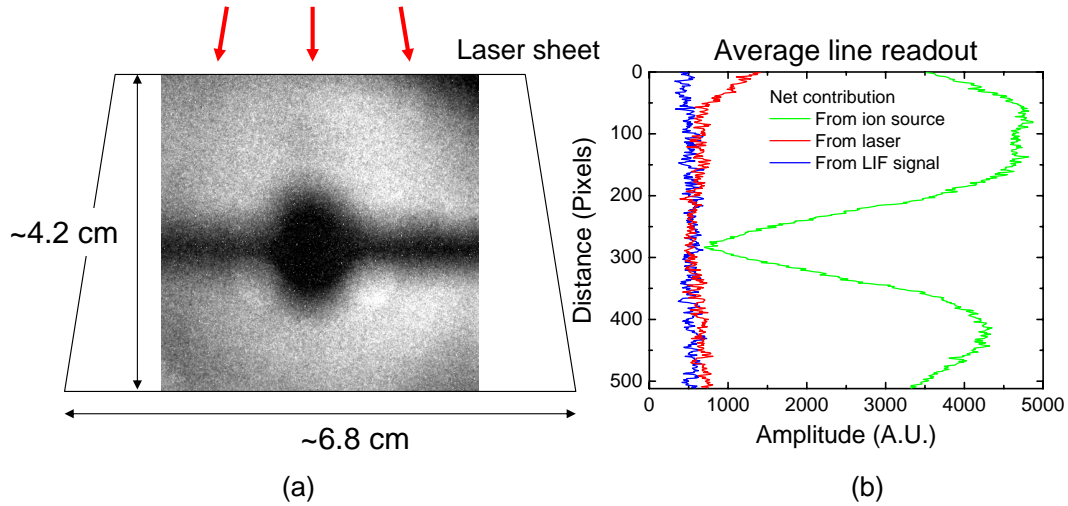
Figure 3.22: Initial test results of the LIF measurements showing (a) the image of the background light and (b) average line readouts of various signal contributions. The dark circle in the image (a) is the inner hole made in the central electrode shown in Fig. 3.21(b). Here, the incident laser power is 360 mW and the integration time is 20 min.

originates from the low level of the initial metastable state population ($\lesssim 0.8\%$). Hence, the best way to further improve the SNR is either to change the dye to excite the ground state directly, or use a second laser to populate the initial metastable state. For these purposes, a high-power pulsed laser system is currently being developed and is expected to increase the LIF intensity by more than an order of magnitude.

3.5 Summary and Discussion

In this chapter, the Paul Trap Simulator Experiment (PTSX) apparatus has been described in detail. The PTSX device is basically a linear Paul trap that has been widely employed for the mass spectrometer, quantum computing, and Coulomb crystal formation [MAJOR *et al.*, 2005]. However, for the PTSX device to confine and

detect the pure ion plasma with parameters relevant for the simulation of the intense beam in the alternating-gradient (AG) focusing channel, the device configuration, electrode control system, vacuum system, ion source, and charge collector have been carefully designed and installed. Initial experiments with a cesium ion source and a radially scanning charge collector diagnostic, which will be presented in **Chapters 4−6** of this thesis, demonstrate the wide operating range and the large degree of flexibility of the PTSX device. As a non-destructive diagnostic method, a laser-induced fluorescence (LIF) diagnostic system and an accompanying barium ion source has also been developed and tested. Due to the low level of the initial target metastable state and the strong background light associated with high-temperature operation of the barium ion source, the LIF signal is insufficient to reconstruct the radial ion density profile. Use of a second laser (or a change in the dye) together with a minimization of the light illumination from the ion source will be the subject of future research on PTSX, which is beyond the scope of the present thesis.

Chapter 4

Ion Injection Optimization

As noted earlier in this thesis, the PTSX device is a compact and flexible laboratory setup that simulates the collective processes and nonlinear transverse dynamics of an intense beam propagating through an alternating-gradient (AG) focusing quadrupole lattice. Externally-created cesium ions are injected and trapped in the long central electrodes of the PTSX to study several important beam physics topics, such as beam mismatch and halo generation [ALLEN *et al.*, 2002; CHUNG *et al.*, 2007c], collective mode excitation and control [DAVIDSON and QIN, 2001; GILSON *et al.*, 2007b], transverse beam compression [DORF *et al.*, 2006; CHUNG *et al.*, 2007b; GILSON *et al.*, 2007a], and random noise effects [BOHN and SIDERIS, 2003; GERIGK, 2004], to mention a few examples. To perform these experimental studies, it is important to have well-characterized initial beam equilibria without effects that may invalidate the physics similarity between an intense coasting beam and a nonneutral trapped plasma. In this chapter, it is shown that the ion injection process is critical for achieving such an initial beam state and can be optimized by minimizing the beam mismatch between the source and the focusing lattice (Sec. 4.1), and by minimizing

the number of ions present in the vicinity of the injection electrodes when the injection electrodes are switched from the fully oscillating voltage waveform to their static trapping voltage (Sec. 4.2). In addition, possible two-stream interactions (Sec. 4.3) and virtual cathode formation (Sec. 4.4) in the injection processes are discussed via 3D WARP particle-in-cell (PIC) simulations.

4.1 Injection Beam Mismatch

The beam physics experiments to be performed on PTSX must begin with a non-neutral ion plasma column that corresponds to a matched beam so that the initial state is well-known and characterized. However, during the injection stage, there can be a beam mismatch between the plasma emitted from the ion source and the transverse focusing lattice created by the applied voltage waveform. Beams are called mismatched when the (applied) focusing and the (space-charge and thermal) defocusing forces are unbalanced. This mismatch induces coherent oscillations of the beam envelope, halo particles, and emittance growth, and finally causes the trapped plasmas to have radial profiles far from those of a thermal equilibrium state [DAVIDSON and QIN, 2001; REISER, 1994]. Because ions are injected continuously from the ion source with a stationary circular cross-section into a transverse focusing system in which the matched state has a pulsating elliptical cross section, the injected plasma column is always mismatched to the focusing lattice to some degree. This type of mismatch is inherent and unavoidable for the ion source as presently configured in the PTSX.

However, it is important to note that the injection mismatch can be minimized by adjusting the envelope of the plasma column to be as close as possible to the cross-section of the ion source. If we apply the smooth-focusing approximation [DAVIDSON and QIN, 2001], a pulsating elliptical beam envelope can be effectively represented on average by a circular envelope with rms radius R_b. Further, if we consider an equivalent KV beam with outer radius $r_b = \sqrt{2}R_b$, then the transverse motion of the beam envelope evolves according to [DAVIDSON and QIN, 2001; REISER, 1994]

$$\frac{d^2 r_b}{dt^2} + \omega_q^2 r_b - \frac{\epsilon^2}{r_b^3} - \frac{K}{r_b} = 0, \tag{4.1}$$

where ω_q is the smooth-focusing frequency, ϵ is the average transverse emittance in the beam frame, and K is the effective self-field perveance. Suppose that the ion source injects a uniform density plasma with initial transverse emittance ϵ_s and perveance K_s, then there can be an envelope oscillation around $\bar{r}_b = \left[\left(K_s + \sqrt{K_s^2 + 4\epsilon_s^2 \omega_q^2} \right) / 2\omega_q^2 \right]^{1/2}$. If the ion source radius r_s is equal to $\bar{r}_b$, then the envelope oscillation and injection mismatch can be minimized. In this case, the mismatch parameter $\mu = r_s/\bar{r}_b$, which is the ratio of the size of the initial beam to that of the matched beam [ALLEN and WANGLER, 1998], becomes $\mu = 1$. We can adjust $\bar{r}_b$ by changing ω_q, ϵ_s, and K_s (or equivalently the initial line density N_s). Changing $\epsilon_s \approx \sqrt{2}r_s(2T_s/m)^{1/2}$ requires controlling the temperature of the emission surface of the ion source T_s, which is not practical in the actual experiments due to the finite thermal response time. Therefore, most of the experiments on minimizing injection mismatch have been carried out by changing ω_q and N_s. For an applied voltage waveform $V_0(t) = \hat{V}_0 \sin(2\pi f_0 t)$, ω_q is proportional to $\hat{V}_0/f_0$. Therefore, by changing $\hat{V}_0$ and f_0, we can increase or decrease ω_q accordingly. However, due to the electronic limitations in generating the voltage waveform in the PTSX device, and the single-particle stability condition in

the smooth-focusing vacuum phase advance $\sigma_v^{sf} = \omega_q/f_0 < 115.6°$, we can only increase ω_q up to about 100×10^3 s^{-1}. On the other hand, the initial line density N_s can be controlled easily by adjusting the voltages on the emission surface (V_s), acceleration grid (V_a), and deceleration grid (V_d) of the ion source. The voltage difference between the emission surface and acceleration grid determines the extraction voltage V_e, and the voltage difference between the emission surface and the deceleration grid adjusts the axial beam velocity v_b. The axial beam velocity remains approximately constant throughout the trap and can be estimated from energy conservation. If we assume space-charge-limited current flow, then line density can be approximated by $N_s \approx I_{CL}/qv_b \propto V_e^{3/2}$, where I_{CL} is the Child-Langmuir current.

Smooth-focusing injection mismatch is observed in experiments in which the extraction voltage is high enough that $\bar{r}_b$ is larger than r_s, i.e., when $\mu < 1$. To best measure this effect by minimizing the relaxation of the plasma to an equilibrium radial profile, PTSX is operated in a single-pass (streaming) mode where the confining electrodes at the diagnostic end of the device do not trap the plasma axially. Ions travel from the ion source to the diagnostic in a single transit of the machine. For the experimental data on single-pass operation, each data point is obtained after averaging over 100 repeated measurements, and the relative error is only a few percent. The experimental data and 3D WARP particle-in-cell (PIC) simulation [FRIEDMAN *et al.*, 1992] results in Fig. 4.1 show the z-integrated radial current profiles for the cases where $\omega_q = 52.2 \times 10^3$ s^{-1} and $\omega_q = 65.2 \times 10^3$ s^{-1}. If we take source parameters corresponding to $T_s \sim 0.1$ eV, $r_s = 0.762$ cm, and $V_e = 7.5$ V, then $\bar{r}_b = 1.41$ cm and $\mu = 0.54$ for $\omega_q = 52.2 \times 10^3$ s^{-1}, and $\bar{r}_b = 1.17$ cm and $\mu = 0.65$ for $\omega_q = 65.2 \times 10^3$ s^{-1}. Hence, we expect a significant injection beam mismatch. Shoulders in the radial profiles are observed both in experiments and simulations. This is
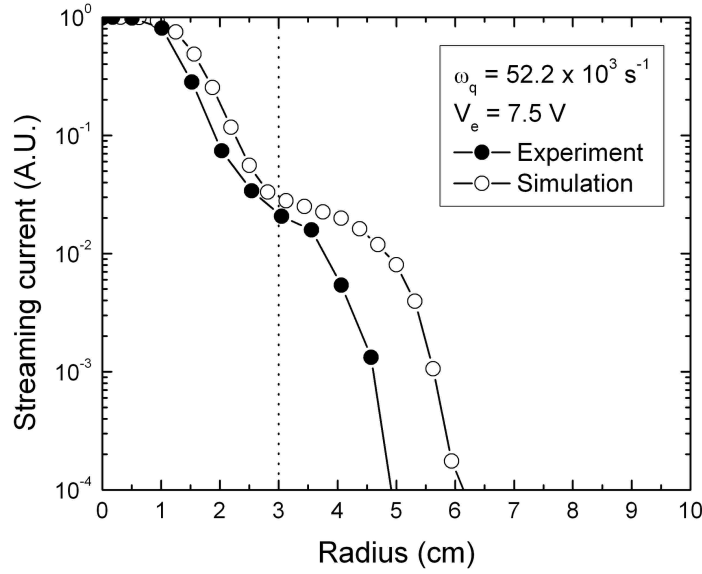
(a) $\omega_q = 52.2 \times 10^3$ s^{-1}.
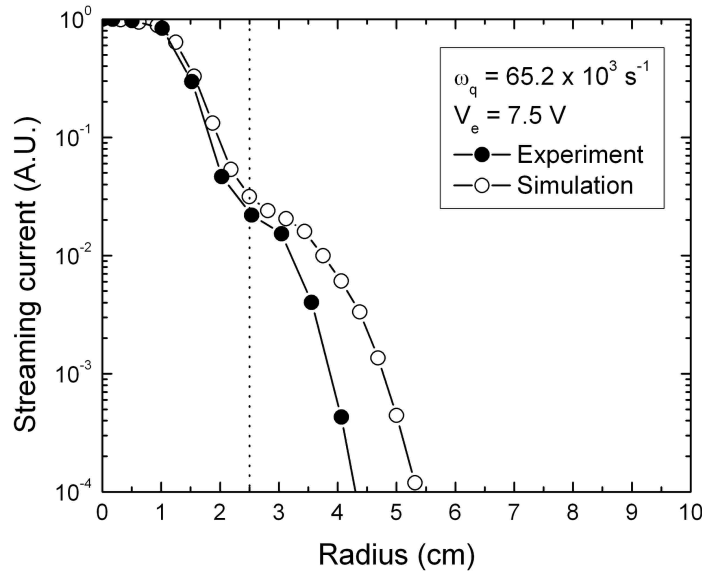
(b) $\omega_q = 65.2 \times 10^3$ s^{-1}.

Figure 4.1: The radial profiles of the axial current streaming from the ion source to the charge collector in a single-pass. Both experiments (solid circles) and simulations (open circles) show shoulders around $r = 3$ cm for $\omega_q = 52.2 \times 10^3$ s^{-1} (a), and around $r = 2.5$ cm for $\omega_q = 65.2 \times 10^3$ s^{-1} (b). Here, the extraction voltage is set at $V_e = 7.5$ V. The solid lines connecting the data points are drawn to guide the eye.
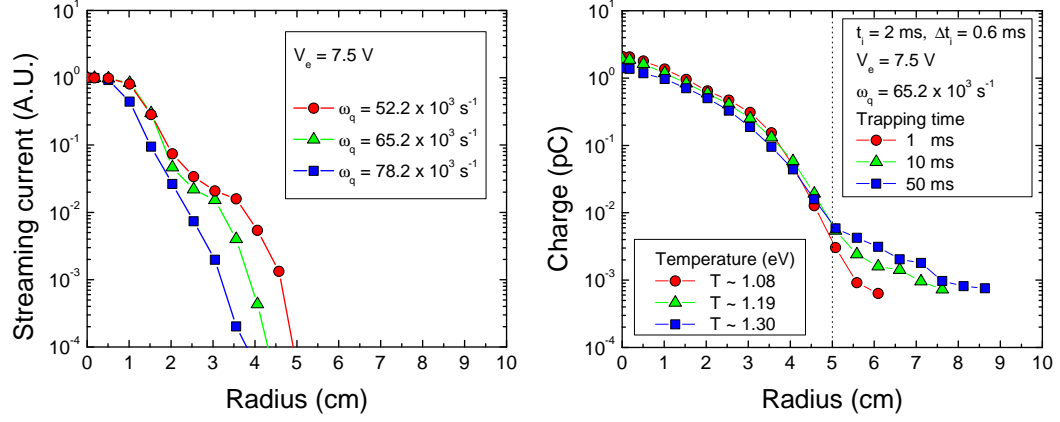
(a) Radial streaming current profiles.

(b) Radial trapped charge profiles.

Figure 4.2: Radial profiles of (a) the axial streaming current for several different smooth-focusing frequencies with fixed extraction voltage $V_e = 7.5$ V, and (b) the trapped charge for several different trapping times with injection mismatch ($\omega_q = 65.2 \times 10^3$ s^{-1}).

the result of the injection mismatch. The radial position of the shoulder scales with ω_q as shown in Fig. 4.2(a); when ω_q is decreased, the shoulder moves outwards, and when ω_q is increased the shoulder moves towards the axis, or disappears. These types of radial profiles induced by beam mismatch were reported previously by Allen *et al.* [ALLEN *et al.*, 2002]. This mismatch, when the plasma is trapped, causes the plasmas to be relaxed and heated considerably, and have radial profiles with super-Gaussian tails at $r > 5$ cm [Fig. 4.2(b)]. When trapped for much longer time durations, the tail part tends to further diffuse toward the wall ($r = 10$ cm), likely due to the end effects (see **Appendix A**). In Fig. 4.2(b), the plasma heating effect is estimated by calculating effective transverse temperature from the global force balance equation [DAVIDSON and QIN, 2001].

The detailed structure of the injection mismatch can be seen in 3D WARP simulations (Fig. 4.3). In the single-pass mode, the time evolution of the beam envelope can be mapped onto a z-varying beam envelope because $z \simeq v_b t$, where $v_b \simeq const.$, and
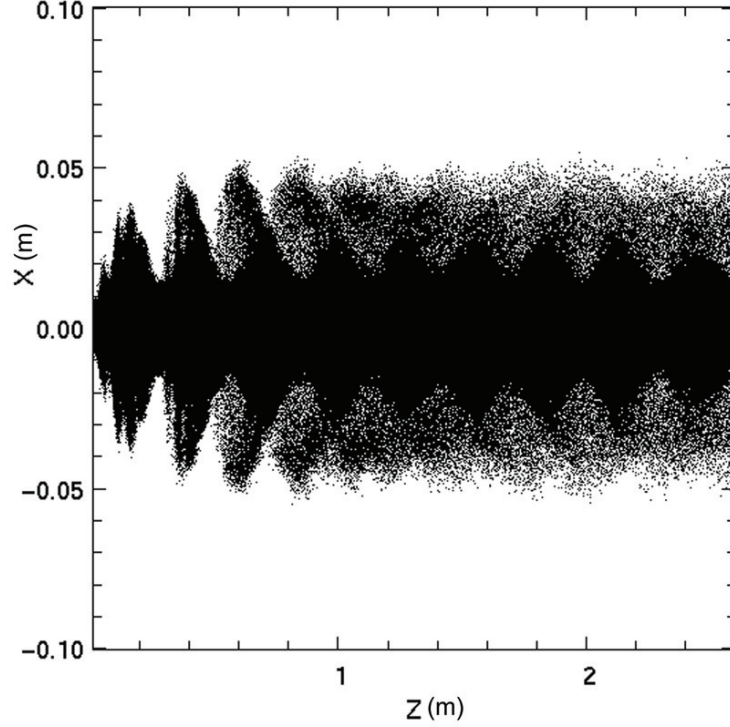
Figure 4.3: 3D WARP PIC simulation of injection mismatch with $\omega_q = 52.2 \times 10^3 \text{ s}^{-1}$ and $V_e = 7.5$ V, showing both rapid and slow oscillations near $z = 0$ m [DORF, 2006]. For larger z, the envelope oscillations result in a diffuse halo around the core.

the axial bouncing is absent. Hence, the simulation results in Fig. 4.3 have similar spatial structure to the evolution of the mean radius $[a(t)b(t)]^{1/2}$ in Fig. 2.6 of **Chapter 2**. Figure 4.3 indicates that near the ion source at $z = 0$, the injection mismatch appears as large-amplitude envelope oscillations at both the applied frequency f_0 and the breathing-mode frequency $\omega_B = 2\omega_q\sqrt{1 - K_s/(2\bar{r}_b^2\omega_q^2)}$. The transverse particle distribution relaxes as the injected particles move downstream, and when $z > 1$ m, consists of a dense core that oscillates with frequency ω_B and a broad diffuse halo. This structure results in a significant shoulder in the density profile measured at the exit of the channel [HOFMANN *et al.*, 2001]. The axial wavelength of the core oscillation is estimated to be $\lambda \sim v_b(2\pi/\omega_B)$, which gives $\lambda \sim 0.287$ m when $V_s = 9$
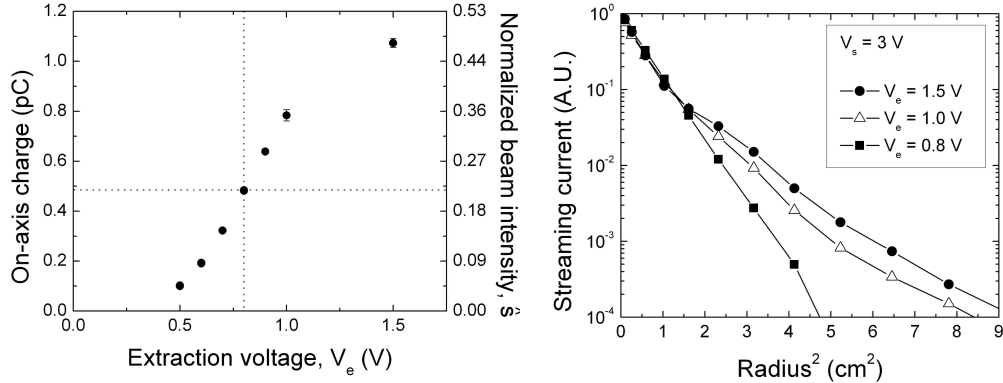
(a) On-axis charge dependence on the extraction voltage V_e.

(b) Radial profiles of the axial streaming currents.

Figure 4.4: Injecting less plasma by decreasing the extraction voltage minimizes the injection mismatch. When beam is matched to the focusing channel, radial profile becomes a Gaussian which is a straight line in the log versus r^2 plot. Here, $V_s = 3$ V, $V_d = 0$ V, and $\omega_q = 52.2 \times 10^3$ s^{-1}.

V, $V_d = 0$ V, $v_b = \sqrt{2q(V_s - V_d)/m} = 3615$ m/s, and $\omega_B = 79.2 \times 10^3$ s^{-1}. This wavelength is consistent with the simulation results, where there are about 9 core envelope oscillations during the 2.6 m transit, enough to see at least the initial stage of halo formation caused by injection mismatch [ALLEN *et al.*, 2002]. The halo is produced by the combined effects of particle-core resonance due to mismatch oscillations [WANGLER *et al.*, 1998] and the finite spread in the axial velocity of the beam particles. Consistent with the particle-core model calculation in Fig. 2.7(a) of **Chapter 2**, particles initially within the core reach a maximum amplitude of $\sim 3\bar{r}_b$, which is about 50% larger than the maximum envelope of the initial mismatched core. In the PTSX, axial smearing of beam particles due to the finite longitudinal temperature and the axial potential distribution, mixes the envelope oscillation structure and saturates the halo formation faster than an actual transport channel.

The simplest way to minimize the injection mismatch is to inject less plasma by decreasing the extraction voltage for a given axial beam velocity, so that the expected

equilibrium radius of the the plasma is close to the radius of the ion source. Figure 4.4(a) shows that the amount of charge injected can be easily adjusted by controlling the extraction voltage. When a plasma with moderately low space-charge density is well-matched to the focusing channel, its radial profile has a nearly Gaussian profile shape, which corresponds to a straight line in the log versus r^2 plot [DAVIDSON and QIN, 2001]. After scanning the acceleration grid voltages, it is found that well-matched plasmas in the single-pass mode can be created with an extraction voltage of $V_e = 0.8$ V [Fig. 4.4(b)]. For the well-matched case in Fig. 4.4, the profile parameter h introduced in Eq. (2.67) of **Chapter 2** is equal to 1.05, and the rms beam radius is $R_b = 0.72$ cm, which is comparable to the source size $r_s = 0.762$ cm. Here, the ion source bias voltage V_s has been lowered from 9 V to 3 V to avoid possible two-stream interactions (discussed in Sec. 4.3). These plasmas, when trapped, correspond to a normalized intensity of $\hat{s} = 0.2 \sim 0.3$, and serve as the baseline case for subsequent experiments.

4.2 Fast Ions

4.2.1 Minimization of Fast Ions

In order to create well-matched one-component plasmas in PTSX, further optimization is required in addition to minimizing the injection mismatch. Experiments show that it is optimal to inject plasma for slightly less than the round-trip transit time of ions in the trap, and stop the ion emission a short time before closing the injection electrodes. Both considerations arise out of the need to minimize the number of ions present in the vicinity of the injection electrodes when the electrodes are switched from the fully oscillating voltage waveform to their static trapping voltage value $\hat{V}$.

(a) After injection with too short Δt_i.

(b) After injection with too long t_i.

(c) After optimum injection.

(d) After 6 ms trapping.

(e) After 12 ms trapping.

(f) At the end of 50 ms trapping.
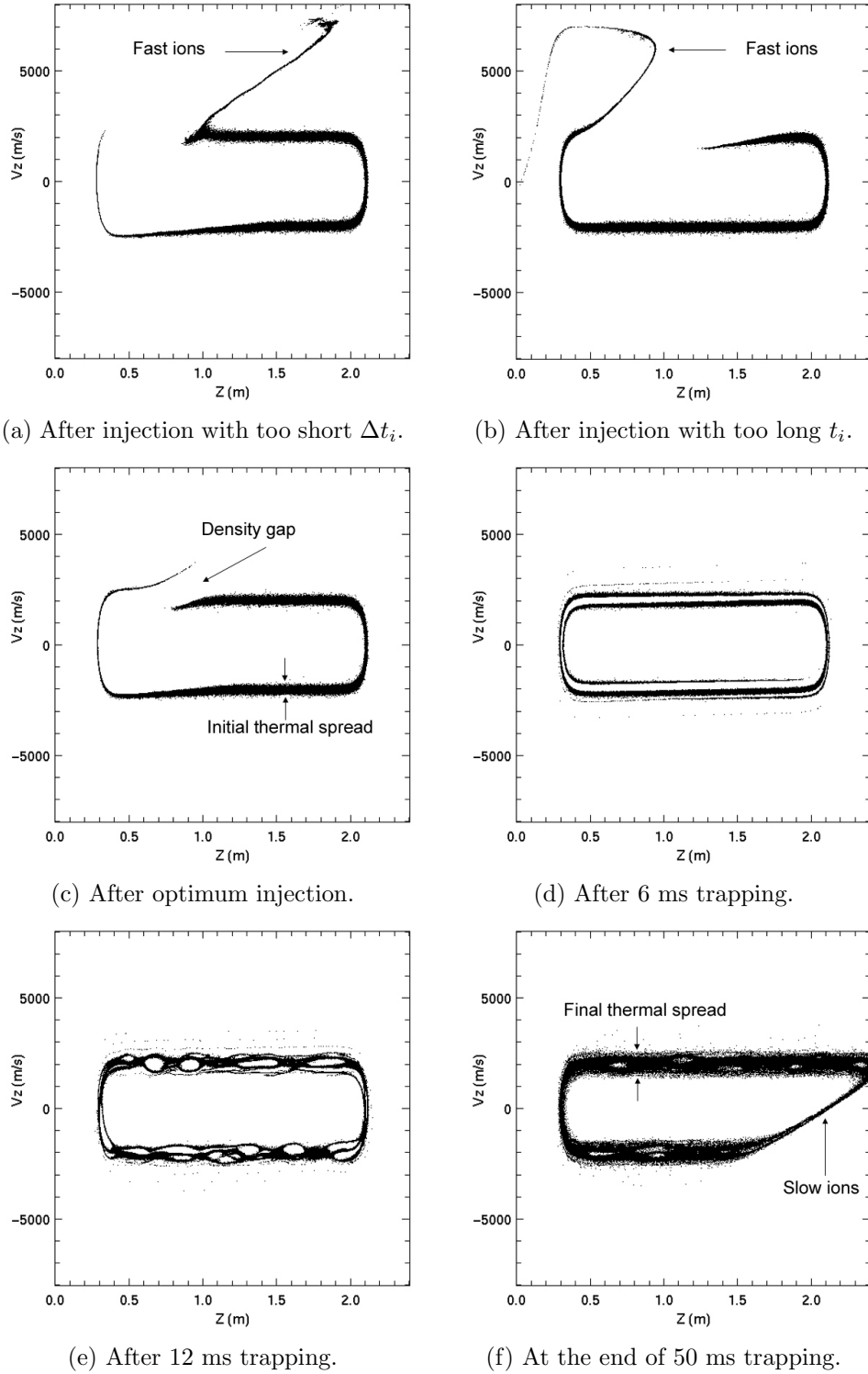
Figure 4.5: 3D WARP simulation results of PTSX operation for $\omega_q = 52.2 \times 10^3$ s^{-1} and $\hat{s} = 0.2 \sim 0.3$. Plots of axial (z, v_z) phase space are made with $V_s = 3$ V and $T_s = 0.1$ eV, which correspond to $v_b = (2qV_s/m)^{1/2} \approx 2087$ m/s and $v_{T\parallel} = (2T_s/m)^{1/2} \approx 381$ m/s initially.
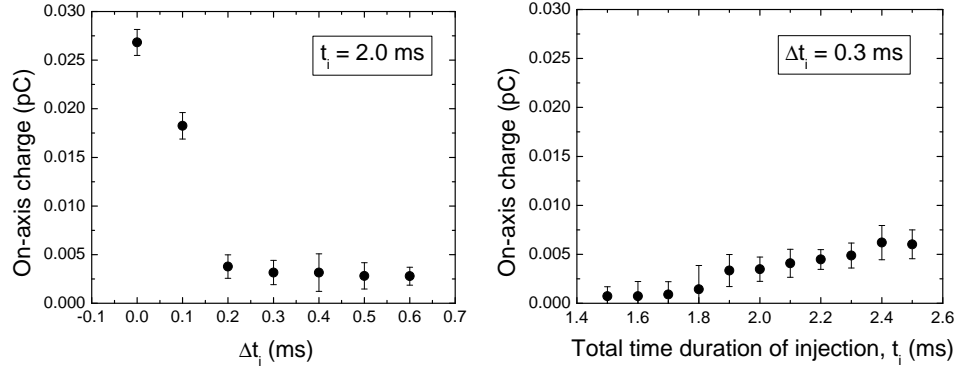
(a) On-axis charge dependence on Δt_i (b) On-axis charge dependence on t_i

Figure 4.6: Minimization of fast ions by optimizing Δt_i (a) and t_i (b). By measuring the on-axis charge with the dumping electrode closed, one can effectively monitor the fast ions. Only ions with large kinetic energy $\gtrsim q\hat{V}$ can escape from the trap and be collected even when the dumping electrodes are closed.

Ions that are near the injection region at the time the end electrodes close are increased to a potential energy as high as $q\hat{V}$ [for example, see Figs. 4.5(a) and 4.5(b)]. These fast ions can stream along the length of the trap, and then be reflected off the end potential of the trap with large radial excursions. Some of these fast ions may escape over the potential barrier on the dumping end and be detected by the charge collector. The result, whether the fast ions are trapped or not, is an unwanted distortion of the measured radial density profile. Inhibiting ion emission with a bias voltage applied to the emission surface allows the already-injected ions to move away from the injection region. An ion source pulsing circuit has been installed for this purpose, which switches the voltage of the emission surface to a negative bias at a short time Δt_i before the end of the injection stage. Keeping the total time duration of injection (t_i) less than a round-trip transit time of the ions (τ_b) minimizes the number of ions that have come back to the injection region. The round-trip transit time of an ion is estimated to be $\tau_b \approx 2 \times 2L/v_b \approx 1.92$ ms for the injection conditions in the previous section.
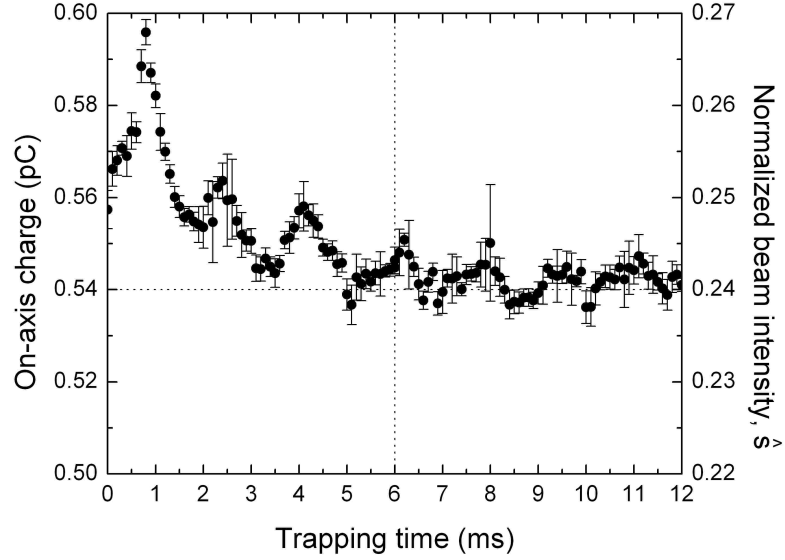
Figure 4.7: Time history plot of on-axis charge after trapping with optimum injection conditions. After about 6 ms, the normalized beam intensity is about $\hat{s} \sim 0.24$. The small residual oscillation has a period equal to the round-trip transit time of the beam ions in the trap.

The data in Fig. 4.6(a) demonstrate that if Δt_i is at least 0.2 ms, the number of ions that overcome the axial potential barrier is minimized. If Δt_i is less than 0.2 ms, then fast ions are generated, and can escape from the trap and be collected even when the dumping electrodes are not opened. The data in Fig. 4.6(b) indicate that the number of ions that pass over the axial trapping potential increases if t_i is greater than about 1.9 ms. This is consistent with the estimate of $\tau_b \sim 1.92$ ms. Therefore, for the injection optimization of the initial beam state in the present experimental studies, Δt_i and t_i are normally chosen to be 0.3 ms and 1.7 ms, respectively. 3D WARP simulation results in Fig. 4.5(c) also confirm that the population of fast ions can be significantly reduced if the injection process is properly optimized. If Δt_i is too large, the trapped plasma becomes bunched axially and has a much smaller number density after debunching.
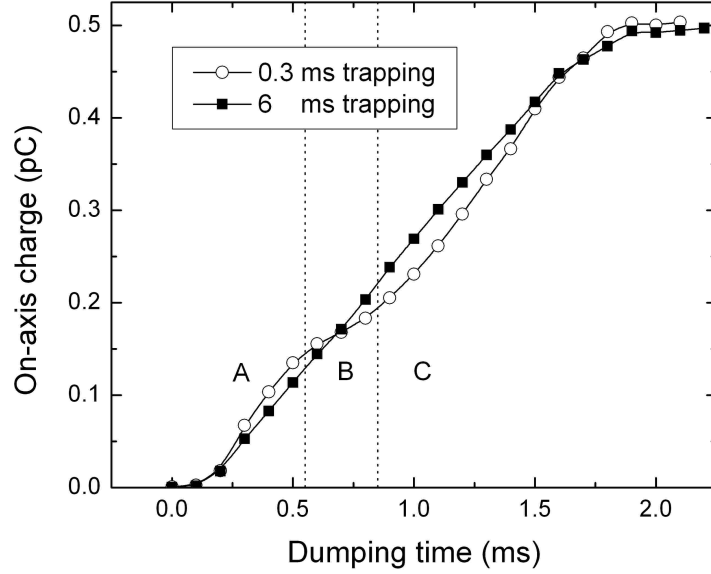
Figure 4.8: The slope of the on-axis charge versus dumping time curve corresponds to the on-axis beam current. If the trapping time is too short, the axial density gap induced by the time delay Δt_i is not fully smoothed out.

After injection is finished, the plasma is allowed to relax for several milliseconds. This relaxation time allows the residual mismatch oscillations to be damped away and the axial density nonuniformity induced by Δt_i to be smoothed out. As shown in Fig. 4.7, the on-axis density saturates in approximately 6 ms of the trapping time. The small residual oscillation in Fig. 4.7 results from the axial density nonuniformity, and has a period equal to the round-trip transit time of the beam ions in the trap. This has been reduced to $\sim$ 1.7 ms due to the shorter axial plasma length after trapping. By measuring the on-axis charge with different dumping times, the on-axis beam current can be estimated. In Fig. 4.8, the instantaneous slope of each curve represents the instantaneous on-axis beam current collected on the charge collector. For the case of 0.3 ms trapping, the instantaneous beam currents have both higher (regions A and C of Fig. 4.8) and lower (region B of Fig. 4.8) values than the average current, which indicates that the beam is still axially nonuniform. The time span of
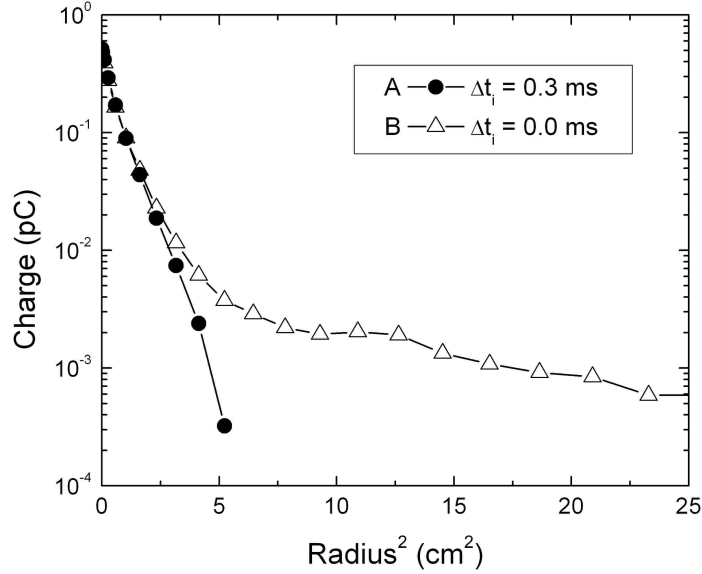
Figure 4.9: Measured radial profiles of trapped plasmas with $\omega_q = 52.2 \times 10^3$ s^{-1}: after minimizing the population of fast ions (A); and with a significant population of fast ions (B). A straight line in the log of the charge versus r^2 plot indicates that the radial profile is a Gaussian.

region B of Fig. 4.8 is nearly matched to $\Delta t_i = 0.3$ ms introduced from the injection. On the other hand, for the case of 6 ms of trapping, the collected beam current remains nearly constant until it is saturated after 2 ms of dumping, which indicates that the beam is mixed axially. 3D WARP simulation results in Fig. 4.5(d) shows that, after several bounces, trapped plasmas are mixed axially with multi-streaming beam components caused by finite thermal spread. Although the beam currents are nearly saturated in 2 ms, to collect the slow ions as well, the total dumping time is set at 15 ms for most of the experiments. Slow ions are generated near the turning point in the diagnostic end during the dumping process. When the dumping electrodes are switched from DC trapping voltages to an AC voltage waveform, ions near the turning point suddenly lose axial acceleration from the DC potential, and remain slow without further increase in axial velocity [Fig. 4.5(f)].

The radial density profile of the trapped plasma after 12 ms becomes nearly Gaussian (curve A in Fig. 4.9), as expected for a thermal equilibrium distribution corresponding to a moderately low space-charge density [DAVIDSON and QIN, 2001]. It is interesting to note that if we do not introduce the time delay Δt_i, then the radial density profile has a super-Gaussian tail due to the presence of fast ions (curve B in Fig. 4.9). The rms radius $R_b = [(1/N) \int_0^{r_w} n(r) 2\pi r^3 dr]^{1/2}$ can be calculated from the measured radial density profile $n(r)$. For the case where $\Delta t_i = 0.3$ ms, R_b is calculated to be 0.85 cm. On the other hand, for $\Delta t_i = 0.0$ ms, R_b has increased to 1.38 cm. Therefore, minimization of the population of fast ions is very important in establishing a well-behaved beam equilibrium. For a thermal equilibrium distribution in the smooth-focusing approximation, the global force balance equation can be written as [DAVIDSON and QIN, 2001]

$$m\omega_q^2 R_b^2 = 2\hat{T}_\perp + \frac{Nq^2}{4\pi\epsilon_0}. \tag{4.2}$$

The transverse temperature inferred from the global force balance equation (4.2) is $\hat{T}_\perp = 0.13$ eV for the trapped plasma with $\Delta t_i = 0.3$ ms, which is consistent with the thermal temperature of the cesium ion source ($\sim 1000\ °C$).

4.2.2 Fast Ion as a Diagnostic Tool

As discussed earlier, fast ions are undesirable for obtaining a well-matched initial beam. However, by intentionally generating fast ions with a different time duration of injection t_i, kicking them out of the DC potential barrier, and measuring their on-axis density evolutions, we can get useful information on envelope oscillations, which are usually averaged out during the dumping process. For this purpose, the DC bias

Input frequency (f_0, in kHz)	Adjusted frequency ($f_0 + \Delta f$, in kHz)	Aliased frequency (f_{alias}, in kHz)	Aliased period (T_{alias}, in ms)
75	75.7576	1.51515	0.66
60	59.5238	0.952381	1.05
50	50	0	∞

Table 4.1: The original input frequency f_0 is adjusted to $f_0 + \Delta f$ via the LabVIEW interface and applied to the electrodes of the PTSX. The aliased frequency associated with the on-axis density oscillation frequency $2(f_0 + \Delta f)$ is estimated by finding an integer l that satisfies $|2(f_0 + \Delta f) - lf_s| < f_s/2$.

voltage $\hat{V}$ has been increased to its maximum value (150 V), which allows the fast ions to be collected almost immediately ($\lesssim$ 0.3 ms) without significant relaxation.

To describe this process, we apply a KV-equivalent beam model introduced in **Chapter 2** of this thesis. We consider an axially-uniform long charge bunch with uniform number density $\hat{n}(t) = N/\pi a(t)b(t)$, in an oscillating quadrupole potential with the waveform $V_0(t) = \hat{V}_0 \sin(2\pi f_0 t + \Phi)$. If we assume that the initial phase is $\Phi = 0$, and the beam is symmetric and matched to the focusing channel, then $a(t) = a(t+T)$ and $b(t) = b(t+T)$, where $a(0) = b(0) = \bar{r}_b$. To the lowest-order Fourier mode analysis, we approximate $a(t) \approx \bar{r}_b + \delta r_b \sin(2\pi f_0 t)$ and $b(t) \approx \bar{r}_b - \delta r_b \sin(2\pi f_0 t)$, and at the instant when the injection is complete at $t = t_i$, the on-axis density is approximately given by

$$\hat{n}(t_i) \approx \frac{N/\pi \bar{r}_b^2}{\left[1 - \left(\frac{\delta r_b}{\bar{r}_b}\right)^2 \sin^2(2\pi f_0 t_i)\right]}. \tag{4.3}$$

The fast ions will be generated near the injection electrodes at $t = t_i$, and the collected on-axis charge signals $Q(0)$ downstream will be directly proportional to $\alpha \hat{n}(t_i)$, where α is the fraction of ions energetic enough to overcome the DC potential barrier near the dumping electrodes (typically, $\approx$ 1%). Since the present LabVIEW program that controls the operation sequence of PTSX is optimized with 0.1 ms time step, we

(a) From theory. (b) From experiment.
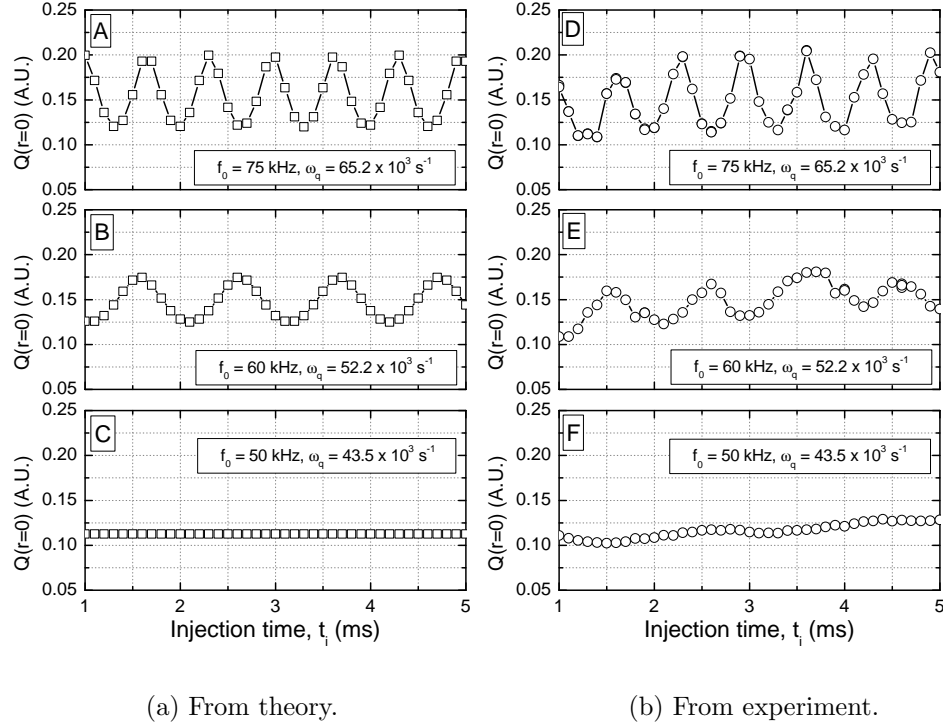
Figure 4.10: On-axis charge oscillations of fast ions are (a) calculated from a KV-equivalent beam model described by Eq. (4.3) and (b) measured from experiments with a 10 kHz sample rate. Here, the smooth-focusing phase advance σ_v^{sf} is fixed at 49.8°, and the injection time t_i varies from 1 to 5 ms.

sample the fast ion signal with a sample frequency $f_s = 10$ kHz. The on-axis density oscillation frequency $f_{\hat{n}}$ is twice the external focusing frequency f_0, and normally an order of magnitude higher than the sample frequency f_s. Therefore, $f_{\hat{n}}$ greater than the one-half of the sample frequency ($f_s/2 =$ Nyquist frequency) is folded back on the frequency scale, and appears as an aliased frequency f_{alias}, which is given by $f_{alias} = |f_{\hat{n}} - l f_s| < f_s/2$ for any integer l (i.e., folding effect). It should be noted here that due to the memory architecture of the arbitrary function generator, the input frequency f_0 is adjusted to $f_0 + \Delta f$ following the restrictions on the waveform size and resolution explained in **Chapter 3** of this thesis. The expected aliased frequencies and periods are summarized in Table 4.1 for several different input frequencies.
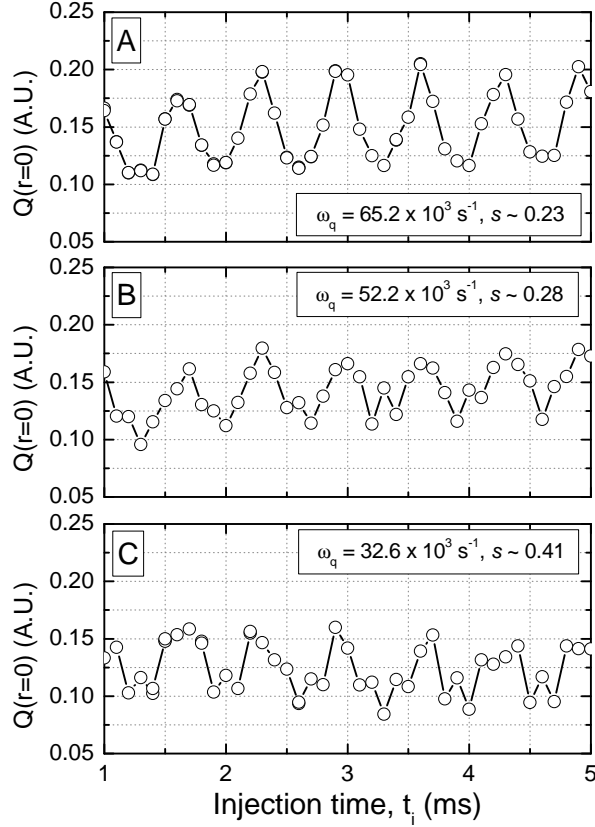
Figure 4.11: On-axis charge oscillations of fast ions are measured from experiments with the same applied focusing frequency $f_0 = 75$ kHz, but with several values of smooth-focusing frequency ω_q and normalized beam intensity $\hat{s}$.

Two free constant parameters $\alpha N / \pi \bar{r}_b^2$ and $\delta r_b / \bar{r}_b$ are scaled to best fit the experimental data. In particular, by measuring the ratio of the maximum to minimum on-axis charge $Q(0)$, one can estimate the relative amplitude of envelope oscillation of the beam by

$$\frac{\delta r_b}{\bar{r}_b} \sim \sqrt{1 - \frac{Q(0)_{\min}}{Q(0)_{\max}}}. \tag{4.4}$$

Figure 4.10 shows good agreement between theoretical estimates and experimental measurements within their aliased periods. In the experimental data, there are slight increases in the oscillation amplitudes after 2 ms. This is because the round-trip transit time of the ion beam is $\tau_b \approx 1.92$ ms, and the returning up-stream particles

start to contribute to the generation of fast ions when $t_i > 2$ ms. The relative
amplitudes of envelope oscillations are estimated to be $\delta r_b / \bar{r}_b \sim 0.6$ for $\omega_q = 65.2 \times 10^3$ s^{-1}, 0.45 for 52.2×10^3 s^{-1}, and 0.32 for 43.5×10^3 s^{-1}, respectively. It is interesting
to note that the case where $f_0 = 50$ kHz has a period exactly divisible by the sampling
period. In this case, it is expected that the discretely-sampled on-axis charges are
constant for a perfectly-matched beam. Hence, the small on-axis charge modulation
observed in case F of Fig. 4.10 can be attributed to the result of mismatch oscillations.
The effects of mismatch oscillations are further noticeable when the average focusing
frequency ω_q is decreased, and the normalized beam intensity $\hat{s}$ is increased for a
given applied focusing frequency. Figure 4.11 shows that as ω_q is lowered, there
appears irregular noise on top of the aliased oscillations, where the period is nearly
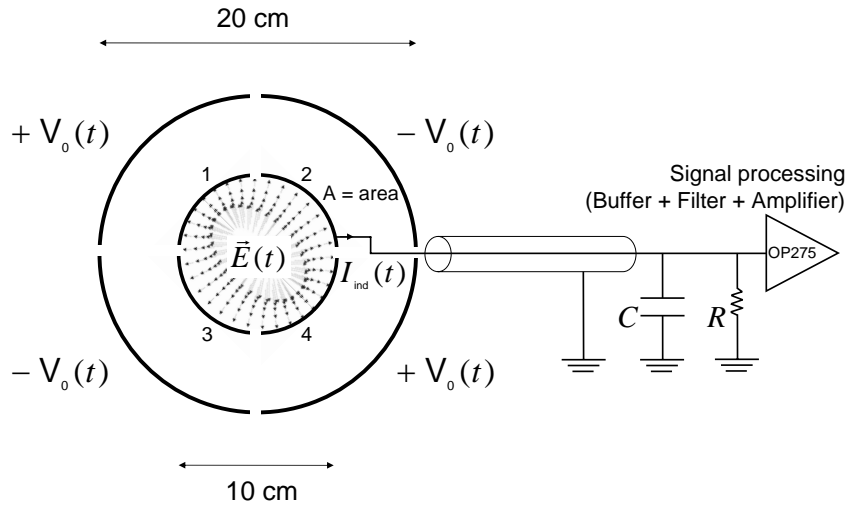
Figure 4.12: Schematic diagram of the collective mode diagnostic based on signal
processing with capacitive pick-ups [GILSON *et al.*, 2007b]. Here, C represents the
capacitance which is determined by the geometry of the pick-up electrodes (inside)
and main electrodes (outside), and by the capacitance distributed over the cable. To
lower the cut-off frequency $f_{cut} = (2\pi RC)^{-1}$ of the high-pass characteristic of the
input circuit, the induced displacement current $I_{ind}(t) \sim \epsilon_0 A[dE(t)/dt]$ is terminated
with a buffer with high input impedance R ($\sim 10^8$ Ω).

constant for a given f_0. Presently, the number of samples is insufficient to resolve the characteristic frequencies of the mismatch oscillations. Future experiments with higher sample frequency and longer time span may provide useful information on collective mode excitation, and can be compared with the collective mode diagnostic which is being developed in PTSX, based on signal processing with capacitive pick-ups (Fig. 4.12) [GILSON *et al.*, 2007b].

4.3 Two-Stream Interactions

During the injection stage, the stream of ions leaving the ion source interacts with the counter-streaming ions that have reflected off the end of the trap. In these counter-streaming plasmas, (electrostatic) two-stream interactions may be a source of noise in the signal, could lead to heating, expansion, and loss of the plasma, and may deteriorate the beam quality [STIX, 1992; GORGADZE *et al.*, 2003]. Electron-cloud effects in proton storage rings are a typical example of dipole-mode two-stream interactions observed in experiments [ZIMMERMANN, 2004].

In a simple counter-streaming uniform plasma system (**Appendix B**), the condition for instability $(\text{Im}\,\omega > 0)$ can be expressed in terms of the threshold value of the normalized intensity $\hat{s}_{\text{th}}$ as

$$\hat{s} > \hat{s}_{\text{th}} = 4 \frac{v_b/v_{T\|}}{\left(1 + v_b/v_{T\|}\right)^2},$$

for $v_b > v_{T\|}$. For $\hat{s} > \hat{s}_{\text{th}}$, the maximum growth rate $(\text{Im}\,\omega)_{\text{max}}$ and corresponding wavelength λ_{max} can be estimated as

$$(\text{Im}\,\omega)_{\text{max}} \simeq \frac{\hat{\omega}_p}{4} \left(\frac{\hat{s}}{2 - \hat{s}}\right)^{1/2} \left[1 - \left(\frac{v_{T\|}}{v_b}\right) \frac{(4 - 3\hat{s})^{1/2}(4 - \hat{s})^{1/2}}{\hat{s}}\right], \qquad (4.5)$$

$$\lambda_{\max} \simeq 2\pi \left(\frac{v_b}{\omega_q}\right) \sqrt{\frac{(1 - \hat{s}/2)}{(1 - 3\hat{s}/4)(1 - \hat{s}/4)}}, \qquad (4.6)$$

respectively. When $\hat{s} \to 1$ and $v_{T\parallel} = 0$, then $(\text{Im}\omega)_{\max} = \hat{\omega}_p/4$ and $\lambda_{\max} = 2\pi(v_b/\omega_q)\sqrt{8/3}$. In this space-charge-dominated limit, similar to the case of symmetric counter-streaming beams (without net transverse focusing), the two-stream instability has a growth rate that scales like the plasma frequency, and enhances the density fluctuation and beam bunching extremely fast [STIX, 1992]. However, when $\hat{s} < 1$, the external transverse focusing force becomes dominant and reduces the growth rate of the unstable modes. Further, if $\hat{s} < \hat{s}_{\text{th}}$, then the external focusing force completely suppresses the excitation of two-stream instabilities. If we take the experimental parameters to be $V_s = 3$ V and $T_\parallel \sim 0.12$ eV, then $v_b = (2qV_s/m)^{1/2} = 2087$ m/s, $v_{T\parallel} = (2T_\parallel/m)^{1/2} = 417$ m/s, and $\hat{s}_{\text{th}} = 0.56$. Therefore, we expect that two-stream interactions are linearly stable if we inject the beams rather slowly with moderately low space-charge intensity ($\hat{s} = 0.2 \sim 0.3$). The phase-space plots Figs. 4.5(c) and 4.5(d) show that the main beam stream remains quiescent during the injection stage and the early stage of trapping, with $|v_z|$ around 2000 m/s and a finite thermal spread, both of which are consistent with simple estimates. However, the simulations also indicate that if we trap the plasma longer for many bounce periods (> 10 ms) inside the axial potential barrier, then eventually two-stream interactions begin to develop even when $\hat{s} < \hat{s}_{\text{th}}$ [Fig. 4.5(e)]. This is most likely due to perturbations in the vicinity of the turning points. Near the turning points, where $v_b \to (v_b - 0)/2$, the local density is much higher than in the trap ($\hat{n} \to 2\hat{n}$), resulting in an enhanced density perturbation and beam bunching [GORGADZE *et al.*, 2003]. These two-stream interactions mix the multi-streaming beams inside the trap, increase the longitudinal temperature, and eventually become saturated [Fig. 4.5(f)]. As noted previously, the

(a) Simulation.   (b) Experiment.
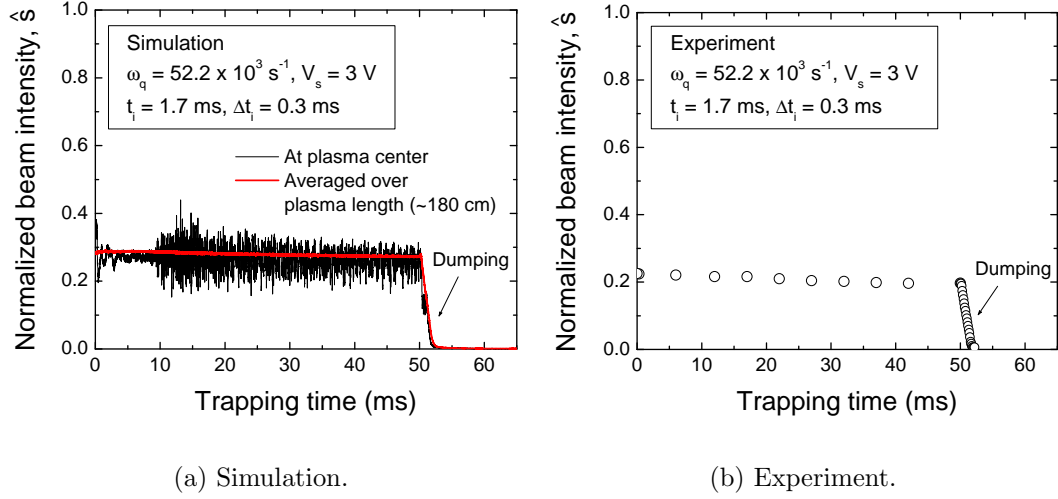
Figure 4.13:   Time history plots of the normalized beam intensity $\hat{s}$ obtained from (a) simulations, and (b) experiments for $V_s = 3$ V.

purpose of the PTSX device is to simulate the transverse dynamics of a continuous beam propagating in kilometer-long periodic-focusing transport lines. In this regard, it is important that the trapped plasma be maintained at least several tens of milliseconds without significant distortion of the radial profiles. For the case of beams with moderately low space-charge intensity and axial beam velocity, the effects of two-stream interactions on the transverse confinement after a long trapping time turn out to be small.   Both the simulations and experiments in Figs. 4.13(a) and 4.13(b) demonstrate that a plasma slowly injected with moderate space-charge intensity is maintained up to 50 ms (3000 lattice periods), and has only a slight decrease in the z-integrated normalized beam intensity $\hat{s}$, despite the local density fluctuations. It is interesting to note that when the trapping time is less than 6 ms in Fig. 4.13(a), the evolution of $\hat{s}$ at the plasma center shows oscillatory behavior similar to the experimental results in Fig. 4.7, both of which are direct consequences of the density gap introduced during the injection stage. The measured radial profiles in Fig. 4.14(a)
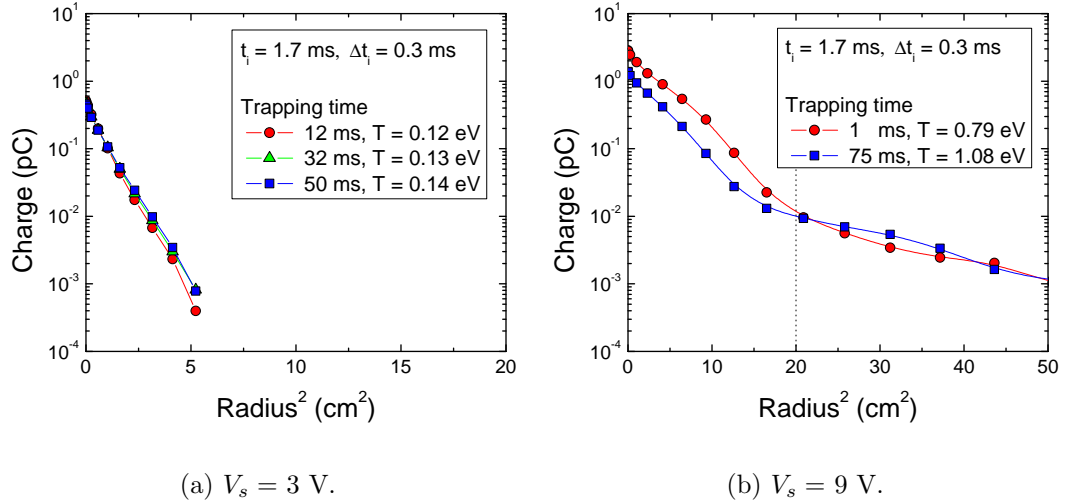
(a) $V_s = 3$ V.

(b) $V_s = 9$ V.

Figure 4.14: Radial trapped charge profiles with long trapping times for (a) $V_s = 3$ V and (b) $V_s = 9$ V. For the case of $V_s = 9$ V, due to the strong injection mismatch and the generation of fast ions during the injection stage, a non-Gaussian tail has already developed in the 1 ms of trapping. Further relaxation of the radial density profile and temperature is likely due to the result of enhanced two-stream interactions expected from the simulations [Figs. 4.15(b) and 4.15(c)].

also indicate that the beam remains undistorted in a thermal equilibrium state, with only a small increase in the transverse temperature.

On the other hand, if we inject a plasma with higher space-charge intensity and beam velocity, then two-stream interactions can affect the transverse dynamics of the trapped plasma. As the two-stream interactions become stronger, ions pick up first-order energy at the expense of the beam's zeroth-order axial kinetic energy. As seen in Figs 4.15(b) and 4.15(c), the first-order ion motion results in beam bunching, and increases the overall longitudinal temperature through space-charge-induced local (axial) electric fields [STIX, 1992]. When there is a coupling of the longitudinal and transverse motion through bouncing off the DC potential barrier and virtual cathode formation, we can expect some additional partitioning of energy between longitudinal ($T_\parallel$) and transverse ($T_\perp$) temperatures. Hence in the PTSX device, an increase in $T_\parallel$

(a) Right after injection.

(b) After 5 ms trapping.

(c) At the end of 40 ms trapping.

(d) In the middle of dumping.
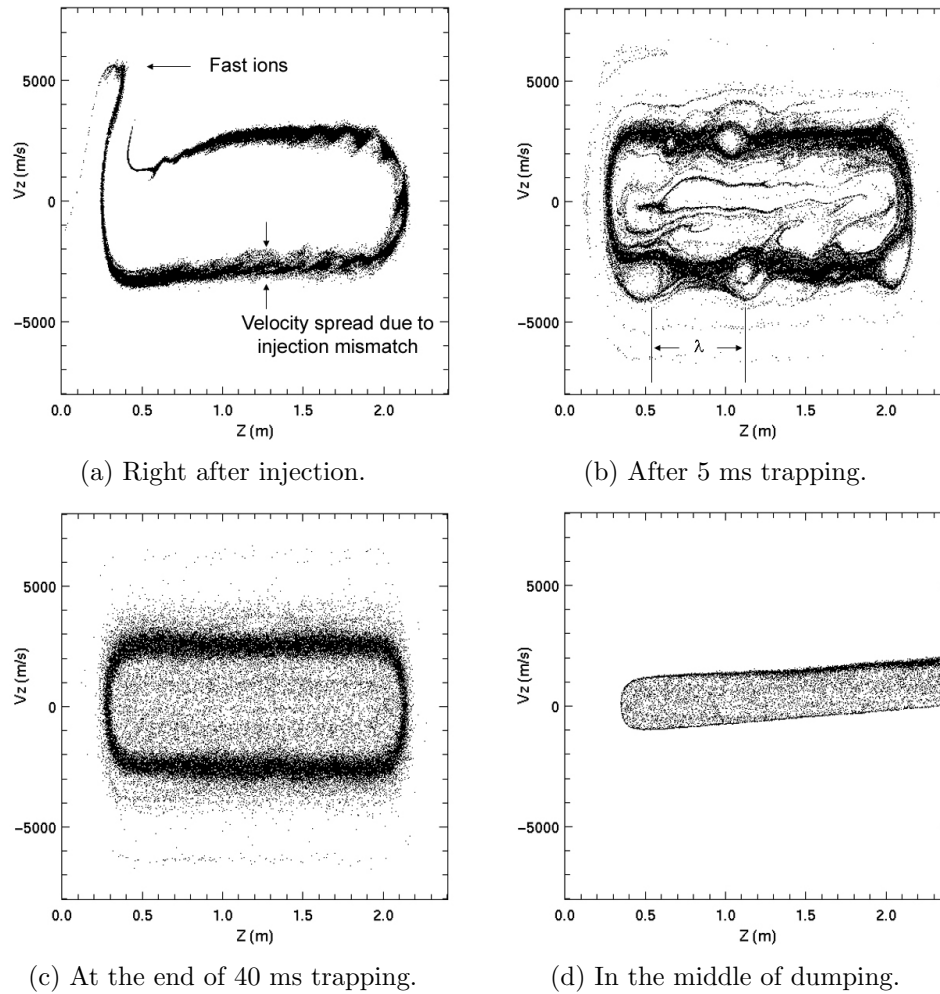
Figure 4.15: Plots of axial (z, v_z) phase space obtained from 3D WARP simulations for $\omega_q = 65.2 \times 10^3$ s^{-1} and $V_s = 9$ V. Due to the strong injection mismatch, the initial longitudinal temperature right after injection is substantially increased from $T_\parallel \approx T_s = 0.1$ eV (compare with Fig. 4.17). Further increase in the longitudinal temperature is attributed to the effects of two-stream interactions.
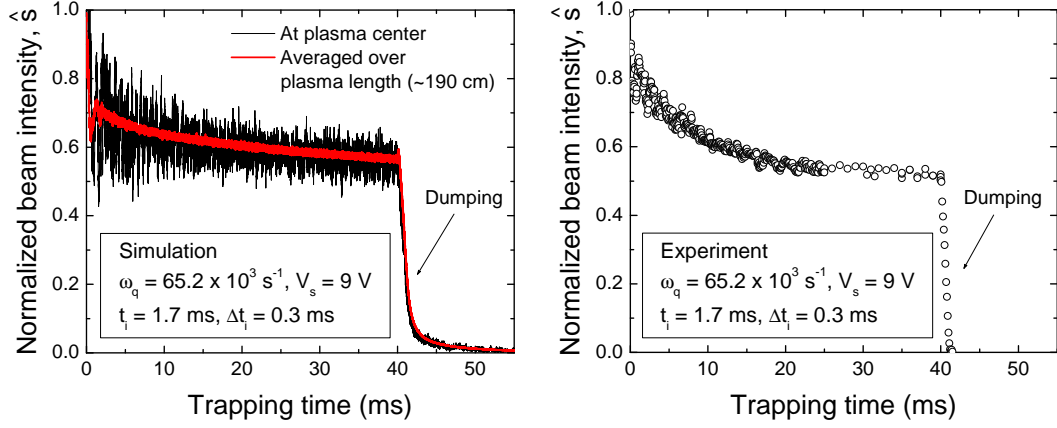
(a) Simulation. (b) Experiment.

Figure 4.16: Time history plots of normalized beam intensity $\hat{s}$ obtained from (a) simulations and (b) experiments for $V_s = 9$ V.

due to two-stream interactions may cause some relaxation in $T_\perp$ [similarly, an increase in $T_\perp$ due to injection mismatch may cause some relaxation in $T_\parallel$ as well. See Fig. 4.15(a)]. Although the longitudinal temperature itself is not practically measurable in PTSX, by assuming $T_\parallel \sim T_\perp$, we can estimate $T_\parallel$ from the effective transverse temperature $\bar{T}_\perp$ inferred from the radial density profile measurement and the global force balance equation [DAVIDSON and QIN, 2001].

Both the simulations and experiments in Figs. 4.16(a) and 4.16(b) indicate that the z-integrated normalized beam intensity $\hat{s}$ decays gradually and becomes nearly saturated after 20 ms of trapping. The local density fluctuations are quite active up to 10 ms and the measured signals are also somewhat noisy during this time period. The rapid decrease in $\hat{s}$ at the very beginning of the trapping ($\lesssim 1$ ms) in Figs. 4.16(a) and 4.16(b) is caused by fast ions. The injection time of $t_i = 1.7$ ms is much longer than the round-trip transit time of the beam ions with $V_s = 9$ V, resulting in considerable amount of fast ion population as seen in Fig. 4.15(a). These fast ions can be lost axially over the DC potential barrier in a single pass, or, after several

$\hat{s}$	V_s (V)	$T_\parallel$ (eV)	v_b (m/s)	$v_{T\parallel}$ (m/s)	$\hat{s}_{\mathrm{th}}$	$(\mathrm{Im}\omega)^{-1}_{\max}$ (ms)	$\lambda_{\max}$ (cm)
0.21	3	~ 0.12	< 2087	~ 417	> 0.56	-	-
0.74	9	~ 0.79	< 3615	~ 1071	> 0.71	> 1.85	< 45.9

Table 4.2: Characteristic parameters of two-stream interactions. We assume $T_\parallel \sim T_\perp$, where $T_\perp$ is estimated from the measured radial profiles. The axial beam velocity v_b will be slightly less than the initial value specified by V_s, due to the virtual cathode effect and increase in temperature. When $\hat{s} > \hat{s}_{\mathrm{th}}$, it is expected that the density perturbation grows with maximum growth rate $(\mathrm{Im}\omega)_{\max}$ and wavelength $\lambda_{\max}$.

bounces inside the trap, can have much higher radial excursions and finally be lost radially to the wall due to end effects (see **Appendix A**).

The typical characteristic parameters of two-stream interactions are summarized in Table 4.2. When $\hat{s}$ and v_b are moderately low, then two-stream instabilities are expected to be absent or weak, even for the relatively cold plasma ($T_\parallel \sim 0.12$ eV). On the other hand, if $\hat{s}$ and v_b are moderately high, then the two-stream interactions become unstable and strong even for relatively warm plasma conditions ($T_\parallel \sim 0.79$ eV). The estimated growth rate, $(\mathrm{Im}\omega)^{-1}_{\max} \sim 1.85$ ms, is much slower than the plasma frequency ($\omega_p^{-1} \sim 0.013$ ms) because of the external transverse focusing and finite thermal spread. In addition, the estimated wavelength of $\lambda_{\max} \sim 45.9$ cm is quite comparable to the velocity perturbation structure observed in Fig. 4.15(b). As an instability grows, the resultant plasma heating and radial expansion will increase $T_\parallel$, decrease $\hat{s}$ and v_b, and finally bring the plasma into the stable regime.

4.4 Virtual Cathode Formation

In principle, unstable two-stream interactions and particle loss (or expansion) associated with end effects can be reduced if the axial beam velocity is lowered. Since, for space-charge limited injection, $\hat{s} \propto n(0)/\omega_q^2 \propto I_{\mathrm{CL}}/v_b \propto V_e^{1.5}/V_s^{0.5}$, we can adjust V_e

(a) $V_s = 9$ V and $V_e = 7.5$ V.   (b) $V_s = 1.5$ V and $V_e = 4.25$ V.
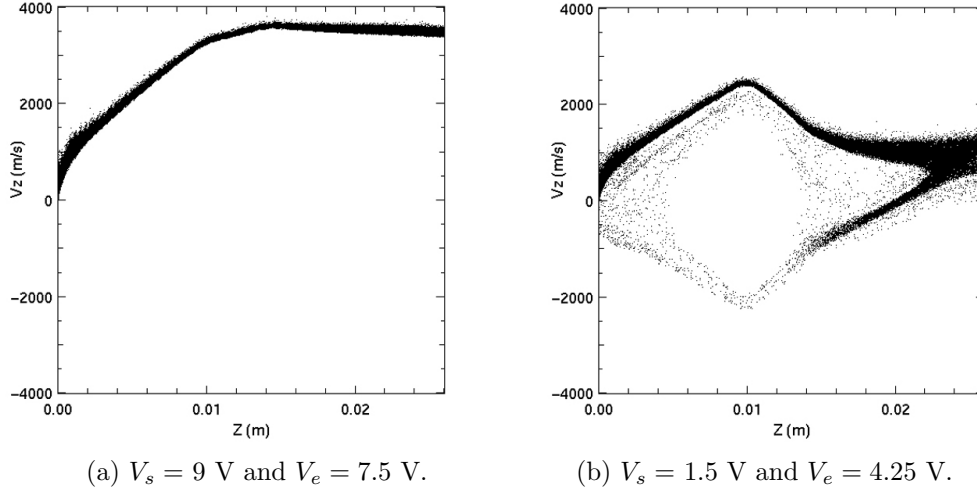
Figure 4.17:   3D WARP simulation results of ion injection with high normalized beam intensity ($\hat{s} \sim 0.85$). Plots of axial (z, v_z) phase space are made with $V_s = 9$ V and $V_e = 7.5$ V (a), and $V_s = 1.5$ V and $V_e = 4.25$ V (b). Here, the emission surface, and acceleration and deceleration grids are located at $z \simeq 0$, 0.01, and 0.014 m respectively. Note that the longitudinal temperature becomes slightly cooled and remains relatively unchanged compared to the initial source temperature (~ 0.1 eV) for case (a), while there is a significant longitudinal heating for case (b).

and V_s in such a way that $\hat{s}$ is kept constant while the axial beam velocity becomes much slower. However, in this case, self-field potential can be comparable to the axial kinetic energy of the beam particle. This self-generated potential barrier (often called a *virtual cathode*) deflects (or even reflects) beam particles and degrades the quality of the beam. As illustrated in the WARP simulation results near the source region (Fig. 4.17), significant particle deflection and beam quality degradation occur when the voltage of the emission surface is lowered from $V_s = 9$ V to 1.5 V keeping $\hat{s} \sim 0.85$. This virtual cathode formation sets the lower limit of axial beam velocity (or equivalent V_s) available in PTSX.

To measure the virtual cathode effect without relaxation of the plasma through injection mismatch, the focusing frequency has been increased to $\omega_q = 93.9 \times 10^3$ s^{-1}, which results in a value of the mismatch parameter μ close to 1. Because both
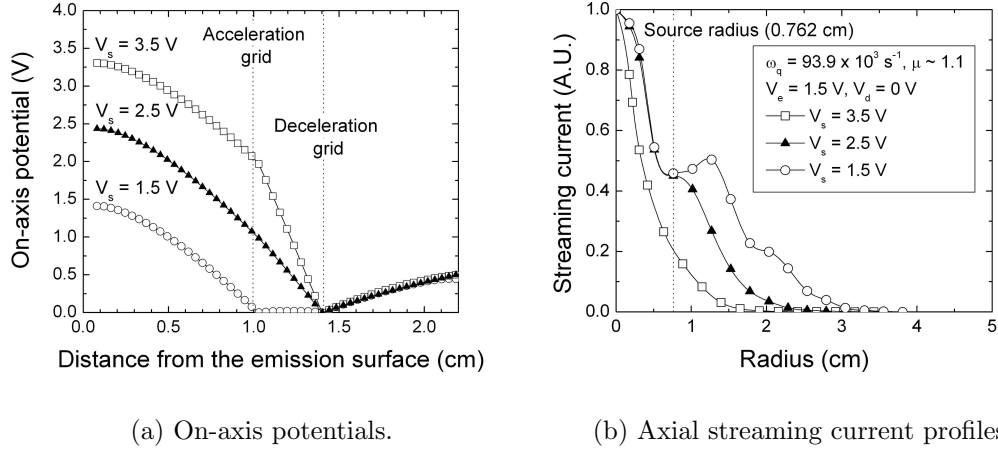
(a) On-axis potentials.

(b) Axial streaming current profiles.

Figure 4.18: Characteristics of the virtual cathode effect. On-axis potential distributions near the source region are estimated from the 3D WARP simulations (a), and axial streaming current profiles are measured by the charge collector at the end of the machine (b). In calculating the potential distributions, space-charge-limited emission and Neumann boundary condition are applied on the emission surface of the source.

injection mismatch and virtual cathode formation originate from too high space-charge density and produce non-equilibrium density profiles, it is somewhat difficult to make a clear distinction between them. While an injection mismatch results from radial force imbalance and mainly affects the transverse dynamics through envelope oscillations and halo formation, a virtual cathode results from an axial potential build-up and mainly affects the longitudinal dynamics through beam deflection. This beam deflection is highly localized near the source region and often produces sudden changes in current density. Figure 4.18 illustrates that, as V_s decreases, the beam becomes more subject to the virtual cathode effect and has a radial density profile with a significant shoulder near $r = r_s$ (source radius).

4.5 Summary and Discussion

This chapter has addressed the issue of how to make an initial quasi-equilibrium plasma in the PTSX that can be used as a baseline for subsequent beam physics experiments. Since most of the beam physics topics in high-intensity accelerators are related to how the initial quasi-equilibrium beam responds to external perturbations such as sudden beam mismatch, transverse compression, and random noise, it is critical to have well-characterized initial beam equilibria without effects that may invalidate the physics similarity between an actual periodic focusing accelerator system and the Paul trap configuration. Hence, in this chapter, the ion injection process on PTSX has been carefully optimized by investigating various factors such as injection beam mismatch (Sec. 4.1), generation of fast ions (Sec. 4.2), two-stream interactions (Sec. 4.3), and virtual cathode formation (Sec. 4.4). Finally, a quasi-equilibrium plasma with $\hat{s} = 0.2 \sim 0.3$ has been obtained, which corresponds to normalized intensities characteristic of the intense proton beams in the Oak Ridge National Laboratory (ORNL) Spallation Neutron Source (SNS) accumulator ring, and Fermi National Accelerator Laboratory (Fermilab) booster synchrotron for the Tevatron collider. This optimized plasma is stable for more than 50 ms, which is equivalent to more than 3000 full FODO lattice periods, and has a defocusing space-charge force that is about 10% of the applied transverse focusing force. In this parameter regime, it is expected that various self-consistent long-time-scale collective processes can be effectively studied in the PTSX.

Chapter 5

Transverse Beam Compression

Applications of present- and next-generation high-intensity accelerators [DAVIDSON and QIN, 2001; REISER, 1994; WANGLER, 1998] to high energy and nuclear physics, high energy density physics, and heavy ion fusion often require transverse and longitudinal compression of the charge bunch to a small spot size at the target location [DORF *et al.*, 2006; SEFKOW and DAVIDSON, 2006]. Typically, the transverse compression can be achieved by means of increasing the focusing strength of the alternating-gradient (AG) lattice along the beam propagation direction [DORF *et al.*, 2006]. However, intense beam propagation through such a lattice transition region inevitably leads to a certain amount of beam mismatch and emittance growth [REISER, 1994; WANGLER, 1998]. Furthermore, a beam mismatch can produce halo particles and may deteriorate the beam quality [WANGLER *et al.*, 1998; ALLEN *et al.*, 2002]. Hence, it is of considerable practical importance to determine how smooth the lattice transition should be in order that the beam mismatch and emittance growth are minimized during the transverse compression process. Because high-intensity accelerator systems are typically very sophisticated and expensive to operate, dedicated

experimental studies of transverse compression are limited in number and scope [HEN-ESTROZA *et al.*, 2004]. On the other hand, the PTSX device provides a compact and flexible laboratory setup for the experimental investigation of transverse compression. The amplitude and frequency of the voltage waveform applied to the electrodes of the PTSX device correspond to the focusing strength and lattice spacing in an AG system, respectively. The computer-generated arbitrary voltage waveform can emulate various types of transition patterns. Hence, in this chapter, we present experimental results describing the transverse compression of an intense beam pulse by compressing a long nonneutral ion plasma trapped in the PTSX device, and compare them with analytical theory and numerical simulations. In Sec. 5.1, analytical estimations are made based on a smooth-focusing model. Four different cases are considered: instantaneous and adiabatic changes in voltage amplitudes; and adiabatic changes in instantaneous and applied focusing frequencies. In Sec. 5.2, experimental results on both compression and expansion ("decompression") are presented. In Sec. 5.3, several key experimental results are analyzed either by WARP 2D PIC simulations or by using a Kapchinskij-Vladimirskij (KV) equivalent beam model.

5.1 Analytical Theory

For simplicity in the theoretical analysis presented in this section, we assume that the beam states before and after the transition are both quasi-equilibrium states, and the average effects of the quadrupole focusing field are described by an equivalent smooth-focusing force [DAVIDSON and QIN, 2001; REISER, 1994]. As described in **Chapter 2** of this thesis, in equilibrium, the global radial force balance on the beam

ions with charge q and mass m in the smooth-focusing approximation is given by

$$m\omega_q^2 R_b^2 = 2\bar{T}_\perp + \frac{Nq^2}{4\pi\epsilon_0}, \tag{5.1}$$

where $N = 2\pi \int_0^{r_w} dr r n(r)$ is the line density, $R_b^2 = (2\pi/N) \int_0^{r_w} dr r r^2 n(r)$ is the (equilibrium) mean-squared radius of the beam, and $\bar{T}_\perp$ is the effective transverse temperature defined by $\bar{T}_\perp = m \left\langle \dot{x}_{sf}^2 + \dot{y}_{sf}^2 \right\rangle_0 /2$. Note that the effective transverse temperature $\bar{T}_\perp$ measures the kinetic energy per particle averaged over the transverse phase space in the smooth-focusing equilibrium.

For a general applied voltage waveform $V_0(t) = \hat{V}_0(t) \sin[2\pi f_0(t) t]$, where $f_0(t)$ is an arbitrary applied focusing frequency, the smooth-focusing frequency is given approximately by [DORF, 2006; GILSON *et al.*, 2007a]

$$\omega_q(t) \approx \frac{1}{2\pi\sqrt{2}} \left(\frac{8q}{m\pi r_w^2} \right) \frac{\hat{V}_0(t)}{d[f_0(t) t]/dt}. \tag{5.2}$$

When $f_0 = const.$, Eq. (5.2) is reduced to Eq. (2.25) of **Chapter 2**. If ω_q is changed, a new quasi-equilibrium state will be achieved satisfying the force balance equation (5.1) with new values of R_b and $\bar{T}_\perp$. When ω_q is increased, the plasma is compressed; and when ω_q is decreased, the plasma expands.

5.1.1 Changes in Lattice Amplitude

In this section, changes in ω_q created by changing the voltage waveform amplitude $\hat{V}_0$ at fixed focusing frequency $f_0 = const.$ are considered. By increasing or decreasing $\hat{V}_0$, we can change ω_q accordingly and achieve a new plasma state. To describe transitions ranging from instantaneous changes to adiabatic changes, we adopt a simple model in which $\hat{V}_0$ varies in time according to

$$\hat{V}_0(t) = V_i + (V_f - V_i) \left[\exp\left(\frac{\tau_{1/2} - t}{\tau/4} \right) + 1 \right]^{-1}, \tag{5.3}$$
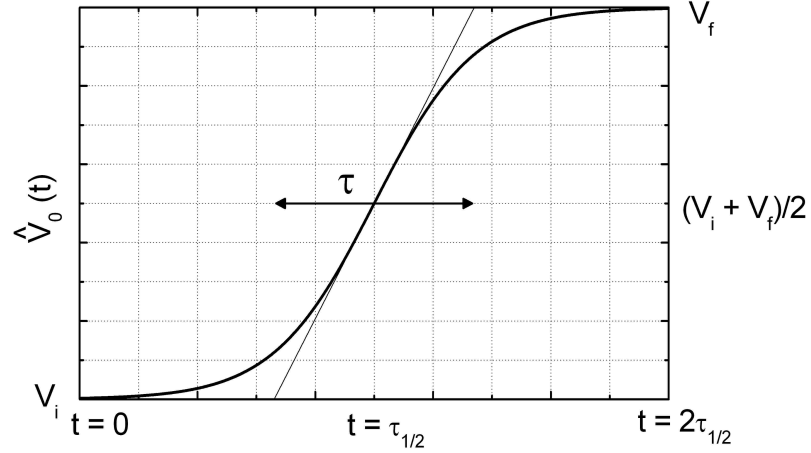
Figure 5.1: Plot of voltage waveform amplitude $\hat{V}_0(t)$ used in the compression experiments. During the characteristic time scale τ, about 80% of the transition is completed. Note that $\tau = 0$ corresponds to an instantaneous change. If τ is too long, there will be small discontinuities in the voltage amplitudes at $t = 0$ and $t = 2\tau_{1/2}$.

where $\tau_{1/2}$ is the time at which the transition is half complete, and τ is the characteristic time scale for the variation of $\hat{V}_0(t)$ from the initial amplitude V_i to the final amplitude V_f (Fig. 5.1). The number of lattice periods for the transition can be defined as $N_t = \tau f_0$, where $N_t = 0$ corresponds to an instantaneous change. We assume that the transition begins at $t = 0$, when the beam is in an initial equilibrium state and well-characterized, and is essentially complete by $t = 2\tau_{1/2}$. For continuity of the voltage waveform at $t = 0$ and $t = 2\tau_{1/2}$, we require $\exp(4\tau_{1/2}/\tau) \gg 1$.

Instantaneous Transition

The analysis in this section makes use of total energy conservation discussed by Reiser [REISER, 1991; CHUNG *et al.*, 2007b]. When a beam is in a quasi-equilibrium state, the average transverse kinetic energy per particle is identified with the effective transverse temperature as $E_k = \bar{T}_\perp$. Moreover, the average potential energy per particle

associated with the external focusing force is calculated to be

$$E_p = \frac{2\pi}{N} \int_0^{r_w} dr\, r \frac{1}{2} m\omega_q^2 r^2 n(r) = \frac{1}{2} m\omega_q^2 R_b^2, \tag{5.4}$$

in the smooth-focusing approximation. The average electrostatic energy associated with the self-electric field is defined by $E_e = (2\pi/N) \int_0^{r_w} dr\, r \frac{1}{2}\epsilon_0(-\partial_r\phi^s)^2$ [DAVIDSON and QIN, 2001]. For analytical simplicity, we assume that the beam has a uniform density profile $n(r) = \hat{n} = const.$ for $0 \le r < \sqrt{2}R_b$. Then the electrostatic energy can be calculated as $E_e = (Nq^2/4\pi\epsilon_0)\left[\ln(r_w/\sqrt{2}R_b) + 1/4\right]$, where r_w is the radius of the perfectly conducting wall. Therefore, the total energy per particle, $E = E_k + E_p + E_e$, for a beam with uniform density profile can be expressed as

$$E = m\omega_q^2 R_b^2 + \frac{Nq^2}{4\pi\epsilon_0}\left[\ln\left(\frac{r_w}{\sqrt{2}R_b}\right) - \frac{1}{4}\right], \tag{5.5}$$

where use has been made of the global force balance equation (5.1) to eliminate $\bar{T}_\perp$.

For an instantaneous change of the focusing field strength from ω_{qi} to ω_{qf}, there will be an energy difference between the initial and final equilibrium states given by $\Delta E = m(\omega_{qf}^2 - \omega_{qi}^2)R_{bi}^2/2$, where R_{bi} is the rms radius of the initial beam, which is assumed to remain constant at the instant of transition [DAVIDSON and QIN, 2001]. Note that $\Delta E > 0$ for compression, while $\Delta E < 0$ for expansion. This energy difference represents the free energy that can be redistributed by nonlinear space-charge forces or instabilities [REISER, 1991]. If the beam relaxes from an initial state with energy E_i into a final quasi-equilibrium state with energy $E_f = E_i + \Delta E$, we obtain the transcendental equation for the final rms radius R_{bf},

$$\left(\frac{R_{bf}}{R_{bi}}\right)^2 - \frac{K}{2\omega_{qf}^2 R_{bi}^2}\ln\left(\frac{R_{bf}}{R_{bi}}\right) - \frac{1}{2}\left(1 + \frac{\omega_{qi}^2}{\omega_{qf}^2}\right) = 0, \tag{5.6}$$

where $K = 2Nq^2/4\pi\epsilon_0 m$ is the effective self-field perveance, and the line density N is assumed to remain constant during the transition. Redistribution of the free energy ΔE usually introduces an emittance growth [REISER, 1994; WANGLER, 1998].

Because there is often a large mismatch after an instantaneous transition, this emittance growth typically occurs on the time scale of the envelope oscillations, and is associated with the formation of a low-density halo region [WANGLER, 1998; WANGLER *et al.*, 1998]. Since the formation of the halo is not included in the present simplified theoretical model, the final rms radius R_{bf} measured in experiments with a significant halo contribution during an instantaneous transition is usually larger than the analytical estimate in Eq. (5.6).

Adiabatic Transition

Beams in an ideal equilibrium do not experience emittance growth. However, beams are rarely in an ideal equilibrium, and any changes in the focusing system and nonuniformities in charge density can produce changes in the beam distribution, usually accompanied by emittance growth [WANGLER, 1998; STRASBURG, 2001]. Transverse compression also induces emittance growth. However, we can minimize the emittance growth by compressing the beam very slowly. For a quantitative description of the adiabaticity of the compression process, we make use of the following equation that describes the evolution of the rms radius of a long charge bunch with uniform density profile [DAVIDSON and QIN, 2001; DORF *et al.*, 2006]

$$\frac{d^2}{dt^2} R_b + \left(\omega_q^2(t) - \frac{K}{2R_b^2} \right) R_b = \frac{\epsilon^2(t)}{4R_b^3}. \tag{5.7}$$

Here, the smooth-focusing frequency $\omega_q(t)$ evolves in time according to Eqs. (5.2) and (5.3), and $\epsilon(t) = 2R_b \left[\left\langle \dot{x}_{sf}^2 + \dot{y}_{sf}^2 \right\rangle - (dR_b/dt)^2 \right]^{1/2}$ is the transverse emittance defined in the beam frame. The statistical average is made over a distribution function of the slow variables in the smooth-focusing approximation. Hence, to describe the time evolution of the transverse emittance self-consistently, we need to solve the nonlinear Vlasov-Maxwell equations numerically. However, for the case of an adiabatic

transition in $\omega_q(t)$, we can assume $\epsilon(t) \approx 2R_b \left\langle \dot{x}_{sf}^2 + \dot{y}_{sf}^2 \right\rangle_0 = 2R_b(2\bar{T}_\perp/m)^{1/2} = const$ [DORF *et al.*, 2006]. Here, $\langle \cdots \rangle_0$ denotes the statistical average over the equilibrium distribution function in the smooth-focusing approximation [DAVIDSON and QIN, 2001]. If we change $\omega_q(t)$ slowly, then there is a small-amplitude perturbation around the quasi-equilibrium radius $\bar{R}_b = \left[\left(K + \sqrt{K^2 + 4\epsilon^2\omega_q^2} \right) / 4\omega_q^2 \right]^{1/2}$, with oscillation frequency given by $\omega_B = 2\omega_q \left(1 - K/4\bar{R}_b^2\omega_q^2 \right)^{1/2}$. As long as the characteristic transition time τ is much longer than ω_B^{-1}, the beam mismatch induced by changing ω_q remains small [DORF *et al.*, 2006]. Therefore, the condition for adiabatic transition is given by

$$\frac{N_t}{f_0} \min \left[2\omega_q \left(1 - K/4\bar{R}_b^2\omega_q^2 \right)^{1/2} \right] > 1. \tag{5.8}$$

It is evident from Eq. (5.8) that for the case of beam expansion ($\omega_{qf}/\omega_{qi} < 1$), a larger number N_t of lattice periods is required for the adiabatic transition to occur (for example, see Fig. 5.6). If the beam relaxes adiabatically from an initial state with $\epsilon_i = 2R_{bi}(2\bar{T}_{\perp i}/m)^{1/2}$ to a final state with $\epsilon_f = 2R_{bf}(2\bar{T}_{\perp f}/m)^{1/2}$, then by assuming $\epsilon_i \simeq \epsilon_f$ and making use of Eq. (5.1) we obtain the simple algebraic equation for the final rms radius R_{bf},

$$\left(\frac{R_{bf}}{R_{bi}} \right)^4 - \frac{K}{2\omega_{qf}^2 R_{bi}^2} \left[\left(\frac{R_{bf}}{R_{bi}} \right)^2 - 1 \right] - \frac{\omega_{qi}^2}{\omega_{qf}^2} = 0, \tag{5.9}$$

where it is assumed that K (or equivalently N) remains constant during the transition.

5.1.2   Changes in Lattice Period

In this section, changes in ω_q created by modulating the applied focusing frequency $f_0(t)$ at fixed voltage waveform amplitude $\hat{V}_0 = const.$ are considered. Modulation in $f_0(t)$ can be made by requiring that either $\frac{d}{dt}[f_0(t)t]$ or $f_0(t)$ itself to be changed adiabatically [i.e., with functional form given in Eq. (5.3)].
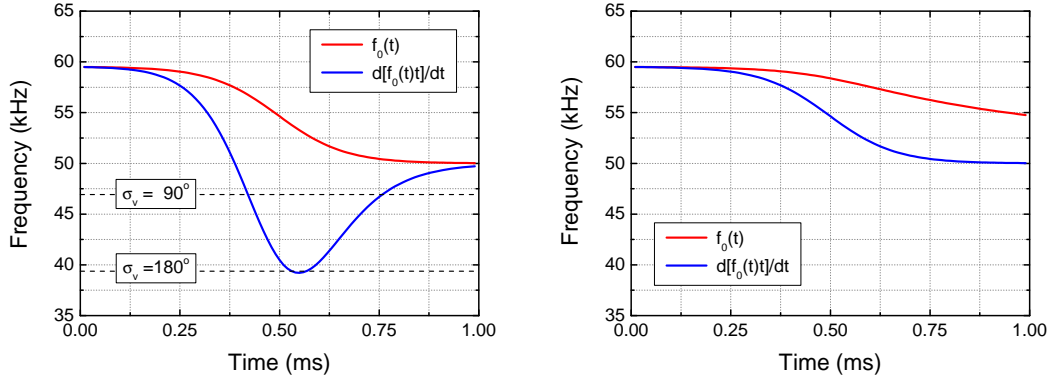
(a) Adiabatic changes in f_0.

(b) Adiabatic changes in $d(f_0 t)/dt$.

Figure 5.2: Evolution of applied focusing frequency $f_0(t)$ (red curve) and instantaneous frequency $d[f_0(t)t]/dt$ (blue curve) after specifying either (a) the applied focusing frequency, or (b) the instantaneous frequency to be adiabatic. Note that for case (a), there can be an undershoot (or overshoot) of the instantaneous frequency depending on the final frequency and the number of lattice periods for the transition.

Adiabatic Transition in Applied Focusing Frequency

Similar to the voltage amplitude change in Eq. (5.3), adiabatic transition in the applied focusing frequency is made according to the functional form given by

$$f_0(t) = f_i + (f_f - f_i) \left[\exp\left(\frac{\tau_{1/2} - t}{\tau/4} \right) + 1 \right]^{-1}. \tag{5.10}$$

Note that $f_0(t = 0) \simeq f_i$ and $f_0(t = 2\tau_{1/2}) \simeq f_f$. Although $f_0(t)$ itself decreases monotonically from its initial value f_i to the final value f_f, there can be an undershoot (or overshoot) in the corresponding instantaneous frequency when transition is not made gradually enough [Fig. 5.2(a)]. Since, ω_q is dependent on $\frac{d}{dt}[f_0(t)t]$ rather than $f_0(t)$ [see Eq. (5.2)], this undershoot will give rise to a nonmonotonic variation of ω_q and a corresponding nonmonotonic transition in the beam equilibrium. In particular, there exits a threshold time scale τ_c of the transition below which the resultant $\frac{d}{dt}[f_0(t)t]$ makes the smooth-focusing vacuum phase advance σ_v^{sf} exceed the single-particle orbit stability limit ($= 115.6°$ for the sinusoidal waveform considered

here) [DAVIDSON and QIN, 2001]. The values of τ_c depend on the final frequency f_f and can be estimated numerically [GILSON *et al.*, 2007a]. For example, both $f_0(t)$ and $\frac{d}{dt}[f_0(t)t]$ are plotted in Fig. 5.2(a) for the case where $f_i = 60$ kHz and $f_f = 50$ kHz. The transition is made over $2\tau_{1/2} = 1$ ms and $\tau = 20/f_i$. Note that near the half-way point of the transition, the instantaneous frequency becomes temporarily too low so that $\sigma_v^{sf} > 115.6°$ (equivalently, the exact vacuum phase advance $\sigma_v > 180°$). In addition to the single-particle orbit instability, the beam may experience mismatches to the focusing channel during the lattice transition. Particularly when $\sigma_v > 90°$, this mismatch can excite the (confluent resonance) envelope instability [REISER, 1994; LUND and BUKH, 2004].

Adiabatic Transition in Instantaneous Frequency

To obtain an adiabatic transition of the instantaneous frequency without an undershoot (or overshoot), we require $d[f_0(t)t]/dt$ to be changed according to

$$\frac{d}{dt}[f_0(t)t] = f_i + (f_f - f_i)\left[\exp\left(\frac{\tau_{1/2} - t}{\tau/4}\right) + 1\right]^{-1}. \tag{5.11}$$

Note that $\frac{d}{dt}[f_0(t)t]_{t=0} \simeq f_i$ and $\frac{d}{dt}[f_0(t)t]_{t=2\tau_{1/2}} \simeq f_f$. Integrating Eq. (5.11) with the initial condition $f_0(t = 0) = f_i$ yields the functional form of the applied focusing frequency given by

$$
\begin{aligned}
f_0(t) &= \frac{1}{2}(f_i + f_f) \\
&+ \frac{1}{2}(f_f - f_i)\left(\frac{\tau/2}{t}\right)\left[\ln\left\{\cosh\left(\frac{\tau_{1/2} - t}{\tau/2}\right)\right\} - \ln\left\{\cosh\left(\frac{\tau_{1/2}}{\tau/2}\right)\right\}\right]. \tag{5.12}
\end{aligned}
$$

Although $f_0(t)$ itself is discontinuous at $t = 2\tau_{1/2}$ [see Fig. 5.2(b)], by slightly adjusting $\tau_{1/2}$ so that $2\pi f_0(2\tau_{1/2})(2\tau_{1/2}) = 2\pi \times$ integer, we can eliminate the phase difference. This transition turns out to be more relevant to emulate transverse compression of an intense beam through lattice period changes.
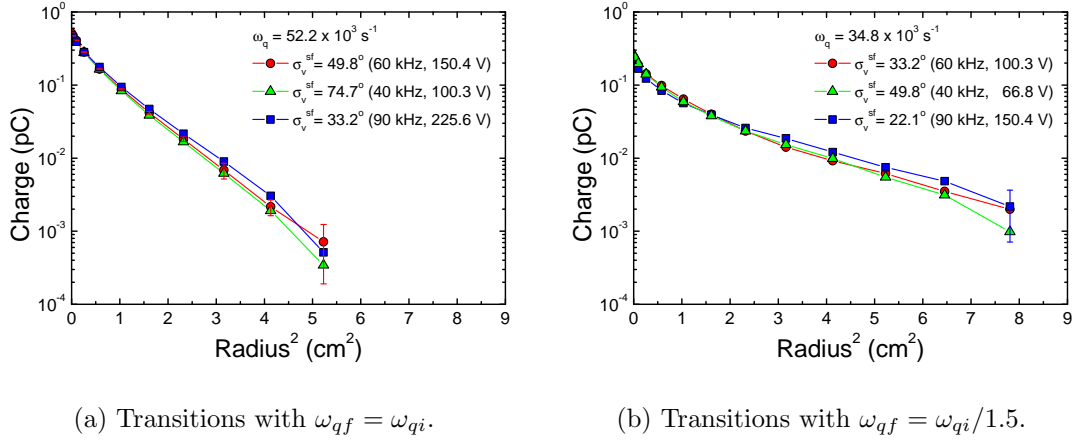
(a) Transitions with $\omega_{qf} = \omega_{qi}$.

(b) Transitions with $\omega_{qf} = \omega_{qi}/1.5$.

Figure 5.3: Measured radial charge profiles after abrupt changes in focusing frequencies and voltage amplitudes are made with (a) $\omega_{qf} = \omega_{qi}$ and (b) $\omega_{qf} = \omega_{qi}/1.5$. The initial beam profile prior to transition is shown in the red curve in frame (a) with error bars. Note that a straight line in the log versus r^2 plot indicates that the radial profile is a Gaussian function of r.

5.2 Experimental Results

The initial charge bunch for the compression experiments is trapped in the PTSX device with a sinusoidal voltage waveform with $f_0 = 60$ kHz and $\hat{V}_0 = 150.4$ V, which corresponds to $\omega_q = 52.2 \times 10^3$ s^{-1} and smooth-focusing vacuum phase advance $\sigma_v^{sf} = \omega_q/f_0 = 49.8°$. Ion injection into the trap has been optimized through the process described in **Chapter 4** of this thesis in order that the initial beam is both well-matched to the focusing lattice and well-characterized [CHUNG *et al.*, 2007c]. The initial beam has normalized intensity $\hat{s} \approx 0.22$, and its density profile is nearly Gaussian with $R_b = 0.85$ cm and $\bar{T}_\perp = 0.13$ eV [red curve in Fig. 5.3(a)]. The total duration of the transition $2\tau_{1/2}$ is typically 1 ms, which is equivalent to 60 lattice periods for $f_0 = 60$ kHz. The radial charge profile $Q(r)$, which is proportional to the number density $n(r)$, is measured by averaging the signal at each radial position over 20 repeated measurements. The size of the charge collector aperture r_c and an
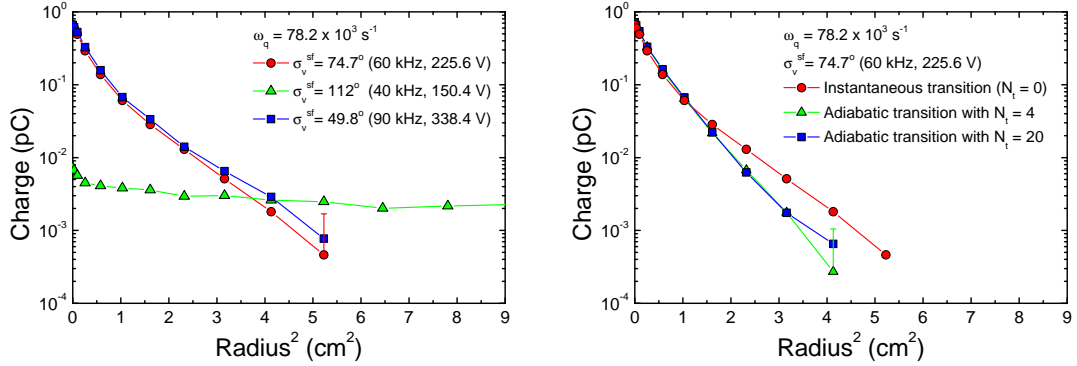
(a) Transitions with $\omega_{qf} = \omega_{qi} \times 1.5$.

(b) Transitions with $V_f = V_i \times 1.5$.

Figure 5.4: Measured radial charge profiles after transitions with $\omega_{qf} = \omega_{qi} \times 1.5$. In case (a), instantaneous transitions are made by allowing both the frequencies and amplitudes to be changed. Note that when the final vacuum phase advance is too high, the plasma is lost completely (green curve). In case (b), the transitions are made instantaneously (circles), adiabatically with $N_t = 4$ (triangles), and adiabatically with $N_t = 20$ (squares). The initial smooth-focusing vacuum phase advance σ_{vi}^{sf} is 49.8°, and the applied focusing frequency f_0 is fixed at 60 kHz during the transitions.

estimate of the length of the trapped plasma L_p are then used to calculate $n(r) \approx Q(r)/q\pi r_c^2 L_p$ (see **Chapter 3** for details). For example, the on-axis charge $Q(0)$ prior to the transition in Fig. 5.3(a) corresponds to an on-axis density $n(0)$ of 0.83×10^5 cm^{-3}. Since the trapped plasmas are highly reproducible and the offset errors in the charge collector system are typically ~ 1 fC, the relative errors in the calculation of low-order moments of the particle distribution (such as line density, rms radius, and emittance) are typically a few percent. Typical standard errors in the radial profile measurement are also shown in Fig. 5.3(a).

To begin with, we exam the validity of the smooth-focusing approximation by changing $\hat{V}_0$ and f_0 abruptly at $t = \tau_{1/2}$, where ω_q is kept fixed. Theory predicts that unless the phase advance is too high, there will be no changes in the smooth-focusing equilibria. Figure 5.3(a) demonstrates that the measured charge profiles are almost identical even after significant changes are made in both $\hat{V}_0$ and f_0. Since ω_q is fixed,

no compression is achieved in the smooth-focusing equilibria as expected. Only the final smooth-focusing vacuum phase advance is rescaled to $\sigma_{vf}^{sf} = \sigma_{vi}^{sf}(f_i/f_f)$. The smooth-focusing approximation is also valid when the beam is actually compressed or expanded. Fig. 5.3(b) indicates that when ω_q is decreased from 52.2×10^3 s^{-1} to 34.8×10^3 s^{-1}, the initial beam is expanded in nearly the same manner regardless of the specific values for $\hat{V}_0$ and f_0. This is also true for the compression cases shown in Fig. 5.4(a). The exception is if σ_v^{sf} becomes too large [green curve in Fig. 5.4(a)]. Note that in Fig. 5.4(a) the transitions are made instantaneously. Therefore, the compression is not effective in the beam tail due to the beam mismatch [compare with Fig. 5.4(b)].

5.2.1 Changes in Lattice Amplitude

In Fig. 5.5, scans of the number N_t of lattice periods for the compression transition reveal that for voltage amplitude increases of 50% and 90%, the compression leads to an increase in the on-axis charge that saturates after the transition is made in several lattice periods. There is no extra benefit in adiabatic compression by making the transition more gradual than approximately four lattice periods. Indeed, the condition for adiabaticity [Eq. (5.8)], $\tau\omega_b \approx 6.9 > 1$, is well satisfied for compressions with $N_t = 4$. It is interesting to note that for $N_t = 0$ (instantaneous transition), due to the beam loss and emittance growth associated with the large beam mismatch, the on-axis charge after the instantaneous transition with $V_f/V_i = 1.9$ becomes smaller than for the case with $V_f/V_i = 1.5$. Figure 5.4(b) indicates that the measured radial profiles for adiabatic transitions with $N_t = 4$ and $N_t = 20$ are almost identical, whereas for the instantaneous case ($N_t = 0$), the radial profile broadens considerably. Another example that illustrates this point is presented in Fig. 5.6, which shows
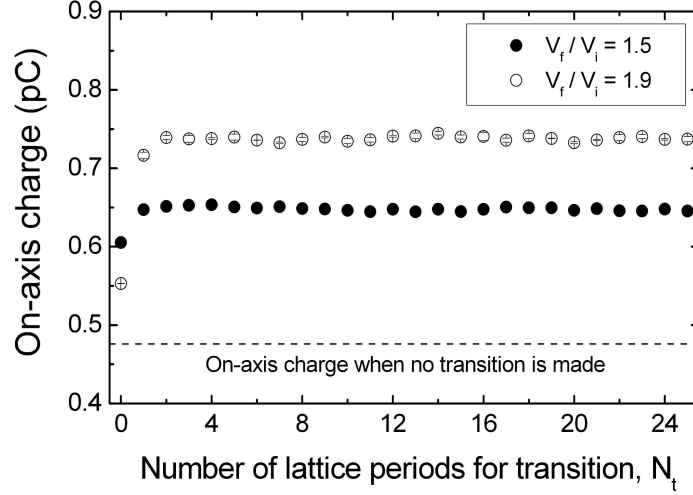
Figure 5.5: Measured on-axis charge dependence on the number N_t of lattice periods for transitions with $V_f/V_i = 1.5$ (solid circles) and $V_f/V_i = 1.9$ (open circles) for $\sigma_{vi}^{sf} = 49.8°$ and $f_0 = 60$ kHz. $N_t = 0$ corresponds to an instantaneous transition. Here, the on-axis charge prior to the transition is 0.476 pC, which is indicated by the dashed line.

the results of solving Eq. (5.7) numerically. For an adiabatic compression with $V_f/V_i = 1.5$, it is evident that $N_t = 4$ constitutes enough lattice periods to avoid mismatch oscillations, as expected from the experimental data. However, to make certain that the transitions are sufficiently gradual, we have performed the subsequent adiabatic compression experiments with $N_t = 20$. On the other hand, as noted earlier in relation to Eq. (5.8), larger values of N_t are required for the case of expansion. As illustrated in Fig. 5.6(b), unlike in the compression, $N_t = 4$ is not enough to suppress mismatch oscillations during the beam expansion. Hence, to make the expansion as smooth as possible, we set $N_t = 40$ for expansion experiments. If $N_t > 40$, then small discontinuities in the voltage amplitude specified by Eq. (5.3) become larger than 5% at the start and end points of the transition, which can be another source of mismatch.

(a) Transitions with $V_f = V_i \times 1.5$.

(b) Transitions with $V_f = V_i/1.5$.
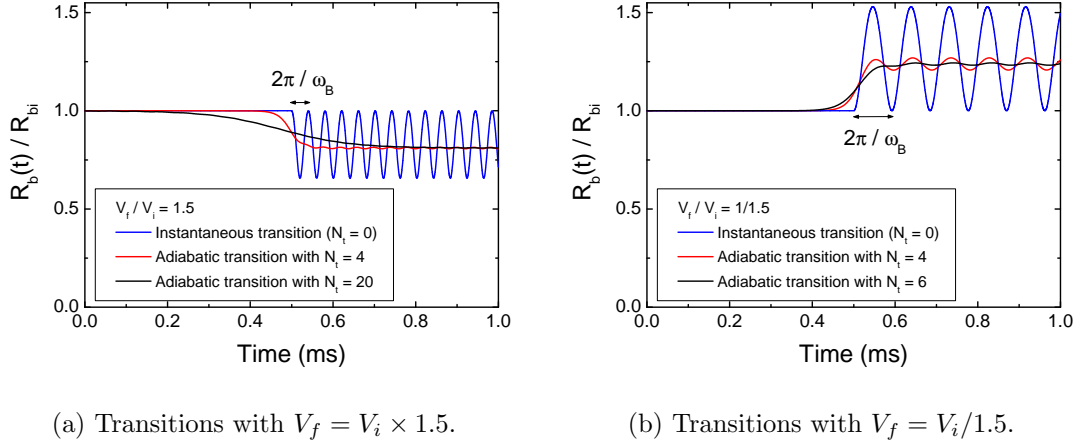
Figure 5.6: Numerical solutions to the envelope equation (5.7) with $\epsilon(t) = const.$ Evolution of the rms beam radius $R_b(t)$ during (a) compressions with $V_f/V_i = 1.5$ and (a) expansions with $V_f/V_i = 1/1.5$. Note that for instantaneous transitions or adiabatic transitions with not enough transition periods N_t, envelope oscillations with breathing mode frequency ω_B are excited. Here, σ_{vi}^{sf} is 49.8°, and $f_0 = 60$ kHz.

In Fig. 5.7, the ratio of the final to initial on-axis beam density $n_f(0)/n_i(0)$ is estimated analytically and measured experimentally. The transition is made either instantaneously or adiabatically, and the ratio of the final to initial voltage amplitude, V_f/V_i, is scanned from 0.1 to 2.2. Since the applied focusing frequency is fixed, we have $V_f/V_i = \omega_{qf}/\omega_{qi} = \sigma_{vf}^{sf}/\sigma_{vi}^{sf}$. Except for the lower $(V_f/V_i < 0.6)$ and upper $(V_f/V_i > 1.6)$ ranges, the experimental data are in relatively good agreement with the analytical estimates. In Fig. 5.7(a), the theoretical estimates are made by using Eqs. (5.6) and (5.9). When it is assumed that the transverse emittance is approximately constant during the adiabatic transition [DORF *et al.*, 2006], the on-axis beam density increases approximately linearly according to the increase in the voltage amplitude. However, the normalized beam intensity decreases after the compression because $\hat{s} \propto \hat{n}\omega_q^{-2} \propto \omega_q^{-1}$ due to linear dependence of $\hat{n}$ on ω_q. In Fig. 5.7(b), the on-axis beam density (or equivalently, the on-axis charge) is measured by opening the diagnostic end electrodes immediately after the transition is complete. Since it takes about 2 ms to dump all
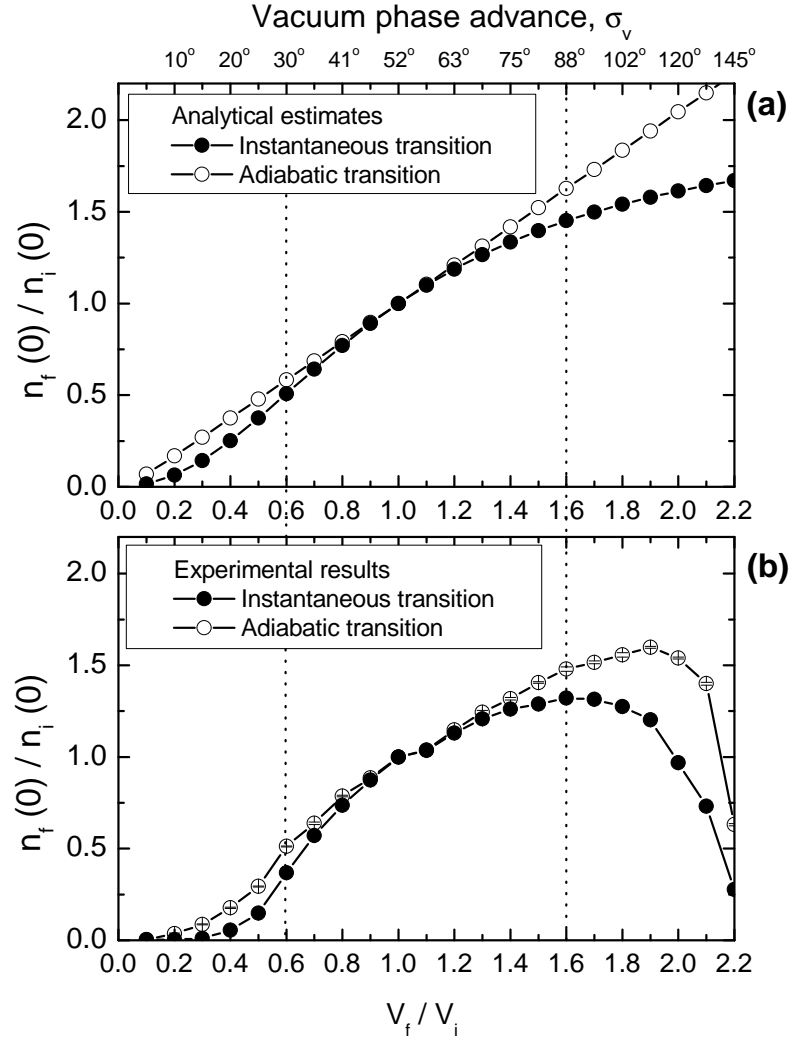
Figure 5.7: Plots of the ratio of final to initial on-axis beam density $n_f(0)/n_i(0)$ for different values of V_f/V_i with $f_0 = 60$ kHz. The values $n_f(0)/n_i(0)$ are either (a) estimated from analytical theory, or (b) measured experimentally. Here, the initial vacuum phase advance is $\sigma_{vi} = 52°$, which corresponds to $\sigma_{vi}^{sf} = 49.8°$. Both instantaneous (solid circles) and adiabatic (open circles) transitions are considered.

(a) Transitions with $V_f = V_i \times 1.2$.

(b) Transitions with $V_f = V_i \times 1.9$.
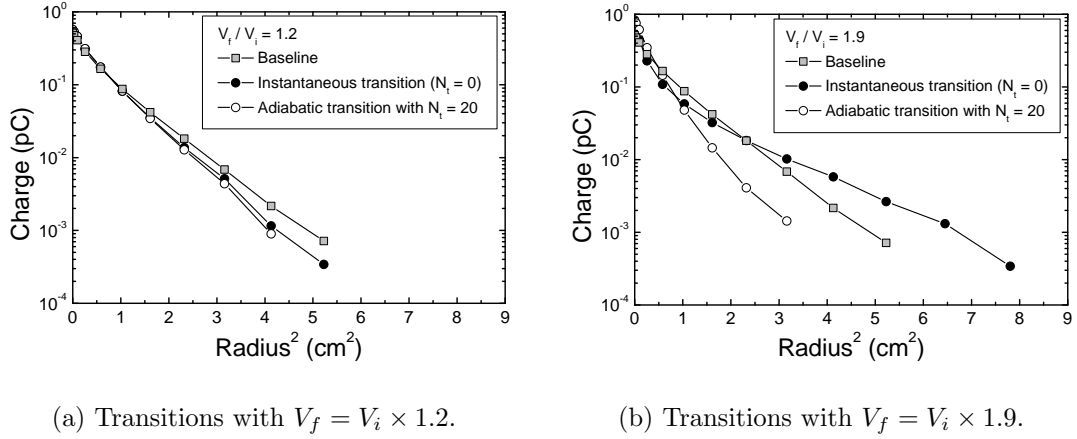
Figure 5.8: Measured radial charge profiles after transitions with (a) $V_f/V_i = 1.2$, and (b) $V_f/V_i = 1.9$ for $\sigma_{vi}^{sf} = 49.8°$ and $f_0 = 60$ kHz. The transitions are made either instantaneously (solid circles), or adiabatically with $N_t = 20$ (open circles). Here, squares correspond to the radial profile for the case where $V_f = V_i$ (no transition). A straight line in the log versus r^2 plot indicates that the radial profile is a Gaussian function of r.

of the trapped plasma to the charge collector, the measured signal for a single inject-trap-dump cycle is necessarily averaged over about 120 lattice oscillation periods for $f_0 = 60$ kHz. It is clear that in the range $0.9 \leq V_f/V_i \leq 1.2$, there is no noticeable difference in the on-axis beam density between the instantaneous and adiabatic cases. In fact, the measured radial profiles for the instantaneous and adiabatic compression cases, for $V_f/V_i = 1.2$, are almost indistinguishable [Fig. 5.8(a)]. This suggests that modest changes ($\lesssim 20\%$) in the focusing field strength may be made abruptly, without the need for a lengthy gradual-transition region. For example, if we increase the voltage amplitude by 20% for each cycle, then after four cycles we find $V_f/V_i = (1.2)^4 \approx 2.1$. This may explain why only several lattice periods are adequate for adiabatic compression when $V_f/V_i = 1.9$ in Fig. 5.5.

It is also interesting to note, for the adiabatic compression case, that the envelope instability can affect the on-axis plasma density when $V_f/V_i > 1.6$. We define

the vacuum phase advance σ_v as the exact (not smooth-focusing) phase advance of a particle oscillating in a quadrupole focusing field in the absence of any space-charge force [REISER, 1994; LUND and BUKH, 2004]. For $V_f/V_i = 1.6$, σ_v is approximately 88°. Therefore, when the initial charge bunch is compressed by more than a 60% increase in the voltage amplitude, the charge bunch enters the unstable parameter region for the envelope instability ($\sigma_v > 90°$) [REISER, 1994; LUND and BUKH, 2004]. However, for the moderate space-charge-density beams ($\hat{s} = 0.2 \sim 0.3$) considered in the present study, the instability band around $\sigma_v = 90°$ is usually very narrow [LUND and BUKH, 2004]. Therefore, if the beam is compressed in such a way that the beam passes through the instability band quiescently without mismatch oscillations (i.e., adiabatically), then we can minimize the emittance growth associated with the excitation of the envelope instability. In the experimental results presented in Fig. 5.7(b), no detrimental beam degradation is observed even when the final vacuum phase advance σ_{vf} becomes larger than 90° (or equivalently $V_f/V_i > 1.6$). Nonetheless, when the initial beam is further compressed with $V_f/V_i \gtrsim 2.2$, then $\sigma_v \rightarrow 180°$, and we begin to lose confinement of the beam particles.

Plots of the ratio of final to initial line density N_f/N_i for different values of V_f/V_i are shown in Fig. 5.9, from which we can verify particle number conservation in the transition experiments. As expected, for the case of transverse compression, adiabatic compression is more effective in minimizing particle losses. Considering the detection limit (~ 1 fC) of the charge collector system, particle loss can be interpreted as the formation of a tenuous halo at large radius. In Figs. 5.10(a) and (b), we plot the ratio of final to initial rms radius R_{bf}/R_{bi} for different values of V_f/V_i. The values of final rms beam radius are either estimated based on analytical theory, or calculated from the measured radial profiles. For the case of adiabatic compression,
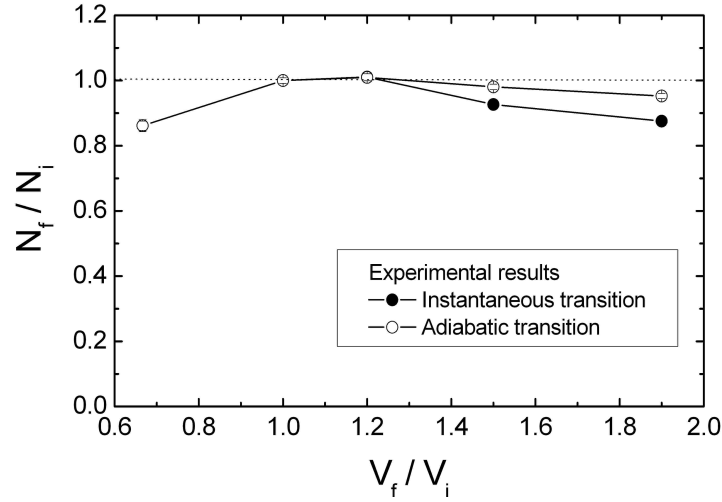
Figure 5.9: Plots of the ratio of final to initial line density N_f/N_i for different values of V_f/V_i. The values of N_f/N_i are measured from experiments with instantaneous transitions (solid circles), and adiabatic transitions (open circles). Here, $\sigma_{vi}^{sf} = 49.8°$ and $f = 60$ kHz.

the experimentally determined rms radius is in good agreement with the analytical estimate [Fig. 5.10(b)]. This is mainly because mismatch oscillations are minimized during adiabatic compression.

On the other hand, an instantaneous transition induces mismatch oscillations, which causes the measured radial profile to have a super-Gaussian tail through halo formation [see, for example, Fig. 5.8(b)]. Hence, the experimentally-determined rms radius for the case of instantaneous transition is somewhat larger than the analytical estimate [Fig. 5.10(a)]. The ratios of final to initial transverse emittance ϵ_f/ϵ_i are illustrated in Figs. 5.10(c) and (d) for different values of V_f/V_i. For the experimental results, the emittance is inferred from Eq. (5.1) and the measured radial profile, which determines N and R_b^2. It is remarkable that the experimental data for adiabatic compression show that the emittance remains almost constant during the compression process, which is approximately consistent with the analytical estimate. When the
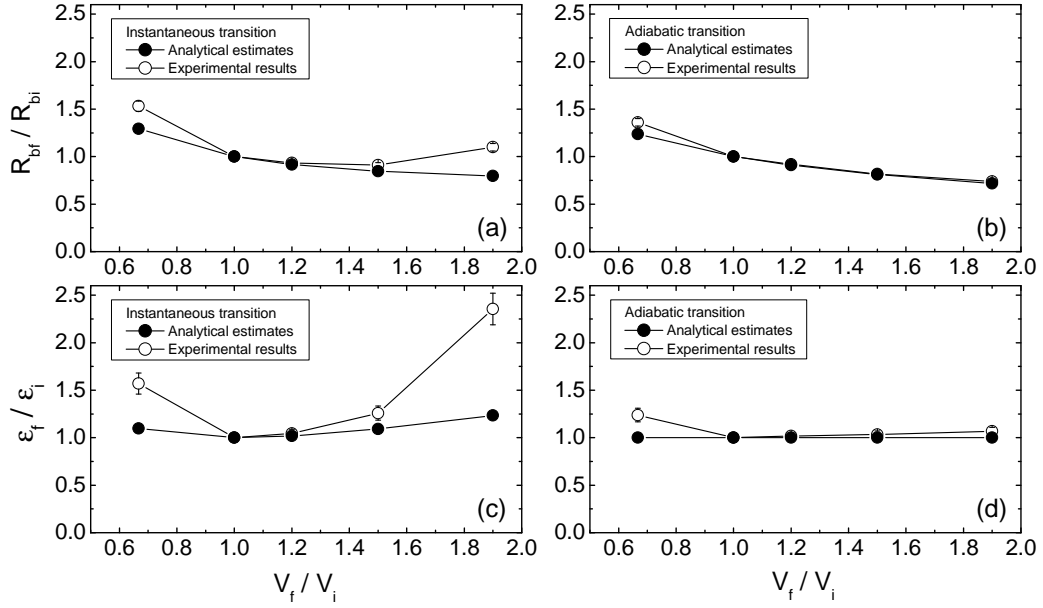
Figure 5.10: Plots of the ratio of final to initial rms radius R_{bf}/R_{bi} [frames (a) and (b)] and transverse emittance ϵ_f/ϵ_i [frames (c) and (d)] for different values of V_f/V_i. The values of R_{bf}/R_{bi} and ϵ_f/ϵ_i are either estimated based on analytical theory (solid circles), or inferred from experimental data (open circles). Frames (a) and (c) correspond to instantaneous transitions, and frames (b) and (d) correspond to adiabatic transitions.

final focusing strength is too small or too large, the rms mismatch induces a significant emittance growth for the instantaneous case, as expected. For the case where $V_f/V_i = 1.9$, the emittance more than doubles. In this case, an adiabatic transition has a large advantage over an instantaneous transition in obtaining high on-axis density, and minimizing the emittance growth. While an instantaneous transition leads to a radial profile that exhibits a broad halo region, an adiabatic transition results in a radial profile that is nearly Gaussian [Fig. 5.8(b)]. Note that a straight line in the log versus r^2 plot indicates that the radial profile is a Gaussian function of r.

In contrast, it should be noted from Figs. 5.9 and 5.10 that for the case of expansion ($\omega_{qf}/\omega_{qi} < 1$), there is no distinct advantage provided by an adiabatic

transition. This is most likely due to the various non-ideal effects present in the PTSX device, such as the 3D end effects caused when the beam pulse reflects from the DC potential (see **Appendix A**), higher-order corrections to the quadrupole focusing field in the off-axis region [DAVIDSON *et al.*, 2000], and image charge effects [ALLEN and REISER, 1996; QIAN *et al.*, 2003], all of which become strong when the beam radius is sufficiently large.

5.2.2 Changes in Lattice Period

So far, we have presented experimental results on transverse beam compression with f_0 fixed. In this section, we discuss compression experiments in which $f_0(t)$ is varied according to time while $\hat{V}_0$ is fixed. Adiabatic transitions are made by specifying either the instantaneous frequency $d\left[f_0(t)t\right]/dt$ or the applied focusing frequency $f_0(t)$. The initial beam state is the same as the baseline case used in the previous section. The voltage amplitude is held constant at $\hat{V}_0 = 150.4$ V, and the initial applied focusing frequency is $f_i = 60$ kHz.

In Fig. 5.11, the final measured on-axis charge is plotted versus the number of initial lattice periods τf_i over which the change in instantaneous frequency is made. An instantaneous transition $(\tau f_i = 0)$ compresses the beam less effectively compared to an adiabatic transition which increases the on-axis charge by 30% over several transition periods. Indeed, the instantaneous transition increases the emittance and distorts the initial Gaussian radial profile (solid circles in Fig. 5.12). On the other hand, the adiabatic transition conserves the emittance and results in the final radial profile being approximately Gaussian (open circles in Fig. 5.12). The experimental tendencies observed in Figs. 5.11 and 5.12 are basically identical to the case of amplitude changes presented in Sec. 5.2.1. This confirms that rather than $\hat{V}_0$ or f_0
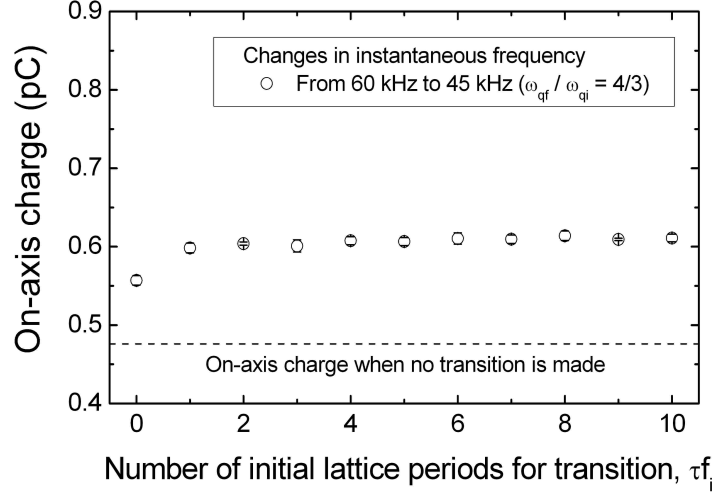
Figure 5.11: Measured on-axis charge dependence on the number of initial lattice periods for a transition τf_i over which a change in the instantaneous frequency is made. Note that $\tau f_i = 0$ corresponds to an instantaneous transition and the on-axis charge prior to the transition is 0.476 pC, which is indicated by the dashed line. Here, the initial smooth-focusing phase advance is $\sigma_{vi}^{sf} = 49.8°$, and the voltage amplitude is fixed to $\hat{V}_0 = 150.4$ V.

alone, the smooth-focusing frequency ω_q given by Eq. (5.2) is an important parameter in characterizing transverse beam compression and obtaining good qualitative predictions for experimental results.

Having demonstrated that adiabatic decreases in instantaneous frequency compress the beam in the same manner as adiabatic increases in voltage amplitude, we now consider adiabatic transitions in the applied focusing frequency $f_0(t)$. In this case, as discussed in Sec. 5.1.2, we expect an overshoot (or undershoot) of the instantaneous frequency in the middle of changing $f_0(t)$ adiabatically from f_i to f_f. It should be emphasized here, however, that the frequency overshoot in the PTSX device is due to the frequency modulation (FM) in generating the sinusoidal voltage waveform. Hence, it is rather irrelevant to the situation that occurs in a FODO lattice channel. Nonetheless, this frequency overshoot demonstrates the flexibility of the
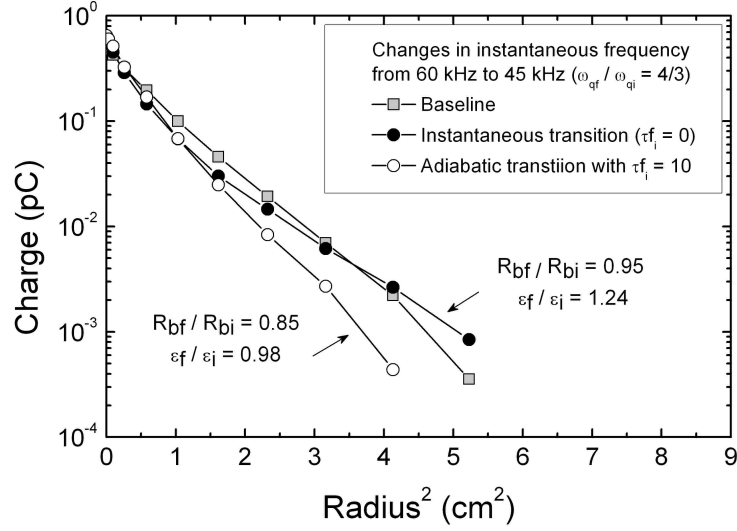
Figure 5.12: Measured radial charge profiles after changes in instantaneous frequency with $\tau f_i = 0$ (solid circles) and $\tau f_i = 10$ (open circles) are made. Here, squares correspond to the radial profile of the baseline case. Both the baseline case and the adiabatically compressed case have Gaussian radial profiles. Note that a straight line in the log versus r^2 plot indicates that the radial profile is a Gaussian function of r.

PTSX device, and allows the opportunity to investigate single-particle orbit stability properties.

Figure 5.13 shows the experimental results of the two cases where the final focusing frequency is decreased to $f_f = 50$ kHz (compression) and increased to $f_f = 90$ kHz (expansion). When the transitions are not made gradually enough, we observe either complete loss (for $f_f = 50$ kHz) or partial loss (for $f_f = 90$ kHz) of the on-axis charge. These results can be interpreted by considering changes in the instantaneous frequency $d\left[f_0(t)t\right]/dt$ in the course of the transition. If τf_i is not large enough for a monotonic decrease (increase) of the instantaneous frequency, then the instantaneous frequency becomes temporarily lower (higher) than the desired final focusing frequency f_f. Even in this case, as long as ω_q is varied sufficiently slowly, the plasma will remain in the quasi-equilibrium state, adjusting its shape according to global radial force balance.
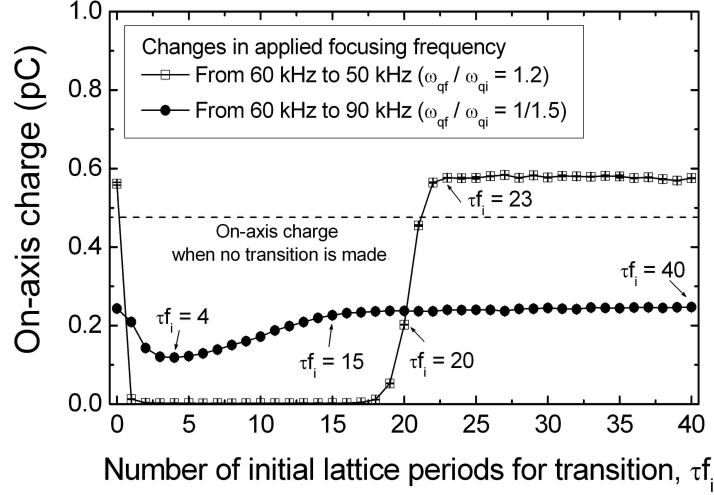
Figure 5.13: Measured on-axis charge dependence on the number of initial lattice periods for a transition τf_i over which a change in the applied focusing frequency is made. The two cases correspond to changes from 60 kHz to 50 kHz (squares) and to 90 kHz (circles). Here, the initial smooth-focusing phase advance is $\sigma_{vi}^{sf} = 49.8°$, and the voltage amplitude is fixed to $\hat{V}_0 = 150.4$ V.

Hence, in this case, we still expect good confinement of the plasma (for example, τf_i = 23 for f_f = 50 kHz and τf_i = 15 for f_f = 90 kHz in Fig. 5.13). When τf_i is further reduced, two distinct mechanisms play roles in breaking force balance, i.e., the single-particle orbit instability and mismatch oscillations.

For the case where f_f = 50 kHz, as the instantaneous frequency decreases, the vacuum phase advance increases closer to the limit of the single-particle orbit insta-bility (σ_v = 180°). Eventually, when τf_i becomes less than a certain critical value $\tau_c f_i$ (for example, $\tau_c f_i$ = 21 ~ 22 in this case), the single-particle orbits of the plasma particles become unstable, and the plasma loses its on-axis charge proportional to the time duration in which $\sigma_v \gtrsim 180°$. The single-particle orbit instability is so abrupt that it can lead to the total loss of the plasma confinement only in several focusing periods. The possibility of the envelope instability could be also considered when
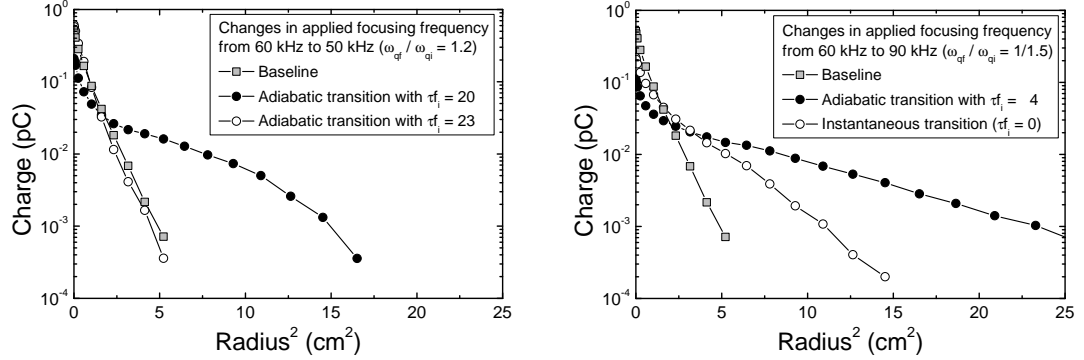
(a) Transition with $f_f = f_i/1.2 = 50$ kHz.   (b) Transition with $f_f = f_i \times 1.5 = 90$ kHz.

Figure 5.14: Measured radial charge profiles after changes in the applied focusing frequency with (a) $f_f = 50$ kHz and (b) $f_f = 90$ kHz are made. Here, squares correspond to the radial profile of the baseline case.

$\sigma_v \gtrsim 90°$ [REISER, 1994; LUND and BUKH, 2004]. However, for the experimental condition considered here (tune depression $\nu/\nu_0 \sim 0.95$), it is found the instability band is so localized around $\sigma_v \approx 90°$ that the beam can be compressed or expanded without noticeable effects of the envelope instability. The measured radial profiles in Fig. 5.14(a) show that the initial beam is indeed expanded significantly when $\tau f_i = 20$, whereas it is compressed slightly when $\tau f_i = 23$. It is also interesting to note that the on-axis charge is not lost when the transition is made instantaneously. This is consistent with the notion that modest changes ($\lesssim 20\%$) in the smooth-focusing frequency lead to nearly indistinguishable results, regardless of whether they are made instantaneously or adiabatically.

For the case where $f_f = 90$ kHz, on the other hand, the single-particle orbit instability is absent. Instead, excitation of the mismatch oscillations do matter. As the instantaneous frequency overshoots more and more, the resultant focusing force becomes highly depressed [see Fig. 5.15(a)]. At some point (for example, $\tau_c f_i < 15$ in this case), mismatch oscillations are excited due to the sudden force imbalance
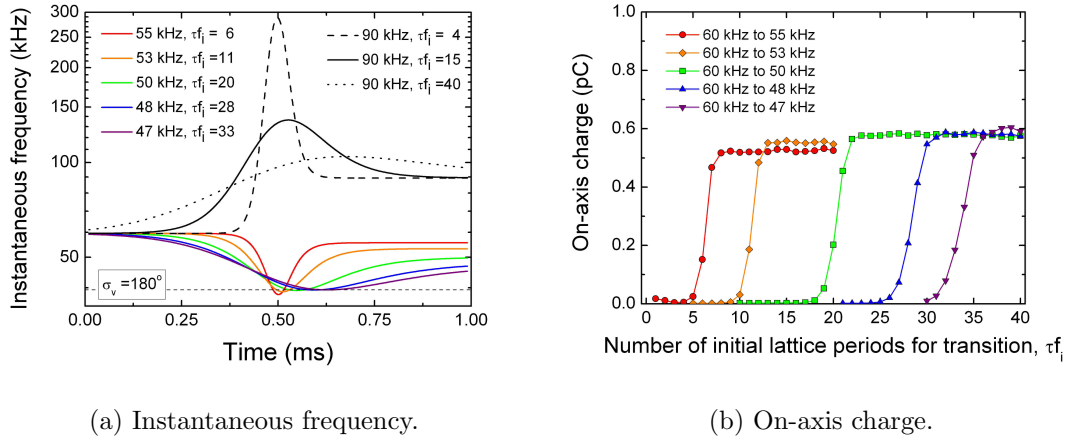
(a) Instantaneous frequency.

(b) On-axis charge.

Figure 5.15: The instantaneous frequency undergoes overshoots or undershoots depending on final frequency and τf_i (a). The onset of the on-axis charge loss matches quite well with the instant when $\sigma_v \gtrsim 180°$ (b). Noth that the instantaneous frequency is plotted on a log scale to cover a wide range of frequency change.

caused by the rapid decrease in ω_q. These mismatch oscillations will eventually lead to emittance growth, and decrease the on-axis charge. The measured radial charge profile in Fig. 5.14(b) shows that the initial beam expands even more broadly than the case with the single-particle orbit instability in Fig. 5.14(a). This is likely due to the formation of a beam halo associated with mismatch oscillations. Since there is no frequency overshoot, the beam mismatch for the instantaneous change $(\tau f_i = 0)$ is less detrimental than for the cases with $1 \lesssim \tau f_i < 15$. Indeed, the on-axis charge is comparable to the case with the most gradual change $(\tau f_i = 40)$, and the measured radial charge profile expands less than the case with $\tau f_i = 4$ [see Fig. 5.14(b)].

For completeness, we measured the changes in the on-axis charge according to τf_i for several different final frequency f_f ranges from 55 kHz to 47 kHz. The onset of particle loss matches quite well with the instant when $\sigma_v \gtrsim 180°$ [compare Figs. 5.15(a) and (b)]. This excellent agreement confirms that the beam particles are lost because of the unstable single-particle orbits for the frequency-decrease experiments.

Note that when the transition is sufficiently gradual, the values of the on-axis charge scales linearly with $(f_f/f_i)^{-1}$.

5.3 Numerical Simulations

5.3.1 Changes in Lattice Amplitude

In this section, we present numerical simulation results using the two-dimensional version of the WARP electrostatic particle-in-cell (PIC) code [FRIEDMAN *et al.*, 1992] for the analysis of experimental data on voltage amplitude changes in regimes where there are significant departures from simple analytical estimates. The WARP code describes the beam's self-consistent response to an alternating-gradient quadrupole focusing field with time-varying amplitude. To describe the effective emittance of such a pulsating beam, we use the mean transverse emittance in the beam frame defined by $\epsilon = (\epsilon_x \epsilon_y)^{1/2}$, where $\epsilon_x = 4 \left(\langle x^2 \rangle \langle \dot{x}^2 \rangle - \langle x\dot{x} \rangle^2 \right)^{1/2}$ and $\epsilon_y = 4 \left(\langle y^2 \rangle \langle \dot{y}^2 \rangle - \langle y\dot{y} \rangle^2 \right)^{1/2}$ [DORF *et al.*, 2006]. The simulation results in Figs. 5.16 and 5.17 show the normalized on-axis density $n(0)/n_i(0)$, and the normalized mean transverse emittance ϵ/ϵ_i as functions of time. Simulation parameters for loading the initial particle distribution have been chosen in such a way that the normalized intensity parameter $\hat{s}$ and initial transverse emittance ϵ_i are close to the measured values of the initial beam parameters in the experiments. By considering a transition time of 1 ms, and a dumping time of 2 ms, we perform simulations extending to 3 ms after the initial quasi-equilibrium state is formed.

The simulation results shown in Fig. 5.16 clearly indicate that instantaneous transitions introduce significant mismatch oscillations and emittance growth. The emittance increase, $\Delta\epsilon/\epsilon_i = (\epsilon - \epsilon_i)/\epsilon_i$, is 33% for $V_f/V_i = 1/1.5$, and 150% for
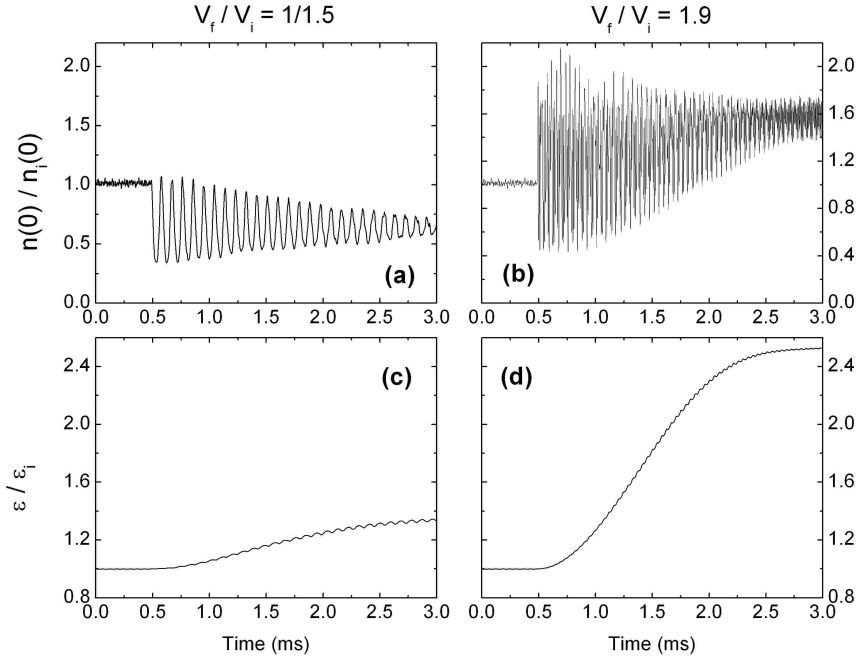
Figure 5.16: 2D WARP simulations for an alternating-gradient quadrupole lattice. The evolution of the normalized on-axis density $n(0)/n_i(0)$ and normalized transverse emittance ϵ/ϵ_i are shown during an instantaneous transition process with $\sigma_{vi}^{sf} = 49.8°$ and $f_0 = 60$ kHz. Frames (a) and (c) correspond to the case with $V_f/V_i = 1/1.5$, and frames (b)and (d) correspond to the case with $V_f/V_i = 1.9$.

$V_f/V_i = 1.9$, which are in much better agreement with the experimental data than the simple analytical estimates, where there is no consideration of halo particle generation. For example, the emittance increase for $V_f/V_i = 1.9$ in Fig. 5.10(c) is 25% based on the analytical estimate, and 140% from the actual measurement. Because of the large mismatch, significant oscillations in the on-axis plasma density last more than 2 ms after the abrupt changes are made at $t = 0.5$ ms. Hence, the measured signals of the on-axis density can be interpreted as the time-averaged values of the on-axis density oscillations during the dumping process. Note that the frequency of the on-axis density oscillations observed in Fig. 5.16(a) is easily identified with the breathing mode frequency ($\omega_B \approx 67.9 \times 10^3$ s^{-1}).
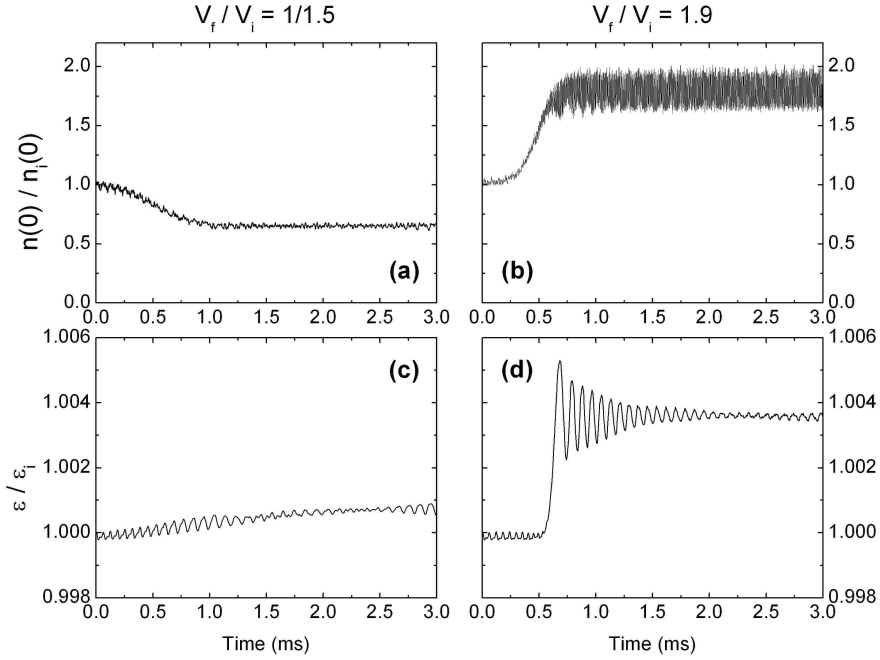
Figure 5.17: 2D WARP simulations for an alternating-gradient quadrupole lattice. The evolution of the normalized on-axis density $n(0)/n_i(0)$ and normalized transverse emittance ϵ/ϵ_i are shown during an adiabatic transition process with $\sigma_{vi}^{sf} = 49.8°$ and $f_0 = 60$ kHz. Frames (a) and (c) correspond to the case with $V_f/V_i = 1/1.5$ and $N_t = 40$, and frames (b) and (d) correspond to the case with $V_f/V_i = 1.9$ and $N_t = 20$.

Simulation results for an adiabatic compression case with $V_f/V_i = 1.9$ are shown in Figs. 5.17(b) and 5.17(d) for $N_t = 20$. As expected from the analytical estimates and experimental results, adiabatic compression assures that the final beam remains well-matched, and the emittance growth during the transition is minimized ($\Delta\epsilon/\epsilon_i < 0.5\%$). However, for the case of adiabatic expansion with $V_f/V_i = 1/1.5$, even the numerical simulations do not reproduce the experimental results [compare Figs. 5.10(d) and 5.17(c)]. As mentioned earlier, the enhanced emittance growth observed in the expansion experiments is likely due to non-ideal effects present in the PTSX device, which are not considered in the two-dimensional version of the WARP code used in the present analysis. In contrast to the instantaneous transition

cases, the on-axis densities relax almost immediately after the adiabatic transitions are complete at $t = 1$ ms. The final normalized on-axis density, $n_f(0)/n_i(0)$, is about 0.65 for $V_f/V_i = 1/1.5$, and about 1.8 for $V_f/V_i = 1.9$, which are slightly less than the analytical estimates in Fig. 5.7. Note that the on-axis density oscillations observed in Fig. 5.17(b) have a frequency of 120 kHz, which is twice the external focusing frequency f_0. This oscillation is a result of the pulsating motion of the beam envelope, and its amplitude increases considerably when the beam is compressed.

5.3.2   Changes in Lattice Period

In this section, we analyze the effects of frequency overshoot (or undershoot) observed in the experiments on the adiabatic changes in the applied focusing frequency in terms of the Kapchinskij-Vladimirskij (KV) equivalent beam model introduced in **Chapter 2** of this thesis. The single-particle orbits in the presence of space-charge forces are described by

$$\frac{d^2}{dt^2}x(t) + \left[+\kappa_q(t) - \frac{2K}{a(t)\left\{a(t) + b(t)\right\}}\right]x(t) = 0, \tag{5.13}$$

$$\frac{d^2}{dt^2}y(t) + \left[-\kappa_q(t) - \frac{2K}{b(t)\left\{a(t) + b(t)\right\}}\right]y(t) = 0, \tag{5.14}$$

in a KV beam model. Here, x- and y-dimension beam envelopes $a(t)$ and $b(t)$ are calculated from the envelope equations. By setting the self-field perveance $K = 0$, we can also track the single-particle orbits in the absence of space-charge effects.

For the case of a frequency decrease, a frequency undershoot causes the single-particle orbits to be unstable as shown in Fig. 5.18(a). The amplitude of the single-particle orbit is increased independent of the space-charge effects and drives the beam envelopes large amplitudes. This numerical result reconfirms that the on-axis charge loss and beam expansion observed in frequency-decrease experiments with $\tau f_i = 20$
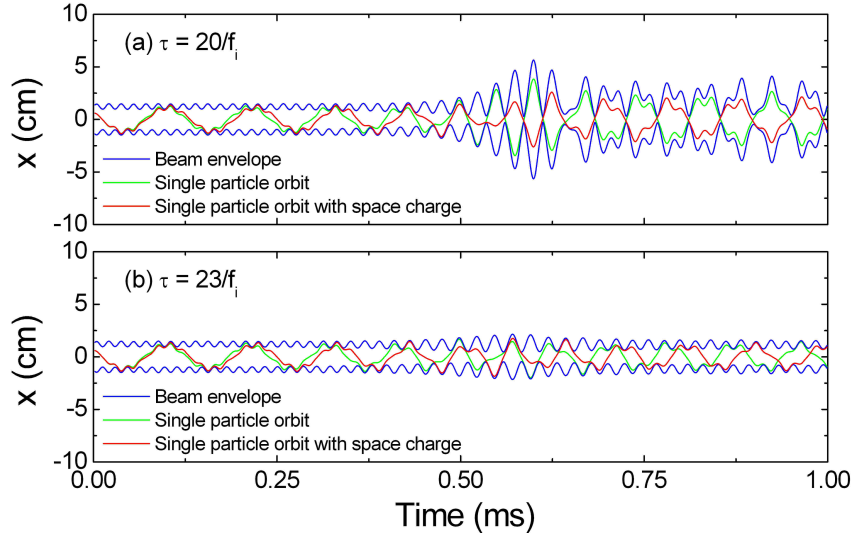
Figure 5.18: Time evolution of the x-dimension beam envelope $a(t)$ (blue), and the single-particle $x(t)$ orbits with (red) and without (green) space-charge effects for the cases where (a) $\tau f_i = 20$ and (b) $\tau f_i = 23$. Adiabatic changes in the applied focusing frequency $f_0(t)$ are made from $f_i = 60$ kHz to $f_f = 50$ kHz with $\hat{V}_0 = 150.4$ V.

are in fact direct outcomes of the unstable single-particle orbits, not due to collective mode excitation [see Fig. 5.14(a)]. Note that due to the space-charge tune shift, there is a phase lag between single-particle orbits with and without space-charge effects. Here, the initial beam is assumed to be matched.

For the case of frequency increase, on the other hand, the frequency overshoot excites envelope oscillations as shown in Fig. 5.19(a). The beam envelopes are oscillating with the breathing mode frequency due to the imbalance between focusing and defocusing (space-charge and pressure) forces, and the amplitude of the single-particle orbit is increased through the action of the space-charge force. In a KV beam model, both the transverse focusing force and space-charge force are linearly proportional to the transverse displacement. Hence, despite the envelope oscillations, there is no phase-space filamentation, emittance growth, and damping of the oscillation amplitudes. However, in the PTSX device, there exists nonlinearity in the beam's
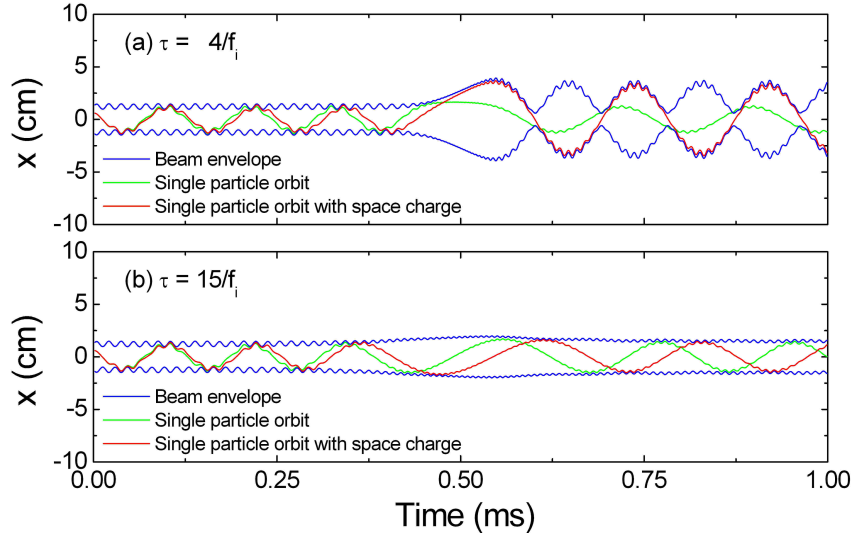
Figure 5.19: Time evolution of the x-dimension beam envelope $a(t)$ (blue), and single-particle $x(t)$ orbits with (red) and without (green) space-charge effects for the cases where (a) $\tau f_i = 4$ and (b) $\tau f_i = 15$. Adiabatic changes in the applied focusing frequency $f_0(t)$ are made from $f_i = 60$ kHz to $f_f = 90$ kHz with $\hat{V}_0 = 150.4$ V.

self-fields. These nonlinear self-fields will eventually damp the envelope oscillations through phase-space filamentation. As the emittance grows, the beam will expand further and the on-axis charge will decrease accordingly. In addition, particles in the beam tail can resonantly interact with the oscillating nonlinear space-charge forces outside the beam core (parametric resonance), and become halo particles with even higher radial excursions $r = (3 \sim 4) \times R_b$. Therefore, the numerical result is consistent with the observation of beam loss and extended beam tails in frequency-increase experiments with $\tau f_i = 4$ [see Fig. 5.14(b)].

5.4 Summary and Discussion

The transverse compression of an intense beam after acceleration allows for the delivery of a large number of particles and a large amount of energy to a small spot size.

Hence, transverse compression is of considerable practical importance in applications such as ion-beam-driven high energy density physics and heavy ion fusion. In this chapter, the PTSX facility has been used to perform transverse beam compression experiments in order to develop a better understanding of the physics of transverse compression of intense beams. Both changes in the lattice amplitude and changes in the lattice period are considered. From a comparison of the analytical estimates (Sec. 5.1), experimental results (Sec. 5.2), and numerical simulations (Sec. 5.3), it is found that the key physics issue in transverse beam compression is how to suppress the excitation of mismatch oscillations, which is usually accompanied by emittance growth and halo formation. In most cases (when phase advance is low enough), adiabatic changes in the smooth-focusing frequency ω_q turned out to be an effective control for transverse beam compression. During the frequency modulation experiments, we observe somewhat artificial (in the sense that this is not directly related with actual accelerators) overshoot (or undershoot) of the instantaneous frequency. Nonetheless, this frequency overshoot provides useful insights into single-particle orbit instabilities and collective mode excitations. So far, the voltage waveform used throughout the experiments has been limited to the sinusoidal waveform. Hence, future experiments with more realistic waveforms for emulating the AG focusing channel, such as a periodic step-function or a periodic trapezoidal waveform [LUND and BUKH, 2004] are expected to further improve our basic understanding of transverse beam compression for high-intensity accelerator applications.

Chapter 6

Machine Imperfection Effects

As emphasized earlier in this thesis, understanding the properties of intense charged particle beam propagation over large distances is of great importance for a wide variety of accelerator applications, including high energy and nuclear physics, heavy ion fusion, ion-beam-driven high energy density physics, nuclear waste transmutation, and spallation neutron sources [DAVIDSON and QIN, 2001; REISER, 1994; WANGLER, 1998]. One critical but unavoidable problem in high-intensity accelerators is the presence of undesired machine imperfections. The machine imperfections include faulty magnet sets which have the incorrect magnetic field strength or misalignments from ideal positions, and randomly distributed small noise in the quadrupole focusing gradient and the RF field amplitude, to mention a few examples. The machine imperfections influence the beam dynamics in a self-consistent way. They induce irregular mismatch oscillations of the beam envelope, produce halo particles, and can result in severe emittance growth and beam degradation, particularly when there are strong nonlinear space-charge forces [BOHN and SIDERIS, 2003; GERIGK, 2004; YOON *et al.*, 2005]. Consequently, the associated beam loss and its damage to the

machine components define the practical and/or economic tolerances in the machine, and can have a direct impact on the project costs [WANGLER, 1998; GERIGK, 2003]. In the PTSX device, the amplitude of the voltage waveform applied to the electrodes corresponds to the quadrupole focusing strength in an AG lattice system. Hence, by modifying the voltage amplitude we can study the imperfection effects of quadrupole magnets in the actual transport channel. In the experimental studies presented in this chapter, faulty magnet sets are emulated by spoiling the voltage waveform for short times, i.e., for a few or several lattice periods (Sec. 6.1), and small noise in the quadrupole focusing gradients is handled by randomly sampling a voltage amplitude ripple for each half lattice period within a given tolerance limit (Sec. 6.2).

6.1 Effect of Faulty Magnet Sets

An accelerator is composed of many focusing, bending, and correction magnets, which are either permanent magnets or electromagnets (normal conducting or superconducting). For example, the currently envisioned International Linear Collider (ILC) [BRAU *et al.*, 2007] is proposed to have 10872 normal conducting magnets (6873 water-cooled and 3999 air-cooled) and 2318 superconducting magnets for the various parts of the accelerator complex. As the beam intensity and energy become much higher for modern accelerator applications, a single magnet failure event and associated accidental beam loss can have a much more severe impact on the project in terms of repair costs and time. Hence, extensive engineering analyses have to be performed to improve the reliability of the magnet system which includes mechanical structure, power supplies, electrical connections, and cooling systems (or cryogenic system for superconducting magnet) [SPENCER and RHEE, 2003; SCHMIDT *et al.*, 2006]. While some obvious

Type of magnet	Type of failure
Permanent magnet	Tuner malfunctioning
Normal conducting magnet	Water leaks
	Overheating
	Electrical shorts
	Power supply failure
Superconducting magnet	Magnet quench
	Cryogenic system problem
	Power supply failure

Table 6.1: Types of magnet failure [SPENCER and RHEE, 2003].

magnet failures can be detected and fixed in the manufacturing, installation, or trial run phases, some magnet failures occur during the actual operation stage (see Table 6.1), and can lead to significant beam degradation or loss by giving incorrect (or zero) magnetic field strength [WU *et al.*, 2005].

6.1.1 Experimental Results

In order to provide the transverse beam dynamics characteristics of an intense beam propagating under such a magnet failure scenario, a series of experiments have been performed in the PTSX device. In the PTSX device, a failure of a single quadrupole magnet in the actual accelerator corresponds to an abrupt change in the voltage waveform $V_0(t) = \hat{V}_0 \sin[2\pi(t - t_0)/T)]$ over a half-period of oscillation. We perturb the initial quiescent plasma trapped in PTSX by changing the voltage amplitude instantaneously from its initial value $\hat{V}_0 = V_1$ to a modified value $\hat{V}_0 = V_2$ at a zero-crossing of the sinusoidal waveform ($t = t_0$), and restoring it to V_1 after a half-period $T/2$. To emulate the essence of the faulty magnet effect and complete the experiment in a timely manner (without drift in the ion source condition), the time-averaged on-axis charge signal is normally measured rather than entire radial profile. The initial
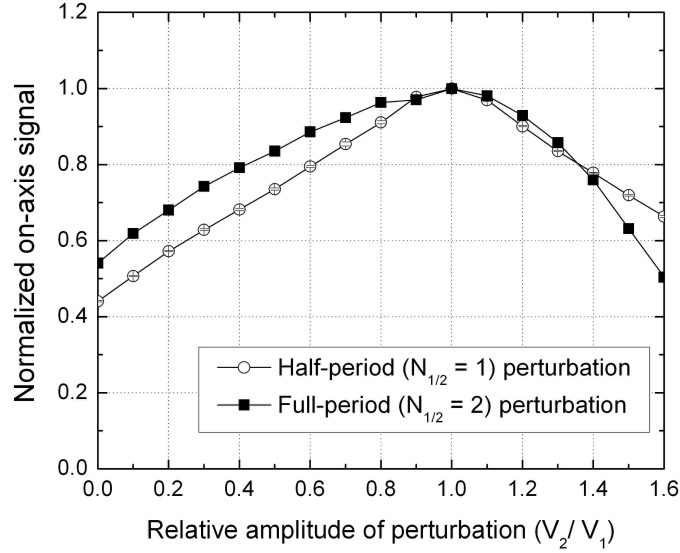
Figure 6.1: Dependence of on-axis charge on relative amplitude of perturbation V_2/V_1 for half-period perturbation (open circles) and full-period perturbation (solid squares). The error bars are typically smaller than the size of the symbol, and, will be neglected in the experimental data presented later in this chapter.

unperturbed plasma is approximately Gaussian in radial profile (see the black curve in Fig. 6.2), and has a normalized beam intensity of $\hat{s} \sim 0.27$, effective transverse temperature of $\bar{T}_\perp \sim 0.26$ eV, and rms radius of $R_b \sim 1$ cm. The plasmas are dumped to the charge collector 3.4 ms after the changes in $\hat{V}_0$ are made, which allows enough lattice periods for the perturbed plasmas to reach a new quasi-equilibrium state. For the moderately low space-charge density beams ($\hat{s} = 0.2 \sim 0.3$) considered in this study, the on-axis density $\hat{n}$ can be approximated as $\hat{n} \approx N/\pi R_b^2$ when the beam is in the quasi-equilibrium state, and can be an effective indicator of beam degradation (increase in the rms radius R_b) or loss (decrease in the line density N). Generally, the magnets in actual accelerators are operated either by individual power supplies, or are in series with adjacent magnets using a single power supply. Hence, to include the possibility of the simultaneous failure of several adjacent magnet sets, the modified
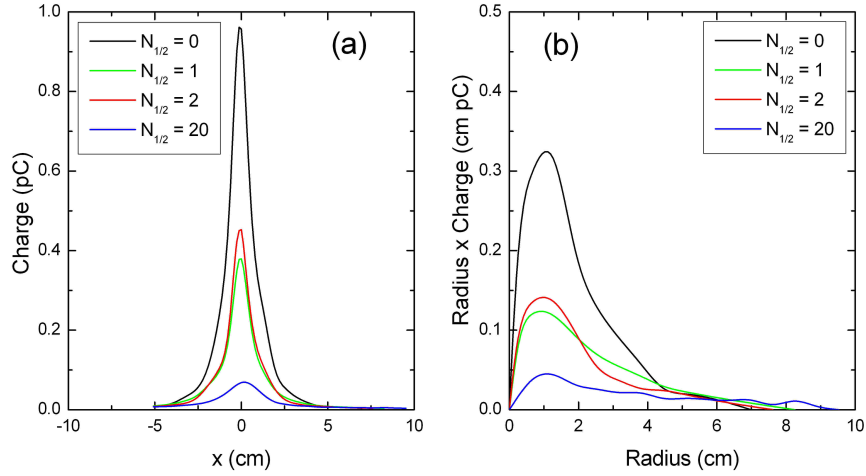
Figure 6.2: Measured radial charge profiles for the case $V_2/V_1 = 0$ for several different values of number of half-periods ($N_{1/2}$) of the perturbation. Radial profiles are plotted for (a) charge versus x-dimension, and (b) radius×charge versus radius to augment the small changes in both the on-axis and off-axis regions.

voltage V_2 is allowed to persist for a variable number $N_{1/2}$ of half-periods before returning to the initial value V_1.

The expectation is that an abrupt change in $\hat{V}_0$ (equivalently, a failure of a quadrupole magnet during the operation of the actual accelerator) will cause a mismatch oscillation of the beam envelope and eventually lead to a degradation or loss in transverse confinement of the plasma. A scan of V_2/V_1 in Fig. 6.1 shows that, regardless of whether $V_2/V_1 > 1$ or $V_2/V_1 < 1$, the on-axis charge is reduced as a result of the perturbation. However, quite interestingly, it is found that for $V_2/V_1 < 1$, the full-period ($N_{1/2} = 2$) perturbation is less detrimental to the on-axis charge signal than the half-period ($N_{1/2} = 1$) perturbation. This behavior is also observed in the radial charge profile measurements. Figure 6.2 shows that not only the on-axis charge, but also the radial charge distribution is slightly less affected by the perturbation with $N_{1/2} = 2$. Simulations using the 2D WARP PIC code demonstrate that, indeed, the half-period ($N_{1/2} = 1$) perturbation produces much larger mismatch oscillations,

(a) $N_{1/2} = 1$ (b) $N_{1/2} = 2$
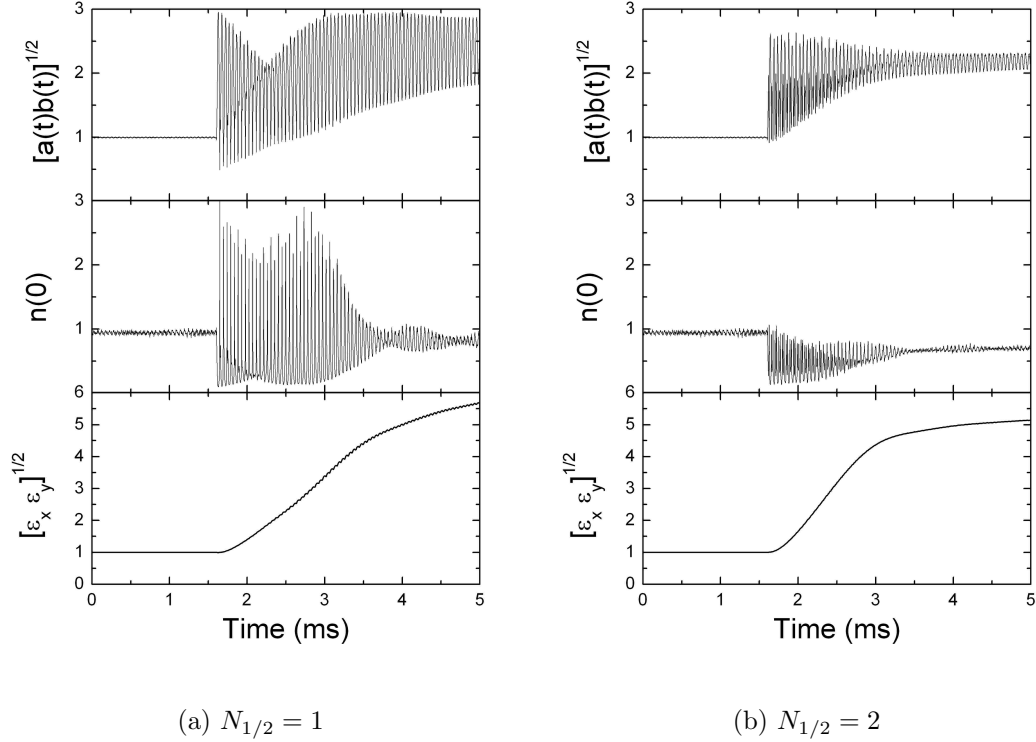
Figure 6.3:   WARP 2D simulation results for the evolutions of the mean radius $[a(t)b(t)]^{1/2}$, the on-axis density $n(0)$, and the mean transverse emittance $[\epsilon_x \epsilon_y]^{1/2}$. Here, each quantity is normalized to its initial value, and the instantaneous change in the strength of the full quadrupole field ($V_2/V_1 = 0$) has been made at time $t = t_0 = 1.6$ ms.

leading to 10% larger emittance growth than the full-period ($N_{1/2} = 2$) perturbation (Fig. 6.3). The final on-axis charge difference between the two cases is rather unclear in Fig 6.3. In the actual experiment where there is an end effect, however, larger mismatch oscillations tend to enhance particle loss to the conducting wall, resulting in a further decrease in the on-axis charge.

To further investigate the beam response dependence on the duration of the perturbation, the on-axis charge is measured as a function of $N_{1/2}$ for a discrete set of values for V_2/V_1. As apparent from Fig. 6.4(a), for $V_2/V_1 > 1$, the on-axis charge signal is not monotonic but oscillates with $N_{1/2}$. For $V_2/V_1 < 1$, a similar oscillatory behavior, but in this case with a beat-wave-like structure, appears in the on-axis

(a) $V_2/V_1 > 1$. (b) $V_2/V_1 < 1$.
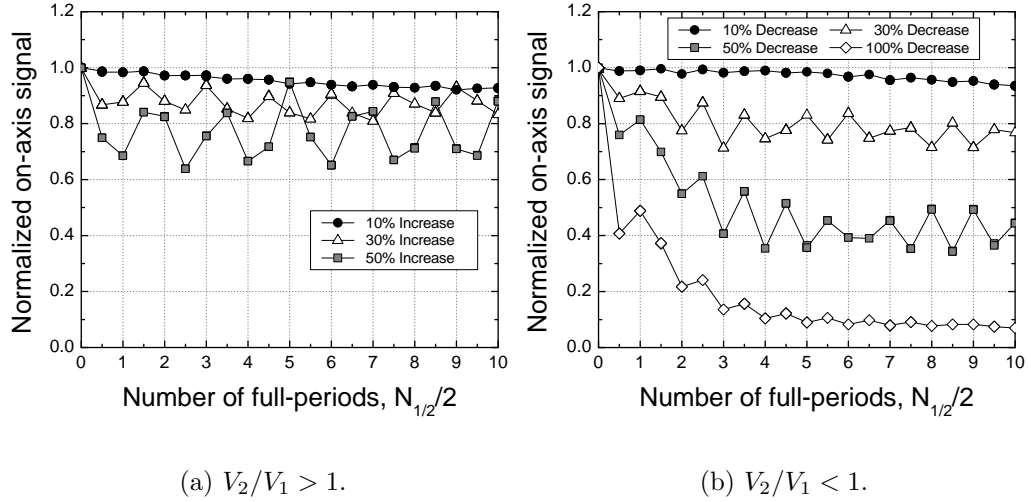
Figure 6.4: Dependence of on-axis charge on the number of full-periods for perturbations with different values of V_2/V_1. An instantaneous perturbation in the amplitude of the voltage waveform causes mismatch oscillations that result in various amount of emittance growth depending on the duration of the perturbation, and various amounts of radial expansion, and corresponding on-axis density decrease.

signal [Fig. 6.4(b)]. Due to the beam expansion and associated beam loss to the conducting wall, the on-axis charge tends to decrease when there is an increase in $N_{1/2}$ for the cases with $V_2/V_1 < 1$. For example, the decay time in the $V_2/V_1 = 0$ case is in an order of the transit time ($0.1 \sim 0.2$ ms) for a thermal ion to reach to the wall of PTSX. For both a 10% increase or a 10% decrease in the waveform amplitude, there is only a small impact on the beam state.

6.1.2 A Smooth-Focusing Model

The physics behind the oscillatory behavior observed in the on-axis signal can be described qualitatively using the smooth-focusing model (see Fig 6.5). In the smooth-focusing model, the average focusing frequency is linearly proportional to the voltage waveform amplitude $\hat{V}_0$ [DAVIDSON and QIN, 2001]. Initially, the trapped plasma is in a quasi-equilibrium state with a constant rms radius $R_b(t = t_0) = R_{b0}$ that satisfies

(a) $V_2/V_1 > 1$.   (b) $V_2/V_1 < 1$.
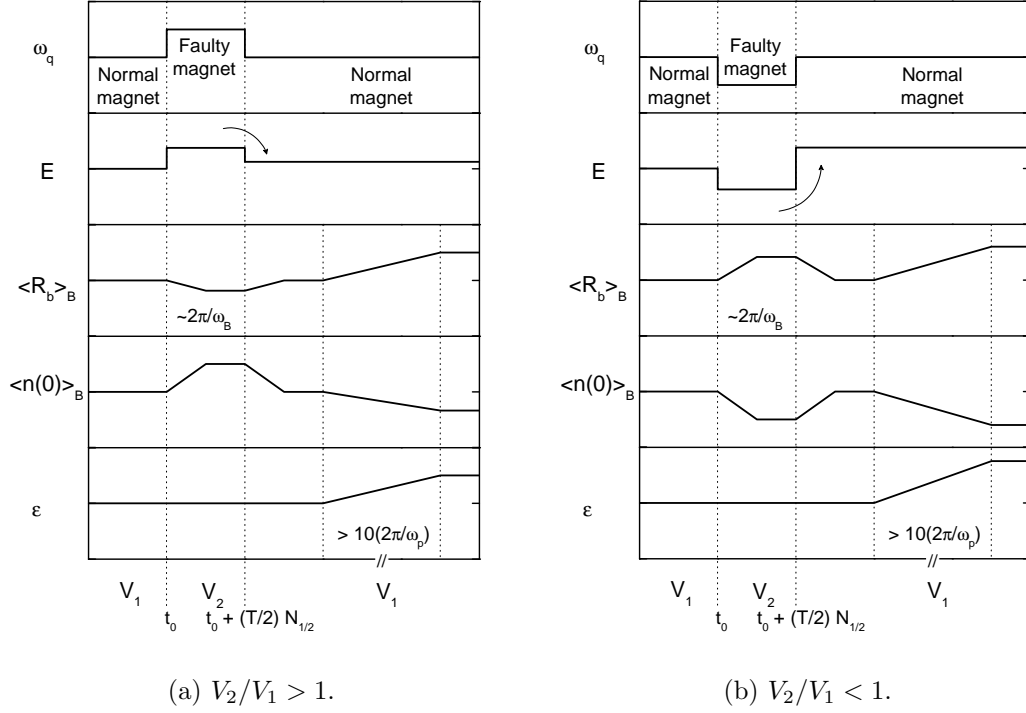
Figure 6.5: Smooth-focusing schematic of the effect of faulty magnet sets. Whenever there is a beam mismatch $(d\omega_q/dt \neq 0)$, we expect long-time-scale emittance growth induced by the oscillation energy of the excited mode. Hence, regardless of whether there is a sudden increase or decrease in the smooth-focusing frequency ω_q, the net result is expected to be an increase in the rms radius R_b, and a decrease in the on-axis density $\hat{n}$.

the global force balance equation given by

$$m\omega_q^2 R_{b0}^2 = 2\bar{T}_\perp + \frac{Nq^2}{4\pi\epsilon_0}. \tag{6.1}$$

When there is an instantaneous increase (decrease) in ω_q at time $t = t_0$, $R_b(t > t_0)$ starts to decrease (increase) from R_{b0} toward a new equilibrium radius $\bar{R}_b = \left[\left(K + \sqrt{K^2 + 4\epsilon^2\omega_q^2}\right)/4\omega_q^2\right]^{1/2}$, and the corresponding on-axis plasma density with moderately low space-charge intensity becomes $\hat{n}(t) \approx N/\pi R_b^2(t)$. Here, the line density N, the self-field perveance K, the effective transverse temperature $\bar{T}_\perp$, and the average transverse emittance $\epsilon \approx 2R_{b0}(2\bar{T}_\perp/m)^{1/2}$ are assumed to be approximately

constant. Although the time-averaged rms radius $\langle R_b(t) \rangle_B$ approaches the new quasi-equilibrium radius on the time scale of the breathing mode period ($\sim 2\pi/\omega_B$), there remain envelope oscillations around $\bar{R}_b$ due to the energy exchange introduced by the external focusing force, which is given by $\frac{1}{2}mR_b^2(t_0)\Delta(\omega_q^2)$ [DAVIDSON and QIN, 2001]. Here, $\langle \cdots \rangle_B$ denotes the temporal average over one breathing mode period $2\pi/\omega_B$, $\Delta(\omega_q^2) = \omega_{q2}^2 - \omega_{q1}^2$, and $\omega_B = 2\omega_q \left(1 - K/4\bar{R}_b^2\omega_q^2\right)^{1/2}$ is the breathing mode frequency.

When ω_q is switched back to its original value at $t = t_0 + (T/2)N_{1/2}$, now $\langle R_b(t) \rangle_B$ approaches its original quasi-equilibrium radius $R_b(t_0)$. The final amplitude of the envelope oscillation around $R_b(t_0)$ is most likely determined from the net energy exchange after $t = t_0 + (T/2)N_{1/2}$, which is given by $\Delta E = \frac{1}{2}m\left[R_b^2(t_0) - R_b^2(t)\right]\Delta(\omega_q^2) \geq 0$, and is strongly dependent on the phase difference between the envelope oscillation and the duration of the perturbation (or equivalently, the number of faulty magnets). The envelope oscillations eventually lead to space-charge-induced emittance growth over a longer time scale (typically, $\gtrsim 20\pi/\omega_p$) [WANGLER, 1998], and a corresponding increase in the equilibrium rms beam radius. If particle number is conserved, an increase in the rms beam radius implies a decrease in the on-axis density. Hence, depending on the degree of mismatch oscillation ($\propto \Delta E$), the measured on-axis charge reveals an oscillatory behavior.

6.1.3   A Kapchinskij-Vladimirskij (KV) Envelope Model

The phase dependence of the amplitude of the mismatch oscillation and the resultant oscillatory behavior in the on-axis signal can be more quantitatively explained in terms of a KV envelope model with full quadrupole focusing field [KAPCHINSKIJ and VLADIMIRSKIJ, 1959; REISER, 1991; DAVIDSON and QIN, 2001]. As described in **Chapter 2** of this thesis, the envelope equations for an equivalent KV beam with

$\epsilon_x = \epsilon_y = \epsilon$ are given by

$$\frac{d^2}{dt^2}a(t) + \kappa_q(t)a(t) - \frac{2K}{a(t) + b(t)} = \frac{\epsilon^2}{a^3(t)}, \tag{6.2}$$

$$\frac{d^2}{dt^2}b(t) - \kappa_q(t)b(t) - \frac{2K}{a(t) + b(t)} = \frac{\epsilon^2}{b^3(t)}, \tag{6.3}$$

where, $\kappa_q(t)$ is the focusing coefficient, $K = 2Nq^2/4\pi\epsilon_0 m$ is the dimensional self-field perveance, and ϵ is the transverse emittance in the beam frame. Introducing the scaled envelope momenta defined by $p_a = da/dt = 4\langle x\dot{x}\rangle/a$ and $p_b = db/dt = 4\langle y\dot{y}\rangle/b$, we can define the envelope Hamiltonian as [LEE, 2004]

$$H_{\text{env}} = \frac{1}{2}(p_a^2 + p_b^2) + \frac{1}{2}\kappa_q(t)(a^2 - b^2) - 2K\ln(a + b) + \frac{\epsilon^2}{2}\left(\frac{1}{a^2} + \frac{1}{b^2}\right), \tag{6.4}$$

and the rate equation for the envelope energy $E_{\text{env}} = H_{\text{env}}$ is given by [DAVIDSON and QIN, 2001]

$$\frac{dE_{\text{env}}}{dt} = \frac{1}{2}\left(\frac{d\kappa_q(t)}{dt}\right)(a^2 - b^2). \tag{6.5}$$

Hence, the envelope energy E_{env} is not a constant in the periodic focusing field $\kappa_q(t) = \hat{\kappa}_q \sin[2\pi f_0(t - t_0)]$, but exhibits oscillatory behavior for a time varying external field and associated envelope oscillations. In particular, for a symmetrically matched beam, where $a(t + T/2) = b(t)$ and $b(t + T/2) = a(t)$, E_{env} oscillates in time with the exact period $T/2$. Hence, a matched beam can be viewed as a state with minimum average energy exchange, i.e., $\langle dE_{\text{env}}/dt\rangle_T = 0$.

Suppose that the matched beam experiences an abrupt change in the focusing strength at $t = t_0$, then E_{env} will oscillate irregularly due to the envelope oscillations induced by the beam mismatch. After allowing the beam to remain in the perturbed state until time $t = t_0 + (T/2)N_{1/2}$, we change the focusing field strength back to the original value. Since the beam has already experienced two severe mismatches at $t = t_0$ and $t = t_0 + (T/2)N_{1/2}$, the final beam is no longer the same as the initial
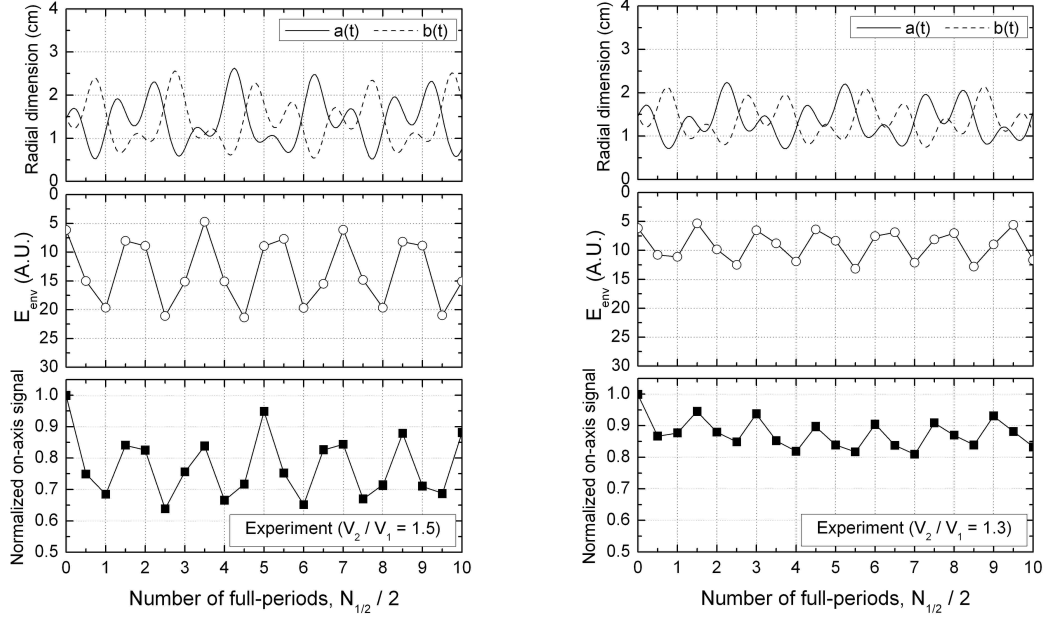
(a) $\frac{V_2}{V_1} = 1.5$, $\sigma_v^{sf} \approx 74.7°$, and $\frac{2\pi}{\omega_B} \approx 2.5T$.

(b) $\frac{V_2}{V_1} = 1.3$, $\sigma_v^{sf} \approx 64.7°$, and $\frac{2\pi}{\omega_B} \approx 2.9T$.
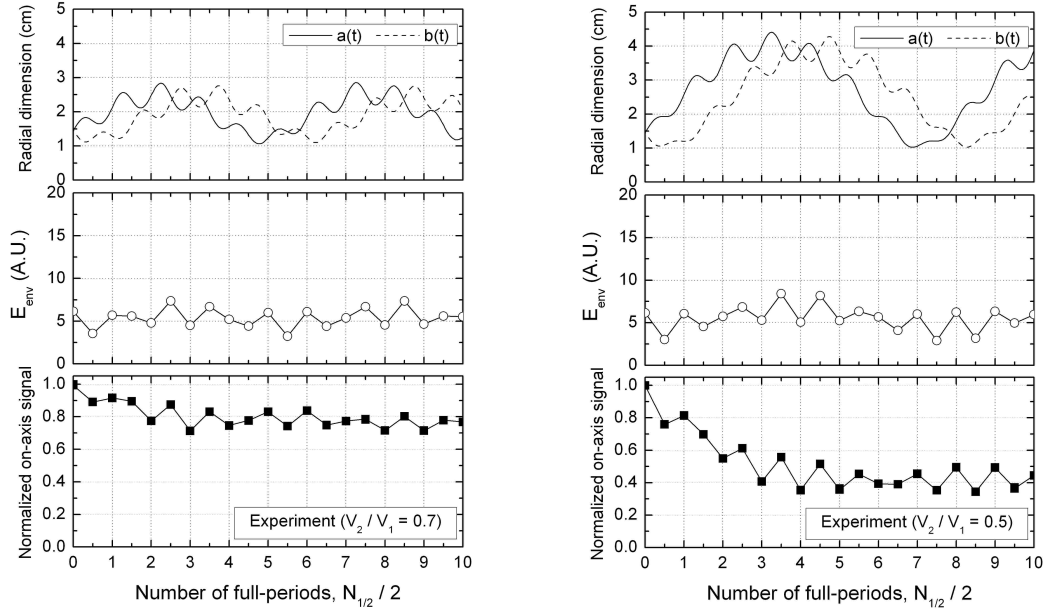
(c) $\frac{V_2}{V_1} = 0.7$, $\sigma_v^{sf} \approx 34.9°$, and $\frac{2\pi}{\omega_B} \approx 5.5T$.

(d) $\frac{V_2}{V_1} = 0.5$, $\sigma_v^{sf} \approx 24.9°$, and $\frac{2\pi}{\omega_B} \approx 7.9T$.

Figure 6.6: The envelope energy E_{env} calculated from the the KV beam envelopes $a(t)$ and $b(t)$ shows qualitatively similar oscillatory patterns to the measured on-axis signals. The vacuum phase advance σ_v^{sf} and the breathing mode frequencies ω_B are estimated in the smooth-focusing approximation. For $V_2/V_1 > 1$, a mixed mode is excited rather than a pure breathing mode. The origin of the E_{env} plot has been adjusted according to the beam mismatch minimization condition discussed in the text.

matched beam. Instead, the beam mismatch eventually causes significant emittance growth and a decrease in the on-axis density when the beam relaxes to a new quasi-equilibrium state with larger beam envelopes. Considering that the amplitude of the mismatch at $t = t_0$ is the same, the amount of final emittance growth is most likely determined by the degree of the mismatch at time $t = t_0 + (T/2)N_{1/2}$. Although a KV beam model cannot describe changes in the emittance, the degree of mismatch and the associated emittance growth can be estimated through the envelope energy $E_{\rm env}$ of the KV beam, which is calculated by solving the envelope equations (6.2) and (6.3) numerically. For the voltage change experiments with $V_2/V_1 > 1$ in the PTSX device, the average $E_{\rm env}$ is supposed to be decreased after $t = t_0 + (T/2)N_{1/2}$ [see the arrow in Fig. 6.5(a)]. Hence, to minimize further beam mismatch, it is desirable that $E_{\rm env}$ has a minimum at $t = t_0 + (T/2)N_{1/2}$. On the other hand, for the case of $V_2/V_1 < 1$, the average $E_{\rm env}$ is expected to be larger after $t = t_0 + (T/2)N_{1/2}$ [see the arrow in Fig. 6.5(b)]. Therefore, in this case, additional beam mismatch can be minimized when $E_{\rm env}$ has a maximum at $t = t_0 + (T/2)N_{1/2}$. In Fig. 6.6, we found that $E_{\rm env}$ shows quite similar oscillatory behavior to the experimental observations in the on-axis signals. For the cases with $V_2/V_1 > 1$ [Figs. 6.6(a) and (b)], the agreement between the estimates and the experiments are particulary good during the initial phase ($N_{1/2}/2 \leq 4$). Although the detailed oscillatory structures are somewhat shifted for $N_{1/2}/2 > 4$ (seemingly due to the betatron tune shift during the course of the strong mismatch oscillations), their periods still remain in good agreement. On the other hand, for $V_2/V_1 < 1$ [Figs. 6.6(c) and (d)], the experimentally measured oscillatory patterns are quite well-matched to $E_{\rm env}$ up to $N_{1/2}/2 = 10$, while there are (downward) shifts of the oscillation center of on-axis signal likely due to the beam loss associated with radial expansion. Therefore, we conclude that the envelope energy
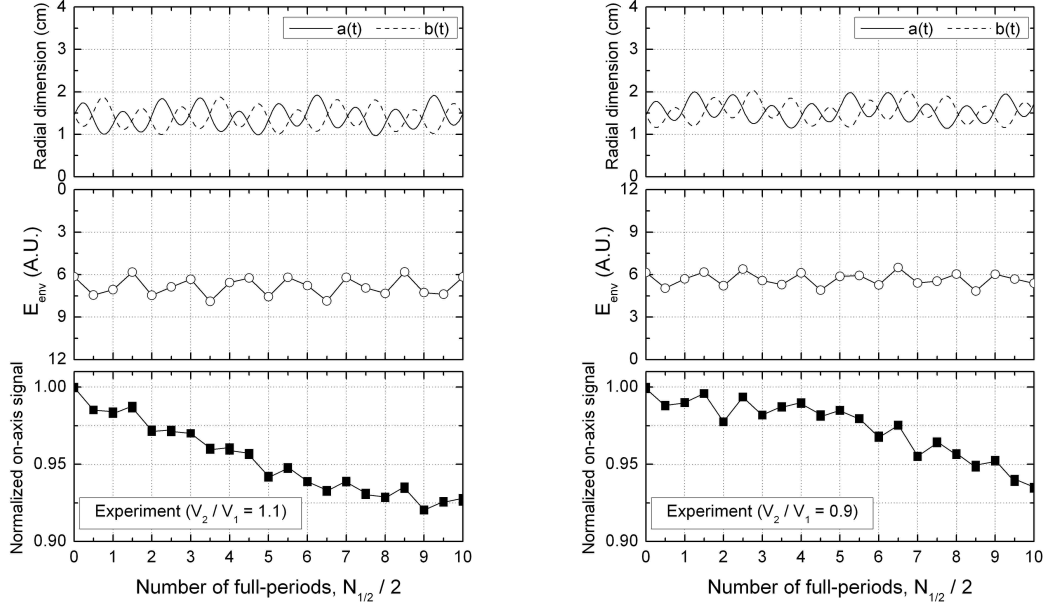
(a) $\frac{V_2}{V_1} = 1.1$, $\sigma_v^{sf} \approx 54.8°$, and $\frac{2\pi}{\omega_B} \approx 3.5T$.   (b) $\frac{V_2}{V_1} = 0.9$, $\sigma_v^{sf} \approx 44.8°$, and $\frac{2\pi}{\omega_B} \approx 4.3T$.

Figure 6.7: A KV envelope model can also resolve the basic features of the small oscillatory patterns for the cases with $\pm 10\%$ changes in the focusing field.

E_{env} during the malfunctioning of the quadrupole focusing field may be an effective single-parameter figure of merit that predicts the final amount of emittance growth and beam degradation. This analysis is sufficiently sensitive that it can even resolve the basic features of the small oscillatory patterns for the cases with $\pm 10\%$ changes (Fig. 6.7).

Here, the envelope equations are solved by the numerical integration for a matched beam with initial parameters and conditions (such as K, ϵ, and $a = b = \sqrt{2}R_b$) inferred from the experimental data. For the experimental data points in Figs 6.6 and 6.7, the error bars are much smaller than the symbol sizes, and the oscillatory patterns are quite reproducible. Simulations using the WARP 2D code [FRIEDMAN *et al.*, 1992] in Fig. 6.8 also confirm the oscillatory behavior in the on-axis charge measurements with comparable oscillation periods.
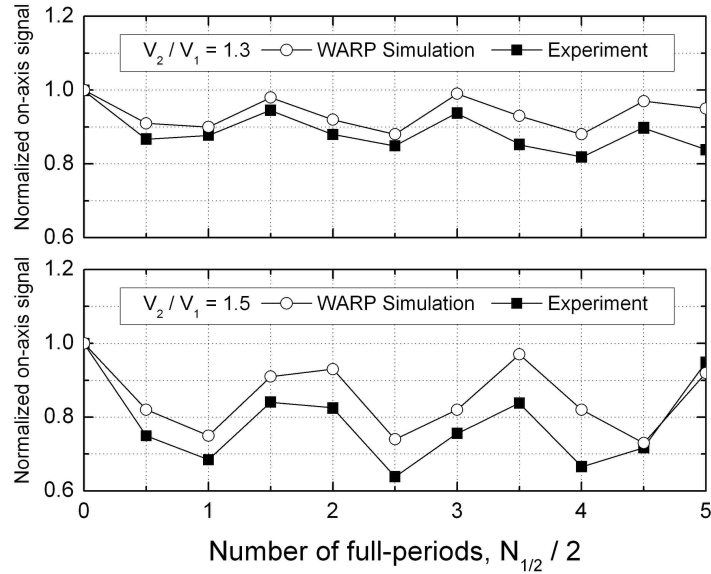
Figure 6.8: Comparison between WARP 2D simulations (open circles) and experimental data (solid squares) for the oscillatory behavior in the on-axis signal [GILSON *et al.*, 2006].

In conclusion, we have demonstrated experimentally that a direct outcome of the faulty magnets is an irregular mismatch oscillation of the intense beam, which eventually leads to significant emittance growth and beam degradation. In particular, we discovered that the amplitude of such a mismatch oscillation depends rather nontrivially on the number of the adjacent faulty magnets, but this can be explained by a simple KV envelope model.

6.2 Effect of Random Noise

One common feature that is unavoidable in high-intensity accelerators is the presence of random noise and its self-consistent influence on the long-time-scale beam dynamics [BOHN and SIDERIS, 2003; GERIGK, 2004]. The random noise includes machine imperfections, such as quadrupole magnet and RF cavity alignment errors, quadrupole

focusing gradient errors, RF field amplitude and phase errors, and jitter in the power supplies, to mention a few examples [QIANG *et al.*, 2001]. Usually, random noise in the machine components acts as a continuous supply of free energy to the intense beam, which results in irregular mismatch oscillations of the beam envelope [GERIGK, 2004], enhanced halo formation [BOHN and SIDERIS, 2003; SIDERIS and BOHN, 2004], and emittance growth [FRANCHETTI and HOFMANN, 2002b], particularly over long propagation distances. From various multiparticle simulations including both space-charge and random noise effects, considerable progress has been made in developing an improved understanding of the random noise-induced beam degradation [QIANG *et al.*, 2001; FRANCHETTI and HOFMANN, 2002b; GERIGK, 2004; IKEGAMI *et al.*, 2004; YOON *et al.*, 2005]. However, experimental verification of these effects has been somewhat limited due to the lack of dedicated experimental facilities which allow the study of long-length-scale phenomena. On the other hand, as explained in pervious chapters, the PTSX device can experimentally simulate the nonlinear transverse dynamics of intense beam propagation over large distances through an alternating-gradient (AG) focusing channel by equivalently putting the observer in the beam frame [DAVIDSON *et al.*, 2000; GILSON *et al.*, 2004]. The amplitude of the voltage waveform applied to the electrodes in the PTSX device corresponds to the quadrupole focusing strength in an AG lattice system. Hence, by slightly modifying the voltage amplitude in every half focusing period ($T/2$), we can emulate the randomly distributed quadrupole focusing gradient error in the actual transport channel.

As mentioned earlier, in intense beams, the action of the nonlinear space charge plays a crucial role in transforming random noise effects into emittance growth [FRANCHETTI and HOFMANN, 2002b]. The relative importance of space-charge effects can be described either in terms of the tune depression $\nu/\nu_0 = (1 - \bar{s})^{1/2}$ or the normalized
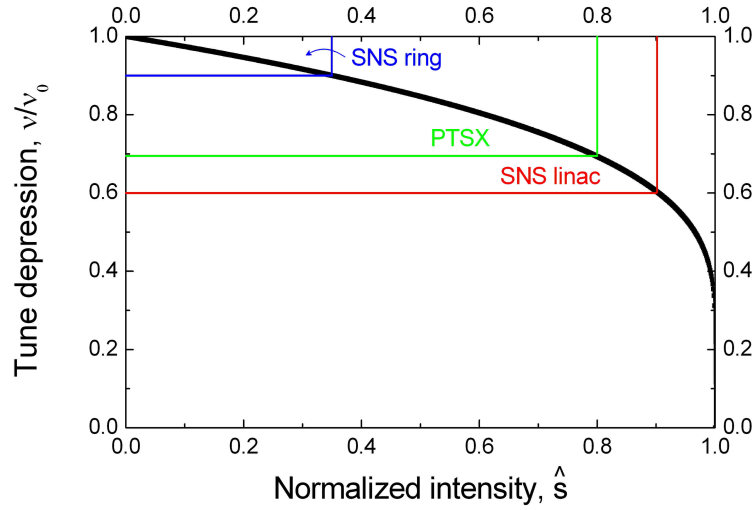
Figure 6.9: Relation between the tune depression ν/ν_0 used to describe average space-charge contribution in high-intensity accelerators and the normalized beam intensity $\hat{s}$ used to characterize a beam equilibrium with space-charge force in the PTSX device. When the beam is in a thermal equilibrium state, the two dimensionless parameters are related by $\nu/\nu_0 = [1 - \hat{s}\zeta(\hat{s})/2]^{1/2}$. Here, $\zeta(\hat{s})$ is the form factor introduced in **Chapter 2**.

intensity parameter $\hat{s}$. Here, $\bar{s} \approx \hat{s}\zeta(\hat{s})/2$ is the normalized intensity parameter for a uniform equivalent beam, and $\zeta(\hat{s})$ is the form factor introduced in **Chapter 2** of this thesis. For example, the newly commissioned Spallation Neutron Source (SNS) is expected to be operated at $\nu/\nu_0 \gtrsim 0.6$ in the linac section (total length ~ 331 m), and $\nu/\nu_0 \gtrsim 0.9$ in the accumulator ring (circumference ~ 248 m) [FRANCHETTI and HOFMANN, 2002a; HENDERSON *et al.*, 2005], which correspond to $\hat{s} \lesssim 0.9$ and $\hat{s} \lesssim 0.35$ respectively (see Fig. 6.9). In the linac section, space-charge effects play a more important role for the noise effect to be significant. In the accumulator ring, however, the long propagation distances associated with the long beam lifetime can have a larger impact on noise-induced beam degradation. Since the PTSX device covers the operating range of $0 \le \hat{s} \le 0.8$, and can confine the plasma up to 300 ms, which is equivalent to nearly 20 km-long beam propagation distances [GILSON *et al.*,

2004], effects of the quadrupole focusing gradient errors in SNS-like high-intensity accelerators can be effectively studied. The typical error limits of the quadrupole focusing gradients in the various components of the SNS are given in Table 6.2.

In performing the actual experiments in PTSX, however, it is quite important to minimize any other sources of beam state change that might be comparable to the random noise effect, such as injection mismatch, two-stream interactions, collision with background neutral gas, or drift in the ion source conditions. Hence, for the initial experiments presented in this chapter, we use a moderately low space-charge-density beam ($\hat{s} \sim 0.2$) that has been carefully optimized through the experimental campaign summarized in the **Chapter 4** of this thesis [CHUNG *et al.*, 2007c]. In addition, the number of error samples (independent set of time series of random numbers) is also an important factor for obtaining good statistics in the experimental data. In multiparticle simulations, the number of error samples has been chosen as small as 20 [IKEGAMI *et al.*, 2004] or as large as 500 [GERIGK, 2004] depending on the computation time and required accuracy for the quantitative analysis. For the experimental studies reported in this chapter, we use 20 error samples for a given error limit and trapping time (which is equivalent to a given propagation distance in the actual AG lattice). In this way, we can reduce the overall experimental time, avoiding any possible drift in the experimental conditions (mostly in the ion source) during the course of scanning the entire parameter range.

6.2.1   A Smooth-Focusing Model

As introduced in **Chapter 2** of this thesis, the evolution of the rms radius $R_b(t)$ of an equivalent KV beam with self-field perveance K and average transverse emittance

Component	Limit on error
MEBT (Medium Energy Beam Transport)	1.732%
DTL (Drift Tube Linac)	0.5%
CCDTL (Coupled-Cavity DTL)	0.25%
CCL (Coupled-Cavity Linac)	0.25%
Accumulator ring	0.01%

Table 6.2: Values of quadruple gradient error limits for various components of the SNS linac and accumulator ring [JEON, 1999; HENDERSON *et al.*, 2005].

ϵ is described effectively by

$$\frac{d^2 R_b}{dt^2} + \omega_{q0}^2 R_b - \frac{K}{2R_b} - \frac{\epsilon^2}{4R_b^3} = 0, \tag{6.6}$$

in the smooth-focusing approximation [DAVIDSON and QIN, 2001]. When there are random errors in voltage amplitudes $\hat{V}_0$ in every half focusing period $T/2$, the trapped plasma encounters a time series in the smooth-focusing frequencies given by $\omega_{q0}(1 + \delta_1), \ldots, \omega_{q0}(1 + \delta_i), \ldots, \omega_{q0}(1 + \delta_{N_{1/2}})$. Here, δ_i is a random number which belongs to a uniform distribution in the range $-\Delta_{\max} \leq \delta_i \leq \Delta_{\max}$, and i and $N_{1/2}$ are the index and the total number of half-periods of the noise duration, respectively. Hence, an error sample is composed of $N_{1/2}$ statistically-independent random numbers, representing white noise in the present analysis.

An example of the numerical solution of Eq. (6.6), having an error sample with $\Delta_{\max} = 1\%$, shows that irregular oscillations of the beam envelopes are excited and grow continuously according to the duration of the noise [Fig. 6.10(a)]. Since the envelope equation itself cannot self-consistently describe the emittance growth resulting from the envelope oscillations, the center of the oscillations remains nearly the same as the initial equilibrium radius R_{b0}. To describe the time evolution of the transverse emittance self-consistently, we need to solve the nonlinear Vlasov-Maxwell equations numerically. A result of WARP 2D PIC simulations with the same error sample used

(a) From the envelope equation.　　　　(b) From the PIC simulation.
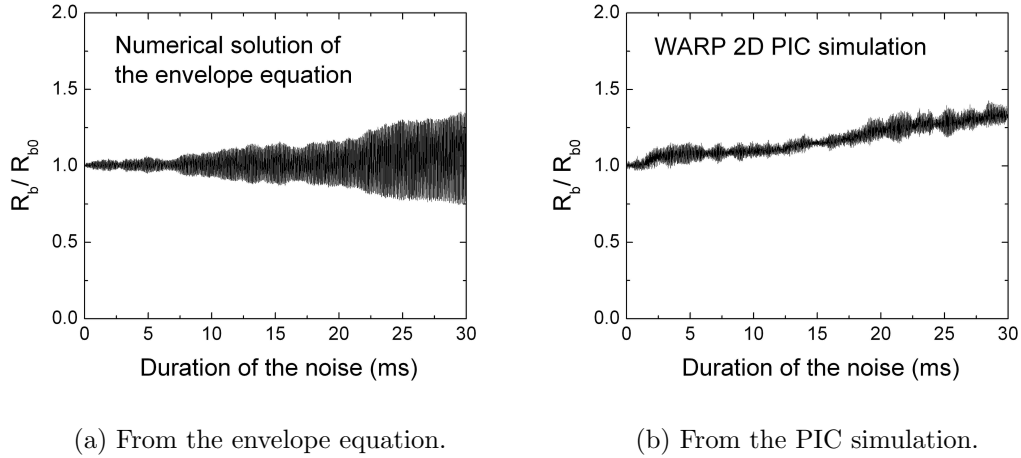
Figure 6.10: Evolution of the rms radius $R_b(t)$ calculated (a) from the envelope equation with constant emittance, and (b) from 2D WARP simulations with emittance growth. Note that the same error sample with $\Delta_{\max} = 1\%$ is used for (a) and (b).

in the envelope equation demonstrates that the oscillation amplitudes are saturated to some extent, and the oscillation center increases linearly with the noise duration [Fig. 6.10(b)], implying the conversion of the free energy available from the envelope oscillations into emittance growth [REISER, 1991]. Even though there are as many negative energy kicks as positive kicks on the average, the simulation results suggest that the random noise has a cumulative effect [GERIGK, 2004], which ends up producing overall increase in the beam energy.

Since the error limit $\Delta_{\max}$ in the focusing force is typically only a few percent, any possible changes due to the random noise in the global quantities such as the line density N, the effective transverse temperature $\bar{T}_\perp$, and the average transverse emittance ϵ will take place quite slowly. In this case, we can still assume that the beam is in a quasi-equilibrium state, which means that the the average focusing force balances both the thermal pressure force of the plasma and the space-charge force over a slow time scale (i.e., many breathing mode periods). Therefore, the global

force balance equation can be expressed as

$$m\omega_{q0}^2 R_b^2 \approx 2\bar{T}_\perp + \frac{Nq^2}{4\pi\epsilon_0}, \tag{6.7}$$

and the evolution of the average transverse emittance can be approximated by

$$\epsilon(t) \approx 2R_b \left(\omega_{q0}^2 R_b^2 - \frac{Nq^2}{4\pi\epsilon_0 m} \right)^{1/2}. \tag{6.8}$$

This equation allows us to estimate the emittance growth due to the random noise simply by using the N and R_b measured from the experiments. However, when there exists a significant population of low-density halo particles below the detection limit ($\lesssim 1$ fC) of the charge collector, then the emittance calculated from Eq. (6.8) necessarily underestimates the actual mean transverse emittance $\epsilon = 4 \left[\langle x^2 \rangle \langle \dot{x}^2 \rangle - \langle x\dot{x} \rangle^2 \right]^{1/2} \times \left[\langle y^2 \rangle \langle \dot{y}^2 \rangle - \langle y\dot{y} \rangle^2 \right]^{1/2}$. Particles far away from the beam core ($> \sqrt{2}R_b$) will be weighted heavily in calculating the emittance in the simulations [YOON *et al.*, 2005; FRIEDMAN *et al.*, 1992].

6.2.2   Experimental Results

To characterize the statistical properties of the beam response to the random noise, we make use of the on-axis charge, which is the most easily and accurately measurable quantity in the present experimental setup. Figure 6.11 represents the time history of the statistical average [E $\{Q(r = 0)\}$] and the standard deviation [square root of the variance Var $\{Q(r = 0)\} = \sigma^2$] of the on-axis charge computed over an ensemble of 20 random error samples. The average of the on-axis charge decays almost linearly with the amplitude and the duration of the noise up to 25 ms. After 25 ms, the decay rate becomes somewhat rapid, which is likely related to the the evolution of halo particles [see also Figs. 6.12(a) and 6.14] and the resultant enhanced particle loss. Because of

(a) $\mathrm{E}\{Q(0)\}$. (b) $\sqrt{\mathrm{Var}\{Q(0)\}}$
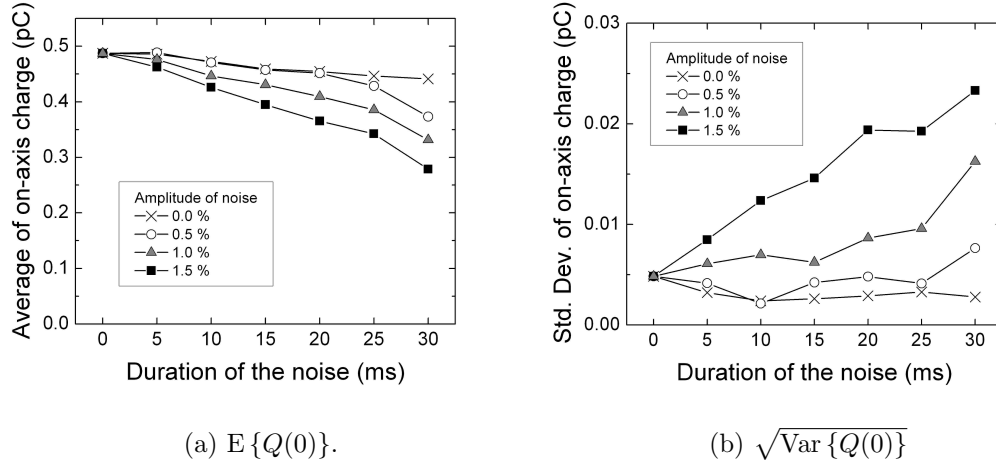
Figure 6.11: Time history of the statistical average (a) and the standard deviation (b) of the on-axis charge computed over an ensemble of 20 random error samples.

the intrinsic noise present in the PTSX device (either physics-originated or device-originated) such as two-stream interactions, collisions with residual gas, drift in the ion source conditions, jitter in the voltage waveform, or mechanical vibration of the vacuum pumps, the on-axis charge for the case with no applied noise also decreases slightly over the 30 ms of trapping with a finite variance that is comparable to the case with 0.5% applied noise. Due to the relatively small number of error samples, it is not clear if the beam response is a random-walk-like diffusion process ($\sigma \propto t^{1/2}$) [STOLTZFUS-DUECK and KROMMES, 2006]. However, the general tendency is that the standard deviation of the the on-axis charge increases with time, which strongly suggests that the fluctuations in the on-axis charge measurements originate from the applied noise rather than from the instrumental uncertainties (i.e., $\sigma \approx const.$) or the statistical fluctuations (i.e., $\sigma \propto \sqrt{\mathrm{E}\{Q(0)\}}$) [BEVINGTON and ROBINSON, 1992].

As mentioned previously, when the beam is in a quasi-equilibrium state, the on-axis charge (or equivalently $\hat{s}$) can be a single parameter that effectively characterizes the equilibrium density profile [DAVIDSON and QIN, 1999]. Hence, except for the

(a) Measured radial profiles.

(b) Evolution of the rms radius.
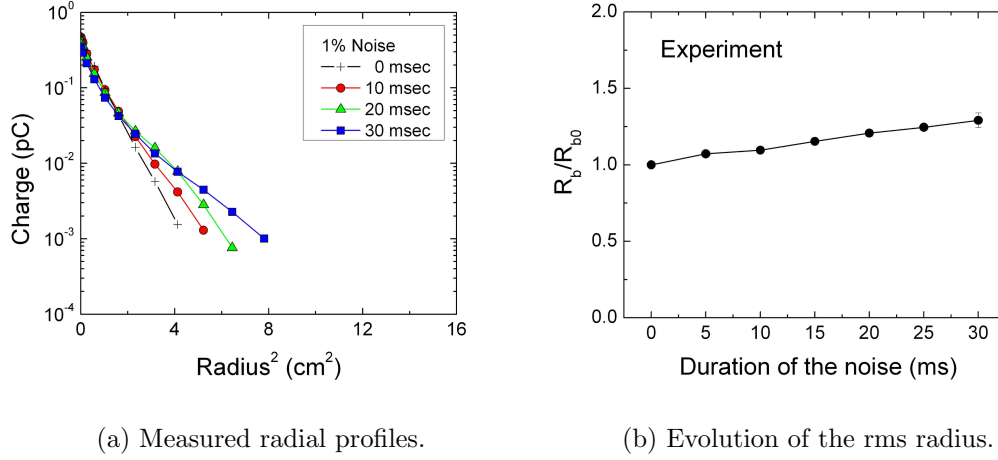
Figure 6.12: Evolution of (a) the measured radial profile, and (b) the corresponding rms radius under the influence of 1% uniform white noise.

case where there is a significant departure from the equilibrium state (such as the formation of a broad halo), we can infer the statistical characteristics of the radial density profile from those of the on-axis charge. Furthermore, when the normalized intensity parameter $\hat{s}$ is moderately low (for example, $\hat{s} \sim 0.2$ in this study), the equilibrium density profile of the beam is nearly Gaussian. In this case, we can relate N and R_b in terms of the on-axis density $\hat{n} = n(r = 0)$ by $N \approx \hat{n}\pi R_b^2$. Since, N is usually constant unless beam particles are lost to the wall, we can further consider R_b to be a function of the single parameter $\hat{n}$ according to $R_b(\hat{n}) \approx \sqrt{N/\pi\hat{n}}$. Therefore, for small changes in $\hat{n}$ due to random noise, we obtain the following simple expressions for the average of the rms radius $\mathrm{E}(R_b)$ and its variance $\mathrm{Var}(R_b)$:

$$\mathrm{E}(R_b) \approx \sqrt{\frac{N}{\pi \mathrm{E}(\hat{n})}}, \tag{6.9}$$

$$\mathrm{Var}(R_b) \approx \frac{N}{4\pi} \frac{\mathrm{Var}(\hat{n})}{\mathrm{E}^3(\hat{n})}. \tag{6.10}$$

The above approximate expressions provide a simple way to perform the experiments on random noise effects. By measuring a single density profile for a certain random error sample that gives $\hat{n} \approx \mathrm{E}(\hat{n})$, we can effectively obtain the statistical information

(a) Experiments.
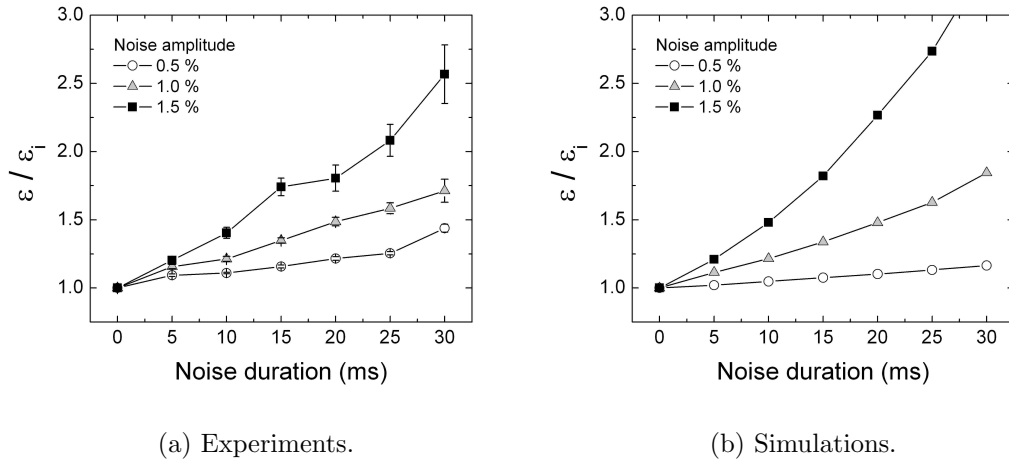
(b) Simulations.

Figure 6.13: The emittance growth is estimated from (a) radial profile measurements and (b) WARP 2D PIC simulations. For the WARP simulations, 20 random error samples are used to calculate the ensemble-averaged emittance.

on rms radius. Otherwise, we would have to measure $n(r)$ for every error sample to calculate the ensemble averaged quantities. This process would be very demanding for the present diagnostic setup, and is vulnerable to any drift in the experimental conditions.

The typical evolution of the measured radial profiles under the influence of uniform white noise (with $\Delta_{max} = 1\%$) is shown in Fig. 6.12(a). It is clear that low-density tails are developing in the radial profiles, and the corresponding rms radius R_b grows almost linearly with noise duration [see Fig. 6.12(b)]. Note that there is good agreement between the rms radius obtained in the WARP 2D simulations presented in Fig. 6.10(b) and the experimental results presented in Fig. 6.12(b). The evolution of the average transverse emittance given in Eq. (6.8) is estimated from the radial profile measurements for a given noise amplitude and duration, using a total of 19 independent radial profiles. Consistent with the WARP 2D simulations, we observe a continuous emittance growth which is approximately linear with the duration and the amplitude of the noise (Fig. 6.13). For the case where $\Delta_{max} = 1.5\%$, however,

(a) $\Delta_{\mathrm{max}} = 0.5\%$.   (b) $\Delta_{\mathrm{max}} = 1.5\%$.
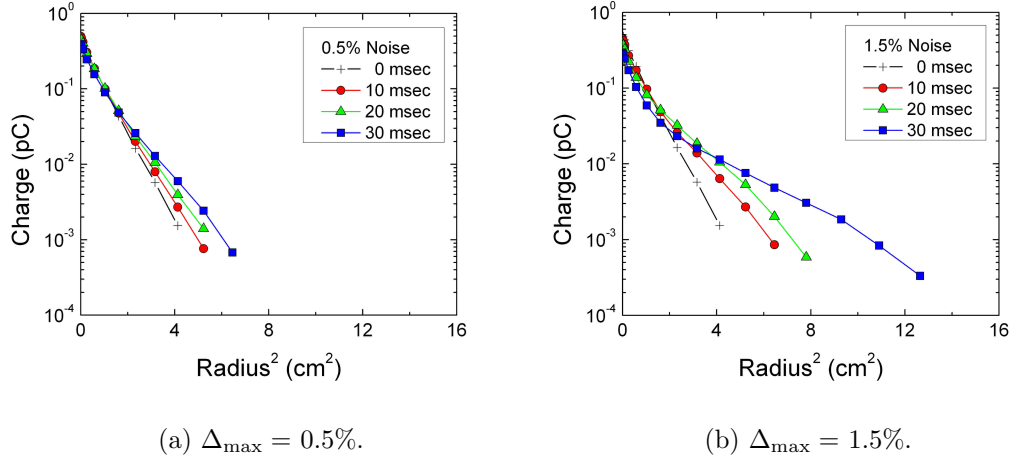
Figure 6.14: Measured radial profiles with different noise amplitudes and duration. Initially, the trapped plasma is in a thermal equilibrium state, for which the radial density profile is a straight line in the log versus r^2 plot.

the experimentally-determined emittance is somewhat underestimated after a noise duration of 15 ms. This is most likely due to the formation of a significant halo population under the detection limit (~ 1 fC) of the charge collector, which is too low to be measured in the experiment but contributes considerably in the simulations. The formation of a significant halo population is apparent in Fig. 6.14(b). On the other hand, for the case with $\Delta_{\mathrm{max}} = 0.5\%$, the experimentally estimated emittance has a slightly larger value than the simulation results, which is likely due to the intrinsic noise present in the PTSX device. For the WARP 2D PIC simulation presented in Fig. 6.13(b), 40000 macroparticles are used, which is comparable to the number of macroparticles adopted for other noise simulations [FRANCHETTI and HOFMANN, 2002b]. The time step for the PIC simulation is $\Delta t = 0.05/f_0 \ll 2\pi/\omega_p$.

6.2.3 Effects of Colored Noise

So far, we have used uniform white noise to model random errors in the quadrupole focusing gradient. In an actual accelerator system, a power supply usually drives
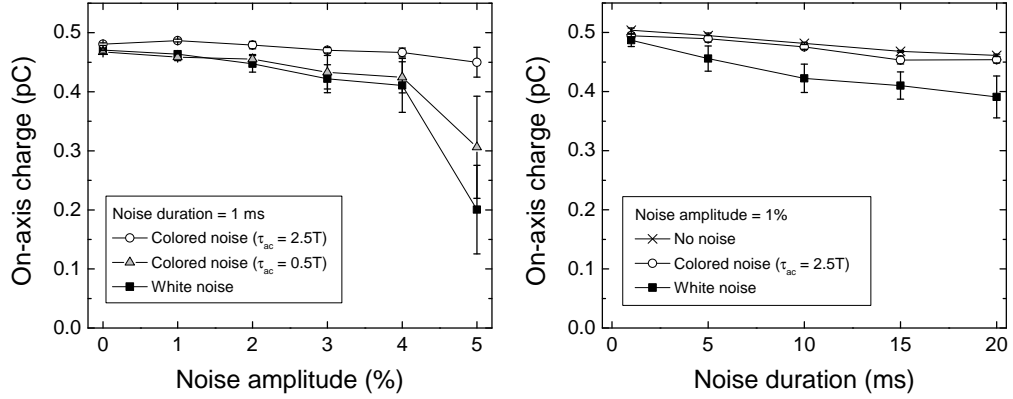
(a) A scan of the noise amplitude.

(b) A scan of the noise duration.

Figure 6.15: Dependence of the on-axis charge signal on (a) noise amplitude and (b) noise duration for white ($\tau_{ac} = 0$) and colored noise ($\tau_{ac} > 0$).

several magnets in series which are mounted on a common mechanical structure. Thus, any ripples in the driven currents or ground vibration can comprise a colored noise in the quadrupole focusing gradient with a finite autocorrelation time (e.g., several focusing periods) [LEE, 2004]. In recent papers [BOHN and SIDERIS, 2003; SIDERIS and BOHN, 2004], Bohn and Sideris pointed out that the presence of colored noise can boost a small number of particles to much larger amplitudes than inferred from a parametric resonance alone [GLUCKSTERN, 1994], by continually kicking halo particles back into the right phase with the core envelope oscillation. Hence, in this section, we present a preliminary experimental study that investigates the possible synergistic effect between colored noise and the collective modes indicated by Bohn and Sideris.

To modify the voltage amplitude with colored noise in every half focusing period $T/2$, we use a numerical algorithm generating Gaussian colored noise based on the integration of the Langevin equation as [STOLTZFUS-DUECK and KROMMES, 2006]

$$\delta_{i+1} = \delta_i e^{-T/(2\tau_{ac})} + w_i \Delta_{\max} \left(1 - e^{-T/\tau_{ac}}\right)^{1/2}. \tag{6.11}$$

Here, w_i is a Gaussian random number generated anew at each step i with zero mean and unit variance, τ_{ac} is the autocorrelation time which measures the memory of randomness, and $\Delta_{\max}$ is the amplitude of the desired colored noise. To excite collective modes, the results of Sec. 6.1 have been applied. We perturb the initial quiescent plasma ($\hat{s} \sim 0.2$ and $\omega_q = 52.2 \times 10^3$ s^{-1} for this case) by instantaneously increasing the voltage amplitude by 1.5 times, and switching back to the original value after one focusing period T. In this way, it is expected that a mixed mode with breathing mode period $2\pi/\omega_B \approx 3.70T$ and quadrupole mode period $2\pi/\omega_Q \approx 3.65T$ is excited similar to the case in Fig. 6.6(a).

For a matched beam where there is no mismatch oscillation, scans of the noise amplitude and duration in Fig. 6.15 demonstrate that white noise is more detrimental than colored noise. Indeed, when the autocorrelation time of colored noise is greater than $2.5T$, there is no significant change in the on-axis signal even for large amplitude and long duration of the colored noise. This can be understood because the energy kicks introduced by the white noise transfer maximum external energy into the system by compressing the beam most abruptly. As we saw in **Chapter 5** of this thesis, a gradual change in the focusing field strength tends to compress (or expand) the beam with less emittance growth.

The simulation results in Fig. 6.16(a) also indicate that the colored noise ($\tau_{ac} = 5T$ for this case) perturbs the initial matched beam only slightly and leaves the average on-axis density nearly unchanged as expected from the experimental results in Fig. 6.15(b). Here, we have chosen the autocorrelation time to be $\tau_{ac} = 5T$ so that the colored noise itself will not affect the initial beam too much (when $\tau_{ac} > 2.5T$), and have a time scale comparable to the collective modes (for instance, $2\pi/\omega_B \approx 3.70T$). From the beam mismatch case presented in Fig. 6.16(b), consistent with the
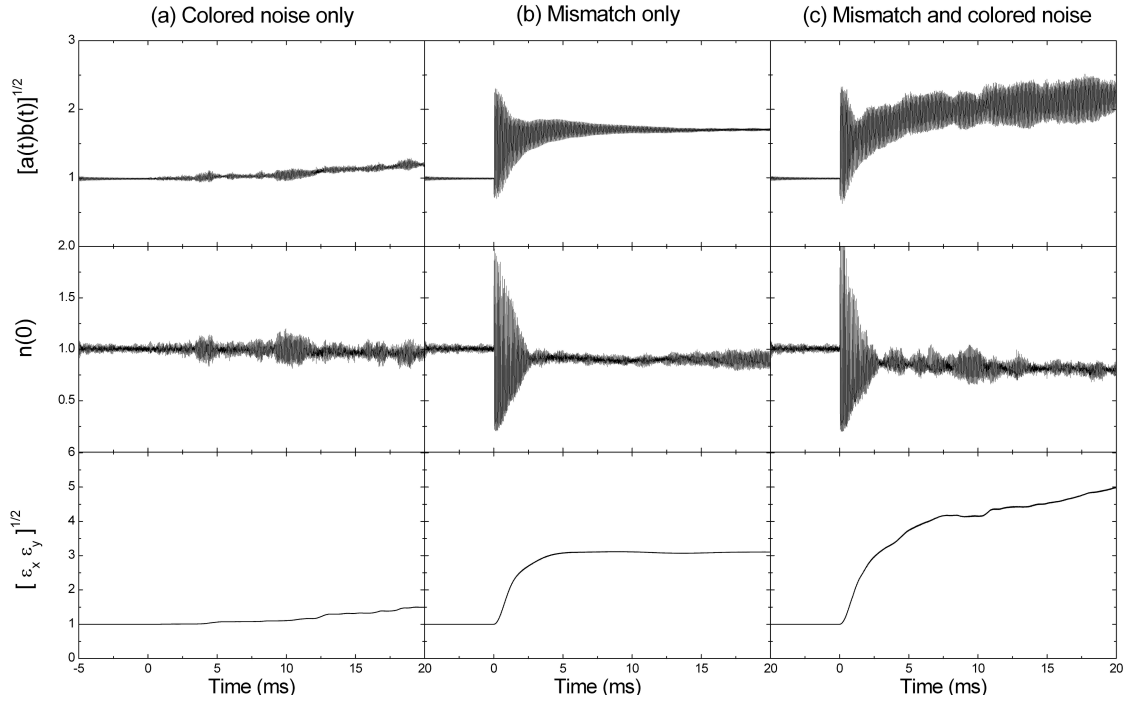
Figure 6.16: WARP 2D PIC simulation results for the beam responses to (a) colored noise with $\tau_{ac} = 5T$ and $\Delta_{max} = 1\%$, (b) beam mismatch introduced by the incorrect (1.5 times stronger in this case) focusing field strength for one FODO lattice period, and (c) the combination of colored noise and beam mismatch. The mean radius $[a(t)b(t)]^{1/2}$ (top), the on-axis density $n(0)$ (middle), and the mean transverse emittance $[\epsilon_x \epsilon_y]^{1/2}$ (bottom) are normalized to their initial values, respectively, and perturbation starts at $t = 0$ ms. For a fair comparison, the same colored noise sample has been applied to the cases (a) and (c).

(a) Experiments. (b) Simulations.
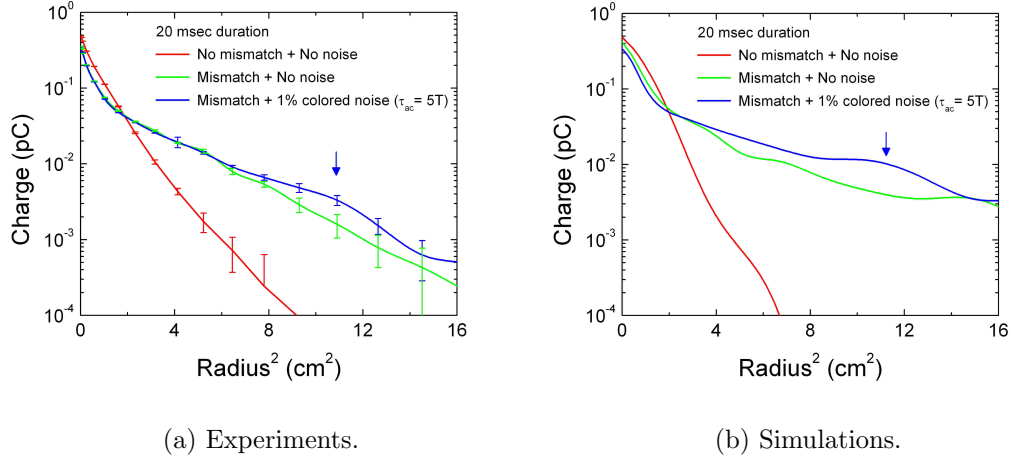
Figure 6.17: Radial profiles are either (a) measured from the experiments, or (b) obtained from the PIC simulations. Three different external perturbation scenarios are considered: no perturbation at all (red curves); instantaneous mismatch only (green curves); and both instantaneous mismatch, and colored noise with $\tau_{ac} = 5T$ and $\Delta_{\max} = 1\%$ (blue curves).

discussion made in Sec. 6.1, we observe the excitation of collective modes, resulting in a 200% emittance growth. The envelope oscillations last for about $5 \sim 10$ ms and eventually damp away. The most interesting case is the beam response in the presence of both the collective modes and the colored noise [Fig. 6.16(c)]. Even though the colored noise itself cannot excite significant envelope oscillations, when combined with the collective modes, it gives rise to continuous emittance growth and an increase in the mean radius with much higher oscillation amplitudes. These simulation results can also be interpreted as indicating enhanced halo formation. One possible underlying mechanism for enhanced halo formation has been recently proposed by Bohn and Sideris [BOHN and SIDERIS, 2003; SIDERIS and BOHN, 2004]. By extending the particle-core model [GLUCKSTERN, 1994; WANGLER *et al.*, 1998], they showed that the combination of colored noise and core envelope oscillations (breathing modes in their case) can eject particles to a much larger degree than would be achieved in the absence of noise.

To experimentally explore the synergistic effect between collective modes and colored noise, and the resultant enhanced halo formation predicted in the simulations, we measured the radial charge profiles corresponding to cases (b) and (c) of Fig. 6.16. In case there is neither induced mismatch nor applied noise, the initial matched beam remains nearly in a quasi-equilibrium state (with $R_b = 0.916$ cm) even after 20 ms of trapping [red curve in Fig. 6.17(a)]. On the other hand, when the beam is instantaneously mismatched in the same manner as in the previous simulation, a large non-thermal ion tail is measured at $r > \sqrt{2}R_b \approx 1.29$ cm [green curve in Fig. 6.17(a)]. More interestingly, in the experiment with both instantaneous mismatch and applied colored noise, we observe a development of a small bump around $\approx (3 \sim 4)R_b$ [blue curve and arrow in Fig. 6.17(a)]. The error bars are determined primarily from the offset errors (~ 1 fC) in constructing the radial profiles. Although the accuracy is not adequate to cover the range below $\lesssim 1$ fC, it still gives enough precision to resolve the small bump illustrated in Fig. 6.17(a). Therefore, the experimentally observed bump might be attributed to the effect of the enhanced halo formation expected for the case of combined perturbations. To check the size and the location of the bump, we also perform WARP 2D PIC simulations for similar experimental parameters. Despite the difference in their absolute values, the relative sizes and locations of the bumps illustrate very good agreement between the experiments and simulations [see Fig. 6.17(b)].

In summary, we have presented experimental verification of the random noise-induced beam degradation theoretically expected in high-intensity accelerators. Externally-driven noise continuously increases the rms radius, transverse emittance, and non-thermal tail of the trapped plasma almost linearly with the amplitude and duration of the noise. In particular, we have observed the combined effects of collective modes

and colored noise, which are consistent with theoretical predictions and numerical simulations.

6.3 Summary and Discussion

In this chapter, we have investigated the transverse beam dynamics in response to various machine imperfection effects present in high-intensity accelerators. This was possible because the PTSX device is a compact experimental setup with flexible control over the external focusing fields that can simulate the nonlinear transverse dynamics of an intense beam propagating through an actual AG focusing system. In Sec. 6.1, we studied faulty magnet effects by spoiling the voltage waveform for short times, i.e., a few or several lattice periods. We observed non-trivial oscillatory behavior in the on-axis signal, which can be effectively explained in terms of collective mode excitation and beam mismatch in a KV-equivalent beam. In Sec. 6.2, we studied random noise effects by adding a small random ripple on top of the applied voltage waveform. We demonstrated a noise-enhanced emittance growth that could affect intense beam transport over long propagation distances in linacs, or long beam lifetime in storage rings. The degree of mismatch (50% increase in the quadrupole focusing gradient) and the amplitude of the noise ($\Delta_{\max} \approx 1\%$) used to emulate machine imperfection effects in this study may seem somewhat larger than the actual tolerance limits adopted in daily accelerator operations. This is a compromise to overcome the difficulty of measuring small changes in charge signals ($10^{-3} \sim 1$ pC) in the PTSX device (particularly for the distribution tail or halo particles in the off-axis regions). Nonetheless, in modern high-intensity accelerators, loss of only a few particles per meter can cause radioactivation that would preclude routine hands-on

maintenance [BOHN and SIDERIS, 2003]. Therefore, it is highly relevant to verify the validity of numerical tools and to test the physics models for beam loss in experiments with parameters even somewhat beyond the actual tolerance limits.

Chapter 7

Conclusions and Future Research

Studies of charged particle beam dynamics on the Paul Trap Simulator Experiment (PTSX) pure ion plasma have been presented in this thesis. A radially scanning charge collector diagnostic has been newly installed, and the ion injection process has been carefully optimized in order to characterize minute changes in beam equilibria in response to transverse beam compression and machine imperfection effects. It is demonstrated that adiabatic changes in the smooth-focusing frequency compress the beam quiescently, minimizing mismatch oscillations and emittance growth. Excitation of collective modes has been observed as a result of focusing field errors, and noise-induced beam degradation has been experimentally verified. As a non-destructive diagnostic, a laser-induced fluorescence (LIF) diagnostic system with accompanying barium ion source has been developed, which is expected to give more detailed information on the trapped plasma properties.

7.1 Conclusions

In this thesis, several important beam physics topics related to the applications of present- and next-generation high-intensity accelerators have been investigated in the PTSX device. This was possible because the PTSX device is a compact and versatile experimental setup with flexible control over the external focusing fields that can simulate the nonlinear transverse dynamics of intense beam propagation through the alternating-gradient (AG) focusing channel.

In **Chapter 3** of this thesis, implementation of the new charge collector system has been described, which is an improvement over the previous Faraday cup configuration. The new charge collector system permits detailed measurements of the radial ion density profile that can be compared with the smooth-focusing beam equilibrium model. To further improve our basic understanding on the trapped plasma in a non-destructive way, a laser-induced fluorescence (LIF) diagnostic system with accompanying barium ion source has also been developed. Initial LIF measurements show that the radial density profile reconstruction is hampered by a low signal-to-noise ratio, which is mainly a consequence of the low initial target metastable population and significant background light from the ion source.

In **Chapter 4** of this thesis, various beam physics phenomena present during the ion injection stage of the PTSX operation have been characterized in order to achieve a well-behaved initial quasi-equilibrium beam. Injection beam mismatch, which gives rise to a shoulder structure in the measured radial density profile, has been identified as a result of the imbalance between the applied focusing force, and the defocusing space-charge and pressure forces (Sec. 4.1). It is demonstrated that injection beam mismatch can be minimized either by increasing the smooth-focusing frequency or by decreasing the extraction voltage. Fast ions, a small number of

particles with considerably larger axial kinetic energy than the main beam of ions, have been detected (Sec. 4.2.1). Fast ions produce a broad non-thermal tail in the radial density profile, compounding the accurate measurements of the emittance growth and halo particle production in the subsequent beam physics experiments. The optimal timing of the inject-trap-dump-rest cycle turned out to be an effective method to resolve this issue. Noting that fast ions are detected without being averaged over focusing periods, a time-resolved diagnostic method based on fast ions has been proposed, together with initial measurements of the envelope oscillations (Sec. 4.2.2). Possible two-stream interactions have been discussed in terms of analytical estimates and 3D PIC simulations (Sec. 4.3). For the nominal injection condition in the PTSX device, effects of two-stream interactions on the transverse beam dynamics turn out to be weak, allowing stable confinement of the trapped plasma for more than 3000 applied focusing periods. Formation of a virtual cathode near the source region is found to set the lower limit of the axial beam velocity available in the trap (Sec. 4.4).

In **Chapter 5** of this thesis, transverse beam compression, which has practical applications in areas such as heavy ion fusion and ion-beam-driven high-energy density physics, has been investigated. Based on energy balance for instantaneous transitions and emittance conservation for adiabatic transitions, simple analytical models for transverse beam compression have been developed, showing good agreement with experimental results, particularly for the adiabatic transition cases (Sec. 5.1.1). Both the experimental results (Sec. 5.2.1) and numerical simulations (Sec. 5.3.1) indicated that the suppression of mismatch oscillations is a key physics issue in transverse beam compression. Adiabatic changes in the smooth-focusing frequency for several lattice transition periods turn out to be an effective method to compress the beam quiescently, minimizing emittance growth and halo particle production. On

the other hand, instantaneous changes induce significant mismatch oscillations which are accompanied by broad halo formation around the beam core. Making use of the flexibility of PTSX operation, experiments on frequency changes have also been performed. Consistent with the smooth-focusing approximation, the instantaneous frequency turned out to be an important parameter for the description of the beam equilibria during the frequency change experiments (Sec. 5.1.2). Onset of the single-particle orbit instability and beam expansion due to the collective mode excitation have been observed during nonmonotonic changes in the instantaneous frequency (Sec. 5.2.2), which is consistent with the Kapchinskij-Vladimirskij (KV) envelope model calculations (Sec. 5.3.2).

In **Chapter 6** of this thesis, machine imperfection effects, which are practically unavoidable during the operation of high-intensity accelerators, are investigated. Malfunctioning of the finite number of magnet sets and randomly distributed small errors in focusing gradients are considered. It is demonstrated that a direct consequence of faulty magnets is an irregular mismatch oscillation of the intense beam, which eventually leads to significant emittance growth and beam degradation (Sec. 6.1.1). In particular, it is found that the amplitude of such a mismatch oscillation depends rather non-trivially on the number of the adjacent faulty magnets, which can be explained either by a smooth-focusing model (Sec. 6.1.2), or more quantitatively by a KV envelope model (Sec. 6.1.3). Noise-induced beam degradation, which has been expected from several previous theoretical and numerical studies, is experimentally verified in the context of the smooth-focusing approximation (Sec. 6.2.1). A continuous increase in emittance proportional to the amplitude and duration of the noise has been observed, consistent with the PIC simulations (Sec. 6.2.2). Enhanced halo

formation due to the combined effects of the collective modes and colored noise has also been investigated (Sec. 6.2.3).

7.2 Future Research

Having demonstrated the flexibility and effectiveness of the PTSX device as a dedicated experimental setup for the study of intense beam dynamics, several future research tasks can be suggested as follows.

Throughout this thesis research, only a sinusoidal waveform has been considered for the quadruple focusing coefficient, mainly because the sinusoidal waveform is least taxing on the bandwidth limit of the PTSX electronics. Use of a periodic step-function or a periodic trapezoidal waveform is expected to give more realistic prediction of intense beam dynamics in an actual FODO (Focusing-Off-Defocusing-Off) lattice, provided that the slew rate and ringing effects on the non-sinusoidal waveform are negligible. In synchrotrons and storage rings, instead of a simple FODO lattice, a double bend achromat (DBA or Chasman-Green) lattice or a triple bend achromat (TBA) lattice are often used to suppress the effects of longitudinal momentum spread (dispersion effect) [WIEDEMANN, 1999; LEE, 2004]. In the limit of small dispersion, it is also possible to study intense beam propagation through the DBA or TBA lattice channel by applying the appropriate voltage waveform in the PTSX device.

The initial beam state used in this thesis work has been limited to normalized beam intensity $\hat{s} \sim 0.2$, which corresponds to the intense beam characteristic of proton accumulator rings or booster synchrotrons. In high-intensity linacs, however, the space-charge effect is more significant and the normalized beam intensity is typically much higher than in rings. Hence, it is recommended to develop an ion injection

scheme to obtain an initial stable beam equilibrium with higher space-charge intensity (for example, $\hat{s} \gtrsim 0.6$).

Once we have developed an excitation method for collective modes (instantaneous change of the focusing strength) and a monitoring tool for them (oscillatory behavior in the on-axis charge) in the PTSX device, several research topics on collective modes can be proposed as follows.

- In the small-angle approximation [LEE, 2004; MINTY and ZIMMERMANN, 2003], where the effects of dipole bending magnets can be neglected in the detailed beam dynamics description of large-curvature circular accelerators, it would be possible to investigate some key physics issues in storage rings using the PTSX device. In storage rings, it is well known that if the betatron tune*(denoted by ν or Q), which is defined as the number of the betatron oscillation period ($\approx 2\pi/\omega_q$ in the smooth-focusing approximation) per revolution, is a half integer, then the perturbations from the quadrupole magnet imperfections accumulate and eventually lead to orbit distortion and beam degradation, particularly when there are nonnegligible space-charge effects [LEE, 2004]. If we perturb the trapped plasma in the PTSX device periodically with time step ℓ/f_0 and scan the integer ℓ over several envelope oscillation periods, it should be possible to observe half-integer resonances modified by space-charge effects (so called space-charge tune shift).

- From the PIC simulation results presented in this thesis, we note that the damping rate of the mismatch oscillation amplitude is directly related to the growth rate of the transverse emittance. The time scale of the emittance growth induced by the rms mismatch is typically $\gtrsim 10(2\pi/\omega_p)$ [WANGLER, 1998]. If

we extend the scan range of the number of half-focusing period $N_{1/2}$ used in Sec. 6.1 until the oscillatory behavior in the on-axis charge signal disappears, we may obtain useful information on the damping of the mismatch oscillations, or equivalently the growth of the transverse emittance.

- In Sec. 6.2, the combined effect of collective modes and colored noise has been investigated with a fixed autocorrelation time $\tau_{ac} = 5T$. By measuring radial profiles with several different autocorrelation times, for example $2\pi/\tau_{ac} \approx \omega_q, \omega_B, \omega_Q, (\omega_Q + \omega_B)/2, (\omega_Q - \omega_B)/2, \ldots$, we may be able to develop a more detailed understanding on noise-enhanced halo formation. Improving the accuracy of the charge collector diagnostic will also facilitate a more detailed resolution of the small changes expected in this type of experiment.

- In Sec. 4.2, we have demonstrated that the fast ion signal can be used to investigate the mismatch oscillations in the injection phase of the PTSX operation. To obtain more quantitative information on characteristic frequencies, future experiments should be performed with higher sample frequency and longer time interval for the collection of the fast ion signal. Optimization of the recently installed collective mode diagnostic system [GILSON *et al.*, 2007b] is also desirable to make comparisons with the fast ion signal.

To resolve the low signal-to-noise ratio (SNR) issue of the present LIF diagnostic, two alternative schemes are proposed. One is to change the dye of the current CW ring-dye laser system so that it can excite the ground state ions directly, and the other is use of a second dye laser to populate the target metastable ions. Both schemes are expected to give at least an order-of-magnitude improvement in the LIF signal. Possible technical issues associated with the new LIF schemes are discussed here.

- The first scheme considers the use of Coumarin 102 dye, for which the lifetime, gain, and solubility are drastically reduced compared with current DCM dye. Changing the optics set of the dye laser system is also required. The image intensifier of the present CCD camera is Gen-II type. Hence, the quantum efficiency (QE) for detecting 649 nm transition from the new scheme is about 50% less than for the 493 nm transition in the original scheme. The bandpass filter should be replaced as well.

- The second scheme involves operation of the high-power excimer laser for pumping. One of the working gases for the excimer laser, HCl, is particularly toxic and corrosive, and needs special safety consideration. The pulse length and repetition rate of the second dye laser will be 10 nsec and 10 Hz, respectively. Hence, to maximize SNR, synchronization of the laser injection, CCD gating, and PTSX operation is essential. The second dye laser will be injected axially along the center of the trap through the entrance window made in the diagnostic end.

In addition to the improvement of the LIF signal itself, further efforts to decrease the background light level should be made as well. As indicated in **Chapter 3**, the dominant contribution to the background light is the glowing barium ion source. Precise control and monitoring of the ion source temperatures are required to perform background subtraction with minimal shot-to-shot variations. Installation of the light baffle in front of the exit nozzle of the ion source will collimate the background light emission, reducing reflection from the gold-plated electrodes.

---

*It is quite interesting that the betatron tune (ν or Q) is a similar concept to the safety factor q used in the toroidal magnetic confinement devices.

Appendix A

End Effects in the PTSX Device

We consider an applied potential $\phi_a(r, \theta, z, t)$ that satisfies boundary conditions at $r = r_w$ depicted in Fig. 2.1

$$
\phi_a = \begin{cases} +V_0(t), & -L < z < +L, 0 < \theta < \frac{\pi}{4}, \frac{3\pi}{4} < \theta < \frac{5\pi}{4}, \frac{7\pi}{4} < \theta < 2\pi, \\ -V_0(t), & -L < z < +L, \frac{\pi}{4} < \theta < \frac{3\pi}{4}, \frac{5\pi}{4} < \theta < \frac{7\pi}{4}, \\ +\hat{V}, & -\infty < z < -L, +L < z < +\infty. \end{cases} \tag{A.1}
$$

Here, we assume that the scale length of the potential leaking into the trap is small compared to the length of the end electrodes, and extend the boundary condition to $z = \pm\infty$ for analytical simplicity. The general solution to $\nabla^2 \phi_a = 0$, which is symmetric in z about $z = 0$, is given by

- For $0 < z < +L$:

$$
\phi_a(r, \theta, z, t) = \phi_q(r, \theta, t) + \sum_{m=0, n=1}^{\infty} A_{mn} J_m(\mu_{mn} r / r_w) \cos(m\theta) \cosh(-\mu_{mn} z / r_w), \tag{A.2}
$$

and

- For $+L < z < +\infty$:

$$\phi_a(r,\theta,z,t) = \hat{V} + \sum_{m=0,n=1}^{\infty} B_{mn} J_m(\mu_{mn} r/r_w) \cos(m\theta) \exp(-\mu_{mn} z/r_w). \quad \text{(A.3)}$$

Here, μ_{mn} is the n-th zero of the Bessel function of the first kind of order m, i.e., $J_m(\mu_{mn}) = 0$, and $\phi_q(r,\theta,t)$ is the solution without end effects given in Eq. (2.14). The boundary conditions at $z = +L$ can be expressed as

- For continuity of ϕ_a:

$$\phi_q(r,\theta,t) + \sum_{m=0,n=1}^{\infty} A_{mn} J_m(\mu_{mn} r/r_w) \cos(m\theta) \cosh(-\mu_{mn} L/r_w)$$

$$= \hat{V} + \sum_{m=0,n=1}^{\infty} B_{mn} J_m(\mu_{mn} r/r_w) \cos(m\theta) \exp(-\mu_{mn} L/r_w), \quad \text{(A.4)}$$

and

- For continuity of $\partial\phi_a/\partial z$:

$$\sum_{m=0,n=1}^{\infty} A_{mn} J_m(\mu_{mn} r/r_w) \cos(m\theta) \sinh(-\mu_{mn} L/r_w)$$

$$= \sum_{m=0,n=1}^{\infty} B_{mn} J_m(\mu_{mn} r/r_w) \cos(m\theta) \exp(-\mu_{mn} L/r_w). \quad \text{(A.5)}$$

Solving for the coefficients A_{mn} from Eqs. (A.4) and (A.5) readily gives ϕ_a inside the trap $(-L < z < L)$. We obtain

$$
\begin{aligned}
\phi_a(r,\theta,z,t) &= \frac{4V_0(t)}{\pi} \sum_{l=1}^{\infty} \frac{\sin(l\pi/2)}{l} \left(\frac{r}{r_w}\right)^{2l} \cos(2l\theta) \\
&+ \hat{V} \sum_{n=1}^{\infty} \frac{J_0(\mu_{0n} r/r_w)}{\mu_{0n} J_1(\mu_{0n})} \left[\exp\left\{-\frac{\mu_{0n}(L+z)}{r_w}\right\} + \exp\left\{-\frac{\mu_{0n}(L-z)}{r_w}\right\}\right] \\
&- \frac{4V_0(t)}{\pi} \sum_{l=1,n=1}^{\infty} \frac{\sin(l\pi/2)}{l} \frac{J_{2l}(\mu_{2l,n} r/r_w)}{\mu_{2l,n} J_{2l+1}(\mu_{2l,n})} \cos(2l\theta) \\
&\times \left[\exp\left\{-\frac{\mu_{2l,n}(L+z)}{r_w}\right\} + \exp\left\{-\frac{\mu_{2l,n}(L-z)}{r_w}\right\}\right]. \quad \text{(A.6)}
\end{aligned}
$$
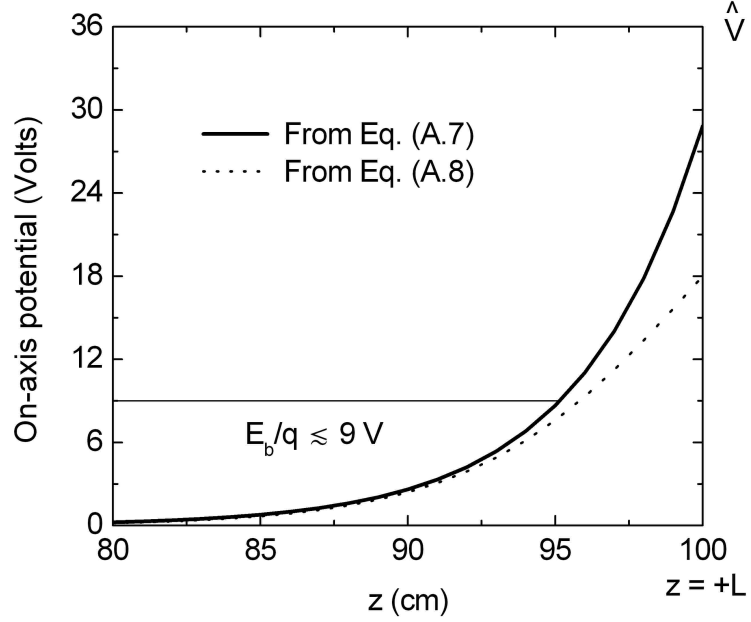
Figure A.1: On-axis potential distributions near $z = +L$ calculated from Eqs. (A.7) (solid line) and (A.8) (dotted line).

For $r \ll r_w \ll L$, to the lowest order, we find

$$
\begin{aligned}
\phi_a(r, \theta, z, t) \;\simeq\; & \frac{4V_0(t)}{\pi} \left(\frac{r}{r_w}\right)^2 \cos(2\theta) \left[1 - \frac{\mu_{21}}{8 J_3(\mu_{21})} \exp\left\{-\frac{\mu_{21}(L - |z|)}{r_w}\right\}\right] \\
& + \;\hat{V} \frac{J_0(\mu_{01} r/r_w)}{\mu_{01} J_1(\mu_{01})} \exp\left\{-\frac{\mu_{01}(L - |z|)}{r_w}\right\}.
\end{aligned}
\tag{A.7}
$$

Here, use has been made of $J_2(\mu_{21} r/r_w) \approx \left(\frac{r}{r_w}\right)^2 \frac{\mu_{21}^2}{8}$ for $r \ll r_w$. The potential leaks from the end electrodes at $z = \pm L$ fall off exponentially with e-folding length r_w/μ_{01}, which is 4.2 cm for the PTSX device. The potential distribution along the axis, $V(z)$, is known analytically by the expression [GRIVET, 1965; REISER, 1994]

$$
V(z) = \frac{\hat{V}}{2} \left[1 - \tanh\left\{\frac{1.318(L - |z|)}{r_w}\right\}\right].
\tag{A.8}
$$

Figure A.1 indicates good agreement between Eqs. (A.7) and (A.8) for axial beam energy $E_b \lesssim 9$ eV and DC bias voltage $\hat{V} = 36$ V.

(a) $E_b = 3$ eV and $x_0 = 1$ cm.

(b) $E_b = 9$ eV and $x_0 = 1$ cm.

(c) $E_b = 9$ eV and $x_0 = 5$ cm.

(d) $E_b = 18$ eV and $x_0 = 1$ cm.
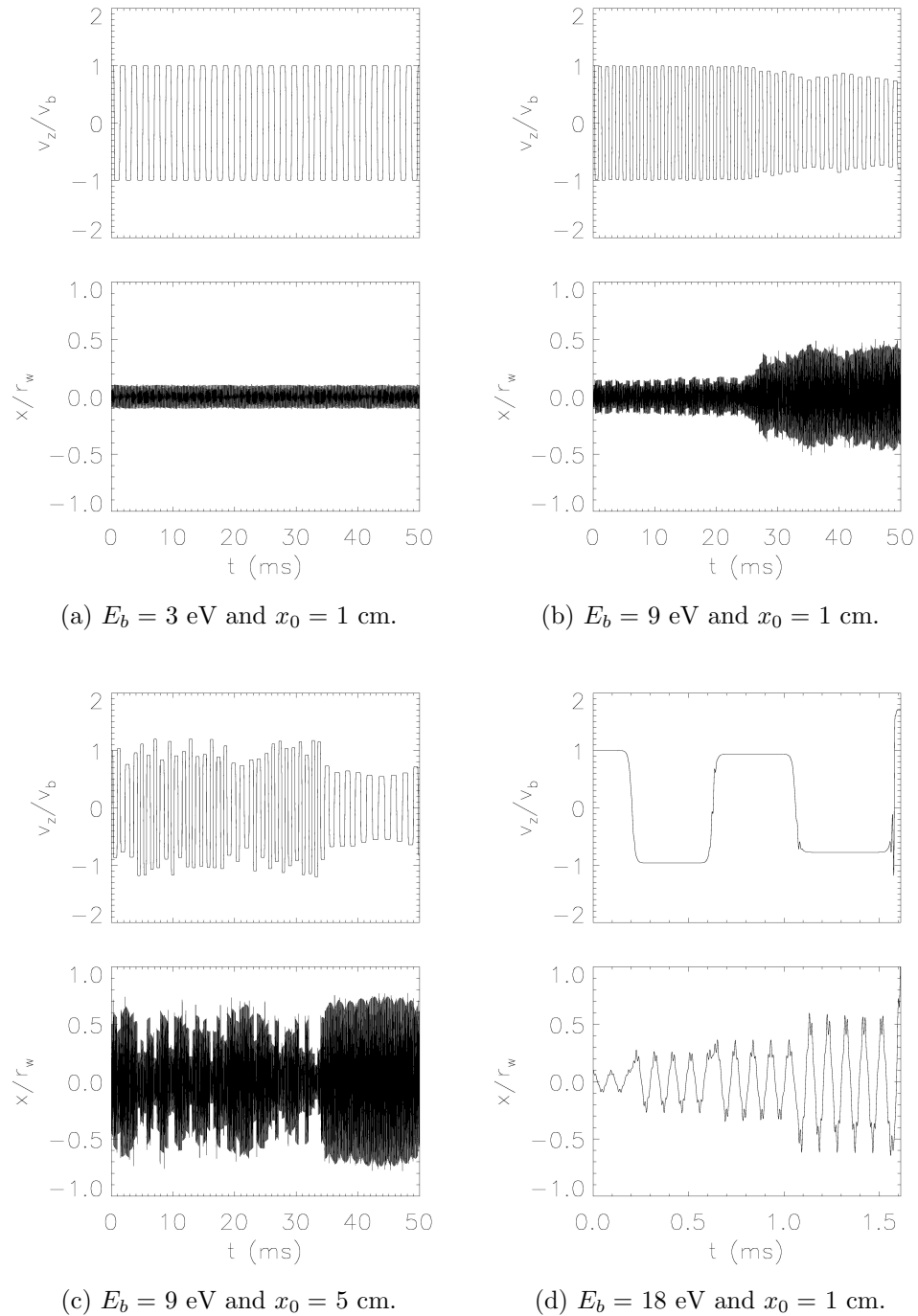
Figure A.2: Time evolutions of the axial velocity v_z and x position of the single-particle motion including end effects in the PTSX. Here, v_b is the initial axial beam velocity given by $v_b = (2E_b/m)^{1/2}$, and $r_w = 10$ cm is the wall radius. Initially, the test particle is located at $(x, y, z)_0 = (x_0, 0, 0)$ with $(\dot{x}, \dot{y}, \dot{z})_0 = (0, 0, v_b)$ and $\Phi = \pi/2$.

Therefore, with the good accuracy given by the approximate solution (A.7), the integration of the single-particle equations of motion including both the radial and axial electric fields produced by end effects can be easily performed. Figure A.2(a) shows that end effects are negligible when $E_b = 3$ eV, which is the nominal operating condition of the PTSX device. However, for the case where $E_b = 9$ eV [Fig. A.2(b)], the radial electric fields associated with the DC potential near $z = \pm L$ transfer axial energy into perpendicular energy, and eventually increase the radial excursion of the particle motion. Since the radial force produced by the DC potential barrier increases with the radial position and axial velocity of the beam particles, this end effect can be troublesome for non-thermal particles present in the PTSX device, such as halo particles [Fig. A.2(c)] and fast ions [Fig. A.2(d)]. Here, halo particles refer to a small number of particles with considerably larger radial excursion than the beam core, and fast ions refer to a small number of particles with considerably larger axial velocity than the main beam of ions. In particular, the fast ions are lost almost immediately after several bounces in the trap.

Appendix B

Condition for Two-Stream Interactions in the PTSX Device

For a non-relativistic beam-plasma system, the dispersion relation that determines the complex eigenfrequency ω of the perturbations about the Kapchinskij-Vladimirskij (KV) beam equilibrium with radius r_{bj} is given by

$$0 = D_l(k_z, \omega) = 1 + \sum_j \frac{\hat{\omega}_{pj}^2}{2l\nu_{bj}^2}\left[1 - \left(\frac{r_{bj}}{r_w}\right)^{2l}\right]\Gamma_j^l(\omega) \tag{B.1}$$

for axial wavenumber k_z, and azimuthal mode number $l = 1, 2, 3, \cdots$. Here, $\hat{\omega}_{pj}^2 = \hat{n}_j q_j^2/\epsilon_0 m_j$ is the plasma frequency-squared, $\nu_{bj}^2 = \omega_q^2 - \sum_j \hat{\omega}_{pj}^2/2$ is the depressed betatron frequency-squared, and the response function $\Gamma_j^l(\omega)$ is defined by [DAVIDSON *et al.*, 1999; DAVIDSON and QIN, 2001]

$$\Gamma_j^l(\omega) = -\frac{1}{2^l}\sum_{m_l=0}^{l}\frac{l!}{m_l!(l-m_l)!}\frac{(l-2m_l)\nu_{bj}}{[(\omega - k_z v_{bj} + i|k_z|v_{T\|j}) - (l - 2m_l)\nu_{bj}]}. \tag{B.2}$$

All the beam components j are assumed to have Lorentzian distributions with axial drift velocity v_{bj} and effective thermal speed $v_{T\|j} = \left(2T_{\|j}/m_j\right)^{1/2}$.

If we consider a uniform density ion beam $j = +$ with charge q, mass m, axial drift velocity $+v_b$, and number density $\hat{n}/2$, which is propagating through another symmetric, counter-streaming ion beam $j = -$ with axial drift velocity $-v_b$ and number density $\hat{n}/2$, then

$$\hat{\omega}_{p+}^2 = \hat{\omega}_{p-}^2 = \frac{1}{2}\frac{\hat{n}q^2}{\epsilon_0 m} = \frac{1}{2}\hat{\omega}_p^2, \tag{B.3}$$

and

$$\nu_{b+}^2 = \nu_{b-}^2 = \omega_q^2 - \frac{1}{2}\left(\hat{\omega}_{p+}^2 + \hat{\omega}_{p-}^2\right) = \omega_q^2 - \frac{1}{2}\hat{\omega}_p^2 = \nu_b^2. \tag{B.4}$$

If we further consider the strongest (largest growth rate) perturbation with $l = 1$ which corresponds to a simple (dipole) transverse displacement of the two counter-streaming ion beams [DAVIDSON $et\ al.$, 1999], then the dispersion relation becomes

$$1 = \frac{\hat{\omega}_p^2/4}{\left[(\omega - k_z v_b + i|k_z|v_{T\parallel})^2 - \nu_b^2\right]} + \frac{\hat{\omega}_p^2/4}{\left[(\omega + k_z v_b + i|k_z|v_{T\parallel})^2 - \nu_b^2\right]}. \tag{B.5}$$

Here, we neglect the effects of finite radial geometry by considering the typical operating condition for the PTSX device ($r_b \ll r_w$).

Before giving the general solution to Eq. (B.5), we briefly summarize the solutions for several limiting cases.

- For $v_b = 0$ and $v_{T\parallel} = 0$:

$$\omega^2 = \omega_q^2. \tag{B.6}$$

  This solution corresponds to a dipole-mode oscillation at the applied focusing frequency. It is one of the stable surface oscillations in a KV beam.

- For $v_b = 0$, $v_{T\parallel} = 0$, and $\hat{s} = \hat{\omega}_p^2/2\omega_q^2 = 1$:

$$\omega^2 = \frac{\hat{\omega}_p^2}{2}. \tag{B.7}$$

This solution corresponds to stable plasma oscillations in the space-charge-dominated limit. The external focusing force provides the necessary restoring force for the oscillations.

- For $v_b = 0$, $v_{T\parallel} = 0$, and $\omega_q^2 = 0$:

$$\omega^2 = \hat{\omega}_p^2. \tag{B.8}$$

This solution corresponds to plasma oscillations in an infinite plasma.

- For $v_b = 0$ and $v_{T\parallel} \neq 0$:

$$\begin{aligned} \text{Re}\,\omega &= \pm\omega_q, \\ \text{Im}\,\omega &= -|k_z|\,v_{T\parallel}. \end{aligned} \tag{B.9}$$

This solution corresponds to damped dipole-mode oscillations. The damping mechanism is well-known collisionless Landau damping [LANDAU, 1946].

- For $v_b = 0$, $v_{T\parallel} \neq 0$, and $\hat{s} = \hat{\omega}_p^2/2\omega_q^2 = 1$:

$$\begin{aligned} \text{Re}\,\omega &= \pm\hat{\omega}_p/\sqrt{2}, \\ \text{Im}\,\omega &= -|k_z|\,v_{T\parallel}. \end{aligned} \tag{B.10}$$

This solution corresponds to damped plasma oscillations in the space-charge-dominated limit.

- For $n_+ = \hat{n}$ and $n_- = 0$ (no counter-streaming beam):

$$\begin{aligned} \text{Re}\,\omega &= k_z v_b \pm \omega_q, \\ \text{Im}\,\omega &= -|k_z|\,v_{T\parallel}. \end{aligned} \tag{B.11}$$

This solution corresponds to a damped sideband oscillation.
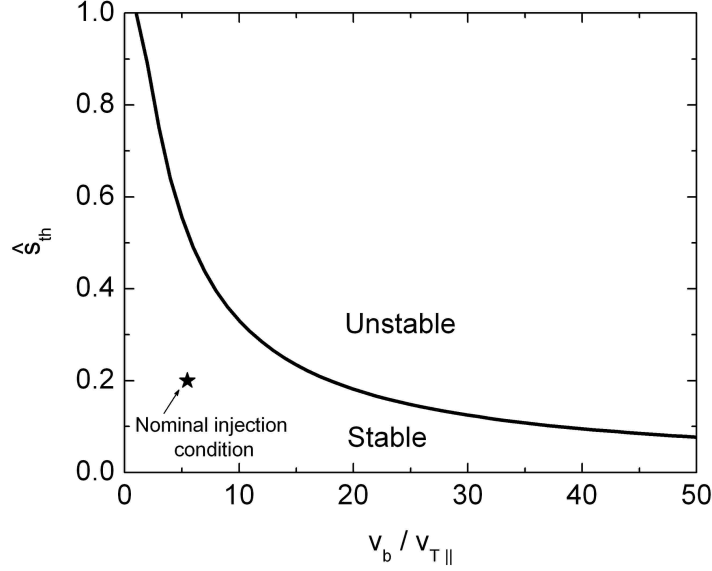
Figure B.1: Plot of threshold value of normalized intensity $\hat{s}_{\text{th}}$ for unstable two-stream interactions as a function of $v_b/v_{T\parallel}$. The nominal injection condition is indicated by the symbol (star).

In general, solving Eq. (B.5) for the imaginary frequency of the unstable mode readily gives

$$\text{Re}\,\omega = 0,$$

$$\text{Im}\,\omega = -\,|k_z|\,v_{T\parallel} + \left(\nu_b^2 + \frac{\hat{\omega}_p^2}{4}\right)^{1/2} \left[\left\{\frac{\hat{\omega}_p^4/16}{(\nu_b^2 + \hat{\omega}_p^2/4)^2} + 8\frac{k_z^2}{k_0^2}\right\}^{1/2} - \left(1 + 2\frac{k_z^2}{k_0^2}\right)\right]^{1/2},$$

(B.12)

where we define $k_0^2 = 2(\nu_b^2 + \hat{\omega}_p^2/4)/v_b^2$. The necessary condition for instability ($\text{Im}\,\omega > 0$) is [STIX, 1992]

$$\frac{1}{2}\left(\frac{\nu_b^2}{\nu_b^2 + \hat{\omega}_p^2/4}\right) < \frac{k_z^2}{k_0^2} < \frac{1}{2}\left(\frac{\nu_b^2 + \hat{\omega}_p^2/2}{\nu_b^2 + \hat{\omega}_p^2/4}\right).$$

(B.13)

Finally, the condition for instability ($\text{Im}\,\omega > 0$) can be expressed in terms of the threshold value of normalized intensity $\hat{s}_{\text{th}}$ as

$$\hat{s} > \hat{s}_{\text{th}} = 4\frac{v_b/v_{T\|}}{\left(1 + v_b/v_{T\|}\right)^2},$$

(B.14)

for $v_b > v_{T\|}$. Note that if $v_b < v_{T\|}$, then $\hat{s}_{\text{th}} > 1$, and instability does not exist because $\hat{s} < 1$ is required for transverse confinement of the beam ions. For nominal injection conditions in PTSX, $\hat{s} \sim 0.2$, $v_b \approx \sqrt{2E_b/m}$ for axial beam energy $E_b \sim 3$ eV, and $v_{T\|} \approx \sqrt{2T_s/m}$ with source temperature $T_s \sim 0.1$ eV, we obtain $\hat{s}_{\text{th}} \approx 0.52 > \hat{s}$. Hence, it is estimated that two-stream interactions are linearly stable for the nominal injection conditions in PTSX operation.

Appendix C

Doppler Broadening in the PTSX Device

Compared to a stationary observer, ions with thermal (random) or drift motion experience a Doppler shift in absorbing or emitting electromagnetic radiation [DEMTRODER, 2002]. For example, an ion can absorb laser radiation only when the Doppler-shifted frequency coincides with its resonance absorption frequency ω_0, i.e.,

$$\omega_L - k_L v_\xi = \omega_0. \tag{C.1}$$

Here, $\omega_L (= ck_L)$ and k_L are the angular frequency and wavenumber of the laser in vacuum, and v_ξ is the ion's velocity component along the laser propagation direction $\hat{\mathbf{e}}_\xi$. We assume perpendicular laser injection into the PTSX device, in which $\hat{\mathbf{e}}_\xi$ is normal to the axial direction $\hat{\mathbf{e}}_z$. When the ions have a thermal equilibrium distribution in the ξ-direction with constant transverse temperature $\hat{T}_\perp$ according to

$$f_\xi(v_\xi) = f_\xi(0) \exp\left[-\frac{\frac{1}{2}mv_\xi^2}{\hat{T}_\perp}\right], \tag{C.2}$$

then the Doppler width (full width half maximum of a Gaussian profile) becomes [DEMTRODER, 2002]

$$\Delta \nu_D = \frac{\omega_0}{2\pi} \sqrt{\frac{8\hat{T}_\perp \ln 2}{mc^2}} \tag{C.3}$$

in frequency units. Here, the transverse temperature $\hat{T}_\perp$ can be independently estimated from the radial density profile measurement.

In the PTSX device, we measure the radial density profile $n(r)$ averaged over many focusing periods $T = 1/f_0$. Hence, the rms radius $R_b = [(2\pi/N) \int_0^{r_w} dr r^2 n(r)]^{1/2}$ calculated from the measurement can be interpreted as the statistical average of the effective radial coordinate of the beam $R_{sf} = (x_{sf}^2 + y_{sf}^2)^{1/2}$ in the smooth-focusing approximation. Here, x_{sf} and y_{sf} are slow variables in the smooth-focusing approximation [DAVIDSON and QIN, 2001]. In particular, when beam is in equilibrium $(\partial/\partial t = 0)$, we have global force balance according to

$$m\omega_q^2 R_b^2 = 2\bar{T}_\perp + \frac{Nq^2}{4\pi\epsilon_0}, \tag{C.4}$$

where

$$R_b = \left\langle R_{sf}^2 \right\rangle_0^{1/2} = \left\langle x_{sf}^2 + y_{sf}^2 \right\rangle_0^{1/2} \tag{C.5}$$

is the (equilibrium) rms radius, and

$$\bar{T}_\perp = \frac{1}{2} m \left\langle \dot{x}_{sf}^2 + \dot{y}_{sf}^2 \right\rangle_0 \tag{C.6}$$

is the effective transverse temperature. Here, $\langle \cdots \rangle_0$ denotes the statistical average over the equilibrium distribution function in the smooth-focusing approximation. The effective transverse temperature $\bar{T}_\perp$, which measures the average kinetic energy of a beam particle, can be inferred from Eq. (C.4) using the rms radius R_b and line density N calculated from the radial density profile measurement. Note that in $\bar{T}_\perp$, the fast micromotion associated with quadrupole focusing frequency f_0 has been averaged.

If we further assume that the beam is in a thermal equilibrium state, then we can approximate $\hat{T}_\perp = \bar{T}_\perp$. Hence, the Doppler width is estimated to be

$$\Delta \nu_D \approx \frac{\omega_0}{2\pi} \sqrt{\frac{8\bar{T}_\perp \ln 2}{mc^2}}. \tag{C.7}$$

However, this estimation does not include possible effect of ion's fast micromotion.

To estimate the Doppler width including the fast micromotion, we adopt Hamiltonian averaging techniques [DAVIDSON and QIN, 2001]. To third order in the small dimensionless parameter ε defined by

$$\varepsilon = \frac{\sigma_v^{sf}}{\pi \sqrt{2}} < 1 \tag{C.8}$$

for a periodic quadrupole lattice with $\kappa_q(t) = \hat{\kappa}_q \sin(2\pi f_0 t)$ with $\hat{\kappa}_q = (8q/\pi m r_w^2)\hat{V}_0$, we obtain statistical averages of the mean-squared velocity components in the laboratory frame as follows:

$$\left\langle \dot{x}^2 \right\rangle (t) = [1 - 2\beta_q(t)] \left\langle \dot{x}_{sf}^2 \right\rangle_0 + \left[\alpha_q(t) - \langle \alpha_q \rangle_T \right]^2 \left\langle x_{sf}^2 \right\rangle_0, \tag{C.9}$$

$$\left\langle \dot{y}^2 \right\rangle (t) = [1 + 2\beta_q(t)] \left\langle \dot{y}_{sf}^2 \right\rangle_0 + \left[\alpha_q(t) - \langle \alpha_q \rangle_T \right]^2 \left\langle y_{sf}^2 \right\rangle_0. \tag{C.10}$$

Here, the lattice functions are defined by $\alpha_q(t) - \langle \alpha_q \rangle_T = -\omega_q \sqrt{2} \cos(2\pi f_0 t)$, and $\beta_q(t) = -\varepsilon \sin(2\pi f_0 t)$. Using the symmetry of the smooth-focusing equilibrium, $\left\langle \dot{x}_{sf}^2 \right\rangle_0 = \left\langle \dot{y}_{sf}^2 \right\rangle_0 = \frac{1}{2} \left\langle \dot{x}_{sf}^2 + \dot{y}_{sf}^2 \right\rangle_0$ and $\left\langle x_{sf}^2 \right\rangle_0 = \left\langle y_{sf}^2 \right\rangle_0 = \frac{1}{2} R_b^2$, we obtain

$$\left\langle \dot{x}^2 + \dot{y}^2 \right\rangle (t) = \left\langle \dot{x}_{sf}^2 + \dot{y}_{sf}^2 \right\rangle_0 + 2\omega_q^2 R_b^2 \cos^2(2\pi f_0 t) \tag{C.11}$$

after adding Eqs. (C.9) and (C.10). Moreover, if we assume that the beam has a thermal equilibrium distribution in the smooth-focusing approximation, we can further express $\frac{1}{2}m \left\langle \dot{x}_{sf}^2 + \dot{y}_{sf}^2 \right\rangle_0 = \bar{T}_\perp = \hat{T}_\perp$ and $\frac{1}{2}m\omega_q^2 R_b^2 = \hat{T}_\perp(1 + \delta_b)$. Here, $\delta_b = (1/4\pi\epsilon_0)(Nq^2/2\hat{T}_\perp)$ is the thermal beam intensity parameter defined in **Chapter 2** of this thesis. Finally, we readily obtain an expression for the statistically-averaged

kinetic energy of a beam particle with micromotion [$\equiv K_\perp(t)$] in terms of the thermal temperature as

$$\frac{1}{2}m \left\langle \dot{x}^2 + \dot{y}^2 \right\rangle (t) = K_\perp(t) = \hat{T}_\perp + 2\hat{T}_\perp (1 + \delta_b) \cos^2(2\pi f_0 t). \qquad \text{(C.12)}$$

Note that the total statistically-averaged kinetic energy $K_\perp(t)$ fluctuates rapidly at the focusing frequency (higher in the focusing or defocusing phases and lower in drift phases). Strictly speaking, the second term in Eq. (C.12) is not a random motion term, and will not contribute significantly to the Doppler broadening when the pulsed-laser is used (pulse length $\ll 1/f_0$). It will rather give rise to a shift of the resonance line. On the other hand, when a continuous-wave (CW) laser is used, the second term in Eq. (C.12) is averaged over many focusing periods and will effectively contribute to the Doppler broadening. The time-averaged $K_\perp(t)$ is then given by

$$\langle K_\perp(t) \rangle_T = \hat{T}_\perp + \hat{T}_\perp (1 + \delta_b). \qquad \text{(C.13)}$$

Here, the first term represents the thermal energy, whereas the second term represents the average oscillatory energy $\frac{1}{2}m\omega_q^2 R_b^2$. The resultant Doppler broadening can be estimated as

$$\Delta \nu_D \approx \frac{\omega_0}{2\pi} \sqrt{\frac{8\hat{T}_\perp (2 + \delta_b) \ln 2}{mc^2}}. \qquad \text{(C.14)}$$

Note that at high beam intensities ($\delta_b \gg 1$), the Doppler broadening becomes more significant. This can be understood as follows. As the beam intensity increases, a stronger focusing field is required to achieve equilibrium, which in turn leads to a faster fluttering of the beam envelope.

In the PTSX device, the thermal temperature is in the range of $0.1 \sim 1$ eV. As a result, the Doppler linewidth is normally two orders of magnitude broader than the natural linewidth of the resonance line. In addition, the absence of magnetic field,

and negligible effects of time-averaged electric field and collision in PTSX allow us to neglect Zeemann, Stark, and collisional broadening effects as well [Muraoka and Maeda, 2001]. Therefore, the Doppler broadening including the fast micromotion estimated in Eq. (C.14) will be the dominant effect for spectral line broadening in the PTSX device. For example, to facilitate the laser-induced fluorescence (LIF) diagnostic, it is desirable to select laser linewidth or scan range according to Eq. (C.14), particularly when the beam intensity is high. For the typical operating condition, $\hat{s} \sim 0.2$ and $\bar{T}_{\perp} \sim 0.1$ eV, we obtain $\Delta \nu_D \approx 1.4$ GHz, which is matched to the laser linewidth in the broadband operation (~ 2 GHz).

Bibliography

ABRAMOWITZ, M. and STEGUN, A. (1972). *Handbook of Mathematical Functions.* National Bureau of Standards.

ALLEN, C. K., CHAN, K. C. D., COLESTOCK, P. L., CRANDALL, K. R., GARNETT, R. W., GILPATRICK, J. D., LYSENKO, W., QIANG, J., SCHNEIDER, J. D., SCHULZE, M. E., SHEFFIELD, R. L., SMITH, H. V., and WANGLER, T. P. (2002). Beam-Halo Measurements in High-Current Proton Beams. *Phys. Rev. Lett.* **89**, 214802.

ALLEN, C. K. and REISER, M. (1996). Image Effects of Cylindrical Pipes on Continuous Beams. *Phys. Rev. E* **54**, 2884.

ALLEN, C. K. and WANGLER, T. P. (1998). Beam Halo Definitions Based upon Moments of the Particle Distribution. *Phys. Rev. ST Accel. Beams* **1**, 084201.

BEVINGTON, P. R. and ROBINSON, D. K. (1992). *Data Reduction and Error Analysis for the Physical Sciences.* McGraw-Hill, New York.

BOHN, C. L. and SIDERIS, I. V. (2003). Fluctuation Do Matter: Large Noise-Enhanced Halos in Charged-Particle Beams. *Phys. Rev. Lett.* **91**, 264801.

BRAU, J., OKADA, Y., and WALKER, N. (2007). *International Linear Collider Reference Design Report.* ILC Global Design Effort.

BROWN, N. and REISER, M. (1995). Thermal Equilibrium of Bunched Charged Particle Beams. *Phys. Plasmas* **2**, 965.

CHEN, F. F. (1984). *Introduction to Plasma Physics and Controlled Fusion.* Plenum Press, New York.

CHUNG, M., GILSON, E. P., DAVIDSON, R. C., EFTHIMION, P. C., and MAJESKI, R. (2007a). Initial Density Profile Measurements Using a Laser-Induced Fluorescence Diagnostic in the Paul Trap Simulator Experiment. In *Proceedings of the 2007 Particle Accelerator Conference*, page 3666. IEEE.

CHUNG, M., GILSON, E. P., DAVIDSON, R. C., EFTHIMION, P. C., MAJESKI, R., and STARTSEV, E. (2005a). Development of Laser-Induced Fluorescence Diagnostic for the Paul Trap Simulator Experiment. In *Proceedings of the 2005 Particle Accelerator Conference*, page 2878. IEEE.

CHUNG, M., GILSON, E. P., DAVIDSON, R. C., EFTHIMION, P. C., MAJESKI, R., and STARTSEV, E. A. (2005b). Laser-Induced Fluorescence Diagnostic of Barium Ion Plasmas in the Paul Trap Simulator Experiment. *Nucl. Instrum. Methods Phys. Res. A* **544**, 514.

CHUNG, M., GILSON, E. P., DORF, M., DAVIDSON, R. C., EFTHIMION, P. C., and MAJESKI, R. (2007b). Experiments on Transverse Compression of a Long Charge Bunch in a Linear Paul Trap. *Phys. Rev. ST Accel. Beams* **10**, 064202.

CHUNG, M., GILSON, E. P., DORF, M., DAVIDSON, R. C., EFTHIMION, P. C., and MAJESKI, R. (2007c). Ion Injection Optimization for a Linear Paul Trap to Study Intense Beam Propagation. *Phys. Rev. ST Accel. Beams* **10**, 014202.

COURANT, E. D., LIVINGSTONE, M. S., and SNYDER, H. S. (1952). The Strong-Focusing Synchrotron - A New High Energy Accelerator. *Phys. Rev.* **88**, 1190.

COURANT, E. D. and SNYDER, H. S. (1958). Theory of the Alternating-Gradient Synchrotron. *Annals of Physics* **3**, 1.

DAVIDSON, R. C. (1990). *The Physics of Nonneutral Plasmas*. Addison-Wesley, California.

DAVIDSON, R. C. and QIN, H. (1999). Single-Parameter Characterization of the Thermal Equilibrium Density Profile for Intense Non-Neutral Charged Particle Beams. *Phys. Rev. ST Accel. Beams* **2**, 114401.

DAVIDSON, R. C. and QIN, H. (2001). *Physics of Intense Charged Particle Beams in High Energy Accelerators*. World Scientific, Singapore.

DAVIDSON, R. C., QIN, H., and SHVETS, G. (2000). A Paul Trap Configuration to Simulate Intense Nonneutral Beam Propagation Over Large Distances through a Periodic Focusing Quadrupole Magnetic Field. *Phys. Plasmas* **7**, 1020.

DAVIDSON, R. C., QIN, H., STOLTZ, P. H., and WANG, T. S. (1999). Kinetic Description of Electron-Proton Instability in High-Intensity Proton Linacs and Storage Rings Based on the Vlasov-Maxwell Equations. *Phys. Rev. ST Accel. Beams* **2**, 054401.

DEMTRODER, W. (2002). *Laser Spectroscopy*. Springer, Berlin.

DORF, M. (2006). private communication.

DORF, M., DAVIDSON, R. C., and STARTSEV, E. A. (2006). Transverse Compression of an Intense Ion Beam Propagating through an Alternating-Gradient Quadrupole Lattice. *Phys. Rev. ST Accel. Beams* **9**, 034202.

EDWARDS, D. A. and SYPHERS, M. J. (1993). *An Introduction to the Physics of High Energy Accelerators*. Wiley, New York.

FOLEY, E. L. (2005). *Development of the Motional Stark Effect with Laser-Induced Fluorescence Diagnostic*. PhD thesis, Princeton University, Princeton, NJ.

FRANCHETTI, G. and HOFMANN, I. (2002a). Anisotropic Free-Energy Limit of Halos in High-Intensity Accelerators. *Phys. Rev. Lett.* **88**, 254802.

FRANCHETTI, G. and HOFMANN, I. (2002b). Effect of Lattice Random Errors on a Space Charge Dominated Beam. In *Proceedings of 2002 European Particle Accelerator Conference, Paris, France*, page 1353, Geneva. EPS-IGA/CERN.

FRIEDMAN, A., GROTE, D. P., and HABER, I. (1992). Three-Dimensional Particle Simulation of Heavy-Ion Fusion Beams. *Phys. Fluids B* **4**, 2203.

GERIGK, F. (2003). Halo Studies for the ESS and Linac4 Front-Ends. In *Beam Halo Dynamics, Diagnostics, and Collimation: 29th ICFA Advanced Beam Dynamics Workshop on Beam Halo Dynamics, Diagnostics, and Collimation*, AIP Conf. Proc. No. 693, page 61, New York. American Institute of Physics.

GERIGK, F. (2004). Beam Halo in High-Intensity Hadron Accelerator Caused by Statistical Gradient Errors. *Phys. Rev. ST Accel. Beams* **7**, 064202.

GILSON, E. P. (2008). private communication.

GILSON, E. P., CHUNG, M., DAVIDSON, R. C., DORF, M., EFTHIMION, P. C., and MAJESKI, R. (2006). Experimental Simulations of Beam Propagation over Large Distances in a Compact Linear Paul Trap. *Phys. Plasmas* **13**, 056705.

GILSON, E. P., CHUNG, M., DAVIDSON, R. C., EFTHIMION, P. C., and MAJESKI, R. (2007a). Transverse Beam Compression on the Paul Trap Simulator Experiment. *Phys. Rev. ST Accel. Beams* **10**, 124201.

GILSON, E. P., CHUNG, M., DAVIDSON, R. C., EFTHIMION, P. C., MAJESKI, R., and GODBEHERE, A. (2007b). Detection of Collective Beam Modes in the Paul Trap Simulator Experiment. In *Bulletin of the American Physical Society*, page 161. American Physical Society, College Park.

GILSON, E. P., CHUNG, M., DAVIDSON, R. C., EFTHIMION, P. C., MAJESKI, R., and STARTSEV, E. A. (2005). Simulation of Long-Distance Beam Propagation in the Paul Trap Simulator Experiment. *Nucl. Instrum. Methods Phys. Res. A* **544**, 171.

GILSON, E. P., DAVIDSON, R. C., EFTHIMION, P. C., and MAJESKI, R. (2004). Paul Trap Simulator Experiment to Simulate Intense Beam Propagation in Alternating Gradient Transport Systems. *Phys. Rev. Lett.* **92**, 155002.

GILSON, E. P., DAVIDSON, R. C., EFTHIMION, P. C., MAJESKI, R., and QIN, H. (2003a). The Paul Trap Simulator Experiment. *Laser and Particle Beams* **21**, 549.

GILSON, E. P., DAVIDSON, R. C., EFTHIMION, P. C., MAJESKI, R., and QIN, H. (2003b). Recent Results from the Paul Trap Simulator Experiment. In *Proceedings of the 2003 Particle Accelerator Conference*, page 2655. IEEE.

GLUCKSTERN, R. L. (1994). Analytical Model for Halo Formation in High Current Ion Linacs. *Phys. Rev. Lett.* **73**, 1247.

GOLDSTON, R. J. and RUTHERFORD, P. H. (1995). *Introduction to Plasma Physics.* Institute of Physics Publishing, Bristol and Philadelphia.

GORGADZE, V., PASQUINI, T. A., FAJANS, J., and WURTELE, J. S. (2003). Injection into Electron Plasma Traps. *American Institute of Physics Conference Proceedings* **692**, 30.

GRIVET, P. (1965). *Electron Optics.* Pergamon Press, London.

HENDERSON, S., ANDERSON, I., HOLTKAMP, N., and STRAWBRIDGE, C. (2005). *SNS Parameters List.* Oak Ridge National Laboratory.

HENESTROZA, E., EYLON, S., ROY, P. K., YU, S. S., ANDERS, A., BIENIOSEK, F. M., GREENWAY, W. G., LOGAN, B. G., MACGILL, R. A., SHUMAN, D. B., VANECEK, D. L., WALDRON, W. L., SHARP, W. M., HOUCK, T. L., DAVIDSON, R. C., EFTHIMION, P. C., GILSON, E. P., SEFKOW, A. B., WELCH, D. R., ROSE, D. V., and OLSON, C. L. (2004). Design and Characterization of a Neutralized-Transport Experiment for Heavy Ion Fusion. *Phys. Rev. ST Accel. Beams* **7**, 083501.

HILL, D. N. (1983). *Wave-Modified Ion Distributions and Cross-Field Transport Measurements by Laser-Induced Fluorescence.* PhD thesis, University of California, Irvine, Irvine, CA.

HOFMANN, I., STOVALL, J., and WEI, J. (2001). *Summary Report of SNS Miniworkshop on Linac Space Charge.* Oak Ridge National Laboratory.

Huba, J. D. (2004). *NRL Plasma Formulary.* Naval Research Laboratory, Washington, DC.

Humphries, S. (1990). *Charged Particle Beams.* Wiley, New York.

Ikegami, M., Ohkawa, T., Kondo, Y., and Ueno, A. (2004). A Simulation Study on Error Effects in J-PARC Linac. In *Proceedings of 2004 International Linear Accelerator Conference, Lubeck, Germany*, page 345.

Jeon, D. (1999). *SNS Superconducting Linac Beam Dynamics (SNS/ORNL/AP Technical Note).* Oak Ridge National Laboratory.

Kaminsky, M. (1965). *Atomic and Ionic Impact Phenomena on Metal Surfaces.* Springer-Verlag, Berlin.

Kapchinskij, I. M. and Vladimirskij, V. V. (1959). Limitations of Proton Beam Current in a Strong-Focusing Linear Accelerator Associated with the Beam Space Charge. In *Proceedings of the International Conference on High Energy Accelerators and Instrumentation*, page 274. CERN Scientific Information Service, Geneva.

Katsumata, I., Yamasaki, M., Murakami, K., Fujimoto, M., Tsukahara, H., and Nanjo, Y. (1994). Ion Beam Generation from a Thermal Contact-Ionization Plasma Source. *Rev. Sci. Instrum.* **65**, 1392.

Kehne, D., Reiser, M., and Rudd, H. (1991). Experimental Studies of Emittance Growth due to Initial Mismatch of a Space Charge Dominated Beam in a Solenoidal Focusing Channel. In *Proceedings of the IEEE 1991 Particle Accelerator Conference*, page 248. IEEE, New York.

KEITHLEY (1998). *Model 6514 System Electrometer Instruction Manual.* Keithley Instrument, Cleveland.

KEITHLEY (2004). *Low Level Measurements Handbook.* Keithley Instrument, Cleveland.

KISHEK, R. (2007). private communication.

KJÆRGAARD, N. and DREWSEN, M. (2001). Crystalline Beam Emulations in a Pulse-Excited Linear Paul Trap. *Phys. Plasmas* **8**, 1371.

KOERBER, T. W., SCHACHT, M. H., HENDRICKSON, K. R. G., NAGOURNEY, W., and FORTSON, E. N. (2002). RF Spectroscopy with a Single Ba^+ Ion. *Phys. Rev. Lett.* **88**, 143002.

LANDAU, L. D. (1946). On the Vibrations of Electronic Plasma. *J. Phys. (USSR)* **10**, 25.

LAPOSTOLLE, P. M. (1971). Possible Emittance Increase through Filamentation due to Space Charge in Continuous Beams. *IEEE Trans. Nucl. Sci.* **NS-18**, 1101.

LAWSON, J. D. (1958). Perveance and the Bennett Pinch Relation in Partially Neutralized Electron Beams. *J. Electron. Control* **5**, 146.

LEE, S. Y. (2004). *Accelerator Physics.* World Scientific, Singapore.

LUND, S. M. and BUKH, B. (2004). Stability Properties of the Transverse Envelope Equations Describing Intense Ion Beam Transport. *Phys. Rev. ST Accel. Beams* **7**, 024801.

MAJOR, F. G., GHEORGHE, V. N., and WERTH, G. (2005). *Charged Particle Traps.* Springer, Berlin.

MALMBERG, J. H. and DEGRASSIE, J. S. (1975). Properties of Nonneutral Plasma. *Phys. Rev. Lett.* **35**, 577–580.

MARTELLI, A. (2003). *Python in a Nutshell*. O'reilly, Sebastopol.

MINTY, M. G. and ZIMMERMANN, F. (2003). *Measurement and Control of Charged Particle Beams*. Springer, Berlin.

MURAKAMI, K., FUKUURA, Y., MIMA, H., and KATSUMATA, I. (1996). Generation of Energetic Barium Atomic Beam for Fusion Plasma Diagnostics. *Rev. Sci. Instrum.* **67**, 1196.

MURAOKA, K. and MAEDA, M. (2001). *Laser-Aided Diagnostics of Plasmas and Gases*. Institute of Physics Publishing, Bristol and Philadelphia.

NRC (1995). *Plasma Science (From Fundamental Research to Technological Applications)*. National Academy Press, Washington, DC.

OKAMOTO, H. and TANAKA, H. (1999). Proposed Experiments for the Study of Beam Halo Formation. *Nucl. Instrum. Methods Phys. Res. A* **437**, 178.

PAUL, W. and STEINWEDEL, H. (1953). Ein Neues Massenspektrometer Ohne Magnetfeld. *Z. Naturforsch. A* **8**, 448.

PENNING, F. M. (1936). Glow Discharge at Low Pressure between Coaxial Cylinders in an Axial Magnetic Field. *Physica.* **3**, 873.

PIERCE, J. R. (1940). Rectilinear Electron Flow in Beams. *J. App. Phys.* **11**, 548.

QIAN, B. L., ZHOU, J., and CHEN, C. (2003). Image-Charge Effects on the Envelope Dynamics of an Unbunched Intense Charged-Particle Beam. *Phys. Rev. ST Accel. Beams* **6**, 014201.

QIAN, Q. (1995). *Nonlinear Dynamics of an Intense Nonneutral Ion Beam Propagating through an Alternating-Gradient Focusing Lattice.* PhD thesis, Princeton University, Princeton, NJ.

QIAN, Q., LEE, W. W., and DAVIDSON, R. C. (1997). Nonlinear δf-Simulation Studies of Intense Ion Beam Propagation through an Alternating-Gradient Quadrupole Focusing Field. *Phys. Plasmas* **4**, 1915.

QIANG, J., RYNE, R. D., BLIND, B., BILLEN, J. H., BHATIA, T., GARNETT, R. W., NEUSCHAEFER, G., and TAKEDA, H. (2001). High-Resolution Parallel Particle-In-Cell Simulations of Beam Dynamics in the Spallation Neutron Source Linac. *Nucl. Instrum. Methods Phys. Res. A* **457**, 1.

QIN, H., DAVIDSON, R. C., and LEE, W. W. (2000). Three-Dimensional Nonlinear Perturbative Particle Simulations of Collective Interactions in Intense Particle Beams. *Phys. Rev. ST Accel. Beams* **3**, 084401; 109901.

REISER, M. (1991). Free Energy and Emittance Growth in Nonstationary Charged Particle Beams. *J. Appl. Phys.* **70**, 1919.

REISER, M. (1994). *Theory and Design of Charged Particle Beams.* Wiley, New York.

REISER, M. and BROWN, N. (1993). Thermal Distribution of Relativistic Particle Beams with Space Charge. *Phys. Rev. Lett.* **71**, 2911.

ROSENZWEIG, J. B. (2003). *Fundamentals of Beam Physics.* Oxford, New York.

RYNE, R. D., QIANG, J., and HABIB, S. (1999). Computational Challenges in High Intensity Ion Beam Physics. In *Proceedings of the 2nd ICFA Advanced Accelerator*

Workshop on The Physics of High Brightness Beams, page 91. World Scientific, Singapore.

SACHERER, F. J. (1971). RMS Envelope Equations with Space Charge. *IEEE Trans. Nucl. Sci.* **NS-18**, 1105.

SAKAI, Y., KATSUMATA, I., and OSHIO, T. (1983). Compact Metal-Ion Beam Source Using Thermal Contact Ionizer. *Jpn. J. Appl. Phys.* **22**, 1048.

SCHMIDT, R., ASSMANN, R., CARLIER, E., DEHNING, B., DENZ, R., GODDARD, B., HOLZER, E. B., KAIN, V., PUCCIO, B., TODD, B., UYTHOVEN, J., WENNINGER, J., and ZERLAUTH, M. (2006). Protection of the CERN Large Hadron Collider. *New J. Phys.* **8**, 290.

SEFKOW, A. B. and DAVIDSON, R. C. (2006). Theoretical Models for Describing Longitudinal Bunch Compression in the Neutralized Drift Compression Experiment. *Phys. Rev. ST Accel. Beams* **9**, 090101.

SIDERIS, I. V. and BOHN, C. L. (2004). Production of Enhanced Halos via Collective Modes and Colored Noise. *Phys. Rev. ST Accel. Beams* **7**, 104202.

SPENCER, C. and RHEE, S. (2003). Cost Based Failure Modes and Effects Analysis (FMEA) for Systems of Accelerator Magnets. In *Proceedings of 2003 Particle Accelerator Conference, Portland, Oregon*, page 345, Piscataway, NJ. IEEE.

STARTSEV, E. A., DAVIDSON, R. C., and QIN, H. (2003). Analytical Theory and Nonlinear δf Perturbative Simulations of Temperature Anisotropy Instability in Intense Charged Particle Beams. *Phys. Rev. ST Accel. Beams* **6**, 084401.

STIX, T. H. (1992). *Waves in Plasmas.* American Institute of Physics, New York.

STOLTZFUS-DUECK, T. and KROMMES, J. A. (2006). private communication.

STRASBURG, S. (2001). *Dynamics of Intense Charged-Particle Beams*. PhD thesis, Princeton University, Princeton, NJ.

STREHL, P. (2006). *Beam Instrumentation and Diagnostics*. Springer, Berlin.

WALTER, M., BAI, G., BERNAL, S., FELDMAN, D., GODLOVE, T., HARBER, I., HOLLOWAY, M., KISHEK, R., O'SHEA, P., PAPADOPOULOUS, C., QUINN, B., REISER, M., STRATAKIS, D., TOBIN, C., and WILSON, M. (2006). Commissioning of the University of Maryland Electron Ring (UMER): Advances toward Multiturn Operation. *Phys. Plasmas* **13**, 056703.

WANGLER, T. (1998). *RF Linear Accelerators*. Wiley, New York.

WANGLER, T. P., CRANDALL, K. R., RYNE, R., and WANG, T. S. (1998). Particle-Core Model for Transverse Dynamics of Beam Halo. *Phys. Rev. ST Accel. Beams* **1**, 084201.

WIEDEMANN, H. (1999). *Particle Accelerator Physics I*. Springer, Berlin.

WIKIPEDIA (2008). `http://en.wikipedia.org/wiki/`.

WILSON, E. (2004). *An Introduction to Particle Accelerators*. Oxford, New York.

WILSON, R. G. and BREWER, G. R. (1973). *Ion Beams*. Wiley, New York.

WU, X., DOLEANS, M., GORELOV, D., GRIMM, T. L., MARTI, F., and YORK, R. C. (2005). Failure Modes Analysis for the MSU RIA Driver Linac. In *Proceedings of the 2005 Particle Accelerator Conference, Knoxville, Tennessee*, page 1868, Piscataway, NJ. IEEE.

YOON, P. S., CHOU, W., and BOHN, C. L. (2005). Simulations of Error-Induced Beam Degradation in Fermilab's Booster Synchrotron. In *Proceedings of the 2005 Particle Accelerator Conference, Knoxville, Tennessee*, page 117, Piscataway, NJ. IEEE.

ZIMMERMANN, F. (2004). Review of Single Bunch Instabilities Driven by an Electron Cloud. *Phys. Rev. ST Accel. Beams* **7**, 124801.